Sand Transport Processes in the Surf and Swash Zones

Joep van der Zanden

SAND TRANSPORT PROCESSES IN THE SURF AND SWASH ZONES

Joep van der Zanden

Promotion committee:

prof. dr. G.P.M.R. Dewulf	University of Twente, chairman and secretary
prof. dr. S.J.M.H. Hulscher	University of Twente, promotor
dr. ir. J.S. Ribberink	University of Twente, co-promotor
prof. dr. T. O'Donoghue	University of Aberdeen
prof. dr. B.G. Ruessink	Utrecht University
prof. dr. ir. A.J.H.M. Reniers	Delft University of Technology
prof. dr. R. Ranasinghe	UNESCO-IHE & University of Twente
dr. ir. J.J. van der Werf	Deltares & University of Twente
dr. ir. C.M. Dohmen-Janssen	University of Twente

The work presented in this thesis was performed at the Department of Water Engineering and Management, Faculty of Engineering Technology, of the University of Twente. This research is supported by the Dutch Technology Foundation STW, which is part of the Netherlands Organisation for Scientific Research (NWO) and partly funded by the Ministry of Economic Affairs (project number 12058), with additional funding by EPSRC (EP/J00507X/1, EP/J005541/1) through the joint UK/Dutch SINBAD project.

ISBN: 978-90-365-4245-6
DOI: 10.3990/1.9789036542456
URL: http://dx.doi.org/10.3990/1.9789036542456
Cover photo: Waves breaking on the Aberdeen beach (by Joep van der Zanden)
Printed by Gildeprint Drukkerijen, Enschede, The Netherlands

SAND TRANSPORT PROCESSES IN THE SURF AND SWASH ZONES

PROEFSCHRIFT

ter verkrijging van
de graad van doctor aan de Universiteit Twente,
op gezag van de rector magnificus,
prof. dr. T.T.M. Palstra,
volgens besluit van het College voor Promoties
in het openbaar te verdedigen
op vrijdag 9 december 2016 om 14.45 uur

door

Joep van der Zanden
geboren op 11 oktober 1987
te Roermond

Dit proefschrift is goedgekeurd door:

prof. dr. S.J.M.H. Hulscher	promotor
dr. ir. J.S. Ribberink	co-promotor

A grain of sand is a moment of creation,
and the universe has taken millions of years to create it.
So all you have to do is contemplate a simple grain of sand,
and you will see in it all the marvels of the world.

- Paulo Coelho (*the Alchemist*)

Contents

Preface

Hoe interessant het gedrag van zandkorreltjes en waterdeeltjes ook is, deze studie was onmogelijk zonder de inspiratie van de mensen om me heen. Iedereen die me geholpen heeft, hetzij door goede wetenschappelijke adviezen of juist door momentjes van ontspanning, wil ik daarom van harte bedanken. Dit boekwerk is ook een beetje van jullie..!

Allereerst wil ik Jan ontzettend bedanken voor de intensieve begeleiding. Van begin tot eind bleek je een schier onuitputtelijke bron van kennis en ideeën, en je bevlogenheid bracht me er telkens toe om nog even een extra onderzoeksstap te zetten. Bovendien voelde je haarfijn de momenten aan waarop het even wat minder lekker liep, en koos je ook op die momenten de juiste toon.

Suzanne, dankzij de uitvoerige samenwerking met Jan en andere SINBAD-collega's volstond voor jou een rol wat meer op de achtergrond. Juist daardoor kon je mijn schrijfsels als neutrale lezer en met frisse blik beoordelen. Bedankt voor alle nuttige feedback, met name tijdens de eindfase.

Dominic, zonder jouw bijdrage was ik nog niet veel verder gekomen dan zand scheppen in het lab. Zes maanden met jou opgescheept zitten in Barcelona was weliswaar vermoeiend (een 9 tot 5-mentaliteit is jou vreemd) maar tegelijkertijd een gezellige en goede leerschool (aan bod kwamen de interessantste papers, de handigste Matlab-routines, de beste recepten, de obscuurste hiphop, de lekkerste biertjes, en de flauwste Breaking Bad-woordgrappen). Ook mijn 'sabbatical' halfjaar in Aberdeen was een groot succes, vooral dankzij de gastvrijheid van jou en Bee – bedankt, en ik kom graag nog eens op bezoek!

Among the best things this PhD research brought me was meeting so many wise, helpful, friendly and passionate researchers. Iván and CIEM lab colleagues, thanks for your hospitality and your sacrifices during the experiments, I'm looking forward to visiting you in Barcelona again. David, it was always a pleasure discussing results with you, I especially appreciate your incredible patience when thoroughly explaining the complex world of acoustics. Tom, your feedback on the results and my writings and your keen eye for detail were invaluable; I also want to thank you for hosting me at the University of Aberdeen. José, your lessons about waves, sediment transport, and data processing techniques during my first PhD years proved to be priceless during the remainder of my research.

Who says that meetings are dull? The SINBAD project meetings were always something to look forward to and I'm very grateful to all other involved researchers (Ming Li, Justin Finn,

Jebbe van der Werf, Alan Davies, Wouter Kranenburg, Niels Jacobsen, Mahesa Bhawanin and Peter Thorne) and users (Henk Steetzel, Noel Beech, Dirk-Jan Walstra, James Sutherland) for their useful feedback and discussions. Special thanks to Àngels: during the daily struggle you were often the one supporting me with good advice and positive vibes. It's an honor that you're one my paranymphs during the defense!

Van een dagelijkse sleur is geen sprake wanneer je gezellige collega's hebt..! Erik, dankzij jouw hartelijkheid vond ik snel m'n draai bij WEM en in Enschede. Bedankt voor alle gezelligheid tijdens etentjes, borrels, en tochtjes op de racefiets! Juancho, we started around the same time, how great is it that we will defend our PhD's on the same day?! 'Living' in W-105 was great fun, especially when sharing similar humor and music preference – I still celebrate the occasional Kanye Friday! Your vision on politics and life in general really widened my own views, but you especially supported me by confronting me with my bad habits. Lianne, als rasechte sfeermaker bracht je ontzettend veel gezelligheid in onze vakgroep, ons kantoor in het bijzonder. Het was fijn om een partner in crime te hebben bij het organiseren van DagHappen en borrels! Pieter, na de wekelijkse lunchruns keerde ik altijd weer met een fris en leeg hoofd terug – met name dankzij de discussies over sport, het nieuws, en de kommer en kwel van de universitair onderzoeker, een en ander opgediend met een continue stroom aan de allerbeste woordgrappen. Geert, ook jij was altijd te porren voor een sociale activiteit, ongeacht of het een lunch(run), een etentje, een spelletjesavond, of een lange fietstocht betrof – bedankt voor de gezelligheid!

Graag wil ik Anke, Joke, Brigitte en Monique bedanken voor al het regelwerk achter de schermen en voor de sociale cohesie binnen WEM! René, bedankt voor je onmisbare hulp tijdens mijn eerste jaar, met name bij het testen van het nieuwe CCM+-systeem. Voor de gezellige dagelijkse babbels in de koffiecorner en tijdens de lunch(-wandelingen) wil ik Abebe, Anouk, Bart, Bas, Denie, Filipe, Joanne, Jolanthe, Juliette, Kathelijne, Kurt, Leonardo, Michiel, Nicholas, Olav, Rick, Ronald, Suleyman, Wenlong en alle anderen hartelijk bedanken! Abe, Bram, Mick, Roelof en Sjoerd: bedankt voor jullie bijdragen aan dit onderzoek, ik heb ontzettend veel van jullie geleerd.

Je zou het bijna vergeten, maar gelukkig is er ook nog een leven naast academia. Ik ben vereerd met zoveel vrienden die me bleven ondersteunen, ook als ik me in de verste uithoeken van Europa begaf. Dit schrijvende besef ik me: wel opvallend dat ik in een paar maanden Aberdeen en Barcelona evenzoveel visite heb ontvangen als in al die jaren Enschede…

Lau, een betere mental coach dan jij kon ik niet treffen: bij momenten van twijfel aan mezelf stond je altijd paraat om mijn zelfvertrouwen weer wat op te vijzelen. Supermooi dat je ook paranimf wil zijn, van Zummere en nie bang! GJ, je buitenlandse avontuurtjes zijn nu wel mooi genoeg geweest hoor – al die tijd moest ik maar weer andere concert- en fietsbuddy's zoeken! Maar zonder gekkigheid: supermooi dat we nog steeds contact hebben en ik kijk uit naar de volgende racefietsvakantie in de bergen. Ken, als levensgenieter pur sang liet je me vaak zien dat er belangrijker zaken dan werk zijn. Je rust en wijze adviezen waren van grote steun, en ik

kijk ernaar uit om weer vaker te kunnen fietsen nu we allebei een burgerlijk huisje in Wageningen betrokken hebben!

Van de hele dag stil zitten is nog nooit iemand gelukkig geworden, dus daarom wil ik graag al mijn sportbuddy's bedanken dat ze me naast m'n PhD activeerden. Allereerst wil ik Arend, Dennis, Evelien, Evi, Feike, Imke, Ivo, Kim, Lennart, Levinus, Lex, Marloes, Mischa, Nout, Uwi, Willemijn en alle andere oud-Tartleten bedanken voor de vriendschap tijdens en naast het hardlopen. Berry, Renske en Tim: de etentjes en weekendjes met oud-Thymos zijn altijd vanouds gezellig..! Ook alle Kronauten bedankt voor de gezelligheid tijdens en naast de trainingen.

Despite the diminishing hope of a successful breakthrough with our punk band, I very much enjoyed the rehearsals with the Swafflers/Kapsalöns. Juancho, Filipe, Mireia and Gérard: many thanks for the good fun!

De families van Buul en van der Zanden wil ik bedanken voor hun betrokkenheid en voor de ouderwetse gezelligheid wanneer we elkaar zien. Bovenal dank aan mijn opa's en oma's Harry, Riet, Frans en Truus: jullie hebben me altijd geïnspireerd om hard te werken, met liefde voor de natuur en de medemens. Helaas hebben jullie allemaal wel het begin, maar niet het eind van dit promotietraject mee mogen maken. Ook wil ik hier graag de familie van de Boer (Roelof, Sierdje, Geert en Annie) danken: met een hoofd vol met resultaten en computerscriptjes zijn de weekendjes in Boijl perfect om weer helemaal tot rust te komen.

Pap en mam: ontzettend fijn dat jullie er altijd voor me zijn, voor wijze raad of gewoon voor een ontspannen weekendje. Broertje: altijd gezellig om je te zien en om samen op te trekken om nieuwe muziek te ontdekken.

Tot slot wil ik graag m'n meisje Anneke bedanken. Na al mijn midweekjes Enschede, maandjes Barcelona en het halfjaartje Aberdeen, zijn we nog steeds niet van elkaar af..! Gelukkig maar, want jij weet vaak beter dan ikzelf wat me gelukkig maakt. Zonder jouw positieve energie, je lieve zorgzaamheid, en je geduld bij het aanhoren van mijn monologen over turbulentie, was ik nu vast al helemaal doorgedraaid. Ik kijk uit naar nieuwe avonturen saampjes!

Joep van der Zanden, November 2016

Summary

Coastal regions are in many ways relevant to society, but are widely threatened by erosion. Long-term predictions of beach morphology using numerical models can help coastal managers to develop cost-effective coastal protection strategies. Such models operate at a large spatial and temporal domain and rely on semi-empirical parameterizations to account for underlying small-scale processes. Parameterizations for sand transport have mainly been developed on the basis of measurements under non-breaking waves. When these sand transport models are applied to the wave breaking region and the swash zone – where waves run up and down on the beach – they fail at properly predicting sand transport rates. This is attributed to a lack of understanding of how sand transport is affected by additional breaking-related processes.

The aim of this thesis is therefore to improve understanding of sand transport physics in the breaking and swash zone. This objective is pursued through controlled experiments in a large-scale wave flume with a mobile medium-sand bed during two campaigns: one focusing on the breaking region, the other on the swash zone. During both campaigns, the use of novel instruments enables measurements of sediment transport processes near the bed with much higher resolution than during previous studies. Effects of wave breaking and flow non-uniformity on sediment transport dynamics are identified by comparing results with existing knowledge of sand transport dynamics for non-breaking waves. The results are then used to suggest improvements for sand transport models in the breaking and swash zone.

Chapters 2 to 4 present measurements of hydrodynamics and sand transport dynamics under a monochromatic plunging breaking wave around an evolving breaker bar. **Chapter 2** focuses on the hydrodynamics in the breaking region, with particular interest on flow and turbulence over the near-bed region which includes the wave bottom boundary layer. The measurements in this region, obtained with a prototype acoustic concentration and velocity profiler (ACVP), are believed to be the first measurements of the complete wave bottom boundary layer under large-scale breaking waves. Wave breaking leads to large turbulence production and an increase in turbulent kinetic energy (TKE) in the complete water column. Breaking-generated turbulence also invades the boundary layer. Near the plunge point, this invasion occurs during two instances of the wave cycle: a first occurrence rapidly after wave plunging, and a second occurrence during the wave trough phase when undertow and periodic velocities transport TKE towards the breaker bar. The invasion results in an increase in TKE inside the wave bottom boundary layer with a factor 3 from shoaling to breaking region. Breaking-generated turbulence travels back and forth between breaking and shoaling region due to advection by orbital and undertow velocities. Consequently, the near-bed region affected by wave breaking extends horizontally to about 3 m offshore from the plunge point. Time-averaged velocities in

the wave bottom boundary layer are offshore-directed and are generally dominated by the undertow. The non-dimensional wave bottom boundary layer thickness increases with a factor 2-3 in the breaking region, which is caused by flow divergence induced by the bar geometry and/or by effects of breaking-generated turbulence.

Measurements during the same experiment are used in **Chapter 3** to assess wave breaking effects on suspended sediment transport processes and to examine the spatial distribution of sediment fluxes. Sediment concentrations are measured at outer-flow elevations using a transverse suction system and near the bed using the ACVP. The ACVP also measures velocities and allows the examination of collocated TKE and suspended sediment concentrations and fluxes in the near-bed region with much higher resolution than previous studies. Results show that suspended sediment concentrations increase by up to one order of magnitude from shoaling to breaking region. This is due to effects of breaking-generated turbulence, which does not only enhance vertical mixing but is in the present study also identified as the main driver for sediment pick-up. Outer-flow wave-averaged sediment fluxes are offshore-directed over most of the water column, but significant onshore contributions are found at elevations between wave trough and wave crest level in the breaking region and at elevations inside the wave bottom boundary layer at locations offshore from the plunge point. The latter is due to a significant onshore-directed wave-related suspended sediment transport contribution that is generally confined to the wave bottom boundary layer. The measurements are used to relate the spatiotemporal variation in suspended sediment concentrations to horizontal advection and to vertical exchange between the bedload and suspension layer. This analysis reveals that the entrainment of sediment in the bar trough occurs primarily during the wave trough phase, when both near-bed velocity magnitude and near-bed (breaking-generated) TKE are highest. The entrained particles are almost instantly advected offshore during the wave trough phase, and are deposited near the bar crest during the wave crest phase when velocity magnitudes reduce. The suspended particles further follow an intra-wave onshore-offshore excursion between shoaling and breaking region. This excursion is consistent with spatiotemporal patterns in TKE, which suggests that sediment particles are trapped in breaking-generated vortices that are advected back and forth following the orbital motion.

Chapter 4 focuses on effects of wave breaking on bedload and grain-size sorting processes, and on bedload and suspended transport contributions to the breaker bar morphodynamics. Two novel conductivity-based concentration measurement (CCM^{+}) tanks measured concentrations and particle velocities in the bedload (sheet flow) layer at the breaker bar crest. Sheet flow layer concentrations and thicknesses do not reveal a significant effect of breaking-generated turbulence, but are affected by cross-shore advection of sediment. This shows that bedload dynamics are not fully controlled by local hydrodynamic forcing. Net bedload transport rates show strong cross-shore variation which relates firstly to variations in acceleration and velocity skewness (for locations from shoaling zone up to bar crest), and secondly to variations in local bed slope and near-bed TKE (in breaking region along shoreward-facing bar slope). During the experiment the bar slowly migrates onshore whilst its crest grows and its trough deepens. This occurs under the influence of (i) onshore-directed bedload transport, which erodes the offshore bar slope and accretes the bar crest, and (ii) offshore-directed suspended load, which induces net pick-up at the bar trough and net deposition at the bar crest. Both transport components are of similar magnitude, but bedload

dominates in the shoaling zone while suspended load is larger in the breaking and inner surf zone. Grain-size distributions of suspended sediment samples show that sediment pick-up and vertical mixing is size-selective (i.e. the fraction of fine sediment is relatively large) in the inner surf zone in presence of vortex ripples, but size-indifferent (i.e. also coarsest grains are entrained) in the breaking region in presence of large and energetic breaking-induced turbulent vortices. Selective transport by both bedload and suspended sediment transport leads to a cross-shore coarsening of sediment in the bed from shoaling to inner surf zone.

Sediment transport in the swash zone is studied through another experimental campaign (**Chapter 5**). The novel CCM$^+$ is deployed for the first time, and is used to study the response of the sheet flow layer and the intra-swash bed level to energetic swash events with strong wave-swash interactions. The highly non-uniform flow conditions under these swash events lead to intra-swash bed level changes of up to 1 cm, with rapid erosion during the early uprush phase and gradual accretion during the backwash. The bed level changes are explained by cross-shore advection of sediment between the lower and mid/upper swash zone at an intra-swash time scale. This advection also affects sheet flow concentrations and thicknesses, leading to much larger sheet flow thicknesses than expected based purely on the horizontal oscillatory velocities. Moreover, the sheet flow thickness increases temporally under events of strong wave-backwash interactions that enhance local turbulence. Both factors (sediment advection and bore turbulence) may affect sheet flow transport rates in the swash zone.

The general discussion (**Chapter 6**) reflects on the implications of the present study's results for the future development of engineering-type sand transport and morphodynamic models.

Samenvatting

Kustgebieden zijn van groot maatschappelijk en economisch belang maar worden wereldwijd bedreigd door erosie. Langetermijnvoorspellingen van kustmorfologie met numerieke modellen kunnen kustbeheerders helpen met het ontwikkelen van kosteneffectieve kustbeschermingsstrategieën. Zulke modellen werken op een grote ruimte- en tijdsschaal en berusten op eenvoudige formules van onderliggende fysische processen. Formules voor zandtransport zijn ontwikkeld op basis van metingen onder niet-brekende golven. In het gebied waar golven breken (branding) en het strand oplopen (golfoploopzone) hebben deze zandtransport-formules echter een grote foutmarge. Hierdoor lukt het niet goed lukt om de kustdynamiek te modelleren. Deze foutieve voorspellingen komen voort uit een onvoldoende begrip van zandtransportprocessen onder brekende golven.

Het doel van dit promotieonderzoek is daarom om de fysische processen van zandtransport in de branding en de golfoploopzone beter te begrijpen. Hiertoe zijn gecontroleerde experimenten met een mobiel zandbed in een grootschalige golfgoot gedaan. Resultaten van twee meetcampagnes worden gepresenteerd: de eerste gericht op de branding, de tweede op de golfoploopzone. Tijdens beide campagnes zijn nieuwe meetinstrumenten ingezet die sedimenttransportprocessen aan het bed met veel hogere resolutie kunnen meten dan tijdens voorgaande studies. De metingen worden vergeleken met eerdere observaties onder niet-brekende golven om zodoende de effecten van golfbreking en de niet-uniformiteit van de stroming op zandtransport te kunnen begrijpen. De resultaten worden vervolgens gebruikt om aanbevelingen te doen voor het verbeteren van zandtransportformules.

Hoofdstukken 2 tot 4 presenteren metingen van hydrodynamica en zandtransportprocessen rond een evoluerende brekerbank onder een regelmatige duikend ('plunging') brekende golf. **Hoofdstuk 2** richt zich op de gemeten hydrodynamica, met name op de stroming en turbulentie nabij het bed, inclusief de golfbodemgrenslaag, waar een groot deel van het sedimenttransport plaatsvindt. De metingen in deze laag, verkregen met een prototype akoestische sensor voor concentratie- en snelheidsprofielen (ACVP), zijn vermoedelijk de eerste metingen van de volledige golfbodemgrenslaag onder grootschalige brekende golven. Golfbreking leidt tot sterke productie van turbulentie en een toename in turbulente kinetische energie (TKE) over de gehele waterkolom. Deze turbulentie bereikt het bed, hetgeen tot een factor 3 toename van TKE in de grenslaag leidt in vergelijking met de pre-breekzone. De aankomst van turbulentie bij het bed gebeurt met name tijdens de golftrogfase, maar plaatselijk in de buurt van het breekpunt gebeurt dit ook tijdens de golftopfase. De breking-geproduceerde turbulentie volgt de orbitaalsnelheden en reist zodoende op en neer tussen de pre-breekzone en de branding. De tijdsgemiddelde snelheden in de grenslaag worden gedomineerd door de retourstroom. De dimensieloze golfgrenslaagdikte neemt met een factor

2 à 3 toe onder de brekende golf, wat verklaard kan worden door de toename in turbulentie en/of door stromingsdivergentie langs de steile helling aan de kustzijde van de brekerbank.

De effecten van golfbreking op gesuspendeerd sediment (concentraties en fluxen) in de brandingszone worden onderzocht in **Hoofdstuk 3**. Zandconcentraties zijn gemeten nabij het bed (met de ACVP) en boven de golfbodemgrenslaag (met een afzuigsysteem). De ACVP meet ook snelheden en levert simultane metingen van TKE en suspensieconcentraties en –fluxen met veel hogere resolutie dan voorgaande studies. Resultaten laten zien dat zandconcentraties met een orde grootte toenemen van de pre-breekzone naar de branding. Dit komt door de breking-geproduceerde turbulentie, die in deze studie niet alleen zorgt voor sterkere verticale menging maar ook voor het oppikken van sediment aan het bed. Suspensiefluxen zijn zeewaarts gericht over het gros van de waterkolom, maar significante kustwaartse fluxen zijn gemeten boven golftrogniveau in de branding en in de golfbodemgrenslaag in de metingen voor het breekpunt. Deze laatste kustwaartse fluxen worden verklaard door een significante bijdrage van het golfgerelateerde suspensietransport dat over het algemeen beperkt blijft tot de golfbodemgrenslaag. De resultaten laten verder een complex patroon van intra-golf sedimentconcentratieveranderingen zien. Deze veranderingen komen door horizontale convectie en door verticale uitwisseling van sediment tussen de bodemtransportlaag en de suspensielaag. Zeewaarts van de top van de brekerbank reist het sediment horizontaal op en neer op eenzelfde manier als de brekinggeproduceerde turbulentie. In het gebied tussen de top en trog van de brekerbank worden sedimentconcentratieveranderingen verklaard door opwerveling (boven de trog van de bank), zeewaartse afvoer, en depositie (op de top van de bank), waarbij elke term sterk verandert binnen de golfcyclus.

Hoofdstuk 4 behandelt de effecten van golfbreking op bodemtransportprocessen en korrelgroottesortering, en behandelt verder hoe het bodem- en suspensietransport bijdraagt aan de groei van de brekerbank. Zandconcentraties en korrelsnelheden in de bodemtransportlaag (sheetflowlaag) zijn gemeten op de brekerbank met twee nieuw gebouwde geleidbaarheidstype meetsystemen (CCM^{+}). Concentraties en diktes van de sheetflowlaag laten geen effecten zien van de aanwezige externe turbulentie, maar worden wel beïnvloed door horizontaal aangevoerd sediment. Het netto bodemtransport verandert duidelijk langs de brekerbank. Deze variatie wordt met name bepaald door veranderingen in de golfvorm en in de lokale helling en aanwezige TKE. Tijdens het experiment migreert de brekerbank richting de kust terwijl de banktop groeit en de zandtrog zich verdiept. Dit komt door een combinatie van (i) kustwaarts gericht bodemtransport, dat leidt tot erosie van de zeewaartse helling en depositie op de top van de bank, en (ii) zeewaarts gericht suspensietransport, dat leidt tot erosie van de zandtrog en depositie op de bank. Beide transportcomponenten zijn van vergelijkbare grootte, maar bodemtransport domineert voor het breekpunt en suspensietransport na het breekpunt. Korrelgrootteverdelingen van suspensiemonsters laten zien dat de grote turbulente wervels in de breekzone weinig onderscheid maken tussen korrels van verschillende grootte, terwijl de kleinere wervels op andere locaties zorgen voor een verticale differentiatie in korrelgrootteverdeling van gesuspendeerd sediment (i.e. het gesuspendeerde sediment is relatief fijner). Door selectief bodem- en suspensietransport wordt de korrelgrootte in het bed steeds fijner in de pre-breekzone en steeds grover in de branding.

Het zandtransport in de golfoploopzone is bestudeerd tijdens een ander experiment (**Hoofdstuk 5**). De CCM$^+$ is tijdens dit experiment voor het eerst toegepast, en wordt gebruikt om de reactie van de sheetflowlaag en het bedniveau op een energieke golfoploop met sterke golf-golfoploop-interacties te bestuderen. Doordat het stromingsveld onder de energieke gofoploopcondities sterk niet-uniform is, verandert het bedniveau sterk (fluctuaties à 1 cm) binnen de golfoploopcyclus. Tijdens de eerste fase van de golfoploop, wanneer golven omhoog lopen op het strand, treedt een plotse, sterke erosie van het bed op. Tijdens de tweede fase van de golfoploop, wanneer het water vanaf het strand terugstroomt, keert het bed langzaam terug naar vrijwel het originele niveau. Dit wordt verklaard door een horizontale excursie van sediment tussen verschillende gebieden binnen de golfoploopzone. Deze excursie beïnvloedt ook de sheetflowlaag: deze is veel dikker dan verwacht op basis van enkel de horizontale oscillerende snelheid. De sheetflowlaag wordt bovendien sterk beïnvloed door turbulentie opgewekt door de interacties tussen verschillende golven. Deze turbulentie en de horizontale advectie van sediment hebben mogelijk een sterke invloed op het bodemtransport in de golfoploopzone.

De discussie in **Hoofdstuk 6** spitst zich onder meer toe op hoe de nieuw verkregen inzichten kunnen bijdragen aan het verbeteren van zandtransportformules en morfodynamische modellen.

1 Introduction

1.1 Research context

Coastal regions are often densely populated and offer various services to society. In the Netherlands, the primary function of the coast is the protection of the hinterland against flooding. Other functions of coastal zones include industries and harbors, drinking water supply, tourism, aquaculture, and ecology (Giardino *et al.*, 2011). At the same time, coasts are dynamic areas. At sandy shores (Figure 1.1), sediment is continuously transported in cross-shore and alongshore direction under action of tides, wind waves, and (wave-induced) currents. During calm-weather conditions, cross-shore sediment transport is generally directed shoreward, leading to accretion of the shoreface. Aeolian processes lead to further inland-directed transport of sediment grains and promote dune growth. However, during storms, energetic waves entrain large amounts of sediment that are transported offshore by wave-induced currents, hence resulting in net erosion of the beach.

The erosion rate of coasts increases as a result of sea level rise, land subsidence, and increased storminess (Giardino *et al.*, 2011) and threatens coasts around the world. Human interferences, such as damming of rivers and estuaries, the application of hard structures for coastal reinforcement, and sand and gas mining, may alter the sediment budget and enhance (local) coastal erosion (Giardino *et al.*, 2011; Van der Spek and Lodder, 2015). Averaged over the complete Dutch coastline, these processes lead to a structural net erosion of the shoreface, beach and frontal dunes areas of an estimated 2.6 million m^3 per year over the period 1990-2005 (Van der Spek and Lodder, 2015). Such erosion forms a direct threat to services provided by the coastal region – safety of the inland not being the least of them.

Current Dutch policy in coastal management is directed at maintaining the coastline of 1990, plus creating an extra buffer to cope with future threats (Giardino *et al.*, 2011). This is typically achieved through sand nourishments (7.4 million m^3/y between 1990–2005), that are preferably applied to the shoreface and not directly to the beach in order not to disrupt beach functions and to save costs (Van der Spek and Lodder, 2015). Once in place, the nourished sand is gradually transported onshore under action of the short wind waves, but also acts as a barrier that forces the most energetic waves to break – hence reducing wave energy and erosion rates at the shoreline (Van Duin *et al.*, 2004).

Coastal management can benefit from medium- (5 years) and long-term predictions of coastal morphology that support understanding of the natural behavior of coastal regions. Such predictions can be made using morphodynamic numerical models (Delft3D, Mike, TELEMAC, XBeach) that couple equations for hydrodynamics (waves and currents), sediment transport (bedload and suspension) and bed level changes. Such morphodynamic models operate on a large spatiotemporal domain and rely on parameterizations of small-scale underlying

processes. Sand transport rates are calculated using semi-empirical formulations, discussed in more detail in Section 1.3. These sand transport models are largely based on observations of sand transport processes and transport rates in controlled laboratory conditions, i.e. in oscillatory flow tunnels or wave flumes with non-breaking waves (Van Rijn *et al.*, 2013), and they generally do not consider effects of wave breaking.

Figure 1.1. Waves approaching the beach in Southern Australia. Photo by Carel van der Zanden

Simulations with morphodynamic models can also be used to assess the (cost-)effectiveness of different management (nourishment) strategies, hence supporting decision-making and contributing to cost reduction. This requires a good model performance in terms of simulating hydrodynamics and cross-shore sediment transport processes in the near-shore region. The performance of morphodynamic models in terms of simulating cross-shore sand bar migration was assessed in a number of studies by Van Rijn *et al.* (2003; 2007d; 2011). It was shown that bar migration for erosive laboratory conditions can be simulated 'reasonably well in qualitative sense' (Van Rijn *et al.*, 2007d; 2011), although results do show a mismatch between the exact location and shape of the migrated bar near the location of wave breaking. 'Bad' results were obtained when simulating accretive conditions (Van Rijn *et al.*, 2011), mainly due to over-prediction of erosion rates near the shoreline.

It is concluded that sediment transport in the inner surf and swash zone cannot be properly predicted, which is partly explained by the swash erosion method (Section 1.3) being too crude (Van Rijn *et al.*, 2011). In addition, net transport in this region is the (relatively small) residual of (much larger) offshore- and onshore-directed transport components, and is therefore notoriously difficult to predict (Van Rijn *et al.*, 2003; 2007d). Not surprisingly, the discrepancies between modelled and measured sand bar evolution grow when the time scale is increased to seasonal scale (Van Rijn *et al.*, 2003). These results show a direct need of improving sand transport model formulations for the near-shore (breaking to swash zone) region. To advance transport models, it is essential to first improve understanding of hydrodynamic and sediment transport processes in the breaking and swash zone.

1.2 Cross-shore hydrodynamic and sand transport processes

This study focuses on cross-shore sand transport processes in the near-shore region from the wave breaking point up to the swash zone. **Figure 1.2** illustrates the coexistence of different sediment transport mechanisms along a cross-shore barred profile, and serves as a reference for the applied terminology. The present section offers a concise description of near-shore sediment transport processes and identifies scientific knowledge gaps that are assessed in this thesis.

Wave dynamics

When waves approach the shore, their wave height increases as their celerity decreases. During this *shoaling* process, waves become increasingly non-linear due to energy transfer from the primary wave components to their higher harmonics (Phillips, 1960; Elgar and Guza, 1985). This results in *skewed* waves that are horizontally asymmetric, i.e. with high short-duration *crests* and long-duration flat *troughs*. The higher harmonic constituents partially act as 'free' superimposed waves (Phillips, 1960) that lag the primary wave (Flick *et al.*, 1981; Beji and Battjes, 1993). This leads to *asymmetric* (saw-tooth-shaped) waves, in which the term 'asymmetric' now refers to asymmetry in the vertical plane.

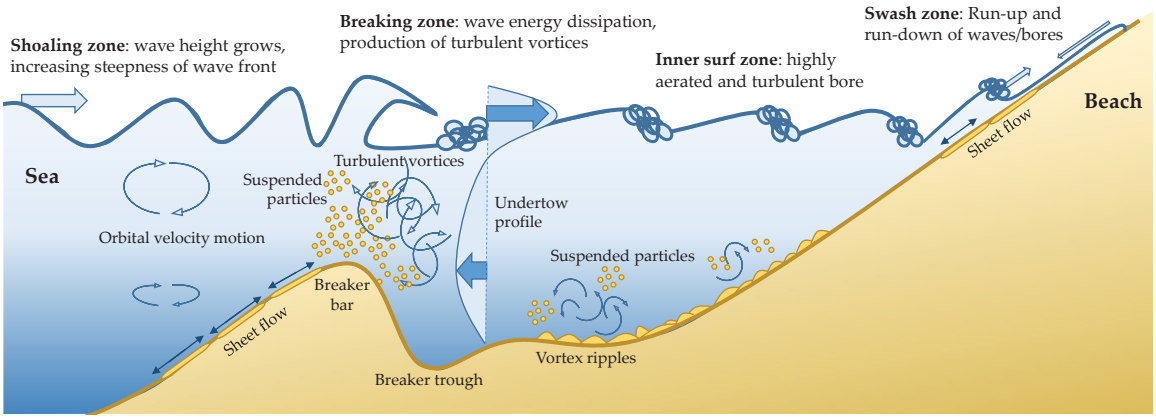

Figure 1.2. Conceptual drawing of cross-shore sediment processes in the near-shore region.

With increasing asymmetry, also the steepness of the wave front increases, eventually leading to *wave breaking*. This can happen in different ways (plunging, spilling, surging, collapsing), depending on wave and bed profile characteristics (Battjes, 1974). Wave breaking leads to a reduction in wave energy and in wave height. The breaking front develops into a *surf bore* (also called surface roller) which continues propagating shoreward along the *inner surf zone* (region between breaking point and the shoreline) while dissipating wave energy. Upon reaching the shore, the surf bore *runs up* on the beach while decelerating due to friction and gravitational forces. The fluid that has ran up on the beach then retreats and accelerates in offshore direction during the *backwash* phase. The region of beach run-up/run-down is termed the *swash zone*. Important for further discussions in this thesis is that hydrodynamics in the swash zone are not solely determined by individual incident short waves, but also by energy contained in *wave groups* (Baldock *et al.*, 2000). In addition, *wave-swash interactions* importantly affect

hydrodynamics (run-up, velocities) and sediment transport processes (e.g. Hughes and Moseley, 2007; Caceres and Alsina, 2012).

Time-averaged velocities

Velocities can be split in a *time-averaged* (net current), *orbital*, and *turbulent* component. Further distinction is made between the *wave bottom boundary layer* (the near-bed region at which orbital velocities are affected by presence of the bed) and the *outer flow* (above the wave bottom boundary layer, up to wave crest level).

Outer-flow net currents are generally offshore-directed in the lower half of the water column as they compensate for the onshore mass flux (Stokes drift) that occurs especially above wave trough level. This time-averaged return current is termed *undertow*. In breaking/broken waves, the onshore mass flux contained in the roller is larger than the mass flux associated with the Stokes drift for non-breaking waves (Svendsen, 1984). Furthermore, the reduction in wave height results in a horizontal momentum flux gradient that drives a horizontally positive (towards the beach) time-averaged pressure gradient (set-up/set-down) (Stive and Wind, 1986). The combination of mass flux increase and the positive pressure gradient leads to an increase in offshore-directed undertow velocities in the breaking region. The shape of the undertow profile is defined by the depth-varying momentum equations which include, next to horizontal gradients in momentum and pressure, terms related to vertical exchange of horizontal momentum by orbital and turbulent velocities (e.g. Svendsen, 1984). All these contributions exhibit strong cross-shore variation, and consequently, time-averaged flow in the breaking region is strongly non-uniform in cross-shore direction.

Orbital velocities have an oscillatory nature, i.e. vary in magnitude and direction during the wave cycle. At outer-flow elevations, orbital velocities are in phase with the water surface level and are directed onshore below the wave crest and offshore below the wave trough. The continuous flow acceleration and deceleration is caused by the time-varying horizontal pressure gradient under progressing waves. Under skewed waves, the orbital crest velocities exceed those during the trough. For asymmetric waves, the *acceleration* during the zero-up crossing (flow reversal from trough to crest) exceeds the acceleration during the zero-down crossing of the wave. Both these processes (termed *orbital velocity skewness* and *asymmetry*) lead to a higher *bed shear stress* exerted by the orbital motion during the crest phase than during the trough phase.

Orbital velocity magnitudes decrease rapidly in a small (compared to the full water column) layer close to the bed. Inside this *wave bottom boundary layer*, horizontal pressure gradients are not the only forcing term for local fluid acceleration/deceleration. Instead, velocities are retarded by bed friction forces that act in the direction opposing the instantaneous velocity vector. The combined forcing of horizontal pressure gradient and bed friction factors yields a phase lead of orbital velocities inside the wave boundary layer over the velocities at *free-stream* elevations in the outer flow directly above this layer. The wave bottom boundary layer is further characterized by time-averaged cross-shore velocities that relate to *streaming* mechanisms, i.e. onshore *progressive wave streaming* under surface waves because horizontal and vertical orbital velocities are not exactly 90° out of phase, and offshore *wave shape streaming*

under skewed and asymmetric waves due to differences in bed-generated turbulence intensities between the crest and trough half-cycle (discussed extensively by Kranenburg, 2013).

The effects of wave breaking on boundary layer hydrodynamics have not yet been examined in detail. Instead, most previous detailed observations of the wave bottom boundary layer were obtained in oscillatory tunnels (e.g. Jonsson and Carlsen, 1976; Sleath, 1987; Jensen *et al.*, 1989; van der A *et al.*, 2011) or under non-breaking waves (Conley and Inman, 1992; Foster *et al.*, 2000; Foster *et al.*, 2006a; Schretlen, 2012). An oscillatory flow tunnel experiment with grid-induced turbulence did show that external (breaking-generated) turbulence importantly affects time-averaged velocities and turbulence dynamics inside the wave bottom boundary layer (Fredsoe *et al.*, 2003).

Turbulence

Turbulent velocity fluctuations are irregular fluctuations associated to 3-dimensional *vortices* (or: *eddies*) and can be generated by a moving fluid's internal shear or by friction with an external object (e.g. Pope, 2000). In the present breaking-wave study, bed friction and wave breaking/surf bores are the primary turbulence production sources (e.g. Feddersen *et al.*, 2007). The magnitude of turbulent fluctuations is commonly expressed in terms of *turbulent kinetic energy*. The turbulent kinetic energy is not fully locally determined, since turbulence spreads horizontally and vertically through advection and diffusion processes (Ting and Kirby, 1995; Boers, 2005). Turbulent vortices are unstable and step-wise break up into smaller vortices, a process that continues until viscous shear stresses trigger the conversion of smallest eddies into heat (*turbulence dissipation*).

Based on turbulence observations in small-scale wave flumes, it has been hypothesized that the correlation between time-varying breaking-generated turbulent kinetic energy and wave phase may contribute to onshore- or offshore-directed sediment transport (Ting and Kirby, 1995; Boers, 2005; De Serio and Mossa, 2006). However, the intra-wave variation in breaking-generated turbulence at the bed has never been examined for large-scale conditions. Instead, most previous studies under large-scale breaking waves in field (e.g. Ruessink, 2010; Grasso *et al.*, 2012) and laboratory (e.g. Scott *et al.*, 2005; Yoon and Cox, 2010) focused on time-averaged turbulence quantities at outer-flow elevations. Therefore, it remains unclear how breaking-generated turbulence may affect time-varying turbulent kinetic energy near the bed, inside the wave bottom boundary layer, and how this in return affects sediment transport.

Bedload transport processes

Total sediment transport in the near-shore region is partitioned into: (i) a *bedload* component, which may be defined on physical arguments as the fraction of sediment grains that is supported by intergranular forces (Bagnold, 1956; Nielsen, 1992) or, more practically, as the moving sediment grains below a particular reference elevation close to the bed (e.g. Van Rijn, 2007a); (ii) a *suspended load* component, primarily driven by turbulence-induced fluid drag (Bagnold, 1956; Nielsen, 1992) and found above the near-bed reference level (Van Rijn, 2007b).

Suspended sediment fluxes can be split into a *current-related* (product of wave-averaged velocities and time-averaged concentrations) and a *wave-related* (product of oscillatory/de-meaned velocities and concentrations) component. The latter can be non-zero in case sediment concentrations are time-dependent during the wave cycle, i.e. in occurrence of higher sediment concentrations during one of the wave half-cycles (crest and trough phase) relative to the other.

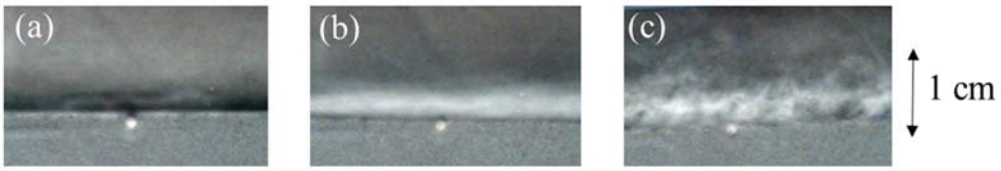

Figure 1.3. Snapshots of sheet flow transport in a small-scale oscillating flow tunnel with fine sand. (a) Start of flow cycle with bed at rest; (b) At maximum orbital velocity, showing a well-developed sheet flow layer with high sediment concentrations; (c) Around flow reversal, showing break-up of the sheet flow layer and the formation of suspension events. Snapshots are taken from video recordings by the author during experiments at the University of Twente as part of the CCM+ development (Chapter 5).

For mildly energetic conditions (e.g. inner surf zone and at deeper water more offshore), bed forms such as *vortex ripples* generally appear. Characteristic for these conditions is the ejection of sediment-laden vortices around each flow reversal (twice per wave cycle), which are transported during the subsequent half-cycle (Van der Werf *et al.*, 2007).

In the breaking region and the swash zone, the energetic waves/surf bores and relatively shallow water depths result in large velocity magnitudes near the bed. If peak velocities are sufficiently large, bed forms are faded out and sediment grains are transported in a thin (O(mm)) high-concentration (100 – 1600 g/L) layer that grows and decays during a wave cycle (Horikawa *et al.*, 1982; Ribberink and Al-Salem, 1995). **Figure 1.3** shows visual observations of such *sheet flow* transport. For medium sand, sand transport in the sheet flow layer responds quasi-instantaneously to bed shear exerted by the flow (Ribberink and Al-Salem, 1995; O'Donoghue and Wright, 2004a). Consequently, under skewed/asymmetric waves, the higher peak bed shear stresses during the crest (relative to trough) phase result in onshore-directed bedload transport for medium sand (O'Donoghue and Wright, 2004b; Schretlen, 2012). Under non-breaking waves, where suspended sediment concentrations are low, the majority of depth-integrated transport over the complete water column is confined to the sheet flow layer (Dohmen-Janssen and Hanes, 2005; Schretlen, 2012).

Transport rates in the sheet flow layer are large and can form a major contribution to total transport rates and to near-shore morphology. Sheet flow dynamics have predominantly been studied in oscillating flow tunnels or in wave flumes with uniform non-breaking waves. An important question from scientific and engineering perspective is whether wave breaking, e.g. due to penetration of breaking-generated turbulence into the wave bottom boundary layer, can significantly affect bedload (sheet flow) transport rates. Observations of bedload transport in a steady flow tunnel with grid-induced turbulence revealed that the presence of external turbulence can significantly enhance bedload transport rates (Sumer *et al.*, 2003). However, no

measurements have been able to reveal if breaking-generated turbulence can affect bedload transport rates and processes.

Suspended sediment transport processes

The bed shear may also lift sediment grains from the bed and bring them into suspension. This lift is driven by an upward-directed pressure gradient that is associated with bed-shear-induced ejected vortices (Sumer and Oguz, 1978). Once suspended, gravitational settling and vertical advective and diffusive mixing lead to vertical concentration profiles that follow an exponential or power-function distribution, depending on the vertical distribution of turbulent kinetic energy (Aagaard and Jensen, 2013). Under breaking waves, higher entrainment and mixing rates lead to an increase in concentrations at outer flow elevations compared to shoaling locations (Nielsen, 1984; Nadaoka *et al.*, 1988; Aagaard and Jensen, 2013). The increased pick-up rates under breaking waves can be attributed to high instantaneous bed shear stresses (Cox *et al.*, 1996) and to upward-directed pressure gradients in the bed under the breaking point (Sumer *et al.*, 2013).

The current-related transport is the depth-integrated product of time-averaged concentrations and velocities (undertow plus streaming profile). Depending on vertical distributions of both variables, the current-related transport can be directed offshore or onshore for non-breaking waves. The net current-related transport is generally directed offshore in the breaking region, due to the increase in undertow magnitudes and in suspended sediment load at outer-flow elevations. If net suspended transport rates are non-uniform, as expected in the breaking region, sediment concentrations at a particular cross-shore location are not only controlled by local vertical processes (i.e. pick-up/deposition and vertical mixing plus settling) but also by the net influx of suspended sediment from adjacent locations (Hanes and Huntley, 1986). This is notably different from suspended transport under non-breaking (shoaling) waves over horizontal beds, which is cross-shore uniform at a wave-averaged time scale.

Based on experimental observations of time-varying turbulence, several small-scale studies have suggested an enhanced wave-related suspended transport rate under plunging waves (Ting and Kirby, 1995; Boers, 2005; De Serio and Mossa, 2006). Onshore-directed wave-related suspended fluxes have indeed been observed in the breaking region (Ruessink *et al.*, 1998; Aagaard and Hughes, 2010; Yoon and Cox, 2012). However, it is not evident whether this relates to breaking-induced turbulent kinetic energy or to wave asymmetry; both parameters are interrelated (as pointed out by van Thiel de Vries *et al.*, 2008). Collocated measurements of turbulence and suspended sediment concentrations in the near-bed region, which includes the wave bottom boundary layer, may likely contribute to the understanding of breaking-generated turbulence effects on wave-related suspended sediment transport.

Sediment transport in the swash zone

The swash zone is characterized by high instantaneous sediment fluxes in both onshore (during uprush) and offshore (backwash) direction, and a relatively small residual net (swash-event-averaged) transport rate (Masselink and Puleo, 2006). High fluxes of bedload (sheet

flow) and suspended load are particularly found during the early uprush and late backwash phases, when velocity magnitudes are at maximum. High suspended sediment concentrations during the uprush phase relate to large amounts of sediment entrained locally by the highly turbulent flow under surf bores (Puleo *et al.*, 2000) but also to pre-suspended sediment which is advected from the inner surf zone into the swash zone (Jackson *et al.*, 2004). Wave-swash interactions may lead to additional local production of turbulence (Chen *et al.*, 2016) and sediment suspension (Caceres and Alsina, 2012). Cross-shore gradients of combined suspended plus bedload transport rates are generally large and vary rapidly in time. This leads to net deposition/erosion that varies along the swash zone and during the event: at the lower swash zone, net erosion occurs during uprush and deposition during backwash, and patterns are opposite for the upper swash (Zhu and Dodd, 2015).

Knowledge on swash zone sediment transport processes is hampered by difficulties encountered in obtaining detailed measurements in the challenging environment that characterizes this zone (highly aerated flow, shallow water depths, large fluxes). In particular, only few studies managed to resolve intra-swash-event bed level changes (Puleo *et al.*, 2014) and to obtain measurements of sheet flow layer processes (Lanckriet, 2014) in a medium-sand swash zone. The bed level in the swash zone fluctuates at time scales of wave groups and of short waves. The net (=event-averaged) bed level change is importantly affected by the duration of a swash event and the interruption of the backwash by incoming swash bores (Puleo *et al.*, 2014). Lanckriet *et al.* (2014) showed that vertical profiles of sheet flow concentrations during the backwash are similar to non-breaking oscillatory flow observations. However, sheet flow layer thicknesses are significantly higher in the swash due to additional factors such as bore turbulence (Lanckriet and Puleo, 2015). These aforementioned studies were done at natural beaches with irregular waves and it is anticipated that the understanding of sheet flow and bed level dynamics at intra-swash time scale may benefit from systematic laboratory experiments with repeating wave conditions and no longshore transport. Such studies may particularly assess the intra-swash cross-shore advection of sediment and the effects of wave-swash interactions on sheet flow dynamics and bed level changes.

1.3 Practical sand transport models

The term *practical sand transport model* is used for semi-empirical models that are developed for application in engineering practice. These models generally operate at a wave-averaged time scale and calculate transport rates based on relatively few hydrodynamic input parameters (e.g. Meyer-Peter and Muller, 1948; Bailard and Inman, 1981; Nielsen, 1986; Ribberink, 1998; Van Rijn, 2007a; Van Rijn, 2007b). This opposes *process-based sand transport models*, that describe the physics of sediment transport processes in much more detail, are used primarily as a research tool, and operate at an intra-wave time scale (e.g. Hsu *et al.*, 2004; Revil-Baudard and Chauchat, 2013; Kranenburg *et al.*, 2014; Finn *et al.*, 2016). Practical sand transport modeling approaches for bedload and suspended load are notably different, as detailed below.

Bedload transport models

Many bedload transport models exist; for an overview, the reader is referred to recent review papers (e.g. Van Rijn *et al.*, 2013) or studies that inter-compare these models (Davies *et al.*, 1997; Davies *et al.*, 2002). Most bedload transport models were developed and calibrated using databases of transport rates under uniform conditions in tunnels or wave flumes (with non-breaking waves) (e.g. van der Werf *et al.*, 2009). Many classical bedload models assume transport to respond quasi-instantaneously to wave forcing. More recently, models have been developed that use a semi-unsteady concept that allows the inclusion of phase lag effects on transport under waves (Dibajnia and Watanabe, 1992; van der A *et al.*, 2013). In morphodynamic models that operate on a wave-averaged time scale, the intra-wave velocity statistics (skewness, asymmetry, peak onshore and offshore velocities) required as input for bedload models are estimated through parameterizations (e.g. Isobe and Horikawa, 1982; Ruessink *et al.*, 2012).

Suspended sediment transport models

Suspended sediment transport in a morphodynamic model is commonly calculated through wave-averaged advection/diffusion models. The advection term represents the horizontal current-related transport, i.e. the product of wave-averaged velocities and concentrations. The diffusion term represents the turbulent sediment fluxes in horizontal and vertical direction, which are modelled as a diffusive process using expressions for the sediment diffusivity that are either purely empirical or based on (separately calculated) turbulent viscosities. Sediment concentration profiles follow from the advection/diffusion rates plus contributions by vertical settling and exchange with the bed (pick-up/deposition).

Vertical exchange between suspension and the bedload layer can be modeled using pick-up rate functions or through a reference concentration close to the bed. Such pick-up/reference concentration models are usually based on horizontal bed shear by waves plus currents and have been developed based on measurements for non-breaking waves (e.g. Nielsen, 1986; Van Rijn, 2007b). However, these models have limited predictive capability in breaking-wave conditions due to additional breaking-related processes (Aagaard and Jensen, 2013). Reference concentration/pick-up formulations that include a parameterization for breaking-wave effects, e.g. through breaking-wave parameters (Mocke and Smith, 1992; Kobayashi and Johnson, 2001) or turbulent kinetic energy (Steetzel, 1993), have been proposed. However, these formulations are not as thoroughly supported by experimental data and are not as widely applied as formulations based on horizontal bed shear.

The near-bed wave-related suspended transport can be included as part of the 'near-bed' load (van der A *et al.*, 2013) or as an additional term to suspended load transport (e.g. Van Rijn, 2007b). The wave-related load is considered importantly affected by wave skewness and asymmetry. An enhancement factor for wave-related fluxes due to wave breaking has been proposed (Van Rijn, 2007b), but this is not supported by a wide range of observational data (see Section 1.2).

Swash zone

Several studies (see Chárdon-Maldonado *et al.*, 2015, for an overview) showed the limited applicability of bedload/total load formulas developed originally for uniform conditions when applied in swash zone conditions. This can be attributed to the importance of additional processes, such as bore turbulence, infiltration/exfiltration, and large time-varying cross-shore pressure gradients, that are not commonly incorporated in sand transport models. O'Donoghue *et al.* (2016) showed that for 'free' swash events, i.e. single swash events with no wave-swash interactions, existing transport models can predict the time-varying transport rates in the swash zone reasonably well. Previous studies have proposed transport models incorporating additional effects of turbulence on bed shear (Aagaard and Hughes, 2006) or directly on sediment transport (Butt *et al.*, 2004), but this has not led to a unified swash zone transport model.

Because of the limited predictive capability of transport models in the swash zone, some morphodynamic models do not explicitly calculate sediment transport rates at grid points covering the swash. Instead, sediment transport rates are calculated up to the 'wet' grid point nearest to the shoreline. This transport yields an erosion or accretion rate which is then spread over the 'wet' and 'dry' cell adjacent to the shoreline (e.g. Delft3D, see Deltares, 2015a), or over the complete swash zone (i.e. up to maximum run-up distance) (Walstra and Steetzel, 2003; Van Rijn, 2009). However, these schematizations neglect many important physical processes and do not always yield satisfactory results (Van Rijn *et al.*, 2011).

1.4 Problem statement and research questions

Present morphodynamic models fail at simulating long-term beach morphology, unless input parameters are heavily calibrated (Van Rijn *et al.*, 2013). This is partly attributed to the inaccuracy of practical sand transport models in breaking-wave and swash zone conditions. There is no unified view on how processes as flow non-uniformity, enhanced turbulence due to wave breaking, and wave-swash interactions, should be incorporated in existing model formulations for bedload and suspended transport in breaking and swash zone. Formulations that account for breaking-wave effects on sediment transport have been proposed (Section 1.3), but are not supported by detailed processes measurements of sand transport processes in the breaking and swash zone.

The inaccuracy of sand transport model predictions reflects the still incomplete understanding of how wave breaking and swash zone processes affect sediment transport. Specific sediment transport processes have not yet been studied in detail, predominantly because high-resolution measurements of these processes are lacking (Section 1.2). Many of the previous studies on wave breaking were done in *small-scale* wave flumes, which cannot give complete insights in the effects of wave breaking on near-bed hydrodynamics, since they do not reproduce the turbulent scales and turbulent wave bottom boundary layer of full-scale conditions. Previous observations of turbulence and suspended sediment in *large-scale* field/laboratory surf zones did not cover the wave bottom boundary layer at all or only with low spatial resolution. In addition, previous studies did not allow examination of cross-shore advective transport processes because the breaking region was not sampled with large

horizontal coverage. The few swash zone studies that address intra-swash bed level changes and sheet flow processes were conducted in the field and it may be expected that controlled wave flume experiments can further unravel effects of specific swash zone processes (e.g. wave-swash interactions, cross-shore intra-swash sediment advection) on sediment transport.

Altogether it is concluded that present understanding of near-shore sediment transport is particularly hampered due to a lack of high-resolution measurements of the following processes:

- The wave bottom boundary layer flow and time-varying near-bed (breaking-generated) turbulence under large-scale breaking waves;
- Bedload and suspended sediment transport processes under breaking waves, in relation to breaking-generated turbulence and the cross-shore non-uniformity of the flow in the breaking region;
- The vertical and horizontal distribution of suspended and bedload fluxes and transport rates under breaking waves, and their contributions to breaker bar morphology;
- Intra-swash-event bed level changes and sheet flow processes in the swash zone under controlled laboratory swash events.

Novel instruments enable much higher resolution measurements of the wave bottom boundary layer and the sheet flow layer than previous studies. These instruments are used in the present study to further explore sediment processes in the surf and swash zone. Hence, the main objective of this study reads:

> *To improve understanding of sediment transport processes and morphodynamics in the surf and swash zone through high-resolution measurements in large-scale laboratory conditions.*

This objective is assessed through four research questions (RQs):

> *RQ 1) How does wave breaking affect near-bed (wave bottom boundary layer) flow and turbulence?*
>
> *RQ 2) How are suspended sediment transport processes affected by wave breaking?*
>
> *RQ 3) How are bedload processes affected by wave breaking and how do suspended and bedload transport contribute to breaker bar morphodynamics?*
>
> *RQ 4) How do swash processes such as wave-swash interactions and cross-shore intra-swash advection of sediment affect bed level changes and sheet flow layer dynamics?*

1.5 Methodology

All research questions are addressed through high-resolution sediment transport process measurements during experiments in the large-scale CIEM wave flume at the Universitat Politècnica de Catalunya, Barcelona (**Figure 1.4**). The scale of this wave flume allows to reproduce the physics at the same scale as natural processes in the field. Compared to observations in the field, wave flumes offer the major advantage that experiments can be exactly repeated as bed profile and wave conditions are controlled (reproducibility). This

improves confidence in the results, as measurements can be ensemble-averaged over numerous wave cycles that are almost identical. In addition, processes of interest can be examined in isolation, i.e. effects of other processes that are not subject of investigation can be omitted or minimized. In the present study, for example, effects of longshore flow and of time-varying wave conditions (tides, infra-gravity waves) are omitted.

Data are collected during two experimental campaigns: one focusing on surf zone, the other on swash zone processes. Both campaigns focus on detailed hydrodynamics and sediment transport processes, with particular interest on the near-bed region, in relation to the larger scale morphology of the bed profile. Of particular relevance in this thesis are data collected with two novel instruments (**Figure 1.4c**): an Acoustic Concentration Velocity Profiler (ACVP; Chapters 2 and 3) and an upgraded Concentration Conductivity Measuring system (CCM$^+$; Chapters 4 and 5). These novel instruments allow high-resolution measurements of processes that could not be studied in such detail before.

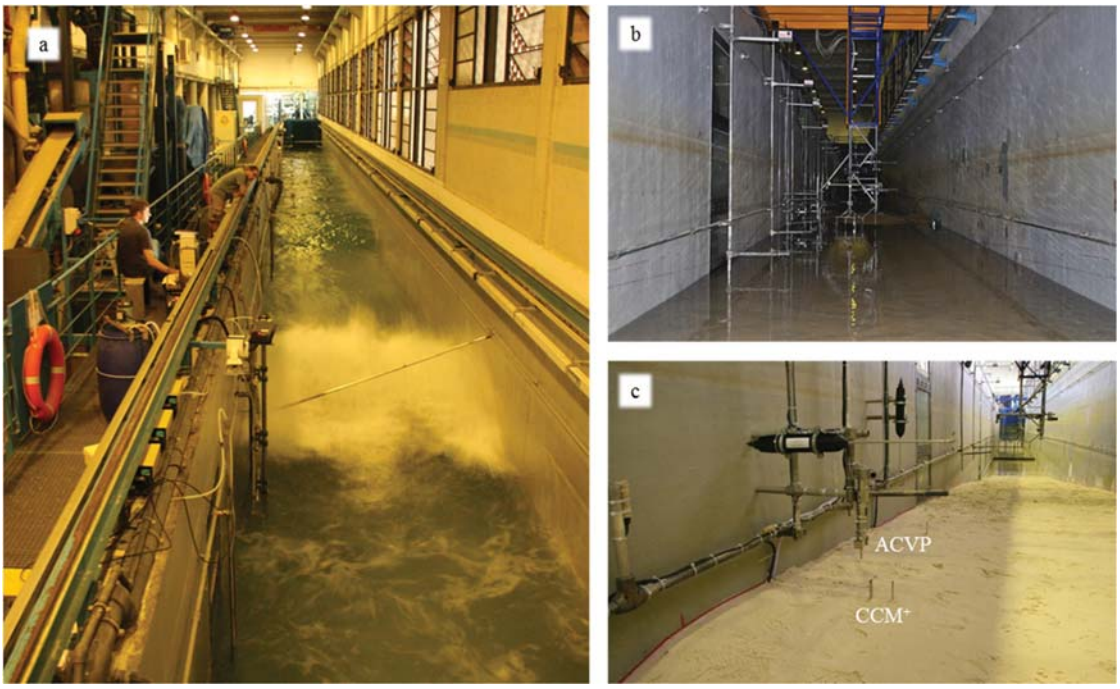

Figure 1.4. Photos of experiments in CIEM wave flume. (a) Plunging breaking waves, observed from mobile trolley above the flume while facing offshore (towards wave paddle); (b) Mobile measuring frame plus equipment, seen from inside flume (while partly filled); (c) Sandy bed profile during SINBAD mobile bed campaign, including novel instrumentation: ACVP (Chapters 2 and 3) and CCM$^+$ (Chapters 4 and 5).

RQs 1 to 3 are answered through large-scale experiments involving regular plunging waves above a mobile medium-sand bed profile consisting of a bar plus trough configuration. A breaker bar and trough are naturally formed at sandy beaches. This topography is expected to have an important effect on controlling hydrodynamics and sediment transport dynamics and is therefore preferred over a horizontal bed or a plane-sloping beach. The experiment involves one monochromatic wave condition and has a duration of 90 min during which the bed profile

evolves. A high spatial coverage of measurements is achieved by repeating the experiment 12 times while measuring at different cross-shore locations. This in-depth exploration of one wave condition allows to study the spatial variation in hydrodynamics and sediment processes, and is therefore preferred over an experiment with a wide range of wave conditions but with limited resolution. It is also anticipated that the in-depth exploration of a single wave condition will be of more benefit to process-based numerical model development. The wave condition is chosen such that the waves approach field conditions, result in energetic near-bed flow (i.e. sheet flow) conditions, and break as a plunging-type. The latter is preferred over a spilling breaker, because previous research showed a stronger temporal variability and larger penetration depth of breaking-generated turbulent kinetic energy under plunging breaking waves.

RQ 4 is answered through another experimental campaign in the same wave flume, focusing on effects of wave group sequencing on beach morphology. During this campaign a new instrument (CCM^+) is applied for the first time. The CCM^+ is used to study time-varying bed level changes and sheet flow processes induced by energetic swash events with strong wave-swash interactions. The present thesis highlights results of two selected bichromatic-wave conditions.

The study presented in this thesis is embedded in a larger research project ('SINBAD') that involves researchers from various European institutes. Next to experiments presented in this thesis, an accompanying experiment involving breaking waves over a rigidized bed profile was also conducted within SINBAD (Van der A *et al.*, Submitted). Breaking-wave effects on sediment transport are further explored within SINBAD using process-based numerical models that simulate bedload transport processes and breaker bar morphodynamics, and through simulations with (engineering-type) morphodynamic models. The experimental data will be made available to the (external) scientific community once the project is finished.

1.6 Outline

Each of the four research questions (Section 1.4) is treated in a technical chapter (see **Table 1.1** for an overview). Chapter 2 addresses near-bed hydrodynamics in the breaking region (RQ 1), with particular focus on temporal and spatial variations of turbulent kinetic energy. Chapter 3 addresses suspended sediment transport processes (RQ 2) under breaking waves. Chapter 4 is focused on bedload processes under breaking waves and also discusses the contributions by bedload and suspended load to breaker bar morphodynamics (RQ 3). Sheet flow and bed level dynamics in the swash zone (RQ 4) are presented in Chapter 5. Chapter 6 presents a discussion, addressing the limitations of the present research, but also giving suggestions on how the presented results can help improving practical sand transport models. Finally, Chapter 7 contains the main conclusions from the study and recommendations for future research.

Table 1.1. Outline of the thesis.

Chapter	Research Question	Experimental campaign
2	RQ1) Breaking waves: near-bed hydrodynamics	*'SINBAD mobile bed'* Large-scale measurements of breaking waves over a medium-sand barred bed profile *CIEM, Barcelona, May/June 2014*
3	RQ2) Breaking waves: suspended sediment processes	
4	RQ3) Breaking waves: bedload processes and morphology	
5	RQ4) Swash zone: sheet flow and bed level changes	*'CoSSedM'* (Alsina *et al.*, 2014) Coupled High Frequency Measurement of Swash Sediment Transport and Morphodynamics *CIEM, Barcelona, Oct-Dec 2012*

2 Near-bed hydrodynamics and turbulence below a large-scale plunging breaking wave over a mobile barred bed profile

Highlights

- ⇨ Breaking-induced turbulence spreads over the full water column and invades the wave bottom boundary layer.
- ⇨ Reynolds stresses and TKE values in the wave boundary layer increase substantially in the breaking zone.
- ⇨ An increased wave boundary layer thickness is observed in the breaking region along the breaker bar's shoreward slope.

Abstract

Detailed measurements are presented of velocities and turbulence under a large-scale regular plunging breaking wave in a wave flume. Measurements were obtained at 12 cross-shore locations around a mobile medium-sand breaker bar. They focused particularly on the dynamics of the wave bottom boundary layer (WBL) and near-bed turbulent kinetic energy (TKE), measured with an Acoustic Concentration and Velocity Profiler (ACVP). The breaking process and outer-flow hydrodynamics are in agreement with previous laboratory and field observations of plunging waves, including a strong undertow in the bar trough region. The WBL thickness matches with previous studies at locations offshore from the bar crest, but it increases near the breaking-wave plunge point. This relates possibly to breaking-induced TKE or to the diverging flow at the shoreward slope of the bar. Outer-flow TKE is dominated by wave breaking and exhibits strong spatial variation with largest TKE above the breaker bar crest. Below the plunge point, breaking-induced turbulence invades the WBL during both crest and trough half-cycle. This results in an increase in the time-averaged TKE in the WBL (by a factor 3) and an increase in peak onshore and offshore near-bed Reynolds stresses (by a factor 2) from shoaling to breaking region. A fraction of locally-produced TKE is advected offshore over a distance of a few meters to shoaling locations during the wave trough phase, and travels back onshore during the crest half-cycle. The results imply that breaking-induced turbulence, for large-scale conditions, may significantly affect near-bed sediment transport processes.

This chapter has been published as:

van der Zanden, J., D. A. van der A, D. Hurther, I. Cáceres, T. O'Donoghue and J. S. Ribberink (2016). *Near-bed hydrodynamics and turbulence below a large-scale plunging breaking wave over a mobile barred bed profile*. Journal of Geophysical Research: Oceans **121(8)**: 6482-6506. doi: 10.1002/2016jc011909.

2.1 Introduction

Motivated by the need to improve understanding of cross-shore sediment transport processes in the near-shore region, a number of laboratory (e.g. Ting and Kirby, 1994, 1995; Yoon and Cox, 2010) and field (e.g. Ruessink, 2010; Feddersen, 2012) studies have addressed the effects of wave breaking on hydrodynamics. Many of these studies focused on the temporal and spatial distribution of breaking-induced turbulence, since turbulent vortices have the potential to entrain and stir sediment particles (Sumer and Oguz, 1978). While wave breaking is highlighted as the dominant source of turbulent kinetic energy (TKE) production in the surf zone (Thornton and Guza, 1983; Ruessink, 2010; Yoon and Cox, 2010), bed-friction-generated turbulence can contribute importantly to turbulence in the lower water column (Feddersen, 2012; Brinkkemper *et al.*, 2015).

Turbulence production and transport mechanisms depend on breaker type (Ting & Kirby, 1994). In the case of a plunging breaker (the focus of the present study), turbulent vortices are formed at the wave front (Kimmoun and Branger, 2007; Sumer *et al.*, 2013) and a major part of the breaking-induced TKE is dissipated within the turbulent bore above wave trough level (Svendsen, 1987; Govender *et al.*, 2002). The remainder is injected into the water column and is advected shoreward and downward by the plunging jet and large-scale vortices (Ting and Kirby, 1995; Christensen and Deigaard, 2001; Melville *et al.*, 2002; Kimmoun and Branger, 2007). Turbulent dissipation rates under breaking waves have been found to be depth-uniform (Grasso *et al.*, 2012) or to decrease with depth (Feddersen and Trowbridge, 2005; Yoon and Cox, 2010), leading to a general reduction of TKE from the water surface downwards (e.g. Ruessink, 2010). Despite the dissipation of breaking-induced turbulence over the water column, a fraction may still reach the near-bed region (Grasso *et al.*, 2012). TKE profiles have been found to vary in the cross-shore direction and depend on the bed topography, with highest TKE found at the breaker bar crest and lower TKE above the bar trough (Scott *et al.*, 2005; Yoon and Cox, 2010).

Small-scale experiments revealed strong phase-dependency of TKE under plunging breakers, with highest values during the wave crest phase for a major part of the water column (Ting and Kirby, 1995; Govender *et al.*, 2002). Depending on breaker characteristics and local water depth, this phase-dependency may reverse near the bed (Boers, 2005). It is believed that the phase-dependency of breaking-induced TKE is coherent with near-bed wave-related sediment transport (Ting and Kirby, 1994; Boers, 2005; Ting and Nelson, 2011).

While significant attention has been paid to hydrodynamics in the breaking region, few studies have focused on the wave bottom boundary layer (WBL) under breaking waves. Breaking-induced vortices may invade the WBL (Cox and Kobayashi, 2000; Huang *et al.*, 2010; Chassagneux and Hurther, 2014) and can substantially enhance near-bed TKE (Scott *et al.*, 2005) and bed shear stresses (Deigaard *et al.*, 1991; Cox *et al.*, 1996; Sumer *et al.*, 2013). Most of these studies were conducted in small-scale wave flumes (mostly over rigid, planar sloping beds), which may not fully reproduce the properties of breaking-induced turbulence and of the WBL hydrodynamics under full-scale waves. To the authors' knowledge, previous *large-scale* experiments have not produced high-resolution measurements within the WBL across the wave breaking region. Such measurements are important for better understanding of wave breaking effects on sediment transport processes.

This paper studies the hydrodynamics under large-scale, plunging breaking waves above a mobile-sand barred bed profile. The paper particularly addresses how wave non-uniformity and wave breaking affect the near-bed hydrodynamics, including the WBL.

The experimental conditions, details of instrumentation, and data processing procedures are presented in Section 2.2. Measurements of the breaking process and outer flow velocities are presented in Section 2.3. Section 2.4 presents the time-averaged and phase-averaged near-bed velocities and Section 2.5 presents the spatial and temporal variability of near-bed turbulence. The wave-breaking effects on the WBL hydrodynamics and the implications for sediment transport processes are discussed in Section 2.6.

2.2 Experiments

2.2.1 Facility and test conditions

The experiments were carried out in the 100 m long, 3 m wide and 4.5 m deep CIEM wave flume at the Universitat Politècnica de Catalunya (UPC) in Barcelona. The experimental set-up and bed profile are shown in **Figure 2.1**. In this figure and throughout the document, the cross-shore coordinate x is defined positively towards the beach with $x = 0$ at the wave paddle. Vertical coordinate z is defined positively upwards from the still water level (SWL); ζ is the vertical coordinate from the local bed level upwards.

The initial bed configuration (i.e. before the waves developed the barred beach) comprised a 1:10 offshore slope, followed by an 18 m long and 1.35 m high horizontal test section (**Figure 2.1a**). The bed profile consisted of sand with median diameter $D_{50} = 0.24$ mm. Shoreward of the test section (x>68.0 m), the profile followed a 1:7.5 slope covered with geotextile and perforated concrete slabs designed to prevent erosion and promote wave energy dissipation. The water depth, h, at the wave paddle was 2.55 m.

Regular (monochromatic) waves were generated with wave period $T = 4.0$ s and wave height $H = 0.85$ m at the wave paddle. The surf similarity parameter is $\xi_0 = 0.54$, where $\xi_0 = \tan(\alpha)/\sqrt{H/L_0}$, α being the 1:10 offshore slope and L_0 the deep-water wave length (Battjes, 1974). The breaking waves were of the plunging type, in agreement with the classification of Battjes (1974).

Figure 2.1b indicates the breaking point (x = 53.0 m), the plunge point (x = 55.5 m) and the splash point (x = 58.5 m). These points were established from measurements and visual observations of the water surface, as described further in Section 2.3.1, and are used to define the shoaling region ($x < 53.0$ m), the breaking region ($53.0 < x < 58.5$ m) and the inner surf zone ($x > 58.5$ m).

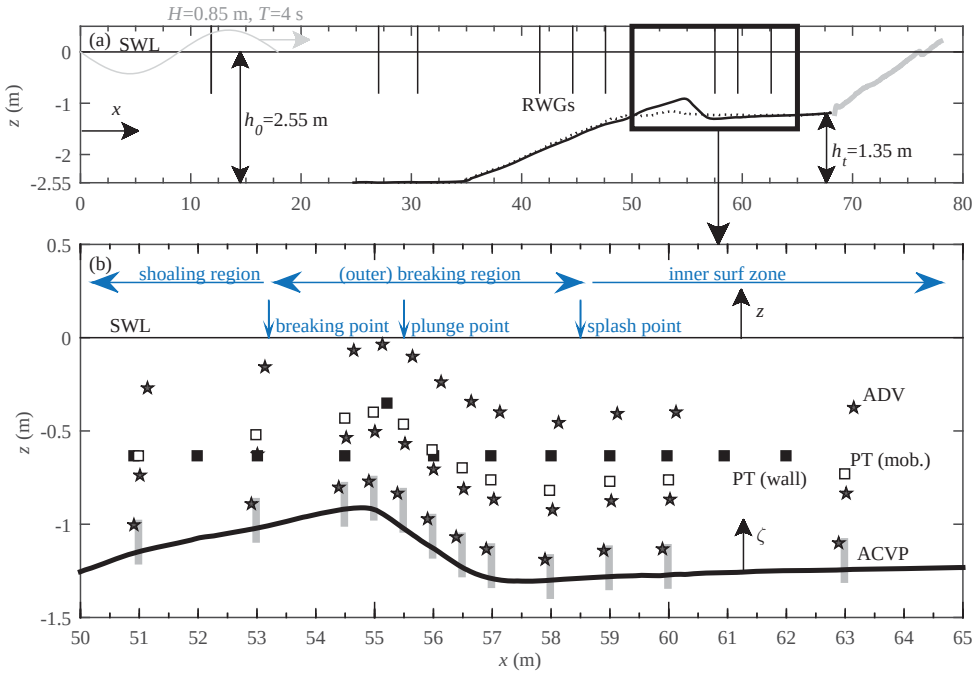

Figure 2.1: Bed profile and measurement locations. (a) General overview of wave flume, including initial horizontal test section (dotted line), reference bed profile (bold black line), fixed beach (solid grey line) and locations of resistive wave gauges (black vertical lines); (b) Close-up of test section, including instrument positions: mobile-frame pressure transducer (PT mob.; white squares); wall-mounted PTs (black squares); mobile-frame ADVs (stars); and ACVP profiles (grey rectangles).

2.2.2 Instrumentation

The primary instrumentation was deployed from a custom-built mobile frame (**Figure 2.2**). The frame was constructed from 30 mm-diameter stainless-steel tubing and was designed to minimize flow interference while being sufficiently stiff to withstand wave forces. The frame was mounted to a horizontally-mobile trolley on top of the flume, and could be vertically positioned with sub-mm accuracy using a spindle. More details of the measurement frame are provided by Ribberink *et al.* (2014).

Outer-flow velocities (i.e. higher than 10 cm above the bed) were measured using a vertical array of three Nortek Vectrino acoustic Doppler velocimeters (ADVs, **Figure 2.2**). All ADVs operated at an acoustic frequency of 10 MHz and provided 3-component (cross-shore, lateral, and vertical, denoted u, v, and w, respectively) velocity measurements at a rate of 100 Hz. The sampling volume is a cylinder-shaped volume with 3 mm radius and 2.8 mm height. The ADVs were located at elevations of approximately 0.11 m, 0.41 m and 0.85 m above the initial (i.e. at start of run) bed.

Near-bed velocities (i.e. below 10 cm above the bed) were measured using a downward-looking High-Resolution Acoustic Concentration and Velocity Profiler (ACVP, **Figure 2.2** inset), described in more detail in Hurther *et al.* (2011). The ACVP measures simultaneous and co-located vertical profiles of (u, w) and sediment mass concentrations (Hurther *et al.*, 2011),

hereby providing the possibility to measure intra-wave, multi-directional sediment flux. In the present experiment, the ACVP acoustic and geometrical settings were set to measure velocities up to 1.8 m/s over a vertical profile of 20 cm with a vertical bin resolution of 1.5 mm, a horizontal radius of the sampling volume of about 3 mm, and sampling frequency of 70 Hz. Operating at an acoustic frequency of 1 MHz, considerably lower than the frequency of commercial ADV technology, the ACVP enables velocity and concentration measurements to be made within the near-bed sediment layer (c.f. Naqshband *et al.*, 2014; Chassagneux and Hurther, 2014; Revil-Baudard *et al.*, 2015).

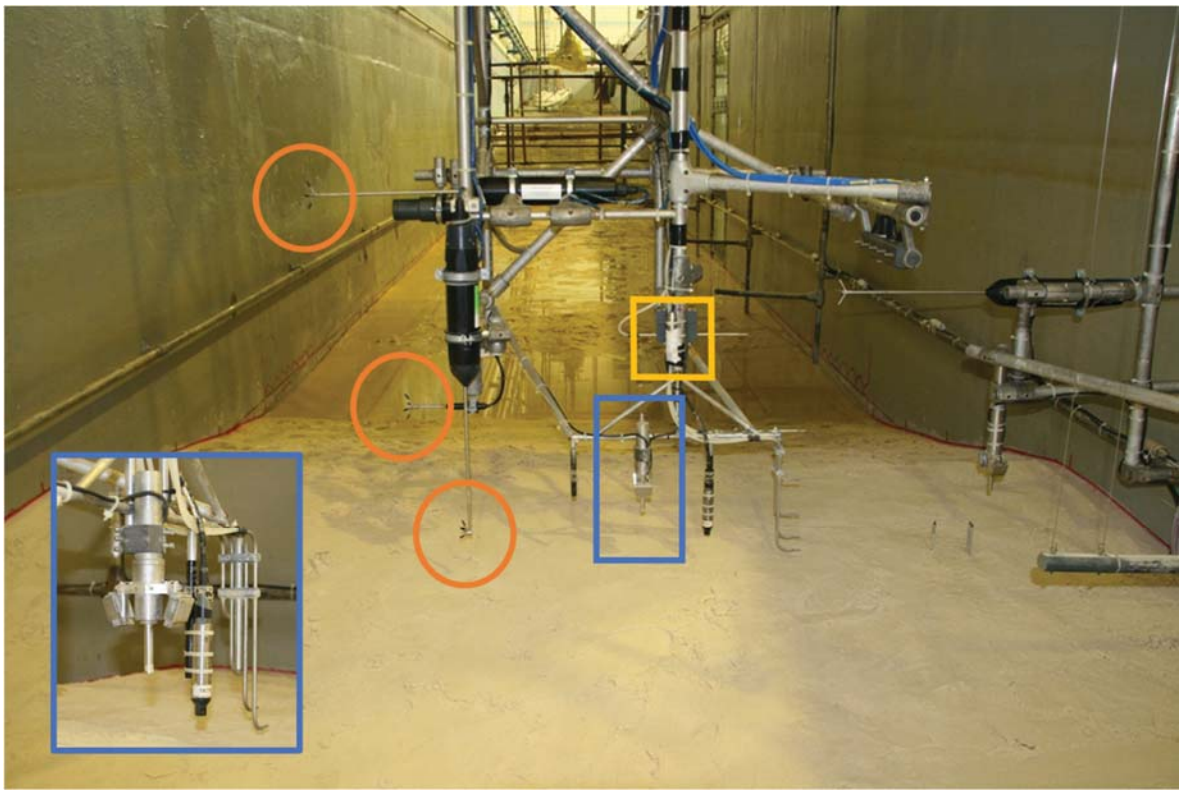

Figure 2.2. Photo of measuring frame, taken from top of breaker bar while facing the beach. Highlighted instruments: ADVs (orange circles); PT (yellow square); ACVP (blue rectangle). Inset shows close-up of ACVP.

Water surface elevations were measured at 40 Hz using resistive (wire) wave gauges (RWGs) and pressure transducers (PTs) at 21 locations along the flume (**Figure 2.1**) and one additional PT attached to the mobile frame (**Figure 2.2**). In the breaking region the horizontal spacing of the measurements was approximately 1 m. In this region, PTs were deployed instead of RWGs because wave splash reduces the data quality of the RWGs. Linear wave theory was used to convert the dynamic pressure measurements (PT) into water surface elevations. Following Guza and Thornton (1980), the conversion was applied to frequencies up to 0.33 Hz, which includes the primary wave component (0.25 Hz) but not its higher harmonics. A comparison with RWG-measured water surface elevation in the shoaling zone indicated that the PT-

derived wave height underestimates the RWG-measured wave height by up to 10%. The underestimation in higher-order statistics (wave skewness, asymmetry) is more severe.

Bed profile measurements were obtained along two transects, using echo sounders deployed from a second mobile carriage, at a horizontal resolution of 2 cm and with an estimated bed measurement accuracy of +/- 1 cm. The transects were taken at a lateral distance of 0.1 m and 0.7 m with respect to the flume's centerline. Bed profiles presented in this paper are based on the average of the two transects.

Table 2.1. Measured water level and velocity statistics at all measurement locations (t=0–15 min.): local water depth (h); local bed slope at start experiment (β); wave height (H); time-averaged horizontal velocity ($\bar{u}$); peak onshore and offshore phase-averaged horizontal velocities (u_{on} and u_{off}); semi-excursion length ($a = \sqrt{2}T\tilde{u}_{rms}/2\pi$); Non-dimensional semi-excursion length a/k_s, with roughness k_s estimated based on grain size and measured ripple dimensions using formulations by Van der A et al. (2013); Velocity skewness ($Sk(u) = \overline{\tilde{u}^3}/\tilde{u}^3_{rms}$); Velocity asymmetry ($Asy(u) = -\overline{H\upsilon(\tilde{u})^3}/\tilde{u}^3_{rms}$, where Hυ is the Hilbert transform (e.g. Ruessink et al., 2011); Reynolds number ($Re = a \cdot \tilde{u}_{on}/\nu$; where kinematic viscosity $\nu = 1.0 \cdot 10^{-6}$ m²/s). Velocity-based variables are based on measurements from the lowest ADV (ζ=0.11 m).

x (m)	h (m)	β (°)	H (m)	$\bar{u}$ (m/s)	u_{on} (m/s)	u_{off} (m/s)	a (m)	$a/k_s/10^3$	$Sk(u)$	$Asy(u)$	$Re/10^5$
51.0	1.10	4	0.79	-0.13	1.04	-0.83	0.54	2.3	0.61	0.68	5.6
53.0	0.97	3	0.74	-0.22	0.80	-0.94	0.48	2.0	0.44	1.01	4.5
54.5	0.88	2	0.64	-0.19	0.84	-0.85	0.47	2.0	0.50	0.82	4.0
55.0	0.88	-6	0.60	-0.24	0.78	-0.90	0.47	2.0	0.48	0.76	4.2
55.5	0.97	-13	0.51	-0.23	0.57	-0.83	0.39	1.6	0.36	0.75	3.3
56.0	1.10	-11	0.50	-0.30	0.25	-0.82	0.31	1.3	0.06	0.77	2.6
56.5	1.19	-10	0.53	-0.51	0.05	-0.83	0.25	1.0	0.67	0.76	2.1
57.0	1.24	-4	0.48	-0.54	0.02	-0.78	0.23	1.0	0.95	0.58	1.8
58.0	1.28	1	0.47	-0.46	0.01	-0.71	0.21	0.03	0.82	0.79	1.5
59.0	1.28	1	0.43	-0.36	0.13	-0.71	0.23	0.03	0.39	0.88	1.7
60.0	1.26	2	0.42	-0.36	0.17	-0.66	0.24	0.03	0.67	0.68	1.6
63.0	1.26	0	0.41	-0.34	0.19	-0.58	0.23	0.03	0.79	0.45	1.3

2.2.3 Measurement procedure

To create the reference bed profile for this experiment, regular waves (H=0.85 m, T=4 s) were generated for 105 minutes over the initial profile described in Section 2.2.1. Subsequently, the

flume was slowly drained, bed forms and lateral bed asymmetries were flattened out, and the resulting barred profile was drawn on the flume sidewalls to give the template for the reference bed profile (**Figure 2.1**).

Each experiment was run for 90 minutes of waves, comprising of six 15-min runs, during which the bed further evolved. The bed profile was measured at the start of each experiment and after every second run, i.e. at 0, 30, 60 and 90 min. After the sixth run, the flume was drained and the reference profile was restored by shoveling back the transported sand and flattening out any bed forms that were generated. This sequence of bed profile development and subsequent restoration to the reference profile was repeated 12 times (12 experimental days), where for each experiment the mobile frame was positioned at a different cross-shore location (**Figure 2.1b**).

As a reference throughout the paper, **Table 2.1** presents wave height, water depth, velocity and local bed slope measurements for each mobile-frame measurement location.

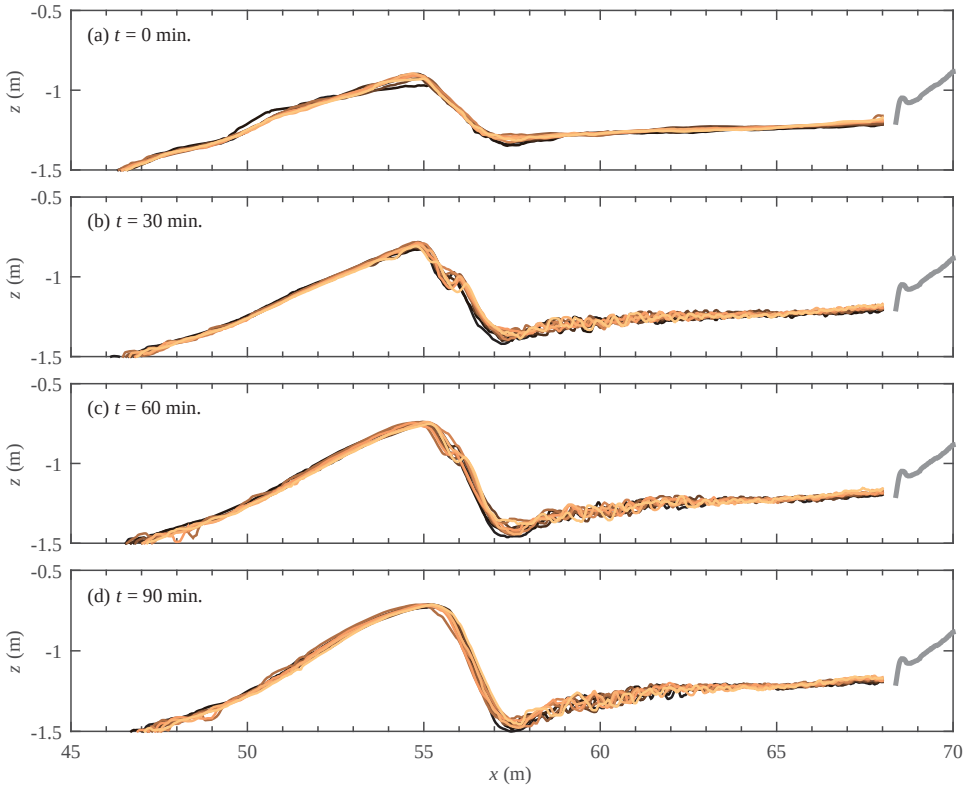

Figure 2.3. Measured bed profiles for each measurement day. Each panel contains 11 profile measurements, taken at the same stage of profile development (data for one measurement day were discarded due to calibration issues).

2.2.4 Morphology and experimental repeatability

A prerequisite for combining the measurements from different cross-shore locations into one dataset is that the experiment is repeatable in terms of wave conditions and bed evolution. **Figure 2.3** shows a comparison of measured bed profiles at different stages of bar development. The good agreement between the profiles confirms the repeatability of the bed evolution. The locations of the smaller bed forms varied with each repeat, but the dimensions and growth rate of the main features of the profile – the breaker bar and trough – were very similar between experiments. The repeatability of bed profile evolution can be quantified by the standard deviation over the 11 profiles at t = 90 min, which was 3 cm in the region 50.0 m < x < 67.0 m, including the variability due to smaller bedforms. Wave heights were also similar between experiments, with a standard deviation (calculated over 12 experimental days) in mean wave height per cross-shore location of less than 2 cm (mean value over all RWGs and PPTs).

During the experiment, the breaker bar increased in height while its trough deepened (**Figure 2.3**). The offshore slope before the bar crest gradually increased in steepness, up to a 1:8 steepness after 90 min. The bar growth and steepening induces enhanced shoaling and an increase in ξ_0 (up to 0.68), resulting in an increasing plunging intensity throughout the experiment.

Figure 2.3 indicates the presence of bedforms, starting at the lee (shoreward) side of the breaker bar. Visual observations of the bed after draining the flume confirmed a gradual transition of shoreward-facing lunate-shaped features in the bar trough (x = 57.0 to 59.0 m), to quasi-2D features (with short wave length in wave direction but long wave length in wave-normal direction; x = 59.0 to 62.0 m), to irregular 3D vortex ripples in the inner surf zone (x>62.0 m). Quasi-2D bed forms were also observed at the lee side of the bar, where they progressively migrated offshore and upslope (**Figure 2.3b-c**). At the bar crest, the absence of bed features indicates sediment transport in the sheet flow regime. Further down the offshore slope (x<48 m), a region that is not further considered in the present study, quasi-2D mega ripples were observed.

2.2.5 Data treatment

This paper focuses on measurements obtained during the first run of each measurement day, i.e. for the first 15 min of profile development. Later stages of bar development showed qualitatively similar behavior in terms of hydrodynamic processes; data for these later stages are included in the Reynolds stress results, which were averaged over the entire 90-min experiment in order to minimize the statistical bias error.

Visual observations and water surface measurements showed that the location of wave breaking varied in time during the first 5 min of each run. After this transient phase, the breaking location stabilized, indicating that a hydrodynamic equilibrium was established. Data obtained during the first 5 min of each run were therefore discarded, leaving 10 minutes of data per run for quantitative analysis. Flume seiching induced a standing wave with an amplitude of O(cm) and a period of about 45 s that matches the natural frequency of the body of water in the flume when h=2.55 m. The standing wave was removed from the velocity and

water surface level measurements by applying a high-pass filter with a cut-off frequency of half the primary wave frequency (0.125 Hz).

ADV data were contaminated with noise, predominantly due to high bubble concentrations in the breaking region and with signal dropout when measuring above the water level. ADV data were considered as outliers wen the signal-to-noise ratio was <15 dB, or the correlation was <50% for time-averaged quantities or <80% for instantaneous (turbulent) quantities. The correlation threshold was lower for time-averaged quantities, because the averaging procedure contributes to noise cancellation. Outliers in phase-ensembles were identified if the value deviated by more than three times the standard deviation from the median at the given phase. Identified outliers were removed from the time series and not substituted by other values. The percentage data points removed varied in the cross-shore direction, from about 10% in the shoaling and inner surf zone, up to 45% in the highly-aerated water column under the plunging wave.

For the ACVP measurements, a ζ level was first assigned to each measurement bin based on the measured wave-averaged bed level. The continuous bed level was obtained from the maximum backscatter intensity, following Hurther and Thorne (2011). Horizontal and vertical velocity measurements were transposed to bed-parallel and bed-normal velocities, using a rotation angle that minimized the periodic component of bed-normal velocities close to the bed (at $\zeta = 0.03$ m). This transposition was applied on a wave-by-wave basis. The mean rotation angle obtained with this method at the different cross shore positions was close to the local bed slope estimated from the mechanical bed profile measurements. For simplicity, we refer to the bed-parallel velocities as the 'horizontal' velocities and the bed-normal velocities as the 'vertical' velocities in what follows.

The phase-averaged value of arbitrary variable ψ is denoted with angle brackets and was calculated from

$$<\psi>(t)= \frac{1}{N}\sum_{n=1}^{N} \psi(t+(n-1)T) \qquad (2.1),$$

where N represents the number of wave cycles. N was about 150 for the water surface and outer-flow velocity measurements, and somewhat lower for the ACVP measurements (typically about 100, with a minimum of 40). The reason for this difference is that data were discarded when the local bed eroded outside the ACVP maximal profiling range or accreted to distances within the first 5 cm of the ACVP profile. Phase-averaged near-bed velocities (ACVP) were calculated for each ζ bin class with 1.5 mm bin size. To calculate the phase-averaged quantities, reference zero-up crossing of the waves were obtained from the RWG at x=47.6 m. Data were then phase-referenced such that t/T=0 corresponds to maximum water surface (wave crest) at the beginning of the test section (x=50.0 m).

The quasi-2D bedforms observed in the breaking zone had cross-shore wave lengths that were (much) higher than the local orbital amplitude a. Hence, it may be assumed that these bedforms do not induce flow separation and do not contribute to apparent wave-related bed roughness (Van Rijn, 2007a). The latter is not true for the inner surf zone (x>59.0 m), where bedforms migrated below the ACVP sensors. For these locations, time intervals for phase-averaging of ACVP measurements were chosen such that an integer number of bedforms was

captured (i.e. the presented data are averaged over exactly one or multiple ripples) and ζ=0 corresponds to the time-varying bed interface of the bedform.

Velocities were decomposed into time-averaged ($\bar{u}, \bar{w}$), periodic ($\tilde{u}, \tilde{w}$) and turbulent (u', w') contributions. Time-averaged quantities are denoted with an overbar and were calculated using

$$\overline{\psi} = \frac{1}{T}\int_0^T <\psi(t)>\mathrm{d}t \qquad (2.2).$$

For the discontinuous velocity measurements above wave trough level, $\overline{\psi}$ represents the truncated mean based on the 'wetted period' instead of the full wave period for T in Equation 2.2. The periodic component is obtained from $\widetilde{\psi} = <\psi> - \overline{\psi}$. Root-mean-square magnitudes of $\widetilde{\psi}$ are denoted with subscript *rms* and are calculated through:

$$\widetilde{\psi}_{rms} = \left[\frac{1}{T}\int_0^T \widetilde{\psi}(t)^2\mathrm{d}t\right]^{0.5} \qquad (2.3).$$

Various methods exist to extract the turbulent component from the time series (Svendsen, 1987; Scott *et al*., 2005). The regular waves in the present experiment enable a Reynolds decomposition based on the ensemble-average, i.e. $\psi' = \psi - <\psi>$. Compared to other methods (see e.g. Scott *et al*., 2005), ensemble-averaging yields the most accurate turbulence estimations since it does not discard contributions of the largest vortices (Svendsen, 1987). However, by adopting this method, wave-to-wave variations due to offsets in phase-referencing and as a result of modulation of velocities and the breaking location by the long wave (flume seiching) may be incorrectly denoted as turbulence (Svendsen, 1987; Scott *et al*., 2005). These 'pseudo-turbulence' contributions are largely suppressed through the aforementioned high-pass filter (0.125 Hz). However, examination of the auto-spectra of u' and w' revealed that the Reynolds decomposition removes most, but not all, of the energy associated with the wave and its higher harmonics (see **Figure 2.A1**). By integrating the auto-spectra of u' with and without the energy still contained at the first three wave harmonic frequencies (0.25 Hz, 0.50 Hz, 0.75 Hz), it was found that the time-averaged turbulence intensities are overestimated by approximately 7%. This error cannot be easily removed from turbulent velocity time series. The error is quite small compared to typical spatial and temporal variations of turbulence intensities in this study and is therefore considered acceptable. The effect of wave bias on the Reynolds stresses was separately tested using ogive curves (Feddersen and Williams, 2007) and led to the exclusion of 9 runs (as detailed in Appendix A).

Phase-averaged *rms* turbulence intensities were calculated through

$$\psi'_{rms}(t) = \left[\frac{1}{N}\sum_{n=1}^{N}\left(\psi(t+(n-1)T) - <\psi(t)>\right)^2\right]^{0.5} \qquad (2.4).$$

Estimates of $<\psi'_{rms}>$ are accepted only for N>40 to guarantee a low statistical bias error. For the 3-component ADV data, the TKE, noted k, can be calculated from the turbulence intensities through

$$<k(t)> = 0.5(<u'(t)^2> + <v'(t)^2> + <w'(t)^2>) \quad (2.5).$$

Because of acoustic noise, the ACVP measurements were processed differently. A full explanation of the ACVP data processing is presented in Appendix A. In short, the acoustic noise was largely removed using a de-spiking routine. Phase-averaged turbulence intensities were then calculated using a two-point cross-correlation applied to velocities measured at two vertical bin elevations (Garbini *et al.*, 1982; Hurther and Lemmin, 2001). $<k(t)>$ was estimated as $1.39 \cdot 0.5(<u'(t)^2> + <w'(t)^2>)$, where the factor 1.39 is the typical value taken for a turbulent WBL (Svendsen, 1987). Contributions from small-scale high-frequency turbulent fluctuations to turbulence intensities are partly removed using the methodology, leading to an underestimation of TKE and Reynolds shear stress (Appendix A). The underestimation increases towards the bed as the length scale of eddies reduces. Analyses in this study will therefore exclude ACVP turbulence measurements within the lowest 5 mm from the bed. Finally it is noted that in dense suspension layers, the ACVP measures (turbulent) velocities of sand grains that may differ from the fluid velocities (Appendix A).

2.3 Water surface elevation and outer-flow velocities

2.3.1 Surface elevation

The breaking process is examined by combining phase-averaged RWG and PT measurements of the water surface elevation (**Figure 2.4**). On arrival at the test section, the pitched-forward, asymmetric shape of the wave is evident and is caused by wave shoaling along the offshore slope. As the wave propagates towards the bar crest, the wave crest starts to turn over at x = 53.0 m (at approximately t/T = 0.17). Following Svendsen *et al.* (1978), this location is referred to as the 'breaking point'. As wave propagation continues, the plunging jet from the breaking wave hits the water surface approximately 2.5 m further at x = 55.5 m and at t/T=0.33 ('plunge point', after Peregrine, 1983). The jet pushes up a wedge of water and creates a new wave that leads the remainder of the original wave; the remainder of the original wave is called the secondary wave in what follows. This breaking process, including the formation of the secondary wave, is similar to detailed descriptions by Ting and Kirby (1995) for a small-scale plunging wave. While propagating further onshore, the water mass pushed up by the plunging wave hits the water surface around x = 58.5 m (t/T = 0.65). At this 'splash point' (Smith and Kraus, 1991), the wave reforms into a surface roller with a quasi-uniform shape throughout the remainder of the test section (x > 58.5 m). Based on these observations and after Svendsen *et al.* (1978), we distinguish (see **Figure 2.1**) the shoaling zone (up to the breaking point at x = 53.0 m), the (outer) breaking zone (from breaking point to splash point; x=53.0 to 58.5 m), and the inner surf zone (x>58.5 m).

The maximum (crest) and minimum (trough) phase-averaged water levels are shown in **Figure 2.5**, and can be used to analyze the cross-shore variation in wave height H (see also **Table 2.1**). The wave height gradually increases over the offshore slope as a result of wave shoaling (**Figure 2.5a**, up to x = 52 m). Wave energy dissipation starts near the breaking point at x = 53 m and continues through the breaking zone; H is reduced by 50% between x = 52 m and x = 59 m. The wave height decay drives a water level set-up (preceded by a set-down in the shoaling

region), leading to a positive cross-shore gradient in the mean water level throughout the breaking and inner surf zone (**Figure 2.5a**).

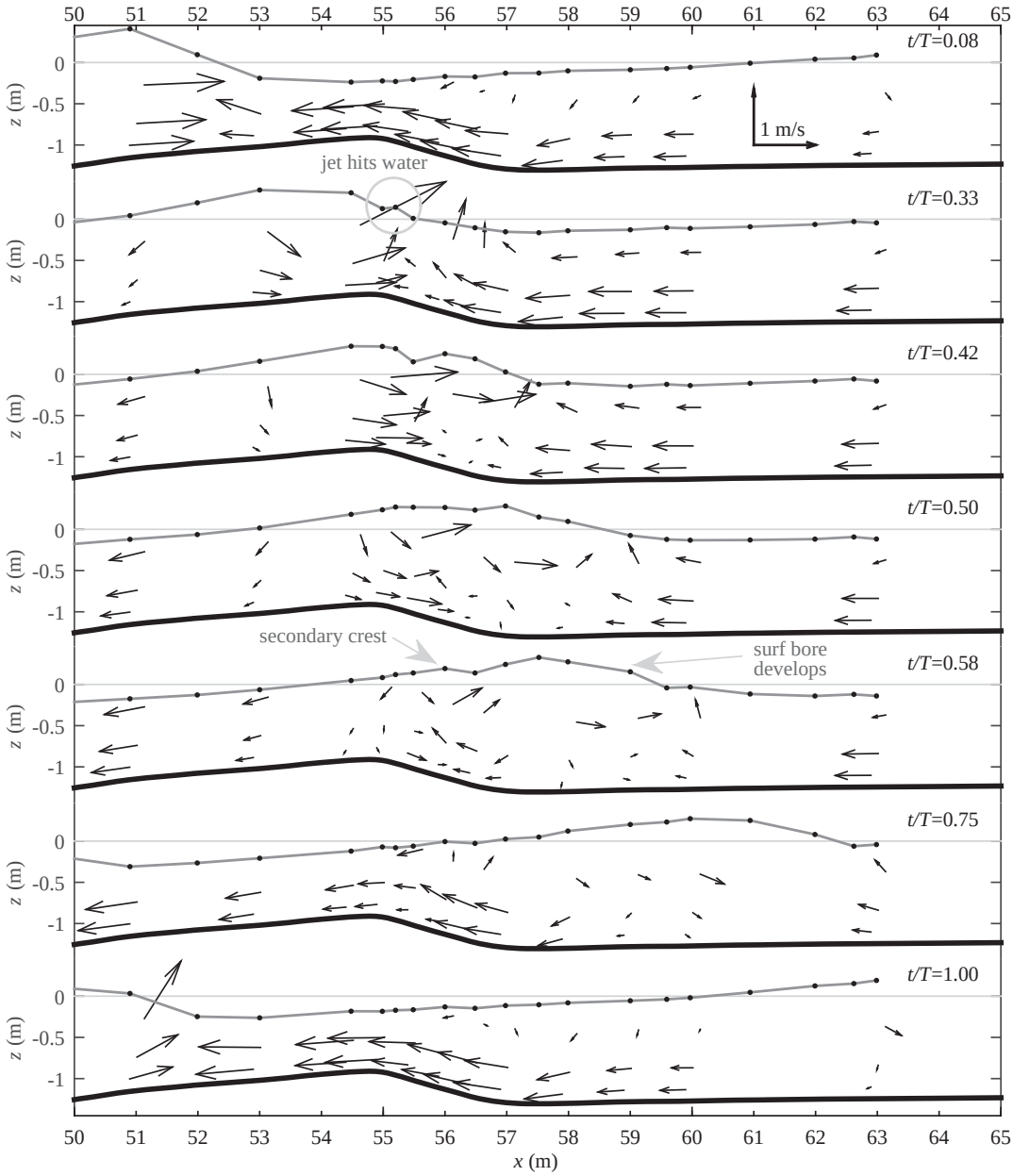

Figure 2.4. Phase-averaged water surface levels (PT and RWG, grey line plus dots) and velocities (ADVs) at selected phases. Horizontal grey lines mark the SWL (η=0) and the thick solid line at bottom marks the reference bed profile.

2.3.2 Outer flow velocities

Figure 2.5 shows vertical profiles of time-averaged velocities (panel a) and *rms* periodic velocities (panel b). Although ACVP (near-bed) measurements are included in **Figure 2.5a-b**, they are discussed separately and in more detail in Section 2.4.

Time-averaged horizontal velocities (**Figure 2.5a**) are positive above wave trough level (η_{tr}), highlighting an onshore mass flux, and are negative (offshore-directed) below η_{tr} due to the compensating return current (undertow). The undertow velocity magnitude increases gradually in the shoaling zone (from x = 51.0 to 53.0 m) and more rapidly in the breaking region, particularly along the lee side of the bar (**Figure 2.5a**). Maximum undertow velocity magnitudes (up to -0.6 m/s) occur in the breaker bar trough (x = 56.5–58.0 m), similar to previous studies involving barred profiles in field (e.g. Garcez-Faria *et al.*, 2000) and laboratory (e.g. Boers, 2005) conditions. In the inner surf zone (x > 58.5 m), undertow velocity magnitudes reduce. Over the bar crest (x = 55.0 m), highest offshore velocities occur in the middle of the water column while at locations around the bar lee side and bar trough the highest offshore velocities occur close to the bed (x = 56.5–59.0 m). A more in-depth analysis of the undertow profiles is not considered in the present study, which focuses primarily on the near-bed velocities.

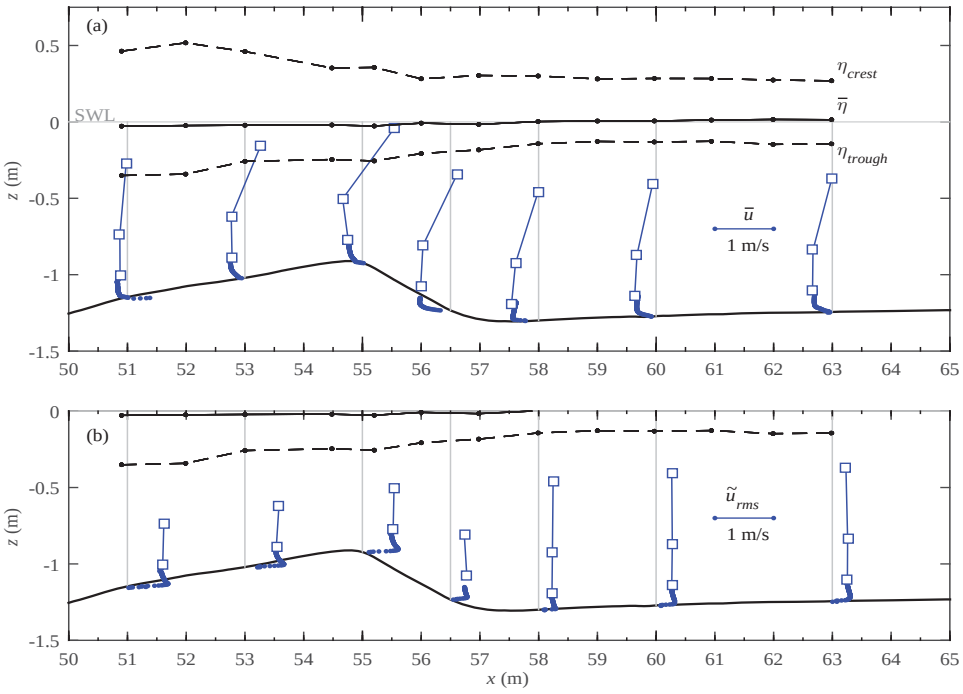

Figure 2.5. Profiles of (a) undertow and (b) *rms* periodic velocities, both for t = 0–15 min., measured with ADV (squares) and ACVP (dotted profiles). Both panels include the cross-shore varying wave trough and crest level (black dots and dashed line) and the time-averaged water surface level (set-up/set-down; black dots and solid line).

Root-mean-square horizontal periodic velocities ($\tilde{u}_{rms}$) are nearly uniform with depth (**Figure 2.5b**), as can be expected in shallow water. Measurements above trough level are not considered, because $\tilde{u}_{rms}$ is undefined when data are discontinuous. $\tilde{u}_{rms}$ is roughly constant between x = 51 and 55 m, decreases rapidly between x = 55 to 57 m, and varies hardly throughout the inner surf zone (x > 58.5 m). The strong reduction in $\tilde{u}_{rms}$ (x = 55 to 57 m) is consistent with the decay of wave energy and the increased water depth in this region. The distinct near-bed increase in $\tilde{u}_{rms}$ towards the bed at all locations (most evident from x = 51 to 55 m) relates to the velocity overshoot in the WBL which will be discussed further in Section 2.4.2.

Figure 2.4 shows ADV-measured phase-averaged velocities at selected wave phases. As the wave arrives at the test section and travels along the offshore slope and bar crest (x = 51 to 55 m), velocities are in phase with the water surface elevation, i.e. directed onshore under the wave crest and offshore under the wave trough. At wave plunging (t/T = 0.33), strong upward-directed velocities under the wave front are evident and agree with earlier observations (e.g. Ting and Kirby, 1995). At the lee side of the breaker bar, the wave orbital motion interacts with the strong undertow. At this location, velocities are directed offshore through almost the complete wave cycle. As the wave crest passes (t/T = 0.42 to 0.58), near-bed velocities become nearly zero due to the counteracting offshore-directed return current and the onshore-directed orbital crest velocities. During the wave trough phase (t/T = 0.75 to 0.2), the combination of the strong undertow and negative orbital velocities results in strong offshore and upward velocities along the bar's lee side.

2.4 Near-bed and wave bottom boundary layer (WBL) flow

2.4.1 Phase-averaged velocities

Figure 2.6 shows profiles of ACVP-measured phase-averaged horizontal velocities. Note that the bed was mobile and intra-wave bed level variations occurred of O(mm). For consistency, ζ=0 m is set as a constant position for the entire wave cycle equal to the highest intra-wave bed level. This level generally occurs around near-bed flow reversal (zero velocity). Due to intra-wave erosion of the immobile-bed level, non-zero velocities can be found at ζ<0 m. As a proxy for the maximum crest-phase WBL thickness we introduce δ, defined as the elevation of maximum *periodic* velocity $\tilde{u}$ at the instance of maximum free-stream velocity (following e.g. Jensen *et al.*, 1989). Note that δ does not need to coincide with the elevation of maximum phase-averaged velocities <u> in **Figure 2.6**, as these include the time-averaged velocity contribution $\bar{u}$.

At the four locations at the offshore slope of the bar (x =51.0 – 55.0 m), the profiles show similar behavior (**Figure 2.6**). Since waves are strongly asymmetric (i.e. acceleration-skewed), the trough-to-crest half-cycle is of shorter duration than the crest-to-trough half-cycle. The highest near-bed velocities, exceeding 1 m/s, occur at the most offshore location (x=51.0 m). The overshooting of velocities close to the bed ($\zeta \approx$ 0.02 m) is addressed in the next section.

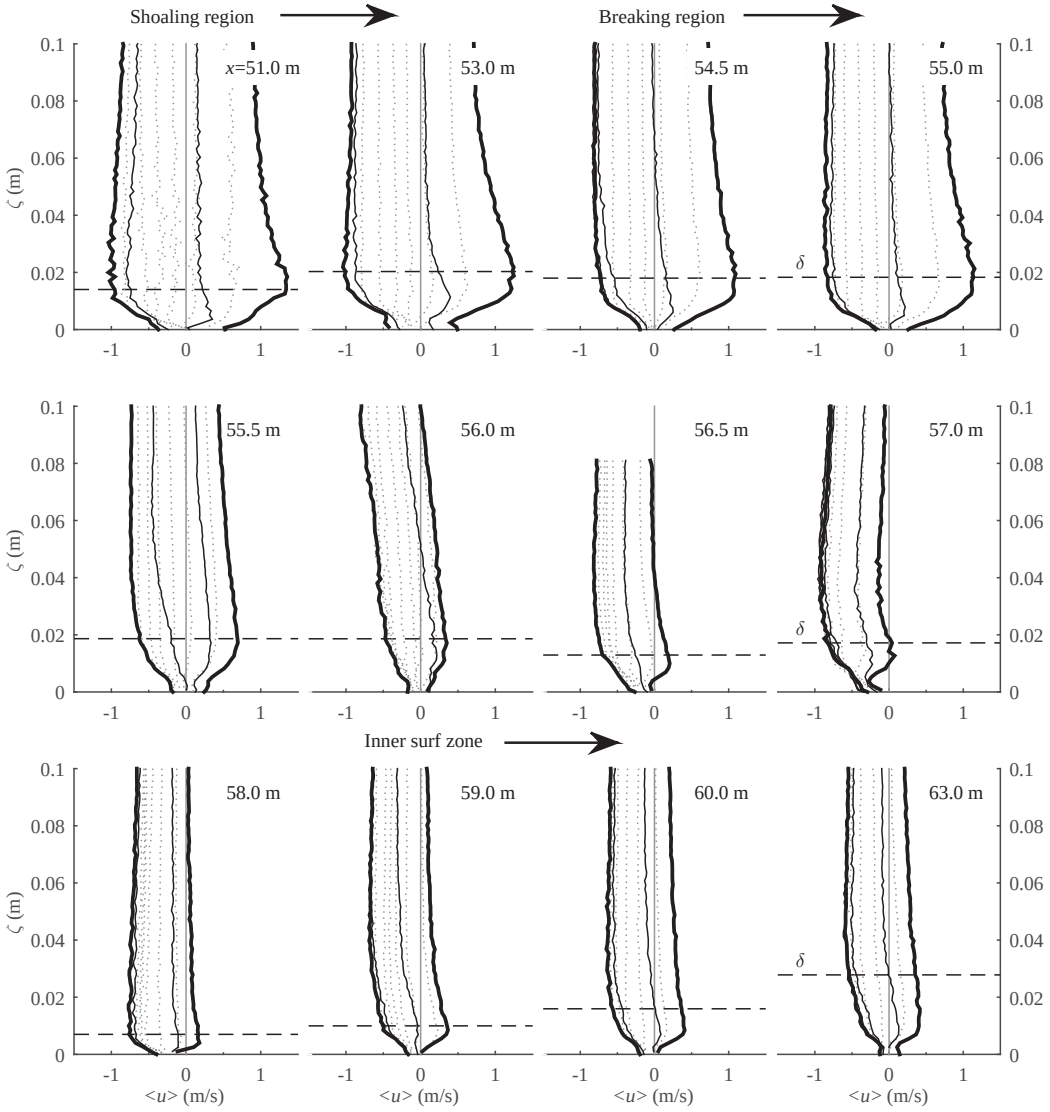

Figure 2.6. Vertical profiles of phase-averaged horizontal velocity near the bed (ACVP; *t*=0–15 min.) for 10 phases evenly separated over the wave period. Distinction is made between trough-to-crest half-cycle (thin solid lines) and crest-to-trough half-cycle (dotted lines). Thick solid lines correspond to times of maximum onshore and offshore free-stream velocity. Also included is the maximum boundary layer thickness δ (horizontal dashed line).

Periodic velocities are lower along the shoreward-facing slope of the bar and bar trough (x = 55.5 – 58.0 m), consistent with the outer-flow observations. At the same time, the offshore-directed return current (undertow) increases. The combined effect yields a reduction in crest velocity magnitudes and in positive (onshore) velocity duration, especially from x = 56.5 to 58.0 m, where velocities are negative (offshore) for almost the entire wave cycle. At some locations (e.g. x = 56.0 m), velocities are increasingly directed offshore with distance from the bed as the magnitude of $\bar{u}(\zeta)$ increases. These profiles are similar to those previously observed for waves propagating against a steady current (e.g. Van Doorn, 1981; Kemp and Simons, 1983). At x = 57.0 m, a positive $d\langle u\rangle/d\zeta$ is observed at elevations slightly above the WBL. This

feature differs from previous wave-current studies and relates to the large undertow velocities close to the bed (Section 2.3; **Figure 2.5a**). At all locations, crest velocities at the elevation of periodic-velocity overshooting ($\zeta = \delta$) are larger than in the free-stream (ζ = 0.10 m). This can lead to a short duration of onshore velocities at $\zeta = \delta$, even when the free-stream velocity is offshore directed for the entire wave cycle (e.g. at x = 56.0 and 56.5 m).

In the inner surf zone, where the orbital velocity amplitude increases and the undertow magnitude decreases (**Figure 2.5**; **Table 2.1**), the duration of onshore velocities gradually increases with x-location (**Figure 2.6**). Compared to the shoaling and breaking regions, velocity profiles in the inner surf zone are more depth-uniform for $\zeta > \delta$.

2.4.2 Time-averaged velocities

Based on previous work, four main processes may affect time-averaged velocities in the WBL in this experiment: (i) offshore-directed undertow; (ii) onshore-directed progressive wave streaming (e.g. Kranenburg *et al.*, 2012); (iii) wave shape streaming, offshore-directed for positively skewed/asymmetric waves (Trowbridge and Madsen, 1984; Fuhrmann *et al.*, 2009b); (iv) flow convergence, leading to onshore-directed near-bed streaming at the seaward-facing side of the breaker bar (e.g. Jacobsen *et al.*, 2014).

Figure 2.7 presents the vertical profiles of time-averaged horizontal velocities $\bar{u}(\zeta)$ within and just above the WBL. $\bar{u}(\zeta)$ is presented both with linear (**Figure 2.7a**) and logarithmic (**Figure 2.7b**) vertical axis, which allows a better comparison with previous WBL studies. All profiles in **Figure 2.7** are scaled with the free-stream velocity at ζ=0.10 m.

For the most offshore location (x = 51.0 m), the profiles in **Figure 2.7a-b** show four distinct segments: (i) a logarithmic increase (in offshore-direction) in $\bar{u}$ from ζ/δ = 0–0.5; (ii) a local maximum (in offshore-direction) between ζ/δ = 0.5–0.8; (iii) a local minimum (in absolute sense) of $\bar{u}$ between ζ/δ = 0.8 and 1.8; and (iv) nearly depth-uniform $\bar{u}$ from ζ/δ = 2–5. The profile shape is similar to previous observations under non-breaking waves over a horizontal bed (Schretlen, 2012). Kranenburg *et al.* (2012) showed that this profile shape can be explained through contributions of offshore-directed wave-shape streaming (segment ii) and onshore-directed progressive wave streaming (segment iii).

At all other cross-shore locations (x>51 m), $\bar{u}(\zeta)$ increases in magnitude with distance from the bed, with no evidence of wave-shape or progressive-wave streaming effects because of the strong undertow. At some locations a double-logarithmic velocity profile is observed, with inflection point above the WBL, as indicated by the blue lines at x=53.0 m (**Figure 2.7b**). Such $\bar{u}(\zeta)$ profiles are typically observed in wave-current conditions, obtained from numerical (Fredsøe, 1984; Davies *et al.*, 1988) and experimental (Van Doorn, 1981; Kemp and Simons, 1983) studies. At locations with particularly strong undertow relative to the orbital velocity, e.g. at x = 56.5 and 58.0 m (c.f. Table 2.1), the $\bar{u}(\zeta)$ profiles follow a single logarithmic distribution for elevations $0.5\delta<\zeta<2\delta$ (**Figure 2.7b**). This suggests that at these locations, near-bed velocities are dominated by the undertow with minor effect of wave-induced mixing. The double-log profile seems to re-establish at the inner surf zone, suggesting that the orbital motion regains importance in affecting the net currents.

Close to the bed ($\zeta<0.5\delta$), time-averaged horizontal velocity profiles deviate from a logarithmic profile. This occurs because $\zeta=0$ is defined as the level of the bed at rest, hence intra-wave and time-averaged velocities may still persist at $\zeta<0$. In addition, for sheet flow conditions (x = 51.0 to 55.0 m), velocities inside the sheet flow layer do not satisfy the logarithmic distribution (Sumer *et al.*, 1996).

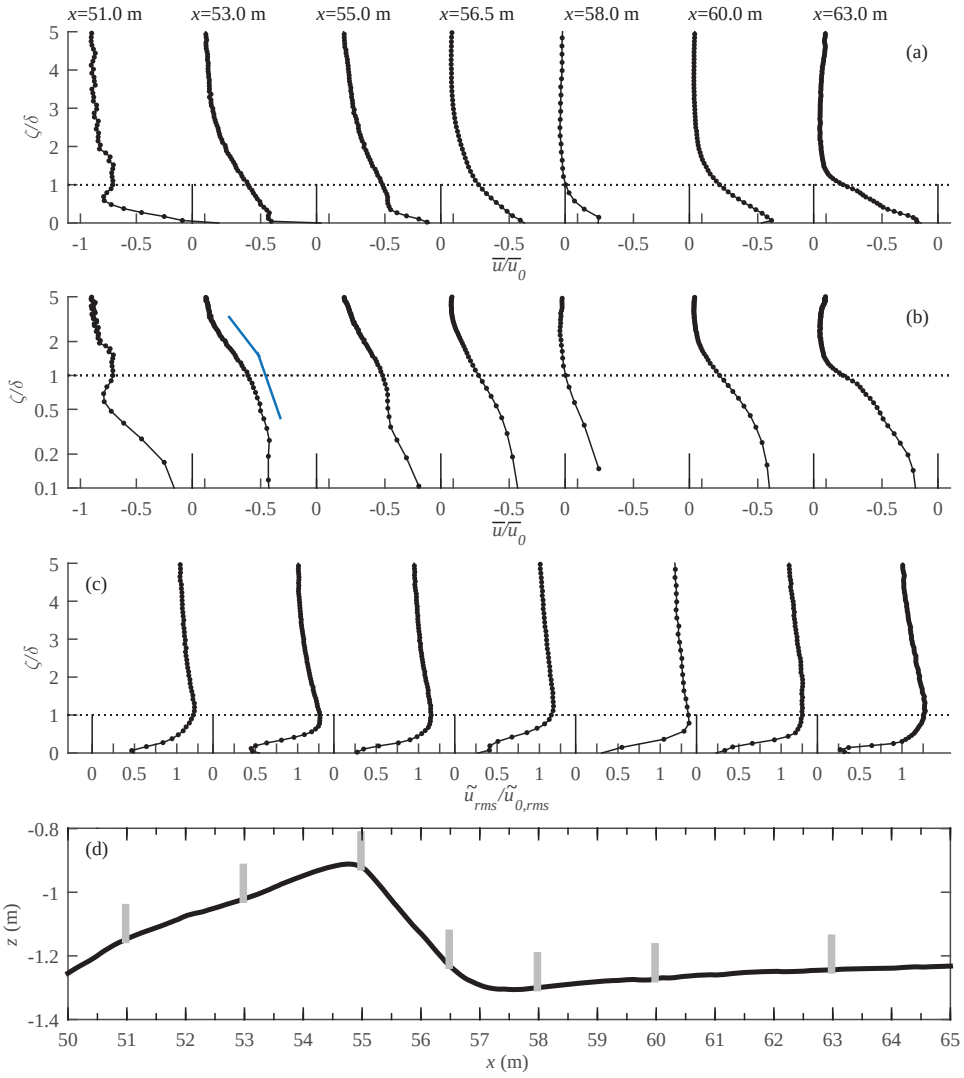

Figure 2.7. Near-bed horizontal velocity profiles at selected locations. (a) Time-averaged velocities; (b) similar to (a), but with vertical axis on logarithmic scale. The blue straight lines depict the velocity gradient, with inflection point that is typical for wave-current interactions; (c) Root mean square periodic velocities; (d) Reference bed profile at t=0 min. and measurement locations. All velocities in (a–c) are scaled with free-stream velocities at ζ=0.10 m.

2.4.3 Periodic velocities and wave bottom boundary layer thickness

Figure 2.8 shows the vertical profiles of horizontal periodic velocity $<\tilde{u}(\zeta)>$ along the offshore slope of the breaker bar. This figure differs from **Figure 2.6** as time-averaged velocities $\bar{u}$ are

subtracted. Overshooting occurs at each location during peak offshore and onshore phases and is most prominent during the crest phase. The overshoot is explained by the velocity defect in the WBL behaving as a damped wave that travels upwards (Nielsen, 1992) and has been observed in boundary layers in oscillating flows (e.g. Jensen *et al.*, 1989; van der A *et al.*, 2011), under laboratory waves (e.g. Schretlen, 2012) and under laboratory spilling waves (Huang *et al.*, 2010). Above $\zeta=\delta$, peak onshore and offshore periodic velocity magnitudes gradually decrease until a near-zero vertical gradient is reached at $\zeta\approx0.10$ m. For all locations, the periodic crest velocities at $\zeta=\delta$ are considerably (about 50%) higher than at 0.10 m. This is partly attributed to a change in the shape of the periodic-velocity time series as the bed is approached: changing phases of the higher harmonics leads to increasing velocity skewness and decreasing acceleration skewness (Berni *et al.*, 2013). In the present experiment, this shape transformation starts at $\zeta \approx 2–5\delta$. Furthermore, the *rms* periodic velocities at $\zeta = \delta$ are notably higher than at 0.10 m (**Figure 2.7c** and **Figure 2.5b**), leading to a larger orbital excursion and peak onshore and offshore orbital velocities. Such increased $\tilde{u}_{rms}$ at $\zeta = \delta$ relates to the velocity overshooting and is also observed at breaking and inner surf zone locations further shoreward ($x > 55.0$ m). In the present study, $\tilde{u}_{rms}(\delta)/\tilde{u}_{rms}(5\delta) \approx 1.2$ (+/- 0.1), which is somewhat higher than the value of about 1.07 found with numerical boundary layer models that were validated against laboratory observations for non-breaking waves (e.g. Nielsen, 1992; Kranenburg *et al.*, 2012).

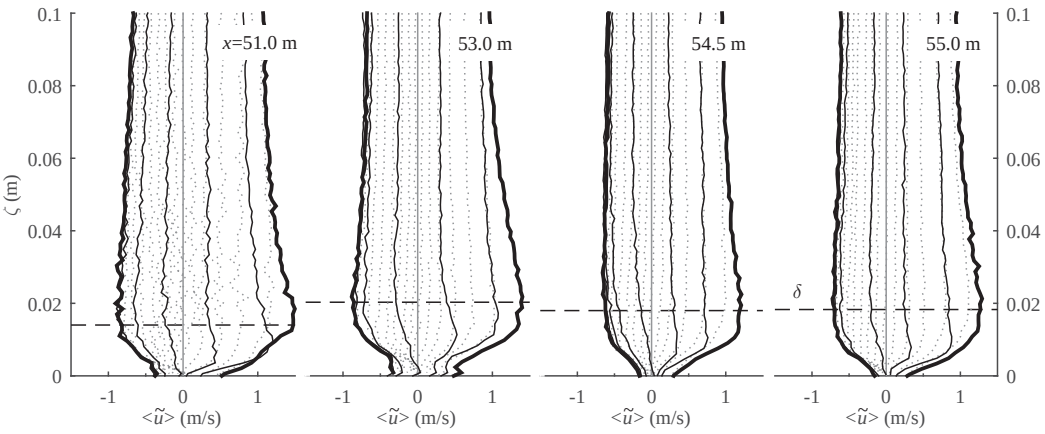

Figure 2.8. Vertical profiles of phase-averaged horizontal periodic velocity at shoaling locations for 20 phases evenly spread over the wave cycle. Distinction is made between trough-to-crest half-cycle (thin solid lines), the crest-to-trough half-cycle (dotted lines), and instances of peak crest and trough free-stream velocity (thick lines).

The elevation of maximum periodic velocity overshoot during the crest phase is used here as a proxy of the WBL thickness (following Jensen *et al.*, 1989). Previous measurements under velocity-skewed waves above a mobile bed showed that the overshoot elevation is at higher elevation during the crest phase than during the trough phase, i.e. when highest velocity magnitudes are reached (Schretlen, 2012). In contrast, for positive acceleration-skewed flows, the WBL thickness is smaller during the crest phase since the WBL has less time to develop compared to the trough phase (van der A *et al.*, 2011). Comparison of the peak onshore and offshore periodic-velocity profiles (**Figure 2.8**) shows that the maximum overshoot elevation occurs at a similar level for the crest and the trough phases. A possible explanation is that the

opposing effects of velocity- and acceleration-skewness on WBL thickness tend to cancel each other out. Approximately similar crest and trough WBL thicknesses were also found at other locations in the breaking and inner surf zones (not included in **Figure 2.8**).

Measurements of δ are compared quantitatively with the empirical formulation of Fredsøe and Deigaard (1992):

$$\delta/k_s = 0.09(a/k_s)^{0.82} \qquad (2.6),$$

in which k_s denotes the roughness. Although Equation 2.6 was based on rigid rough-bed experiments, it has been shown to predict reasonably well WBL thickness for mobile-bed sheet flow conditions for a range of sediment sizes in full-scale oscillatory flows (O'Donoghue and Wright, 2004a; Campbell *et al.*, 2007) and non-breaking progressive surface waves (Schretlen, 2012). In these studies, the roughness was taken as $2.5D_{50}$ rather than relating k_s to the sheet flow thickness. Hence, the roughness k_s is here also set equal to $2.5D_{50}$.

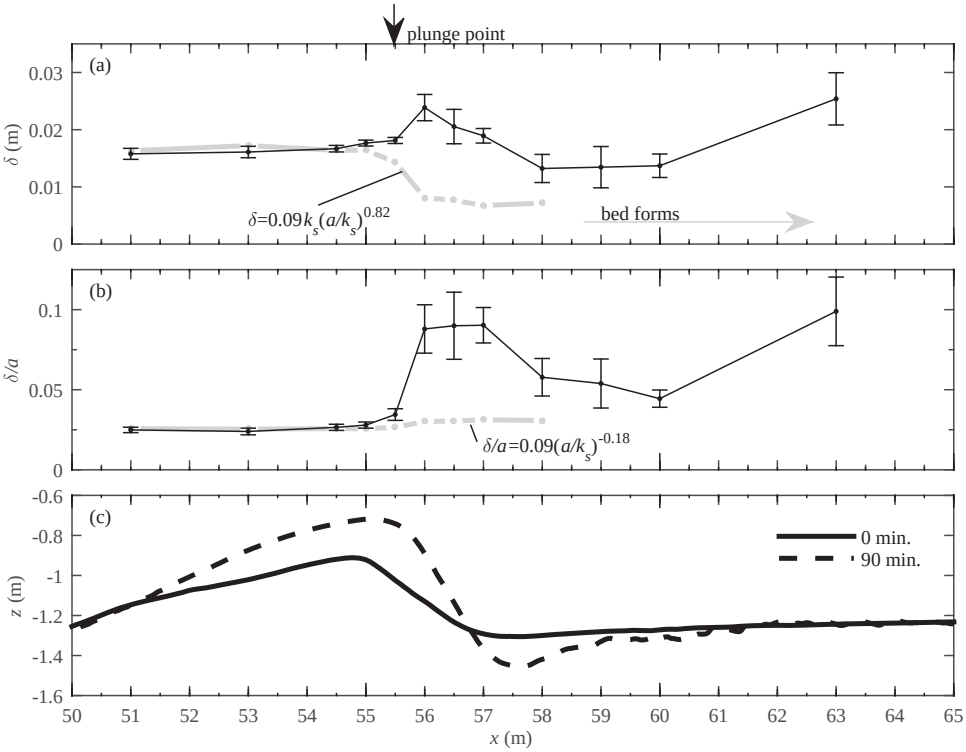

Figure 2.9. Overshoot elevation (δ), as proxy for WBL thickness, along test section. (a) Dimensional δ; (b) δ/*a* at ζ = δ; (c) Bed profiles at start (solid) and end (dashed) of experiment. Values depicted in (b) and (c) are averaged over six runs per location (crosses and black line), with error bars marking +/- one standard deviation of mean. The grey dots and dashed line in (a) and (b) mark the empirical prediction by Equation 2.6 (Fredsøe and Deigaard, 1992).

Equation 2.6 is applied here in a situation with a superimposed current. This can be justified based on the results of Nielsen (1992) who analyzed the dataset of van Doorn (1981) and found no effect of a moderate-strength superimposed current on *rms* periodic velocities (this is further discussed in Section 2.6). Equation 2.6 is applied only for flat-bed locations, as rippled-bed conditions are considered outside the equation's application range.

The cross-shore variation in δ and predictions of δ using Equation 2.6 are shown in **Figure** 2.9**a**. Note that the measured δ values are averaged over six runs per location and that due to variability of δ between runs, values in **Figure** 2.9**a** may differ slightly from values depicted in **Figures 2.6 and 2.8**.

Between x = 51.0 and 55.0 m, δ is almost constant. This may be expected as the free-stream velocities show little cross-shore variation (**Figure 2.5c**). The measured δ is in good agreement with predicted δ from Equation 2.6 and, consequently, is in good agreement with δ from previous oscillatory flow mobile-bed experiments. This suggests that flow non-uniformity under progressing surface waves over the sloping bed has little impact on the WBL thickness across the shoaling and breaking locations offshore from the bar crest.

Near the plunge point, along the shoreward slope of the breaker bar, δ increases slightly, even though the periodic-velocity amplitude decreases in this region. Consequently, δ/a increases substantially shoreward from the plunge point (**Figure** 2.9**b**). In addition, measured δ are substantially larger than predicted δ; especially from x=56.0 to 57.0 m, where the difference exceeds a factor 2. Possible physical explanations for this observation are given in Section 2.6.

Towards the bar trough, both δ and δ/a decrease again. Further into the inner surf zone, at x=63.0 m, δ increases due to an increasing bed roughness in the presence of sand ripples and the associated ripple vortex regime.

2.5 Turbulence

2.5.1 Time-averaged turbulent kinetic energy

Figure 2.10a shows vertical profiles of time-averaged turbulent kinetic energy (TKE), Froude-scaled ($\sqrt{\overline{k}/gh}$) to enable comparison with previous studies. An offset between the ADV- and ACVP-measured TKE becomes apparent and is discussed further in Section 2.6. The down-looking ACVP could induce wake turbulence, leading to enhanced turbulence magnitudes near the sensor. However, no local increase in TKE near the sensor becomes apparent from the figure, and the effect is therefore assumed negligible compared to other sources of TKE.

In the outer flow, TKE decreases from the top of the water column downwards. This decay is consistent with many previous breaking-wave studies (e.g. Scott *et al.*, 2005; Yoon and Cox, 2010), and implies that turbulence production by wave breaking and the surf bore dominates turbulence levels in the upper half of the water column. The cross-shore evolution of TKE in the middle of the water column shows an increase from shoaling zone towards the bar crest, followed by a decay of $\overline{k}$ in the inner surf zone. This pattern is consistent with previous studies involving a barred profile (Boers, 2005; Scott *et al.*, 2005; Yoon and Cox, 2010). High values at the bar crest relate to wave breaking, while the decrease towards the bar trough and inner surf zone is attributed to an increase in water depth (turbulence spreads over a larger water mass) and reduced wave energy (Yoon and Cox, 2010).

At the bar crest, and in the middle of the water column, we find $\sqrt{\overline{k}/gh} \approx 0.043$. This matches well with the magnitude of about 0.04 reported for similar-scale flume experiments involving

plunging (but irregular) waves (Scott *et al.*, 2005; Yoon and Cox, 2010; Brinkkemper *et al.*, 2015). However, $\sqrt{\bar{k}/gh}$ is substantially smaller compared to the plunging wave tests of Ting and Kirby (1994) and Govender *et al.* (2002), who found values of about 0.08. In addition, both these studies found $\bar{k}$ profiles that were almost depth-uniform, indicating less decay of TKE with depth compared to the present study and other large-scale experiments. These differences may relate to the smaller scale and the plane sloping bed geometry (i.e. no bar) of Ting and Kirby (1994) and Govender *et al.* (2002), leading to relative wave heights H/h near the plunge point that are substantially larger than in the present study.

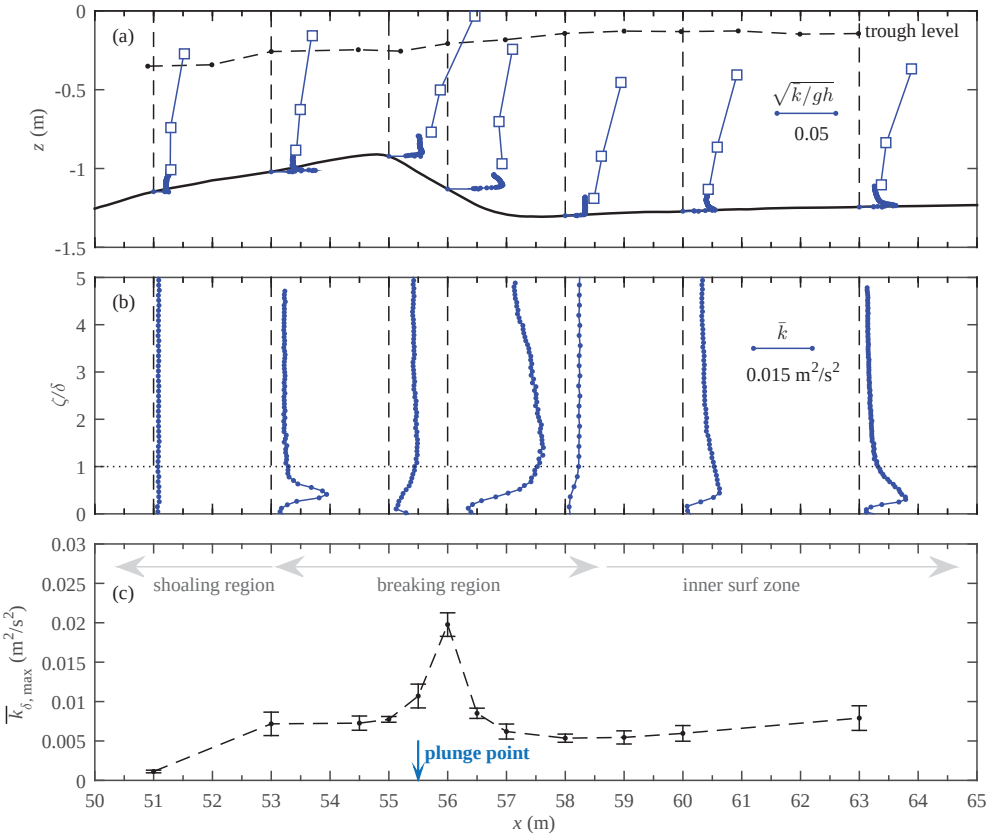

Figure 2.10. Time-averaged TKE, measured with ADVs (squares) and ACVP (dots). (a) Froude-scaled TKE over complete water column; (b) close-up of TKE profiles near the bed and in the WBL; (c) Maximum time-averaged TKE measured in the WBL, mean (dots and dashed line) +/- standard deviation of mean (error bars).

Figure 2.10b shows ACVP-measured vertical profiles of $\bar{k}(\zeta)$ inside the WBL, and **Figure 2.10c** shows the cross-shore evolution of maximum TKE inside the WBL. Near-bed $\bar{k}$ at the most offshore location (x = 51.0 m) is depth-uniform and its magnitude in the WBL is much lower compared to all other cross-shore locations. Apparently, the amount of turbulence produced at the bed is small. Further shoreward (x = 53.0 m), $\bar{k}$ magnitudes increase rapidly from the bed upwards, reach a maximum at around $\zeta = 0.5\delta$, and decrease at higher elevations. The shape of this profile, with highest values close to the bed, is similar to previous measurements from

rigid-bed oscillatory boundary layer experiments where the main turbulence production was due to bed shear (e.g. Jensen *et al.*, 1989; van der A *et al.*, 2011). The decrease in $\overline{k}$ for $\zeta < 0.5\delta$ (**Figure 2.10b**, x = 53.0 m) is not consistent with results from rigid-bed experiments, for which the highest values of $\overline{k}$ are typically found much closer to the bed. This difference may be due to physical processes in mobile bed conditions, such as turbulence damping (Dohmen-Janssen *et al.*, 2001; Hsu *et al.*, 2004) or reduced turbulent mixing efficiency in the dilute suspension layer above a dense bedload layer (Revil-Baudard *et al.*, 2015). However, instrument limitations (Appendix A) may also be a factor. The strong increase in $\overline{k}_{\delta,max}$ at x=53.0 m relative to x=51.0 m, for the complete near-bed layer including the WBL (**Figure 2.10c**), is remarkable since magnitudes of free-stream velocities are similar at both locations (**Table 2.1**). This suggests that turbulence at x = 53.0 m is not only produced locally at the bed and that there is a significant contribution of breaking-generated turbulence that arrives at this location.

In the breaking region at x = 55.0 and 56.0 m, the near-bed $\overline{k}$ profiles are more depth-uniform without a distinct maximum within the boundary layer. The vertical distribution and the magnitudes of $\overline{k}$ suggest that TKE generation by bed friction is small compared to contributions of breaking-induced turbulence. Magnitudes of TKE increase from shoaling to breaking zone for the complete near-bed region including the WBL (**Figure 2.10c**). Of particular note is the increase in $\overline{k}_{\delta,max}$ near the plunge point around the breaker bar crest (a factor 2.7 increase from x=54.5 to 56.0 m), despite the strongly decreasing peak onshore and offshore near-bed velocities in this region (**Table 2.1**). The bed is plane in this region, which excludes an increase in TKE due to small-scale bed forms. The strong undertow current at these locations is expected to have a minor effect on local turbulence values. This was shown previously in experiments with waves and superimposed current for which $\overline{k}$ values were not much larger compared to the same waves without a current (c.f. Kemp and Simons, 1983). Hence, results indicate that the substantial increase in $\overline{k}_{\delta,max}$ in the breaking zone is primarily caused by breaking-induced turbulence that invades the WBL.

In the bar trough (x=57.0–59.0 m), magnitudes of $\overline{k}_{\delta,max}$ are significantly lower than at bar crest locations but are nevertheless notably higher than in the shoaling zone (c.f. x = 51.0 m). The latter suggests that breaking-generated turbulence still reaches the bed in the bar trough, despite the much larger vertical distance between water surface and bed compared to bar crest locations. The vertical profile of near-bed $\overline{k}(\zeta)$ at x=58.0 m is almost depth-uniform (**Figure 2.10b**). The absence of a near-bed increase in $\overline{k}(\zeta)$ suggests that bed shear by orbital velocities does not add significantly to local TKE. However, bed shear by time-averaged velocities (undertow) may result in similar depth-uniform profiles (see e.g. Sleath, 1991) and may therefore contribute to near-bed TKE in the bar trough. Vertical profiles of $\overline{k}(\zeta)$ in the inner surf zone (x>58.5 m) show that bed-generated turbulence due to orbital-velocity shear gradually regains importance. Throughout the inner surf zone, $\overline{k}_{\delta,max}$ increases due to increasing bed form roughness (**Figure 2.10c**).

2.5.2 Time-varying turbulent kinetic energy

Figure 2.11 shows detailed measurements of $\langle k \rangle$ inside the WBL and in the layer immediately above it (ζ/δ=0–5). A dominance of bed-generated turbulence in near-bed time-varying $\langle k \rangle$ occurs at locations relatively far from the plunge point, i.e. at $x \leq$ 54.5 m and at $x >$ 58.5 m. At x=53.0 and 54.5 m, large turbulent events are formed at the bed during instances of peak trough

and crest velocities. The bed-generated TKE remains confined to the WBL at x=53.0 m, but appears to diffuse outside the WBL at x=54.5 m. Bed-generated TKE at the inner surf zone (x>58.5 m) is particularly observed during the crest phase. Turbulence production at the bed occurs due to the presence of vortex ripples in the inner surf zone which increase the bed roughness. At these inner surf zone locations, similar to x = 53.0 m, bed-generated TKE remains largely confined to the WBL.

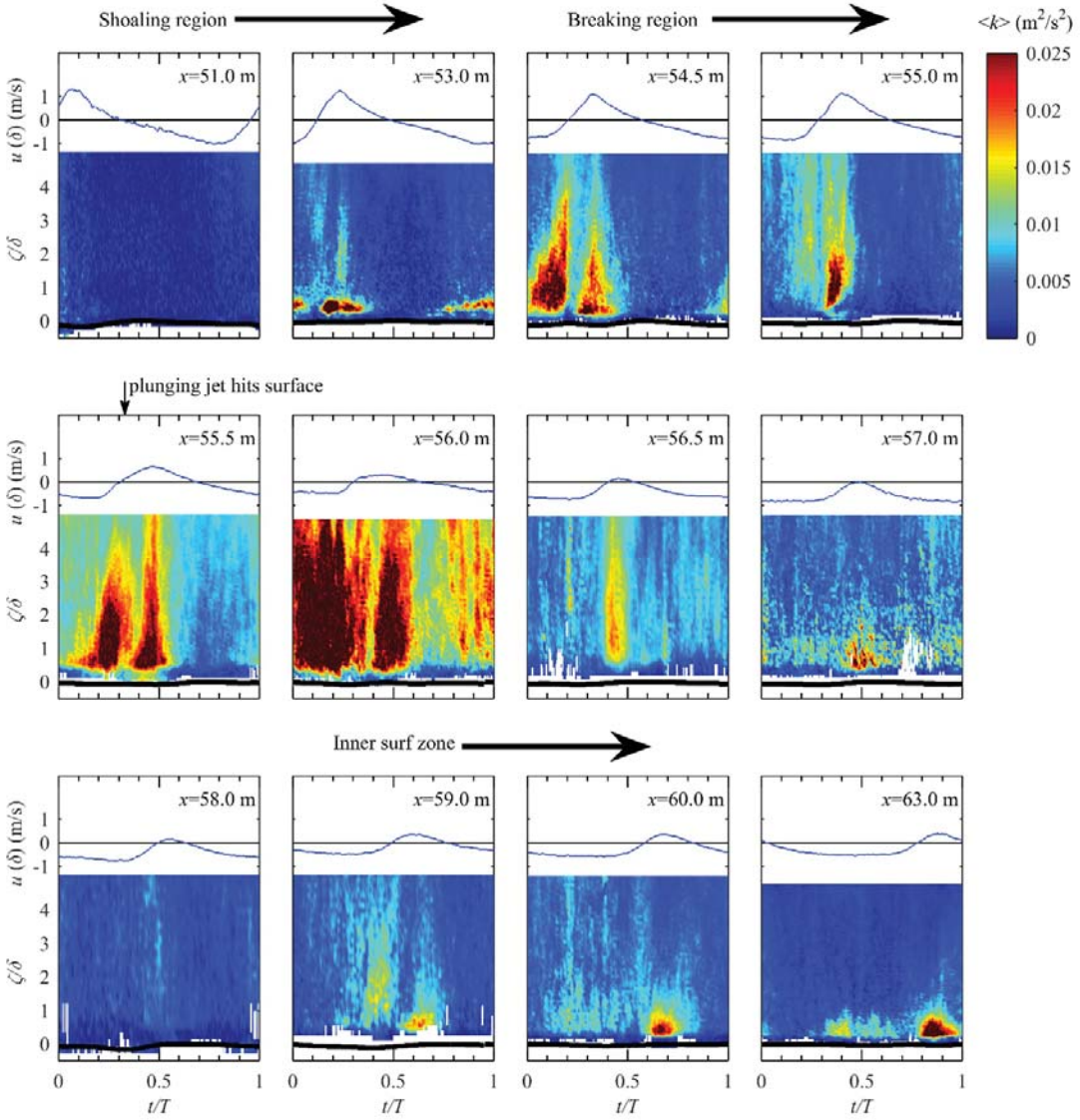

Figure 2.11. Time-varying turbulent kinetic energy <k> near the bed, measured by ACVP for t=0–15 min. Free-stream horizontal velocities at ζ=δ are included in each panel as a reference.

Breaking-generated turbulence affects time-varying near-bed <k> at locations close to the plunge point at x = 55.5 m. At x = 55.5 – 56.0 m, i.e. roughly below the plunge point and close to the bar crest, <k> increases during the early crest phase (t/T=0.4–0.6). This increase occurs rapidly and uniformly over the complete near-bed layer, which indicates that the source is breaking-induced TKE that comes from above and mixes rapidly over the near-bed layer. This

peak in TKE lags the instance of the plunging jet hitting the water (at x = 55.5 m and $t/T \approx 0.33$) by $\Delta t \approx 0.5$ s ($\Delta t/T \approx 0.1$–0.2). At x = 56.0 m, $\langle k \rangle$ increases a second time during the wave trough phase (t/T=0–0.3), marking a second event of turbulence arrival. A trough-phase increase in TKE can also be identified at x=55.5 m, particularly when focusing on elevations outside the WBL (ζ=4–5δ). Closer to the bed at x=55.5 m, bed-generated turbulence merges with breaking-induced TKE, leading to maximum $\langle k \rangle$ values that are much higher than at offshore locations with similar near-bed velocities (x=53.0 to 55.0 m).

Offshore from the plunge point, at x=55.0 m, a sudden increase in TKE above the WBL during the end of the wave trough phase (t/T=0.2) can be identified. This increase is rather uniform over depth, suggesting that this TKE is not produced locally at the bed but relates instead to the arrival of breaking-induced turbulence. After passage of the wave crest (t/T=0.4), TKE decreases depth-uniformly. Shoreward from the region of high turbulence below the plunge point, at x=56.5 m, $\langle k \rangle$ increases rapidly during the crest phase (t/T=0.4 to 0.5). Again, the depth-uniformity of this increase suggests that it is not due to local turbulence production at the bed. Further shoreward, in the region covering the lower lee-side of the breaker bar and the bar trough (x=57.0–58.0 m), the limited temporal variation in TKE indicates that there is little turbulence production by wave-related bed shear and limited arrival of advected breaking-induced TKE.

Due to strong cross-shore gradients in near-bed TKE, the temporal behavior seen in **Figure** 2.11 is not fully explained by local processes, i.e. production at the bed or at the water surface and advection/diffusion in vertical direction only. Instead, we may expect significant contributions of horizontal turbulence advection to the temporal variation in near-bed TKE. The horizontal TKE advection is seen in **Figure 2.12c**, which shows the spatiotemporal variation in TKE at ζ=0.11 m. The continuously high near-bed TKE magnitudes at x=55.5 and 56.0 m stand out. Along the offshore slope of the bar (x=51.0–55.0 m), the highest TKE values are found during the zero-up crossing of the surface elevation. This relates not only to production at the bed (**Figure** 2.11), but also to the arrival of TKE generated below the plunge point which is advected offshore by orbital and undertow velocities during the trough phase. The latter is identified as a patch of high TKE that travels offshore from the plunge point at x = 55.5 m to the shoaling zone at $x \approx 52.0$ m (**Figure 2.12c**, grey arrow). After flow reversal to positive velocities, the arriving fluid at shoaling locations comes from x<52.0 m and is relatively low in TKE. Consequently, net advection of TKE is onshore (white arrow in **Figure 2.12c**) leading to a decrease in TKE at shoaling locations.

An excursion of TKE also occurs from the plunge point to onshore locations, although the horizontal extent over which TKE is advected is much more restricted, and consequently, the effect is much less apparent. In **Figure 2.12c**, the onshore excursion is observed as the patch of high TKE at x = 55.0-56.0 moves slightly onshore to x=56.5 m around t/T = 0.4, and back offshore around t/T = 0.6. The effect is also observed in **Figure** 2.11 as a depth-uniform increase in $\langle k \rangle$ during this time interval. The reduced orbital amplitude and the strong offshore-directed undertow velocity lead to a short duration of onshore-directed phase-averaged velocities in this region, and consequently, restrict the onshore and downward transport of TKE along the shoreward slope of the bar.

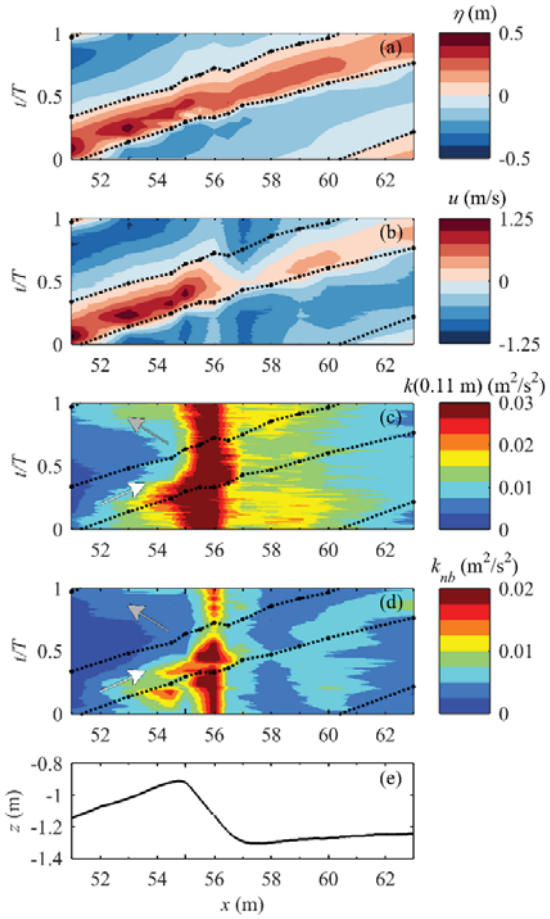

Figure 2.12. Surface plots of spatial (horizontal axis) and temporal (vertical axis) variation in (a) Water surface levels; (b) Horizontal velocities at ζ=δ; (c) TKE, measured by ADV at ζ=0.11 m; (d) Near-bed TKE, measured by ACVP, depth-integrated over the lowest 0.10 m (k_{nb}). Dashed lines depict zero crossings of η. Arrows in panels c-d are explained in main text. Panel (e) shows the reference bed profile.

Figure 2.12d shows the spatiotemporal variation in depth-averaged (over ζ=0–5δ) near-bed TKE (annotated k_{nb}), which resembles the behavior at ζ=0.11 m. Hence, also in the WBL, cross-shore advection of breaking-generated turbulence has a significant effect on <*k*>. Differences between **Figure 2.12c,d** are mainly attributed to contributions of bed-generated turbulence to k_{nb} (**Figure** 2.11).

2.5.3 Reynolds shear stress

Figure 2.13 shows the Reynolds shear stress ($-\rho\langle u'w'\rangle$) at ζ=δ. The Reynolds shear stress at the bed (ζ=0) could not be resolved due to instrument limitations (Appendix A).

In the vicinity of the plunge point (at *x*=55.5 m +/- 0.5 m), peak onshore and offshore Reynolds stresses are found to increase rapidly, with a factor two increase relative to *x* = 54.5 m. The increase is likely associated with the effects of breaking-induced turbulence that reaches the bed, because peak onshore and peak offshore velocities decrease between shoaling and breaking zone (**Table 2.1**). Indeed, the increase in onshore/offshore Reynolds stresses occurs

in approximately the same region where TKE in the WBL was observed to increase (c.f. **Figure 2.10a**). Further shoreward (x=56.5–57.0 m), Reynolds shear stresses are almost continuously directed offshore, similar to the near-bed velocities at these locations. The time-averaged Reynolds stresses (crosses in **Figure 2.13**) are predominantly negative, which is explained by the negative time-averaged near-bed velocities.

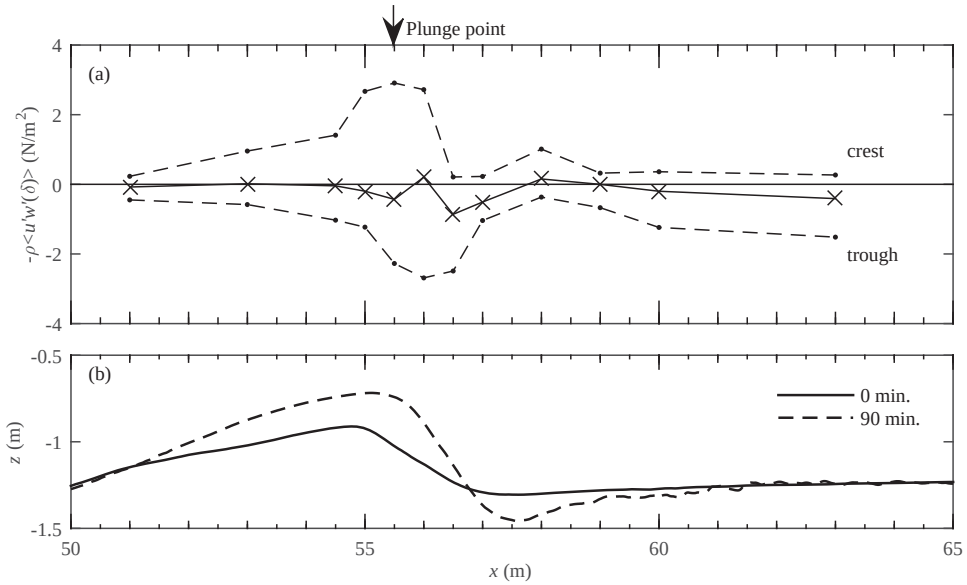

Figure 2.13. Near-bed Reynolds stresses at ζ=δ, averaged over t=0-90 min. (a) Time-averaged (crosses and solid line) and phase-averaged peak onshore and offshore (dots and dashed lines) Reynolds stresses; (b) Bed profiles at t=0 min. (solid line) and t=90 min. (dashed line).

2.6 Discussion

Offsets between ADV- and ACVP-measured $\bar{k}$ can be seen in **Figure 2.10a**. Whether these shifts are attributed to differences between ADV and ACVP measurement resolution, differences in acoustic frequencies and associated sensitivity to different particle sizes, slight differences in system orientation relative to the local bed slope (ADV data have not been corrected) or even invalid TKE approximation for the 2C-velocity measurement of the ACVP (see Section 2.2.5), is difficult to determine. Because the ACVP measures systematically lower $\bar{k}$ than the ADV, the discrepancies might be attributed to the lack of spatial-temporal resolution of the ACVP, enhanced by the application of the Doppler noise correction method (Appendix A).

For the same reason, the ACVP-measured Reynolds shear stress (Section 2.5.3) may also underestimate the actual fluid shear. It is not expected that this underestimation varies along the bed profile since the same ACVP settings were used throughout the experiment. Nevertheless, for this reason, a quantitative analysis of the different terms contributing to the total bed shear was not carried out. It should be noted that the Reynolds shear forms only one component of the total bed shear. The time-averaged and periodic velocities can also contribute to – and even dominate – bed shear in the surf zone (Chassagneux and Hurther, 2014).

The present results highlight an important contribution of breaking-induced turbulence to TKE inside the wave boundary layer. This agrees with other large-scale laboratory (Scott *et al*., 2005) and field (Grasso *et al.*, 2012) studies over a barred profile that included measurements of velocities within, or close to, the WBL. The WBL invasion of breaking-generated turbulence is most apparent at the bar crest and near the plunge point, where TKE increases after arrival of a highly turbulent water body that follows rapidly (about 0.5 s) after the plunging jet strikes the water column (**Figure** 2.11, x = 55.5–56.0 m). This is consistent with previous studies that showed rapid downward turbulence transport under plunging breakers, associated with large vortices below the wave front (Ting and Kirby, 1995; Christensen and Deigaard, 2001; Kimmoun and Branger, 2007). It is expected that in the present study the rapid mixing of TKE over the complete water column including the WBL is partly facilitated by the shallow water depths at the bar crest. This suggests that the barred bed profile and cross-shore-varying water depth are important factors controlling the extent to which breaking-induced TKE can reach the WBL.

Breaking-induced TKE is not fully determined by local vertical processes, i.e. production, dissipation and vertical advection and diffusion. Instead, breaking-generated turbulence travels offshore, leading to an increase in phase- and time-averaged TKE over the complete water column including the WBL up to about 3 m offshore from the plunge point. The phase-dependency of the excursion suggests that transport of TKE is advective and links closely to the orbital motion. The distance over which TKE is advected (3 m) equals approximately 6 times the semi-excursion length a and it corresponds to about 15 s ($3 \cdot T$) of advection by offshore-directed time-averaged velocities. This suggests that offshore TKE advection occurs over multiple wave cycles and that breaking-generated TKE does not dissipate within one wave cycle. At the same time, previous research has shown that turbulence transport under plunging waves is not fully advective; diffusive transport may also be important (e.g. Ting and Kirby, 1995). A more detailed analysis of turbulence transport mechanisms is not considered here due to the relatively limited spatial coverage of outer-flow velocity measurements. Results of an accompanying rigid-bed experiment involving similar wave conditions and barred profile are expected to extend insights into the TKE transport mechanisms.

The increase in near-bed Reynolds shear stresses in the breaking region agrees qualitatively with previous observations of enhanced bed shear in the breaking region (Cox and Kobayashi, 2000; Sumer *et al.*, 2013) or under external-grid turbulence (Fredsøe *et al.*, 2003). Quantitative comparisons between these previous studies are difficult, because of significant differences in scale, bed geometry, breaking intensity and instrumentation (i.e. the Reynolds stress in the present study differs physically from the total bed shear). It was shown by Fredsøe *et al.* (2003) that external turbulence may increase the apparent bed roughness and the WBL thickness. This raises the question to what extent the present study's distinct increase in δ/a (factor 2-3 compared to previous studies) in the breaking region (**Figure** 2.9, from x=56.0 to 57.0 m) relates to breaking-induced turbulence or other factors. Three factors are discussed here.

Fredsøe *et al*. (2003) showed that external turbulence may enhance the turbulent exchange of momentum between free-stream flow and the WBL, resulting in larger wave friction factors over a wide range of Reynolds regimes ($O(Re) = 10^4$–10^6). This leads to an increase in apparent bed roughness and an upward displacement of periodic velocity in the inner WBL, similar to

how wave-induced mixing can affect steady current profiles (Fredsøe *et al.*, 2003). In addition, the invasion of external turbulence leads to an earlier transition to turbulence in the WBL, which can increase δ/a with as much as a factor 2. Reynolds stresses (**Figure 2.13**) suggest a similar enhanced momentum exchange between WBL and outer flow in the present study (x = 55.0 – 56.5 m) which is likely to affect velocity distributions inside the WBL. Whether this effect can explain the significant increase in δ/a cannot be concluded by quantitative comparison with results by Fredsøe et al. (2003), because their results were obtained for a smooth bed which differs substantially from hydraulically rough conditions in terms of turbulence intensities and Reynolds stresses at elevations close to the bed ($\zeta < \delta$) (c.f. Jensen *et al.*, 1989).

A second factor that may affect the WBL thickness is time-averaged undertow velocity, that is particularly strong (relative to periodic velocity) from x=56.5 to 58.0 m. Nielsen (1992), using the dataset of van Doorn (1981) that included values of relative current strength to *rms* periodic velocity ($|\bar{u}|/\tilde{u}_{rms}$) up to 1.11, found no effects of the superimposed current on WBL thickness. In the present study, locations from x = 56.5 to 58.0 m have $|\bar{u}|/\tilde{u}_{rms}$ values that exceed 1.11 (Table 2.1). However, based on the results of Nielsen (1992) we deem that the superimposed current cannot explain the strong (factor 3) enhancement of WBL thicknesses in the present study. In addition, the enhanced WBL thickness is observed already at x=56.0 m, where the undertow strength is of moderate strength compared to periodic velocities ($|\bar{u}|/\tilde{u}_{rms}$<1.11).

A third factor that potentially affects WBL thicknesses is the bed geometry. Sumer *et al.* (1993) showed that the WBL thickness for converging/diverging flow may differ substantially from uniform flow conditions. In a tunnel with 0.20 m flow depth and with a local bed slope of 1°, the maximum WBL thickness during a diverging flow can be almost twice as thick as a WBL above a uniform (zero inclination) bed (Sumer *et al.*, 1993). In the present experiment, the maximum WBL thickness is estimated during the crest phase when the flow indeed diverges. One may expect that the importance of this effect depends on a relative vertical divergence rate during a wave cycle, i.e. the vertical expansion during the orbital motion relative to the local water depth. This can be expressed as a ratio $a\cdot\tan(\beta)/h$, in which a is the semi-excursion amplitude, β is the local slope, and h is the water depth (c.f. Fuhrmann *et al.*, 2009a). In Sumer *et al.* (1993), this divergence ratio is approximately 0.26 (a=3.0 m). In the present experiment, along the lee side of the bar at x = 56.5 m, this ratio equals about 0.06 at the start of the experiment (a=0.31 m, β=11°, h=1.1 m; Table 2.1) and about 0.12 at the final stage of bar development (as β increases to 25°). Based on this, we may expect flow divergence effects in the present study to be smaller but of same order of magnitude as the experiments of Sumer *et al.* (1993). Hence, effects of flow divergence on WBL thickness along the shoreward bar slope cannot be dismissed.

The high contributions of breaking-induced turbulence to TKE in and just outside the WBL may have important implications for sediment transport. Not only is turbulence able to entrain sediment from the bed into suspension (Sumer and Oguz, 1978), it has also the ability to increase bedload transport (Sumer *et al.*, 2003). The effects of breaking-induced turbulence on suspended and bedload sediment transport processes will be addressed in a forthcoming paper.

2.7 Conclusions

The present study examines velocities and turbulence dynamics near a sand bed under near-full-scale, plunging breaking waves in a laboratory wave flume. In contrast with previous experiments, detailed measurements were obtained inside and directly above the wave bottom boundary layer (WBL) with high spatial and temporal resolution. These measurements were taken along a mobile sandy breaker bar at shoaling, breaking and inner surf zone locations. The following conclusions are made:

1. Phase-averaged WBL velocities show similar behavior to non-breaking and oscillatory WBL studies, including distinct velocity overshooting. Time-averaged velocities in the WBL are largely dominated by the strong undertow and show consistent behavior with previous observations for wave-current interactions. Wave (shape) streaming mechanisms, as usually observed for uniform non-breaking waves, are evident only in the shoaling region where the undertow is relatively weak.
2. The dimensionless WBL thickness along the offshore slope of the breaker bar agrees with previous mobile-bed oscillatory flow studies, suggesting that wave non-uniformity does not affect the WBL thickness. However, near the breaking-wave plunge point and along the shoreward slope of the bar, δ/a is about 3 times higher than predictions based on uniform oscillatory flows. This can be attributed to the combined effects of breaking-induced turbulent kinetic energy (TKE) and flow divergence induced by the bed geometry.
3. Outer-flow TKE observations match with previous breaking-wave studies, showing highest values in the breaking region at the breaker bar crest, followed by a decrease in the bar trough. In close vicinity of the plunge point (+/- 0.5 m), TKE is almost depth-uniform over the complete water column (including the WBL), indicating large turbulence production and a strong penetration into the water column down to the bed. At shoaling and inner surf zone, vertical profiles of TKE show that also bed-friction is a significant source of near-bed turbulence.
4. Near the plunge point, TKE enters the boundary layer during two instances of the wave cycle: a first occurrence rapidly (about 0.5 s) after wave plunging, when breaking-induced TKE rapidly saturates the complete water column including the WBL; a second occurrence during the wave trough phase, when undertow and periodic velocities transport TKE towards the breaker bar. This invasion results in an increase in maximum TKE inside the WBL with a factor of almost three between shoaling and breaking region, despite decreasing near-bed velocity magnitudes.
5. Breaking-generated turbulence travels horizontally offshore (during trough phase) and back onshore (during crest phase) between breaking and shoaling zone, leading to increased phase- and time-averaged TKE over the near-bed region (including the WBL). Hence, the area affected by breaking-generated turbulence is not restricted to the breaking region itself, but extends to shoaling locations about 3 m offshore from the plunge point. Advection of TKE from plunge point in onshore direction is restricted by the combination of a decreased orbital velocity amplitude and strong offshore-directed undertow velocities.
6. Wave breaking affects near-bed Reynolds shear stresses, leading to an increase in maximum onshore and offshore phase-averaged Reynolds stresses at the WBL

overshoot elevation. The effect is mostly apparent for the region comprising +/- 1 m around the plunge point, where phase-averaged Reynolds stress magnitudes are a factor 2 higher than at shoaling locations at the bar crest.

2.A. Additional information on ACVP measurements and data treatment

Additional data treatment was required for ACVP-measured turbulence. An example spectrum of ACVP-measured horizontal velocities is shown in **Figure 2.A1**. A contribution of Doppler noise appears as a deviation from the -5/3 slope that is expected at inertial subrange frequencies. In the present measurement conditions, this Doppler noise is caused by a lack of suspended particles as acoustic targets. Noise contributions are higher at shoaling than surf zone locations, as more sediment grains are entrained in the breaking and inner surf zone regions.

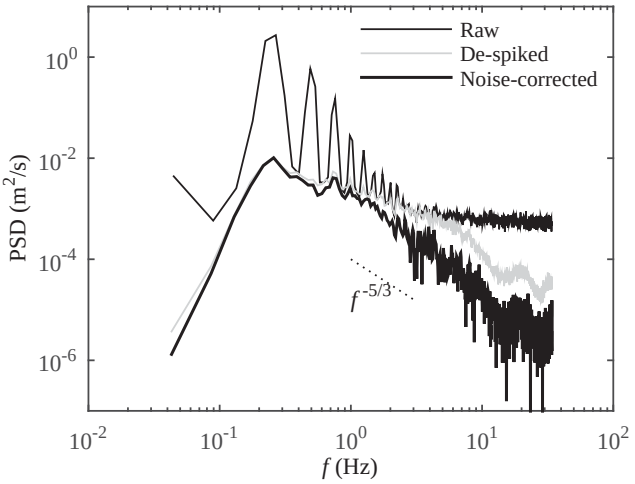

Figure 2.A1. Spectra of horizontal velocity measurements by ACVP at edge of boundary layer (ζ=δ), shoaling region. Figure includes auto-spectrum of raw data (thin black line), auto-spectrum of decomposed turbulent signal after applying de-spiking through moving median (grey line), and cross-spectrum of turbulent velocities at ζ=δ-Δz and ζ=δ+Δz, equivalent to Equation 2.7 (thick black line).

A two-step correction was applied to reduce the Doppler noise contribution. Firstly, data were de-spiked by applying a moving median with a window width of 5 samples. **Figure 2.A1** shows that this step importantly reduces energy at frequencies contaminated with Doppler noise (f > 5 Hz). Secondly, phase-averaged turbulent intensities were calculated using a two-point cross-correlation method as proposed by Garbini *et al.* (1982):

$$<u'_{rms}(z,t)>=\sqrt{<u'(z-\Delta z,t)u'(z+\Delta z,t)>} \qquad (2.7).$$

This method is based on the assumption that the most energetic turbulent eddies are larger than the separation distance 2Δz, with Δz equal to the ACVP's vertical resolution (1.5 mm).

Consequently, the uncorrelated velocity fluctuations constituted mainly by Doppler noise do not contribute to the turbulence co-variance given by Equation 2.7. This method was previously applied successfully in Hurther and Lemmin (2001, 2008) in shear and purely diffusive turbulent flows to supress the Doppler noise contribution in the normal Reynolds stress and TKE profile measurements. **Figure 2.A1** shows that the applied cleaning methodology effectively removes Doppler noise, as the cleaned turbulent velocity spectrum follows the expected -5/3 slope in the inertial subranges. Although Doppler noise was largely restricted to the horizontal velocity measurements (due to the strong geometrical weighting, c.f. Hurther and Lemmin, 2001), Equation 2.7 was also applied to the vertical turbulent velocities w'_{rms} for consistency.

In terms of noise effects on Reynolds stresses, previous research found that Doppler noise is intrinsically uncorrelated in the horizontal and vertical directions (Hurther and Lemmin, 2001). However, this is only true if the transmission direction of the ACVP is normal to the local bed slope. As this is not the case in the present experiment, Equation 2.7 is similarly applied to the Reynolds shear stress using a centered scheme version:

$$-\langle u'w'(z,t)\rangle = -0.5[\langle u'(z-\Delta z,t)\cdot w'(z+\Delta z,t)\rangle + \langle u'(z+\Delta z,t)\cdot w'(z-\Delta z,t)\rangle] \quad (2.8).$$

The Reynolds shear may be affected by contributions of wave velocities that are still present in u' and w' after the Reynolds decomposition (see Section 2.2.5). Feddersen and Williams (2007) proposed testing of wave bias effects on $u'w'$ using the cumulative distribution of the cross-spectrum of u' and w' (ogive curves). Wave bias appears in the ogive curves as a local increase in curve steepness around frequencies associated with the waves. The curves were calculated following the mathematical expression by Feddersen and Williams (2007) for each individual run. Following previous studies in field (Feddersen and Williams, 2007; Ruessink, 2010) and laboratory (Brinkkemper *et al.*, 2015) surf zones, the Reynolds stresses were removed from the analysis if the ogive curves exceeded limits of -0.5 and +1.6 at any frequency or when visual inspection of the curves revealed a dominance of wave contributions to Reynolds shear. In total, 9 out of 72 runs failed the ogive test and were excluded. The exclusion of these runs did not significantly alter the results.

In order to interpret the ACVP data properly, a few considerations regarding the estimates of turbulence quantities from the ACVP measurements are addressed. First, the ACVP measures velocities of sand grains as the dominant source of acoustic scattering. Depending on the local hydrodynamic conditions, the particle velocity may lag the fluid velocity due to particle inertia effects. Consequently, the near-bed turbulence data provided by the ACVP might differ from pure fluid turbulence data. Unfortunately, to our knowledge, this measurement limitation cannot be overcome presently in the absence of instrumentation capable of measuring fluid-velocity data under such dense water-sediment mixtures. Second, application of Equation 2.7 also eliminates the fraction of TKE contained in eddies smaller than the separation distance $2\Delta z$. However, while the noise correction reduces spectral energy at inertial subrange frequencies ($f > 1$ Hz), the energy associated with the larger energy-containing vortices that contribute most to TKE ($f \approx 0.25$ to 1.0 Hz) is hardly affected (Figure 2.A1). Third, inside the WBL, the size of eddies reduces significantly within proximity of the bed. These small-scale turbulent eddies may not be properly resolved by the ACVP due to a lack of spatial-temporal resolution (Soulsby, 1980). This may lead to an underestimation of turbulence intensities;

especially for the vertical turbulent fluctuations w', which in the vicinity of the bed exhibit much smaller turbulent scales than u' (Soulsby, 1980). At the same time, near-bed TKE is dominated by strongly anisotropic eddies with u'_{rms} much larger than w'_{rms} (Cox and Kobayashi, 2000). As a result, TKE is not severely underestimated by the ACVP. In order to quantify the underestimation, a comparison was carried out between the ACVP and a two-component LDA system (with a roughly 4 times higher spatial-temporal resolution), simultaneously deployed in an equivalent clear-water wave experiment over a rigid bed. The ACVP measurements showed an underestimation in $\sqrt{\overline{k}}/u_{max}$ of 10 to 15% at a distance ζ = 8 mm above the rigid bed (corresponding to about half the WBL thickness). The spatial averaging effect on Reynolds stress measurements is supposedly limited due to the much larger size of shear-producing eddies – typically of the order of the WBL thickness (Soulsby, 1980).

3 Suspended sediment transport around a large-scale laboratory breaker bar

Highlights:

- ⇨ Near-bed reference concentrations correlate significantly with near-bed turbulent kinetic energy.
- ⇨ Depth-integrated suspended transport is dominated by offshore-directed current-related fluxes at outer flow elevations; the onshore wave-related transport is generally confined to the wave bottom boundary layer.
- ⇨ The contributions of horizontal sediment advection and of vertical exchange with the bedload layer (pick-up/deposition) are quantified to explain the complex intra-wave spatiotemporal behavior of near-bed suspended sediment concentrations.

Abstract

This paper presents novel insights into suspended sediment concentrations and fluxes under a large-scale laboratory plunging wave. Measurements of sediment concentrations and velocities were taken at 12 locations around an evolving breaker bar, covering the complete breaking region from shoaling to inner surf zone, with particular high resolution near the bed using an Acoustic Concentration and Velocity Profiler. Wave breaking evidently affects sediment pick-up rates, which increase by an order of magnitude from shoaling to breaking zone. Time-averaged reference concentrations correlate poorly with periodic and time-averaged near-bed velocities, but correlate significantly with near-bed time-averaged turbulent kinetic energy. The net depth-integrated suspended transport is offshore-directed and primarily attributed to current-related fluxes (undertow) at outer-flow elevations (i.e. above the wave bottom boundary layer). The wave-related suspended transport is onshore-directed and is generally confined to the wave bottom boundary layer. Cross-shore gradients of sediment fluxes are quantified to explain spatial patterns of sediment pick-up and deposition and of cross-shore sediment advection. Suspended particles travel back and forth between the breaking and shoaling zones following the orbital motion, leading to local intra-wave concentration changes. At locations between the breaker bar crest and bar trough, intra-wave concentration changes are due to a combination of horizontal advection and of vertical exchange with the bedload layer: sediment is entrained in the bar trough during the wave trough phase, almost instantly advected offshore, and deposited near the bar crest during the wave crest phase. Finally, these results are used to suggest improvements for engineering-type suspended transport models.

This chapter is under review for publication in Coastal Engineering as:

van der Zanden, J. van der A, D. A., Hurther, D., Cáceres, I., O'Donoghue,T. and J.S. Ribberink. *Suspended sediment transport around a large-scale laboratory breaker bar*.

3.1 Introduction

Over the last decades, experimental and numerical studies have significantly advanced the understanding of sediment transport processes and the ability to predict suspended and bedload transport rates for non-breaking waves (Van Rijn *et al.*, 2013). However, in the breaking region, existing formulations for suspended sediment concentrations and transport may not be valid due to effects of breaking-generated turbulence and of cross-shore hydrodynamic non-uniformity (i.e. cross-shore changes in wave shape and undertow) which are not fully understood (Van Rijn *et al.*, 2013).

Laboratory (Steetzel, 1993; Roelvink and Reniers, 1995; van Thiel de Vries *et al.*, 2008) and field studies (Nielsen, 1984; Yu *et al.*, 1993; Beach and Sternberg, 1996) have reported large amounts of suspended sediment in the breaking zone, related to the enhancing effects of breaking-generated vortices on sediment entrainment from the bed (Nielsen, 1984; Nadaoka *et al.*, 1988; van Thiel de Vries *et al.*, 2008; Scott *et al.*, 2009; Aagaard and Hughes, 2010; Sumer *et al.*, 2013) and on vertical sediment mixing (Nielsen, 1984; Ogston and Sternberg, 2002; Aagaard and Jensen, 2013; Yoon *et al.*, 2015). These processes depend on the characteristics of the breaking wave, with plunging breakers being more effective in entraining and mixing sediment than spilling breakers (Nielsen, 1984; Aagaard and Jensen, 2013). This relates to differences in turbulence behavior, with higher production rates and a more rapid downward spreading of breaking-induced turbulence found under plunging than under spilling waves (Ting and Kirby, 1994).

Due to the dominance of breaking-induced vortices on sediment pick-up, existing formulations for near-bed reference concentrations that are based on orbital and time-averaged velocities (Nielsen, 1986; Van Rijn, 2007b) may not apply in the wave breaking region (Aagaard and Jensen, 2013). Instead, formulations that are based on breaking-induced turbulence and that take the breaker type into account (e.g. Mocke and Smith, 1992; Steetzel, 1993; Kobayashi and Johnson, 2001) appear more appropriate. An additional complication is that due to strong horizontal sediment advection in the breaking region (Scott *et al.*, 2009; Yoon and Cox, 2012) the near-bed concentrations may not always be related to local hydrodynamics only.

The net horizontal suspended flux in the breaking region is the result of two opposing fluxes with similar magnitudes: an offshore-directed current-related flux and an onshore-directed wave-related flux (Osborne and Greenwood, 1992; Ogston and Sternberg, 1995; Thornton *et al.*, 1996; Ruessink *et al.*, 1998). The former is driven by the undertow, whereas the latter relates to the wave asymmetry (Elgar *et al.*, 2001; Hoefel and Elgar, 2003). Time-varying breaking-generated turbulence, with higher intensities during the crest half-cycle, has been suggested as an additional factor contributing to onshore wave-related suspended sediment fluxes (Ting and Kirby, 1994; Boers, 2005). Yoon and Cox (2012) presented experimental evidence for increased onshore wave-related suspension fluxes due to intermittent suspension events that occur preferentially during the wave crest phase following events of high turbulent energy. However, Scott *et al.* (2009) found, by combining data from the same experiment with numerical simulations, that suspension events occur mainly during the wave trough phase and contribute to offshore-directed fluxes. The individual effects by turbulence and wave

asymmetry on sediment fluxes are difficult to assess because the two parameters correlate positively in the breaking region (van Thiel de Vries *et al.*, 2008; Aagaard and Hughes, 2010).

Although previous research highlighted clear effects of wave breaking on sediment suspension and fluxes, there are still open research questions. Most of the aforementioned studies are based on local point measurements of sediment concentrations at few elevations in the water column, sometimes combined with co-located velocity measurements to estimate the local sediment fluxes. These measurements did not capture the complete vertical distribution of fluxes since the near-bed region including the wave bottom boundary layer (WBL), where large contributions to total suspended transport can be expected, was not accurately resolved. Such measurements of WBL flow and time-varying near-bed turbulence are also essential in relating the observed sediment processes to hydrodynamic forcing. In addition, most of the previous experimental studies covered only a few cross-shore locations in the shoaling and breaking region. This strongly limits the study of cross-shore advection of suspended sediment and the effects of cross-shore non-uniformity in hydrodynamics (i.e. flow and turbulence) on suspended sediment processes.

Here we present new high-resolution measurements of suspended sediment transport processes under a plunging wave in a large-scale wave flume. Measurements were obtained at 12 cross-shore locations along a sandy breaker bar, covering the complete breaking region from shoaling zone to inner surf zone. Sediment concentration and velocity measurements cover most of the water column, with particular high resolution of time-varying concentrations and sediment fluxes in the near-bed region (including the WBL). The aim is to improve insights into suspended sediment processes in the breaking region, with particular focus on the current-related, wave-related and turbulent suspended sediment flux components and their contributions to the total net suspended transport. These fluxes are also used to explain the intra-wave near-bed concentration field in terms of horizontal sediment advection and vertical exchange of sediment between the suspension and bedload layer (pick-up and deposition). Results of the sediment dynamics are related to the detailed near-bed flow and turbulence measurements obtained from the same experiment and reported in **Chapter 2**.

The paper is organized as follows: the experiment is described in Section 3.2. Section 3.3 presents the bed profile evolution and the cross-shore variation in the main hydrodynamic parameters. Section 3.4 presents results on suspended sediment concentrations (3.4.1), fluxes and net transport rates (3.4.2) and horizontal advection and pick-up/deposition (3.4.3). The results are used to discuss potential improvements to engineering-type suspended sediment transport formulations for breaking-wave conditions (Section 3.5).

3.2 Experimental description

3.2.1 Facility and test conditions

The experiments were carried out in the large-scale CIEM wave flume at the Universitat Politècnica de Catalunya (UPC) in Barcelona. The flume is 100 m long, 3 m wide and 4.5 m deep, and is equipped with a wedge-type wave paddle. **Figure 3.1** shows the experimental set-up and bed profile for the present study. Cross-shore coordinate x is defined positively towards the beach, with $x = 0$ at the toe of the wave paddle. Vertical coordinate z is defined

positively upwards with $z = 0$ at the still water level (SWL); ζ is the vertical coordinate positive upwards from the local bed level.

The initial bed profile consisted of a bar-trough configuration (**Figure 3.1*a***, black line) that was produced by 105 minutes of wave action over an initially flat horizontal test section (see **Chapter 2**). The test section can be roughly divided into an offshore-facing slope of the breaker bar (x = 35.0 to 54.8 m; steepness tan(α) = 1:10), followed by a steeper shoreward-facing bar slope (x = 54.8 to 57.5 m; –tan(α) = 1:4.7), and a mildly sloping bed shoreward from the bar trough (x = 57.5 to 68.0 m; tan(α) = 1:95). The test section consisted of medium sand (median diameter D_{50} = 0.24 mm), which had a measured settling velocity w_s = 0.034 m/s. The profile shoreward of the mobile test section (x > 68.0 m) followed a 1:7.5 slope, and was fixed with geotextile and covered with perforated concrete slabs that promoted wave energy dissipation.

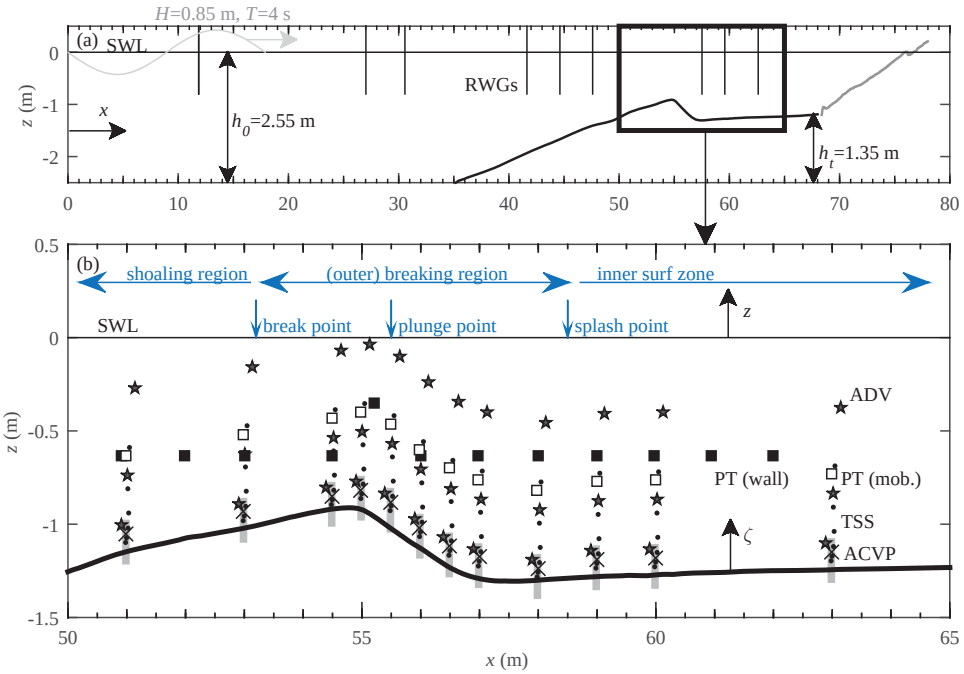

Figure 3.1. Experimental set-up and measurement locations. (a) Initial bed profile (black line) and fixed beach (grey line), and locations of resistive wave gauges (RWGs, vertical black lines); (b) Measurement positions of ADVs (star symbols), mobile-frame Pressure Transducers (PT, white squares), wall-deployed PTs (black squares), Transverse Suction System nozzles (TSS, black dots), Optical Backscatter Sensor (black crosses), and measuring range of mobile-frame ACVP (grey boxes).

The experiments involved monochromatic waves with wave period T = 4 s and wave height H_0 = 0.85 m at water depth h_0 = 2.55 m near the wave paddle. These conditions correspond to a surf similarity parameter ξ_0 = 0.54 (where $\xi_0 = \tan(\alpha)/\sqrt{H_0/L_0}$, tan($\alpha$) is the offshore bar slope and L_0 is the deep-water wave length), which, in agreement with the classification of Battjes (1974), resulted in a plunging type breaker.

Based on measurements and visual observations of the water surface and following the terminology of Smith and Kraus (1991), we define the break point (x = 53.0 m) as the location

where the breaking wave starts to overturn, the plunge point (x = 55.5 m) where the plunging jet hits the water surface, and the splash point (x = 59.0 m) where the pushed up water strikes the water surface a second time and where the breaking wave has transformed into a surf bore. Following Svendsen *et al.* (1978) we define the shoaling zone as the region up to the plunge point (x < 55.5 m), the breaking zone as the region between plunge and splash point (55.5 < x < 59.0 m), and the inner surf zone as the region shoreward from the splash point (x > 59.0 m).

3.2.2 Instrumentation

Most instruments were deployed from a custom-built mobile frame (**Figure 3.2**). This frame consisted of stainless-steel tubing with 30 mm diameter and was designed such that it would have minimum flow perturbation while being sufficiently stiff to withstand wave impact. The frame was mounted to a horizontally-mobile trolley on top of the flume, and could be positioned with sub-mm accuracy in the vertical direction using a spindle (for more details, see Ribberink *et al.*, 2014). The mobile frame set-up enabled measurements at various cross-shore positions, while maintaining an approximately equal elevation of the instrumental array with respect to the bed at the start of each run. The positions of the various instruments above the initial bed level are presented in **Table 3.1**.

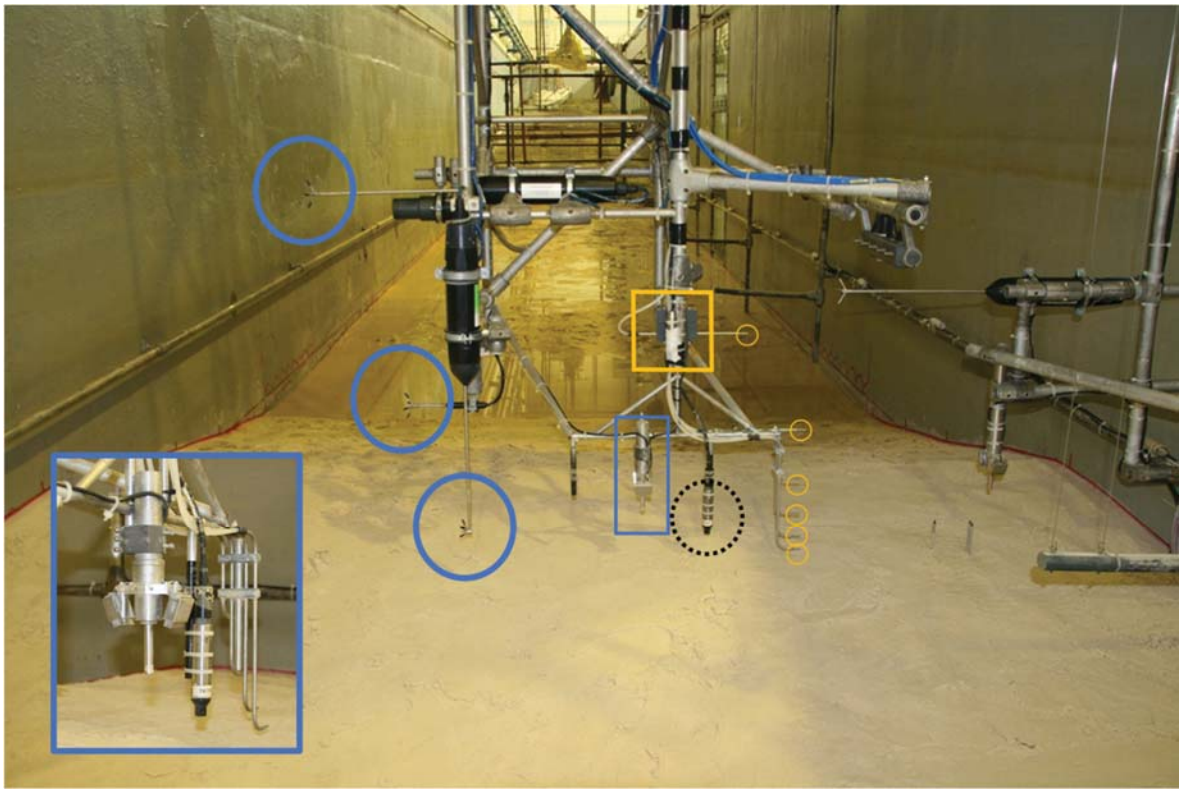

Figure 3.2. Mobile measuring frame and instrumentation. Instrumentation includes three ADVs (blue solid circles), one Pressure Transducer (yellow square), a six-nozzle Transverse Suction System (yellow circles), an OBS (black dashed circle) and an ACVP (blue square). Inset shows close-up of near-bed instrumentation.

Outer-flow velocities were measured with a vertical array of three three-component (cross-shore, lateral, and vertical; annotated u, v, and w, respectively) Acoustic Doppler Velocimeters (ADVs; **Figure 3.2**). The ADVs operated at an acoustic frequency of 10 MHz and had a sampling volume of approximately 3 mm radius.

Near-bed flow and sediment concentrations were measured with a High-Resolution Acoustic Concentration and Velocity Profiler (ACVP) that is fully described in Hurther *et al.* (2011). The ACVP measures simultaneous and co-located vertical profiles of 2-component (u, w) particle velocity and sediment concentration. Operating at an acoustic frequency of 1 MHz, i.e. considerably lower than the frequency of commercial ADV technology, the ACVP is particularly suitable for measuring velocities and sediment concentrations across a dense near-bed sediment layer, as demonstrated in recent mobile-bed studies with steady (Naqshband *et al.*, 2014; Revil-Baudard *et al.*, 2015) and wave-driven (Chassagneux and Hurther, 2014) flows. In the present experiment, the ACVP's acoustic and geometrical settings were set to measure velocities up to 1.8 m/s over a 20 cm near-bed profile, with a vertical sampling bin resolution of 1.5 mm and a sampling frequency of 70 Hz. Since the bed is contained within the measuring volume and changes during a run, the effective profiling length above the bed was in the range of 10 to 15 cm. Section 3.2.3 explains the inversion of the measured acoustic intensities to sediment concentrations.

Table 3.1: Elevations of mobile-frame instrumentation with respect to initial bed level.

Instrument	Elevation ζ (m)
Acoustic Doppler Velocimeters (ADVs)	0.11, 0.38, 0.85
High-Resolution Acoustic Concentration and Velocity Profiler (ACVP)	0.12 (elevation transmitter)
Transverse Suction System (TSS) nozzles	0.02, 0.04, 0.10, 0.18, 0.31, 0.53
Optical Backscatter Sensor (OBS)	0.07
Pressure Transducer (PT)	0.48

Time-averaged sediment concentrations were obtained with a six-nozzle Transverse Suction System (TSS), consisting of six stainless-steel nozzles, each connected through plastic tubing to a peristaltic pump on top of the wave flume. Following Bosman *et al.* (1987), the TSS was designed to have intake velocities of 2.3 m/s, i.e. exceeding the maximum orbital velocity by approximately 1.5, in order to guarantee a constant sediment trapping efficiency. The nozzle intake diameter was 3 mm (same as Bosman *et al.*, 1987) and the pump discharge was 1 L/min. The 30 mm long nozzles were oriented parallel to the bed and perpendicular to the wave direction (**Figure 3.2**).

The TSS tubing consisted of 2 m-long, 4 mm-diameter rigid air hose tubing at the lower part of the frame, and 4 m-long, 8 mm-diameter silicone tubing at higher levels. The estimated water velocity in the widest suction hose was 0.3 m/s, which exceeds the sediment settling velocity by an order of magnitude. The sampled water plus sediment mixture was captured in 15 L buckets, which were weighted (to measure the water content), carefully drained to remove excess water, transferred to aluminum cups, and then dry-weighted to give a first measure of the concentration C_s. The actual concentration C_{true} is then obtained from $C_{true} = \beta_t C_s$,

where the factor $\beta_t = 1 + 1/3\arctan(D_{50}/0.09)$ is the inverse of the nozzle's trapping efficiency (Bosman *et al.*, 1987). The estimated TSS measuring error is 10% and includes errors in the various processing steps (estimation of trapping efficiency, transfer of samples, water volume estimation, dry-weighting) and also uncertainties in the time-varying elevation with respect to the bed (Bosman *et al.*, 1987).

Additional time-varying concentration measurements were obtained at 40 Hz using an Optical Backscatter Sensor (OBS), which was located close to the bed and within the ACVP measuring range (**Figure 3.2**). The OBS was calibrated at UPC through experiments with a replica of the apparatus described by Downing and Beach (1989) using samples of the sand in the flume. The OBS data were used for validating the phase-averaged calibrated ACVP concentrations.

Water surface levels were sampled at 40 Hz, using pressure transducers (PTs) and resistive (wire) wave gauges (RWGs) that were deployed from the side-walls of the flume (**Figure 3.1**) and an additional PT on the mobile frame (**Figure 3.2*).*** PT measurements of the dynamic pressure were converted to water surface levels using linear wave theory (following Guza and Thornton, 1980). This conversion could be applied up to a frequency of 0.33 Hz, which in the present study includes the primary wave frequency (0.25 Hz) but not the higher harmonics. The actual wave height is therefore underestimated by approximately 10%.

Using echo sounders deployed from a second mobile trolley, bed profile measurements were obtained at 2 cm cross-shore resolution along two transects at lateral distances of 0.1 and 0.7 m with respect to the flume's centerline. The echo sounders had an estimated accuracy of +/– 1 cm. The measured bed profile was taken as the mean of the profiles measured by the two sensors.

3.2.3 Measurement procedure

One experiment consisted of 90 minutes of waves, consisting of six individual 15-minute runs, during which the bed profile evolved. The bed profile was measured prior to the first run and after every 2nd run, i.e. at t = 0, 30, 60 and 90 min. After the sixth run, the flume was drained. The initial bed profile, drawn as template on the side-walls, was then restored by shoveling back transported sand and flattening any bed forms that were generated. The 90-minute experiment was repeated 12 times, with the mobile measuring frame moved to a new cross-shore location for each experiment, which resulted in a high spatial coverage of measurements (**Figure 3.1b**). The measurement locations cover 0.9L, where L is the measured wave length in the test section, and comprise the shoaling to inner surf zone. The high repeatability of the hydrodynamics and bed profile evolution following this procedure was demonstrated in **Chapter 2**.

3.2.4 Data treatment

For each 15-minute run the first 5 minutes of data were discarded because the breaking location varied with time since no hydrodynamic equilibrium was established yet. The breaking point stabilized after the 5-minute period, leaving 10 minutes of data for analysis. Flume seiching induced a standing wave with an amplitude of O(cm) and a 45-s period. This

long wave was removed from all water surface and velocity data by applying a high-pass filter with a cut-off frequency of half the primary-wave frequency (0.125 Hz). The auto-spectra and autocorrelation functions of suspended sediment concentrations (OBS, ACVP) and time-varying bed levels (ACVP) did not reveal any distinct peaks at the seiching-wave frequency. This shows that flume seiching had a negligible effect on sediment transport.

ADV and ACVP velocity data were de-noised as explained in **Chapter 2**. The instantaneous bed level was obtained from the ACVP using the acoustic bed interface tracking method proposed by Hurther and Thorne (2011). The bed level was used to correct the ACVP data for local bed evolution by assigning a ζ level to each vertical measurement bin for each wave, with $\zeta = 0$ corresponding to the measured bed level during the zero-down crossing of the water surface when the bed is considered to be at rest. The ACVP data were then ensemble-averaged for each ζ bin class. Following this procedure, bed level changes at intra-wave time scale are still considered in the ensemble means. Horizontal and vertical velocity u and w were rotated to bed-parallel u_R and bed-normal w_R components, calculated using

$$u_R = u\cos(\beta) + w\sin(\beta)$$
$$w_R = w\cos(\beta) - u\sin(\beta) \qquad (3.1)$$

where β is the rotation angle that minimized the orbital velocity amplitude of w_R close to the bed (at $\zeta = 0.03$ m). Equation 3.1 was applied per individual wave cycle, i.e. β was determined for each individual wave. The mean rotation angle for each run was found to match closely the local bed slope obtained from the bed profile measurements, which supports the validity of the rotation procedure.

The inversion of the ACVP's backscattered acoustic intensity to give sediment concentrations followed the iterative implicit inversion method described by Hurther *et al.* (2011). Sediment concentrations $C(\check{z})$ at distance $\check{z}$ from the transmitter were calculated iteratively, by moving from the transmitter downwards while accounting for attenuation of the backscattered signal along the travel path of the acoustic beam:

$$C(\check{z}) = J(\check{z}) \qquad \text{for } \check{z} = 0$$
$$C(\check{z}+\Delta\check{z}) = C(\check{z})\frac{J(\check{z}+\Delta\check{z})}{J(\check{z})}\exp(\zeta_s C(\check{z})\Delta r) \qquad \text{for } \check{z} + \Delta\check{z} > 0. \qquad (3.2),$$

where ζ_s is a sediment attenuation constant that depends on theoretical and empirical sediment properties; Δr is the change in distance with respect to the acoustic receivers that corresponds with a vertical displacement $\Delta\check{z}$; and $J(\check{z})$ is the normalized back-scattered voltage calculated using

$$J(\check{z}) = \frac{I(\check{z})}{A_{h,s}(\check{z})} \qquad (3.3),$$

where $I(\check{z})$ is the backscatter voltage and $A_{h,s}(\check{z})$ is a depth-varying function that depends on hardware characteristics, water absorption effects and sediment characteristics. For the present experiments, both $A_{h,s}(\check{z})$ and ζ_s are used as calibration parameters, with the former varying with cross-shore location and the latter a constant value for all experimental runs. The calibration was effected by matching the time-averaged ACVP concentrations with the TSS

measurements. Before the inversion, the acoustic backscattered voltage was de-spiked using a moving median filter with a window width of 5 measurements.

Data were phase-averaged over a wave cycle using the zero crossings of the RWG-measured water surface elevation at $x = 47.6$ m as a phase reference. The number of wave cycles for phase-averaging was about 150 for water surface and outer-flow velocity data, but somewhat lower (typically about 100, with a minimum of 40) for the ACVP data. ACVP measurements were discarded when the local bed eroded beyond the ACVP measuring volume or when it accreted to within 5 cm of the ACVP transmitter. In the inner surf zone, where bed forms migrated slowly offshore below the ACVP, intervals of time series used for phase-averaging were chosen such that exactly 1 or 2 complete bed forms were captured (i.e. the data presented here are ripple-averaged). Phase-averaged quantities are annotated with angle brackets and are normalized such that $t/T = 0$ corresponds to maximum water surface level (wave crest) at x = 50.0 m. Velocities were decomposed into time-averaged ($\overline{u}, \overline{w}$), periodic ($\tilde{u}$, $\tilde{w}$) and turbulent (u', w') components. Subscript *rms* is used to denote root-mean-square magnitudes of periodic velocities. Additional information on the applied data cleaning procedures and the method to estimate turbulent kinetic energy k can be found in **Chapter 2**.

3.3 Bed evolution and hydrodynamics

This section discusses the bed profile evolution and the cross-shore variation in hydrodynamic parameters. A more extensive description of the measured near-bed hydrodynamics, including turbulence, can be found in **Chapter 2**.

The profile development in **Figure 3.3a** shows that the bar crest grows and migrates slightly onshore during the experiment. This leads to an increase in the bar's offshore slope from $\tan(\alpha)$=0.10 to $\tan(\alpha)$=0.13 and an increase in the surf similarity parameter ξ_0 from 0.54 to 0.68. At the same time the bar trough deepens, resulting in a steepening of the shoreward-facing slope of the bar from $\tan(\alpha) = -0.21$ to $\tan(\alpha) = -0.48$. At 90 minutes, the slope approaches the natural angle of repose (α = 26–34°) for sandy materials (Nielsen, 1992).

Bed forms were observed after draining the flume. The bed was flat in the shoaling region until the bar crest (x = 48.0 to 55.5 m). Quasi-2D features (quasi-uniform in longshore direction) were identified along the shoreward-facing slope of the bar (x = 55.5 to 57.0 m), where they migrated progressively offshore. Shoreward-facing lunate-shaped features were present at the bar trough (x = 57.0 to 59.0 m). In the inner surf zone, a gradual transition to quasi-2D bed features occurred (from x = 59.0 to 62.0 m). Further shoreward these features became increasingly irregular while their wave length reduced, resulting in 3D sand ripples (x = 62.0 m to 68.0 m). Only in the inner surf zone ($x \geq 59.0$ m), bed form lengths were of similar magnitude as the orbital semi-excursion length a (**Table 3.2**).

Figure 3.3a shows that wave height decreases by 50% between the break point (x = 53.0 m) and splash point (x = 59.0 m). Time-averaged water levels $\overline{\eta}$ show set-down in the shoaling zone and set-up in the inner surf zone. **Figure 3.3b** shows the maximum offshore and onshore phase-averaged velocities in bed-parallel direction at $\zeta = \delta$, where δ (≈0.01 to 0.02 m) is the WBL overshoot elevation during the crest phase. The reduced wave height and the increasing water depth shoreward of the bar crest (x = 55.0 to 57.0 m) leads to a strong decrease in

amplitudes of periodic velocities while the offshore-directed time-averaged velocity (undertow) increases in magnitude. Consequently, along the shoreward-facing slope of the bar (x = 56.0 to 57.5 m) the near-bed velocities are directed offshore during (almost) the entire wave cycle.

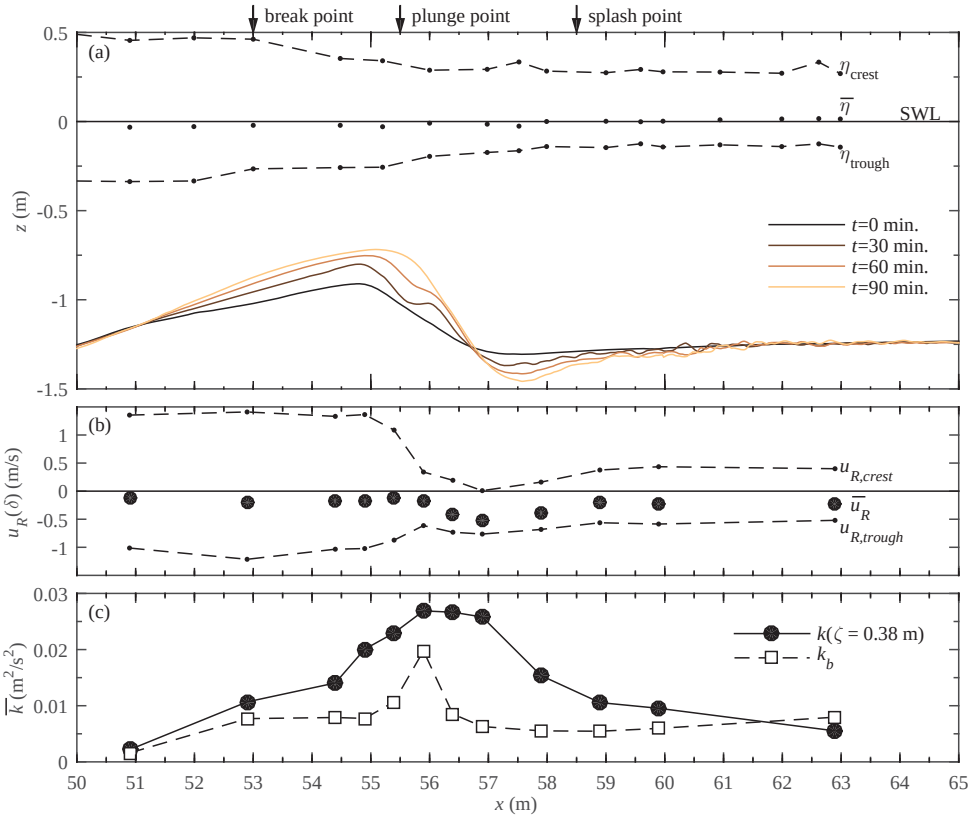

Figure 3.3. (a) Bed profile evolution (solid lines, with each line representing the mean value over all experimental days), and water levels for t=0–15 min. (dots and dashed lines depict time-averaged and envelope, respectively); (b) ACVP-measured bed-parallel velocities at the WBL overshoot elevation, $u_R(\delta)$, for t=0–15 min., mean (circles) and maximum onshore and offshore values (dots and dashed line); (c) Turbulent kinetic energy, mean values over experiment (t=0–90 min.) at outer-flow elevation ζ = 0.38 m (measured with ADV, solid line and circles) and maximum time-averaged TKE inside the WBL (measured with ACVP, dashed line and squares).

Figure 3.3c shows the time-averaged turbulent kinetic energy ($\overline{k}$) at outer-flow elevation ζ = 0.38 m and inside the WBL (k_b). The latter is defined as the maximum $\overline{k}$ at $\zeta \leq \delta$. Turbulence production by wave breaking leads to large magnitudes of outer-flow $\overline{k}$ in the vicinity of the plunge point at x = 55.5 m. At most locations, $\overline{k}$ decreases towards the bed, indicating that at outer-flow elevations the dominant source of turbulence is production near the water surface due to wave breaking. Breaking-generated turbulence is advected to offshore locations while gradually dissipating, leading to a decrease in TKE from the breaking zone in the offshore direction (from x = 55.5 to 51.0 m). TKE inside the WBL (k_b) increases by an order of magnitude from the shoaling zone (x = 51.0 m) to the breaking region (x = 53.0 to 58.0 m). This increase occurs in spite of a reduction in peak onshore/offshore velocities, which shows that the

increase is not due to turbulence production by bed shear, but instead is due to the invasion of breaking-generated TKE into the WBL. The increase in k_b throughout the inner surf zone ($x \geq 59.0$ m) is due an increase in bed roughness (i.e. due to bed forms) and in turbulence production at the bed.

Table 3.2: Hydrodynamic parameters at all measurement locations (t=0–15 min.): water depth (h); wave height (H); time-averaged bed-parallel velocity ($\bar{u}_R$); maximum (crest phase) and minimum (trough phase) phase-averaged bed-parallel velocities; semi-excursion length ($a = \sqrt{2}T\tilde{u}_{R,rms}/2\pi$). Velocities are based on measurements from the lowest ADV at ζ=0.11 m.

x (m)	h (m)	H (m)	$\bar{u}_R$ (m/s)	$<u_R>_{max}$ (m/s)	$<u_R>_{min}$ (m/s)	a (m)
51.0	1.10	0.79	-0.13	1.04	-0.83	0.54
53.0	0.97	0.74	-0.22	0.80	-0.94	0.48
54.5	0.88	0.64	-0.19	0.84	-0.85	0.47
55.0	0.88	0.60	-0.24	0.78	-0.90	0.47
55.5	0.97	0.51	-0.23	0.57	-0.83	0.39
56.0	1.10	0.50	-0.30	0.25	-0.82	0.31
56.5	1.19	0.53	-0.51	0.05	-0.83	0.25
57.0	1.24	0.48	-0.54	0.02	-0.78	0.23
58.0	1.28	0.47	-0.46	0.01	-0.71	0.21
59.0	1.28	0.43	-0.36	0.13	-0.71	0.23
60.0	1.26	0.42	-0.36	0.17	-0.66	0.24
63.0	1.26	0.41	-0.34	0.19	-0.58	0.23

3.4 Suspended sediment transport processes

Several definitions for bedload and suspended load can be found in the literature. From a physical perspective, bedload can be defined as the transport that is supported by intergranular forces and the suspended load as transport supported by fluid drag (Bagnold, 1956). Others, following a more pragmatic approach, have defined bedload (suspended load) as the transport below (above) a reference elevation, i.e. the level of the bed (Nielsen, 1986) or a roughness-dependent elevation slightly above the bed (Van Rijn, 2007a; Van Rijn, 2007b). In the present study, we use a wave-averaged reference elevation at $\zeta = 0.005$ m to distinguish between bedload ($\zeta < 0.005$ m) and suspended load ($\zeta > 0.005$ m). This is based firstly on physical arguments, as bedload in the present experiment occurs partly in the sheet flow regime and sheet flow transport is usually considered part of bedload (Ribberink, 1998). In the present study, detailed sheet flow layer measurements were obtained near the bar crest where the top of the sheet flow layer was found at $\zeta \approx 0.005$ m (**Chapter 4**). Secondly, although the ACVP is capable of measuring sediment fluxes in the upper part of the bedload layer (Naqshband *et al.*, 2014), the bedload fluxes derived from the ACVP were in the present study very sensitive to the acoustic inversion parameter due to the very high vertical gradient of sediment concentrations in the sheet flow layer. For these two reasons, which potentially result in large errors of estimated depth-integrated transport inside the WBL, it was decided to truncate the ACVP measurements for $\zeta < 0.005$ m.

3.4.1 Suspended sediment concentrations

3.4.1.1 Time-averaged concentrations

Figure 3.4 shows vertical profiles of time-averaged suspended sediment concentrations $\overline{C}(\zeta)$. At x =51.0 m, sediment concentrations were below the OBS detection limit and were therefore discarded. The different instruments (TSS, OBS, ACVP) generally yield consistent results. Comparison of the different panels reveals a strong cross-shore variation in suspended sediment concentration profiles. At all twelve locations, $\overline{C}(\zeta)$ follows a rapid decrease within the first few cm from the bed, and follows a more gradual decrease at outer-flow elevations. Such upward-concave profiles on log-linear scale are indicative of Rouse-shaped concentration profiles, which have been observed in oscillatory flow tunnel measurements over plane-beds (Ribberink and Al-Salem, 1995) and under small-scale laboratory breaking waves (Kobayashi *et al.*, 2005). These profiles can be described with a power function:

$$\overline{C}(\zeta) = C_0(\zeta/z_a)^{-m} \qquad (3.4)$$

where C_0 is the time-averaged concentration at reference elevation z_a close to the bed and m is a mixing parameter. Alternatively, exponential distributions for $\overline{C}(\zeta)$ have been proposed for non-breaking (Nielsen, 1986) and breaking waves (Aagaard and Jensen, 2013). In the present study, $\overline{C}(\zeta)$ follows an exponential decrease with ζ for parts of the water column, but the full profile of $\overline{C}(\zeta)$ from near-bed to water surface is better described through Equation 3.4.

At x = 51.0 m, low concentrations are found throughout the water column (of order 0.1 – 1 kg/m^3). Much higher concentrations are found in the breaking region at the bar crest (x = 53.0 to 55.5 m). At these locations, $\overline{C}(\zeta)$ is almost depth-uniform and is of substantial magnitude (>1 kg/m^3) up to wave trough level. Over the shoreward slope of the bar (x = 56.0 and 56.5 m), $\overline{C}(\zeta)$ shows strong depth-dependency with particularly high concentrations (1 to 10 kg/m^3) in the lower half of the water column. Over the bar trough (x = 57.0 to 58.0 m) sediment concentrations are much lower than over the bar crest. In the inner surf zone (x = 59.0 to 63.0 m), $\overline{C}(\zeta)$ exponentially decreases between ζ = 0.02 and 0.3 m (i.e. a straight line at this log scale). This is consistent with previous observations over rippled beds (e.g. Nielsen, 1986) and suggests that ripple vortex suspension controls $\overline{C}(\zeta)$ in the lower 0.3 m. At higher elevations $\overline{C}(\zeta)$ tends to a more depth-uniform distribution, which may relate either to enhanced mixing by breaking-generated TKE in the higher part of the water column or to arrival of horizontally advected suspended sediment.

The strong sediment mixing at the bar crest occurs in the presence of large and energetic breaking-generated vortices (**Figure 3.3c**). An accompanying experiment with similar bed profile and the same wave conditions (Ribberink *et al.*, 2014) showed that the near depth-uniform concentration profiles above the bar crest extend up to wave crest level, yielding significant concentrations at elevations above wave trough level.

The reference concentration C_0 (Equation 3.4) is an important parameter in suspended sediment transport modeling and is commonly predicted based on the wave- plus current-induced shear stress (Nielsen, 1986; Van Rijn, 2007b). For the present study, the time-averaged C_0 was estimated at a reference elevation z_a = 0.005 m by log-fitting Equation 3.4 through the ACVP-measured $\overline{C}(\zeta)$ between $\zeta = z_a$ and 0.10 m.

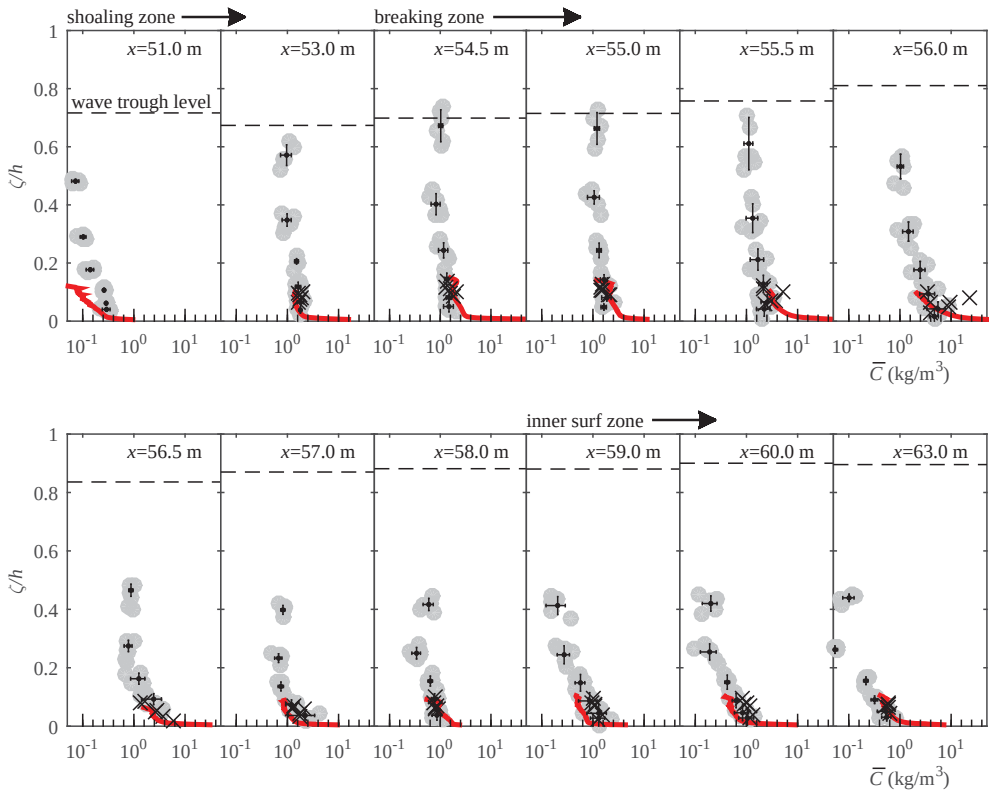

Figure 3.4. Time-averaged sediment concentrations (note log scale for horizontal axis). TSS concentrations are depicted with grey circles (each circle corresponding to a 15-min. average over a run) and with black dots plus error bars (depicting mean value and standard deviation for a given nozzle, averaged over all (six) runs per location). Also included are near-bed OBS measurements (for each run; black crosses) and ACVP measurements (only first run, i.e. t=0–15 min.; red line).

Figure 3.5 shows scatter plots of C_0 versus *rms* orbital velocities taken at the velocity overshoot elevation δ (panel a) and versus maximum time-averaged TKE in the WBL, k_b (panel b). Distinction is made between the region up to the plunge point above the bar crest (x < 55.5 m), the breaking region along the shoreward-facing bar slope and bar trough (55.5 ≤ x < 59.0 m) and the inner surf zone (x ≥ 59.0 m). **Figure 3.5a** shows that C_0 varies by an order of magnitude along the test section, with much higher C_0 in the breaking region along the shoreward-facing bar slope than at locations further from the plunge point. Linear regression between C_0 and $\tilde{u}_{rms}$ revealed no significant correlation (significance level P<0.05). In addition, C_0 did not correlate significantly with estimates of wave- plus current-induced shear stress (obtained following Ribberink, 1998) nor with the Sleath parameter that is a measure for pressure gradient induced sediment mobilization (Foster *et al.*, 2006). Note that the poor correlation between C_0 and $\tilde{u}_{rms}$ is particularly caused by the high C_0 values in the breaking region between x = 55.5 and 57.0 m. When these points are omitted, C_0 does correlate significantly with $\tilde{u}_{rms}$, as is to be expected based on previous observations for non-breaking waves.

Figure 3.5b shows that C_0 correlates significantly with k_b. In the absence of externally generated turbulence k_b would be related to $\tilde{u}_{rms}^2$, hence these results suggest that breaking-generated TKE that invades the WBL is an important driver for sediment entrainment. The entrainment can be explained physically through large instantaneous bed shear stresses induced by

intermittent TKE arriving at the bed (Cox and Kobayashi, 2000) or through upward-directed pressure gradients in the bed under breaking-induced vortices (Sumer *et al.*, 2013).

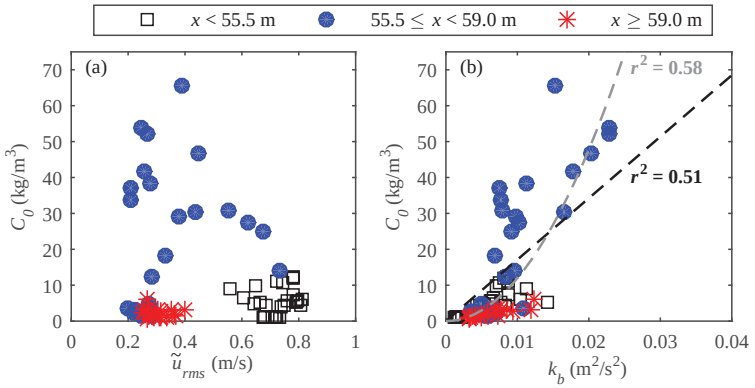

Figure 3.5. Scatter plots of the time-averaged reference concentration C_0 versus (a) root-mean-square orbital velocities at $\zeta=\delta$ and (b) maximum time-averaged TKE in the WBL, k_b. Each measurement point corresponds to a 15-minute run. Distinction is made between measurements from the shoaling and breaking region up to bar crest (white squares), the breaking region over the shoreward bar slope and bar trough (blue circles) and the inner surf zone (red asterisks). In panel (b), the black dashed line corresponds to a linear relation $C_0 = 1.7 \cdot 10^3 \cdot k_b$ while the grey dashed line denotes a quadratic relation $C_0 = 1.2 \cdot 10^5 \cdot k_b^2$.

3.4.1.2 Time-varying concentrations

Figure 3.6 shows ACVP-measured concentrations $\langle C(\zeta,t)\rangle$ in the near-bed layer from ζ = 0.005 m to 0.10 m. The figure includes the phase-averaged bed-parallel velocities $\langle u_R\rangle$ and near-bed TKE $\langle k_{nb}\rangle$ for reference purposes. The overshoot elevation δ during the crest phase is included as a proxy for the WBL thickness. The figure also shows depth-averaged concentrations (C_{nb}) over the near-bed layer between ζ = 0.005 m and 0.10 m. The C_{nb} values were normalized by their time-averaged equivalent to illustrate the relative temporal variation in the near-bed suspended load.

Consistent with results in the previous section, the color contours in **Figure 3.6** reveal strong spatial (both horizontally and vertically) variation in concentration. Compared to this spatial variation, the temporal variation in concentration seems more limited. This holds particularly for elevations above the WBL and at locations far from the breaking point (e.g. x = 51.0 m and 59.0–63.0 m). The temporal variation was quantified by computing the normalized coefficients of variation ($\langle C\rangle_{rms}/\overline{C}$), yielding typical values of about 10% above the WBL, but much larger values (50–80%) inside the WBL. Apparently, the temporal variation in sediment concentration is mostly restricted to the WBL, whereas outer-flow concentrations are fairly constant throughout the wave cycle.

The shoaling locations (x = 51.0 – 55.0 m) consistently reveal a distinct short-duration peak of increased sediment concentrations inside the WBL, which occurs between the moment of offshore-to-onshore flow reversal and the moment of maximum $\langle u\rangle$ during the crest phase. This can be explained by local sediment entrainment during instances of maximum flow velocity; the suspension events lead the maximum free-stream onshore/offshore $\langle u\rangle$ because

of the WBL phase lead. Additional processes contributing to high concentrations during the crest phase are the accumulation of sediment under the wave front by the convergence of horizontally advected sediment (Kranenburg *et al.*, 2013), and the vertical sediment advection by upward periodic velocities during the trough-to-crest flow reversal (Deigaard *et al.*, 1999). At outer-flow elevations ($\zeta>\delta$), C increases gradually during the wave trough phase (e.g. at x = 54.5 m from $t/T \approx 0.7$) and decreases during the crest phase (e.g. at x = 54.5 m from $t/T \approx 0.3$).

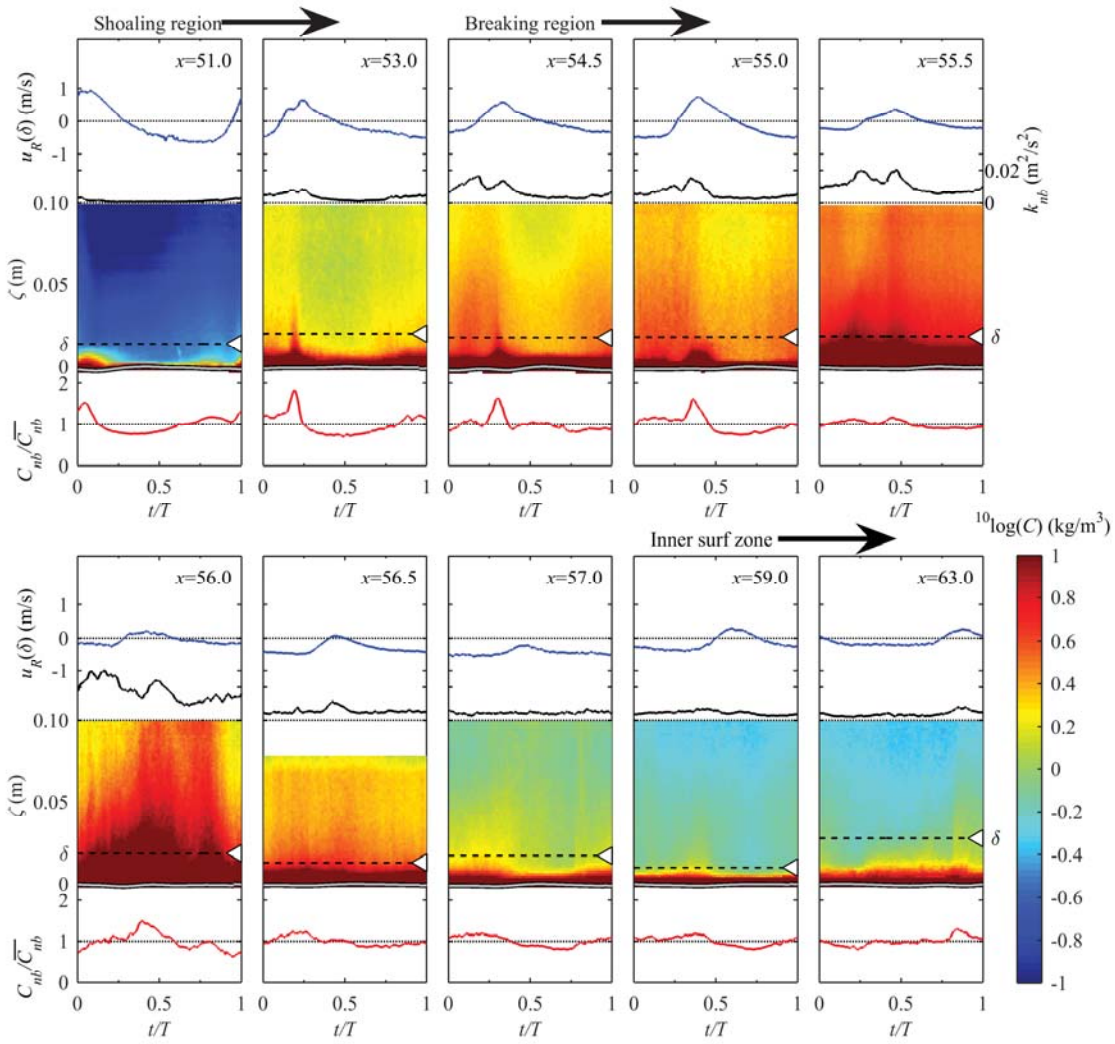

Figure 3.6. Time series of phase-averaged near-bed velocities, turbulence, and suspended sediment concentrations, measured with ACVP at ten locations during t=0–15 min. From top to bottom, each panel contains: bed-parallel velocities at overshoot elevation (blue line); depth-averaged (from ζ=0.005 to 0.10 m) turbulent kinetic energy $\langle k_{nb} \rangle$ (solid black line); suspended sediment concentrations (contour in log scale); normalized suspended sediment concentrations, vertically averaged over near-bed layer (ζ = 0.005 to 0.10 m; red line). The color contour plots contain the time-varying bed level (solid grey line) and the overshoot elevation δ as proxy for maximum WBL thickness (black dashed line + white triangle).

In the breaking region (x = 55.0 – 59.0 m) the temporal variation in <C> is relatively small. Close to the plunge point (x = 55.5 – 56.0 m), highest concentrations are found at around the passing of the wave crest. Further shoreward (x = 56.5 – 59.0 m), concentrations are highest during the trough phase when highest near-bed velocity magnitudes are reached. Further into the inner surf zone (at x = 63.0 m) concentrations are slightly higher during the crest phase than during the trough phase. In this rippled bed region, it is likely that vortex formation contributes to the higher concentrations at the wave crest phase (Van der Werf *et al.*, 2007; Hurther and Thorne, 2011).

At most locations, <C_{nb}> is roughly phase-coherent with <k_{nb}>. It was shown in **Chapter 2** that <k_{nb}> for the present experiment is not only explained by local processes, i.e. production at the bed or near the water surface and vertical advection/diffusion, but that it is also affected by horizontal advection. Similarly, we may expect <C_{nb}> to be affected by a combination of local vertical processes and horizontal advection. Both contributions are quantified in Section 3.4.3.

3.4.2 Cross-shore sediment flux

This section analyses the flux components contributing to the total net suspended sediment transport. Section 3.4.2.1 analyses the near-bed flux, while Section 3.4.2.2 analyzes the flux over the whole water column.

3.4.2.1 Near-bed flux

Local horizontal sediment fluxes Φ_x are the product of velocity u and concentration C and are decomposed in the same way as velocities into:

$$\overline{\Phi}_x = \overline{uC} = \overline{u}\,\overline{C} + \overline{\tilde{u}\tilde{C}} + \overline{u'C'} = \overline{\phi}_x + \tilde{\phi}_x + \phi'_x \qquad (3.5).$$

Here, $\overline{\phi}_x$ (current-related), $\tilde{\phi}_x$ (wave-related) and ϕ'_x (turbulent) represent the three components of the total time-averaged horizontal sediment flux $\overline{\Phi}_x$. The co-located ACVP measurements of velocities and sediment concentration enable quantification of all fluxes in Equation 3.5, including the turbulent diffusive flux ϕ' (see e.g. Naqshband *et al.*, 2014). In the present experiment the turbulent flux was measured up to frequencies of about 5 Hz since higher frequencies were contaminated by acoustic noise.

Figure 3.7 (color contours) shows phase-averaged sediment fluxes <Φ_x> in the bed-parallel direction. Highest (onshore/offshore) flux magnitudes occur between x = 53.0 and 56.0 m. Flux magnitudes decrease rapidly with distance from the bed, with fluxes outside the WBL up to an order of magnitude lower than fluxes inside the WBL.

Figure 3.7 further shows the time-averaged bed-parallel fluxes $\overline{\Phi}_x$ and the contributions of each transport component indicated in Equation 3.5 (2nd and 4th row of panels). At most locations, the vertical profile of $\overline{\Phi}_x$ shows a sharp transition around $\zeta = \delta$, with much higher $\overline{\Phi}_x$ inside the WBL ($\zeta < \delta$) than at outer-flow elevations ($\zeta > \delta$). At shoaling and breaking locations before the bar crest (x = 51.0 – 55.0 m), wave-related fluxes $\tilde{\phi}_x$ inside the WBL are directed onshore. This is explained by two processes. Firstly, the velocity- and acceleration-skewed oscillatory flow leads to higher bed shear during the crest phase and the quasi-instantaneous

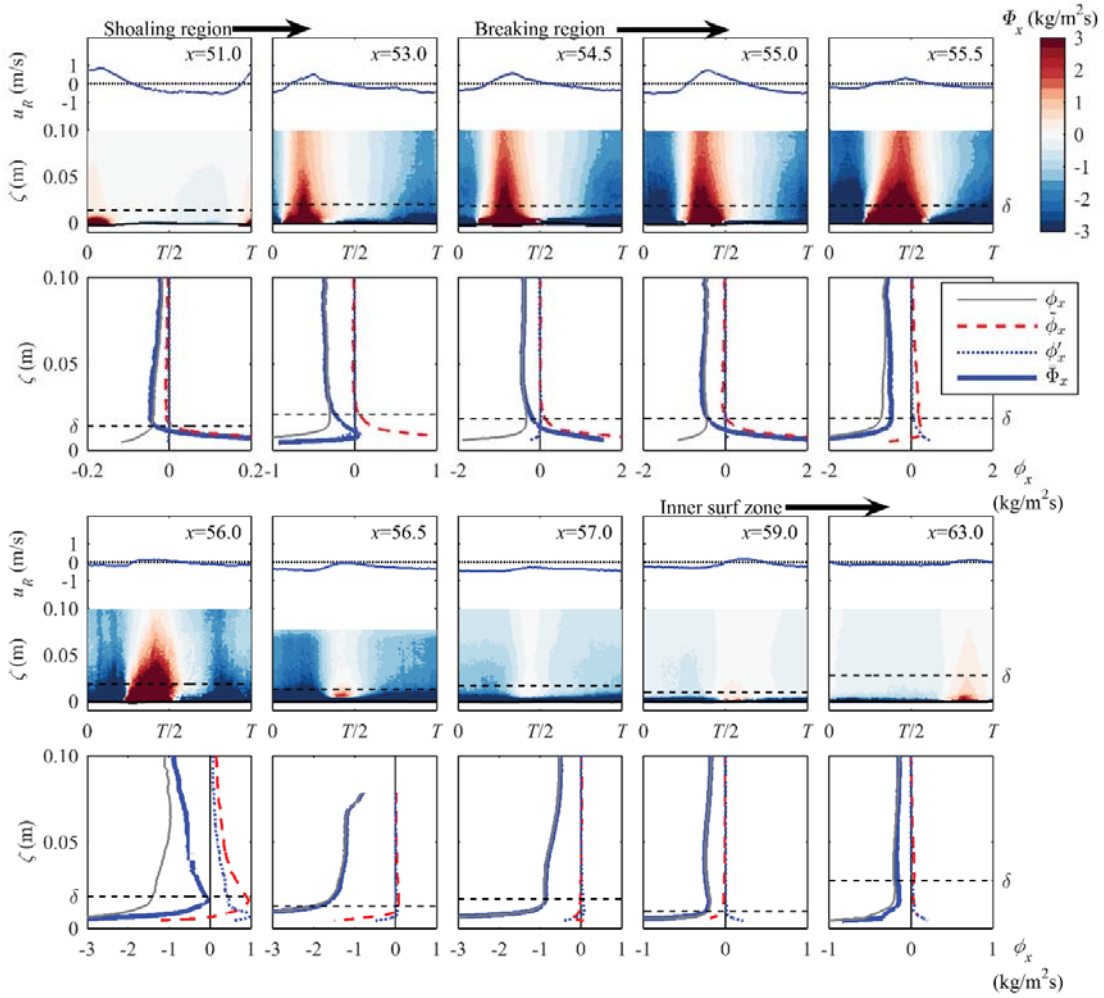

Figure 3.7. Time series of phase-averaged bed-parallel sediment flux, measured near the bed with ACVP at 10 cross-shore locations during *t*=0-15 min. First and third row of panels: bed-parallel velocity at ζ=δ (blue line); phase-averaged bed-parallel fluxes <Φ_x> (color contours). Second and fourth row of panels: corresponding vertical profiles of the time-averaged bed-parallel sediment flux (solid blue line) and the contributions of three components, i.e. current-related (solid grey line), wave-related (dashed red line), and turbulent (blue dotted). The horizontal dashed line depicts the WBL overshoot elevation. Note the varying x scale for the time-averaged flux profiles.

response of medium-sediment transport leads to an onshore wave-related suspension flux in the WBL (e.g. Schretlen, 2012). Secondly, the free-surface effect leads to upward sediment advection during the wave upward zero crossing, leading to stretching of the concentration profile under the crest and compression during the trough phase which also results in a net onshore-directed wave-related flux in the WBL (Deigaard *et al.*, 1999; Kranenburg *et al.*, 2013). Current-related fluxes $\overline{\phi}_x$ inside the WBL at shoaling locations are offshore-directed due to the undertow. The onshore-directed wave-related fluxes balance (at x = 53.0 m) or exceed (x = 51.0, 54.5, 55.0 m) the offshore current-related fluxes inside the WBL. Above the WBL, the net flux $\overline{\Phi}_x$ is dominated by the current-related component. Although temporal variation in sediment concentrations exists above the WBL, it does not result in a significant contribution to the time-

averaged wave-related fluxes at x = 51.0 – 55.0 m . The different flux behavior inside and above the WBL yields a transition from onshore-directed $\overline{\Phi}_x$ for $\zeta < \delta$ to offshore-directed $\overline{\Phi}_x$ for $\zeta > \delta$.

In the breaking zone, the total net flux $\overline{\Phi}_x$ at all elevations is dominated by the current-related contribution. Significant contributions of $\widetilde{\phi}_x$ and $\overline{\phi}'_x$ occur at x = 56.0 m at both WBL and outer-flow elevations. Note that this is the location that is most directly influenced by breaking-induced TKE (**Figure 3.3c**). The wave-related fluxes at this location are directed onshore as the crest-phase concentrations exceed the concentrations during the trough phase. The onshore-directed $\widetilde{\phi}_x$ counterbalances about 30% of the offshore-directed $\overline{\phi}_x$ (depth-averaged over $\zeta = \delta$ to 0.10 m). $\widetilde{\phi}_x$ declines much more rapidly than $\overline{\phi}_x$ with distance from the bed. Consequently, at ζ = 0.10 m, the wave-related flux is minor (< 10%) compared to the current-related flux. Similar to $\widetilde{\phi}_x$, the diffusive flux $\overline{\phi}'_x$ declines rapidly with distance from the bed and it may be neglected outside the near-bed region (ζ > 0.10 m). Time series of diffusive fluxes (not shown) revealed that $\overline{\phi}'_x$ is predominantly driven by relatively large turbulent events with time scales of O(1 s). These events likely relate to large-scale breaking-induced vortices that arrive at the bed, entrain sediment, and carry it onshore and downslope along the shoreward slope of the bar.

In the inner surf zone, $\overline{\Phi}_x$ is dominated by the current-related flux $\overline{\phi}_x$, which can be attributed to the strong undertow. The wave-related flux remains negligibly small, despite the presence of orbital sand ripples for which significant wave-related flux contributions to total net transport have been measured for oscillatory conditions without a free-stream mean (undertow) current (c.f. van der Werf *et al.*, 2008).

3.4.2.2 Flux over whole water column

The depth-integrated, time-averaged suspended transport rate q_s is given by

$$q_s = q_{s,wbl} + q_{s,outer} = \int_{z_a}^{\delta} \overline{uC}\,d\zeta + \int_{\delta}^{\eta_{crest}} \bar{u}\bar{C}\frac{t_f}{T}\,d\zeta \qquad (3.6),$$

where $q_{s,wbl}$ is the net transport rate inside the WBL; $q_{s,outer}$ is the net transport rate over the outer flow; z_a=0.005 m is the elevation taken to separate suspended and bed load; δ is the WBL overshoot elevation (≈0.02 m); η_{crest} is the wave crest level; and the parameter t_f/T is the relative 'wet period', i.e. the fraction of the wave cycle for which an elevation is immersed. Note that $\bar{u}$ in Equation 3.6 is defined as the time-averaged horizontal velocity over the wet period and not over the full wave cycle. The ACVP-measured fluxes allow direct computation of $q_{s,wbl}$. In the previous section it was shown that outer-flow fluxes are dominated by the current-related contribution, i.e. $\overline{\Phi}_x \approx \overline{\phi}_x$ for $\zeta > \delta$. Therefore, to compute $q_{s,outer}$, the profile of horizontal fluxes over the complete water column was estimated by vertical inter- and extrapolation of time-averaged velocities and concentrations.

Figure 3.8a shows an example of measured and fitted $\bar{u}(\zeta)$. Profiles of $\bar{u}(\zeta)$ were based on a combination of ACVP measurements (for $\delta < \zeta < 0.10$ m) and a semi-empirical fit through ADV measurements (for ζ>0.10 m). For 0.10 m < ζ < η_{trough}, the profile was approximated with a parabolic distribution following undertow approximations by Kobayashi *et al.* (2005). At

elevations above wave trough level, $\bar{u}(\zeta)$ was approximated through a linear increase with a slope that was chosen such that the time-averaged depth-integrated mass balance is zero ($\int_0^{\eta_{crest}} \bar{u} t_f/T \mathrm{d}\zeta=0$). Note that other distributions of $\bar{u}(\zeta)$ for $\zeta>\eta_{trough}$ (e.g. exponential or quadratic increase) did not result in large differences in the depth-integrated suspended transport, because $\overline{C}(\zeta)$ is nearly depth-uniform for $\zeta>\eta_{trough}$. The profile of suspended sediment concentrations $\overline{C}(\zeta)$ in the outer flow was estimated by fitting a Rouse profile (Equation 3.4) through the TSS measurements (**Figure 3.8b**). Equation 3.4 was log-fitted instead of linearly fitted to reduce a bias towards high concentrations near the bed. The extrapolation of $\overline{C}$ to $\zeta>\eta_{trough}$ seems justified based on an accompanying experiment (Ribberink *et al.*, 2014) which included TSS measurements between wave trough and crest level. The relative wet period t_f/T was extracted from PT-measured water surface levels (**Figure 3.8c**). The product of these three terms yields the time-averaged $\overline{\phi}_x$ profile (**Figure 3.8d**), used for the estimation of $q_{s,outer}$ in Equation 3.6.

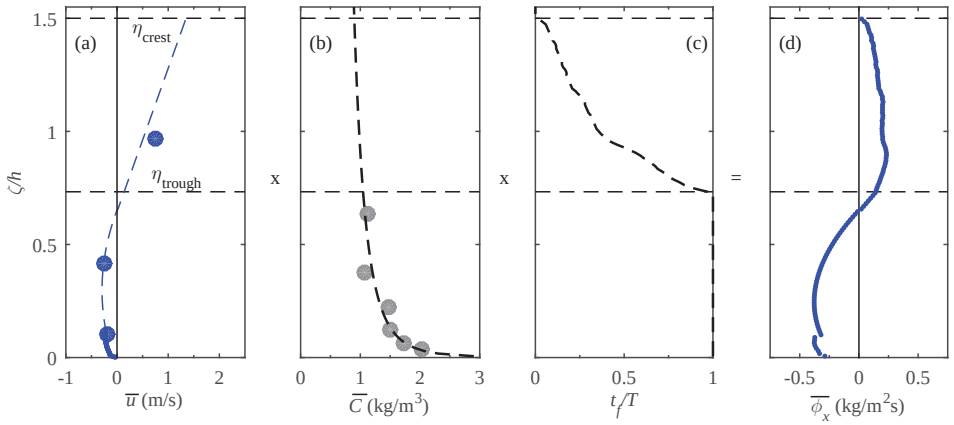

Figure 3.8. Example of outer-flow sediment flux calculation near the breaker bar at x = 54.5 m: (a) Time-averaged horizontal velocities, measured with ADVs (filled circles) and ACVP (dots), and fitted values (dashed line); (b) Time-averaged sediment concentrations, measured with TSS (circles) and power-function fit (dashed line); (c) Relative 'wet period' t_f/T; (d) Current-related sediment flux profile $\overline{\phi}_x(\zeta)$, as the product of the dashed lines in panels a-c.

Figure 3.9b shows the resulting vertical profiles of the approximated net suspended sediment flux ($\overline{\Phi}_x$) at seven cross-shore locations. **Figure 3.9c** shows the spatial flux distribution and includes the elevations below which 50% and 90% of the flux is found. These levels are based on the depth-integrated *absolute* values of the flux $\int_{z_a}^{\eta_{crest}} |\overline{\Phi}_x| \mathrm{d}\zeta$. Note that the fluxes $\overline{\Phi}_x$ inside the WBL (**Figure 3.7**) are significantly higher than the outer-flow fluxes. Hence, for presentation purposes, the WBL fluxes are omitted in **Figure 3.9b-c**. **Figure 3.9a** shows the undertow profiles for reference.

At x = 51.0 m, $\overline{\Phi}_x$ is much lower at outer-flow elevations than inside the WBL. In the breaking region at the bar crest (x = 53.0 to 55.5 m), i.e. between break point and plunge point, significant $\overline{\Phi}_x$ contributions to q_s occur between wave trough and wave crest level. This is attributed to strong vertical mixing of suspended sediment in combination with relatively shallow water depths. At these locations the onshore-directed fluxes between η_{trough} and η_{crest} counterbalance a large portion (about 70%) of the offshore-directed flux below wave trough level. The highest

offshore-directed fluxes are found along the shoreward-facing bar slope (x = 55.5 to 57.0 m) in the lower 0.2 m above the bed. This relates to the combination of high near-bed concentrations and the shape of the undertow profile, with strong offshore-directed $\bar{u}$ (up to –0.8 m/s) close to the bed (**Figure 3.9a**). Along the bar trough and inner surf zone (x > 57.0 m), fluxes within 0.3 m from the bed are the main (>50%) contributors to q_s while fluxes above trough level are minor (<10% of q_s).

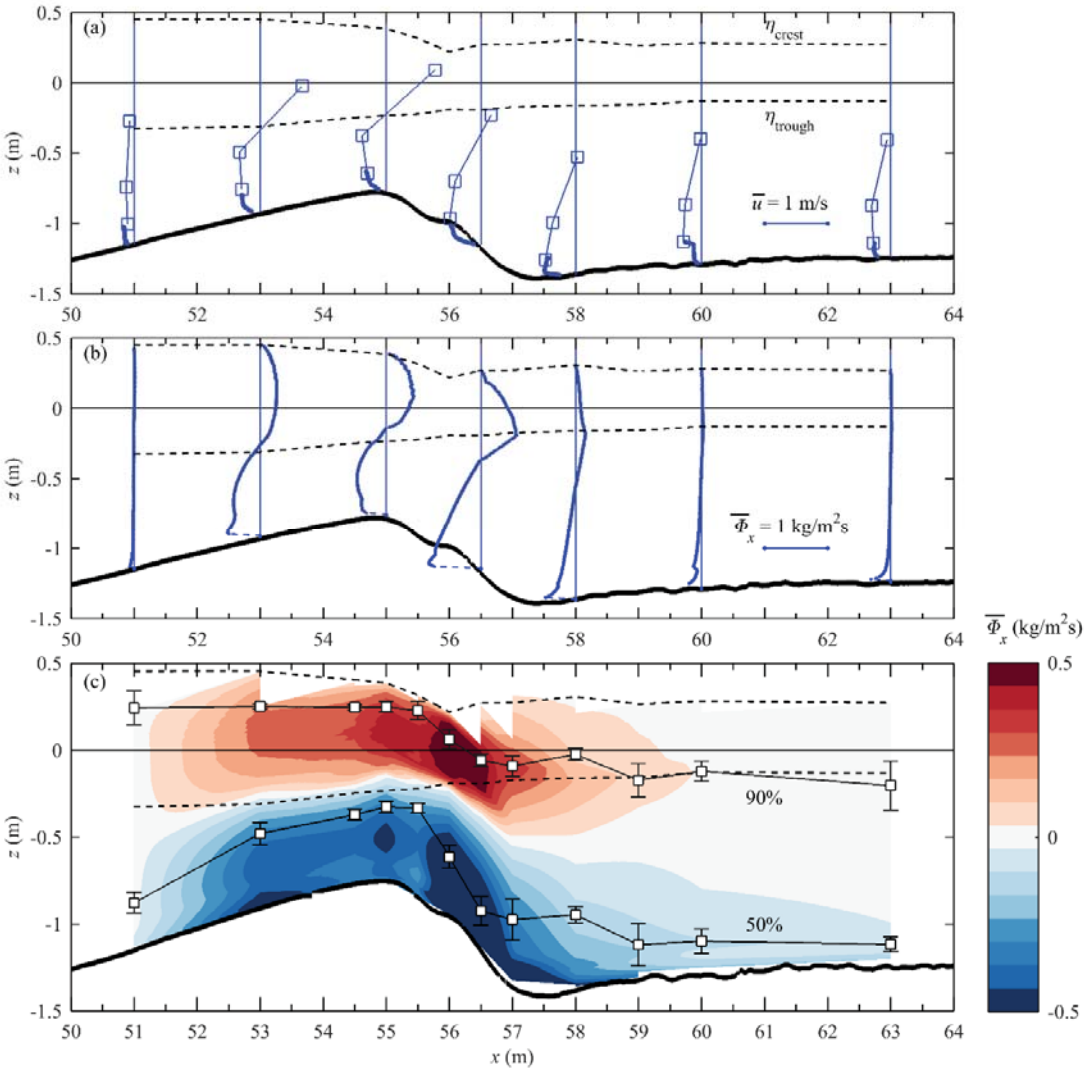

Figure 3.9. Vertical distribution of net suspended sediment horizontal flux $\overline{\Phi}_x$. (a) Time-averaged horizontal velocities, measured with ADV (squares) and ACVP (dots); (b) Vertical profiles of $\overline{\Phi}_x$ at seven locations halfway through the experiment (t=45 – 60 min.); (c) Color contour plot of $\overline{\Phi}_x$ for t=45 – 60 min. For presentation purposes, panels a-b do not show all 12 measurement locations and panels b-c do not include the fluxes inside the WBL. White squares in panel (c) mark elevations where the integrated flux from the bed upwards reaches 50% and 90% of the depth-integrated absolute $\overline{\Phi}_x$ from $\zeta = z_a$ to η_{crest} (values are averaged over six runs, with error bars marking the 95% confidence interval). The bed profile corresponds to t=45 min.

Figure 3.10a shows the depth-integrated net suspended transport rate within the WBL ($q_{s,wbl}$) and over the outer flow ($q_{s,outer}$) following Equation 3.6 along the bed profile. The relative importance of $q_{s,wbl}$ and $q_{s,outer}$ to total suspended transport is quantified by relative fractions f_{wbl} and f_{outer}, based on the sum of the absolute values of both contributions (i.e. $f_{wbl} = |q_{wbl}|/(|q_{wbl}|+|q_{outer}|)$ and $f_{outer} = 1 - f_{wbl}$). **Figure 3.10b** shows the cross-shore variation in these relative fractions.

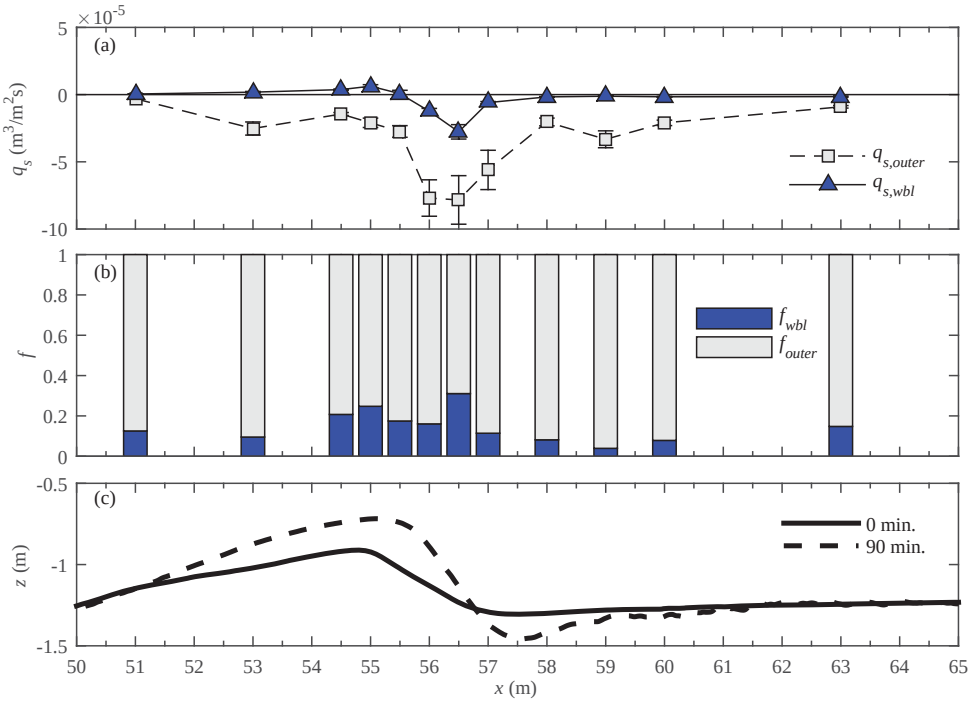

Figure 3.10. Cross-shore variation in depth-integrated total net suspended transport inside the WBL and in the outer flow. (a) Suspended transport rates inside the WBL (blue triangles and solid line) and in the outer flow (grey squares and dashed line). (b) Relative fraction of transport inside the WBL (blue) and in the outer flow (grey); (c) Bed profiles at 0 and 90 min. Results are averaged over six runs with error bars in (a) marking one standard deviation of the mean.

The magnitude of $q_{s,outer}$ increases strongly from x = 51.0 to 53.0 m, due to increasing concentrations and undertow magnitudes (**Figure 3.10a**). Between x = 53.0 and 55.5 m, $q_{s,outer}$ remains roughly constant which is partly due to the increasing significance of transport for $\zeta > \eta_{trough}$. Along the shoreward-facing bar slope (x = 56.0 – 57.5 m), $q_{s,outer}$ magnitudes increase rapidly due to the large offshore-directed fluxes close to the bed. $q_{s,outer}$ magnitudes decrease gradually along the inner surf zone as suspended sediment concentrations decrease.

The suspended transport inside the WBL ($q_{s,wbl}$) is onshore-directed in the shoaling zone and in the breaking region up to the bar crest (x = 51.0–55.0 m), indicating that onshore wave-related transport contributions generally exceed the offshore-directed current-related transport inside the WBL. The relative contribution of $q_{s,wbl}$ to total suspended transport at shoaling locations is about 10–20% (**Figure 3.10b**). Note that $q_{s,wbl}$ is formed by two transport components of similar magnitude but with opposite sign, which partly explains why f_{wbl} is small. Both $q_{s,wbl}$ and f_{wbl} increase gradually from the shoaling zone to the bar crest, with

maximum onshore transport found at the bar crest (x = 55.0 m). In the breaking region along the shoreward slope of the bar (x = 55.5 – 57.0 m), $q_{s,wbl}$ becomes offshore-directed and its magnitude increases. Also the fraction of transport confined to the WBL increases slightly, with an f_{wbl} of about 20–30 %. At the bar trough and inner surf zone (x = 58.0 – 63.0 m), $|q_{s,wbl}|$ decreases and the total suspended transport is largely (> 80 - 90%) determined by the outer-flow transport.

3.4.3 Cross-shore advection, pick-up, and deposition

The flux measurements presented earlier are used in this section to study the cross-shore advection of sediment in relation to the vertical sediment exchange between the suspension and bedload layer (pick-up/deposition) at a wave-averaged time scale (Section 3.4.3.2) and at an intra-wave time scale (Section 3.4.3.3).

3.4.3.1 Calculations

We introduce a sediment mass balance for a control near the bed (**Figure 3.11**), given by

$$\int_{z_a}^{D} \frac{\partial \langle C(\zeta,t)\rangle}{\partial t} \mathrm{d}\zeta + \int_{z_a}^{D} \frac{\partial \langle \Phi_x(\zeta,t)\rangle}{\partial x} \mathrm{d}\zeta + \int_{z_a}^{D} \frac{\partial \langle \Phi_z(\zeta,t)\rangle}{\partial z} \mathrm{d}\zeta = 0 \qquad (3.7),$$

where $\langle \Phi_x \rangle$ and $\langle \Phi_z \rangle$ are the phase-averaged ACVP-measured total fluxes in the horizontal and vertical direction, respectively. The control volume extends vertically from $\zeta = z_a$ = 0.005 m up to $\zeta = D$ = 0.10 m and matches the near-bed layer covered by the ACVP. It follows from Equation 3.7 that local concentration changes (term 1) are the result of horizontal gradients in cross-shore sediment flux, i.e. horizontal sediment advection (term 2), and of vertical gradients in the vertical sediment flux (term 3).

Equation 3.7 was evaluated at each cross-shore location using a central-difference scheme in both time and space, with a time step Δt equal to 0.05 s and spatial step size Δx equal to the distance between adjacent measurement locations (i.e. 0.5 m in the breaking zone and up to 3 m in the inner surf zone, c.f. Table 3.1). Concentrations and vertical fluxes are weighted averages of measurements at the x location of interest and at the onshore and offshore adjacent locations. The horizontal gradient in sediment flux is calculated over location x using $\langle \Phi_x \rangle$ measurements at the two adjacent locations. Δx is of similar magnitude as the semi-excursion length a and much smaller than the wave length L (≈ 15 m). It is therefore considered sufficient small to estimate the horizontal flux gradients with appropriate accuracy. Nevertheless, it is acknowledged that the finite number of cross-shore measurement locations leads to smoothing of the actual gradients in flux. The horizontal flux gradient cannot be estimated for the furthest offshore and onshore locations. For these locations we assume negligible contribution by horizontal advection because of the low cross-shore gradients in suspended sediment concentration and in q_s compared to the strongly non-uniform concentrations and transport rates in the breaking region.

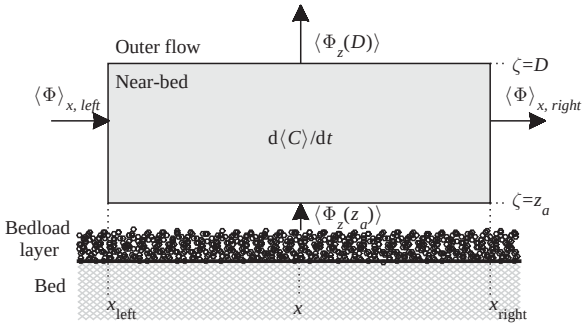

Figure 3.11. Definition sketch of control volume and fluxes. The control volume extends vertically from z_a (=0.005 m) to D (=0.10 m).

The depth-integrated vertical gradient in vertical flux (term 3 in Equation 3.7) equals the difference between the vertical flux at the bottom of the control volume $<\Phi_z(z_a)>$ and the flux at the top $<\Phi_z(D)>$. However, the vertical velocities very close to the bed were not properly resolved by the ACVP (**Chapter 2**), leading to errors in $<\Phi_z(z_a)>$. Therefore, an alternative approach was adopted as follows. The first two terms of Equation 3.7 were determined from the data and the third term then follows from the mass balance. This term can be rewritten as

$$\int_{z_a}^{D} \frac{\partial <\Phi_z(\zeta,t)>}{\partial z} d\zeta = <\Phi_z(D)> - <\Phi_z(z_a)> \qquad (3.8),$$

which, in combination with measured $<\Phi_z(D)>$, allows $<\Phi_z(z_a)>$ to be solved. $\Phi_z(z_a)$ is the vertical exchange between the bedload layer ($\zeta < z_a$) and the suspension layer ($\zeta > z_a$). It can be decomposed into a deposition rate d (defined positively downward) and a pick-up rate p (defined positively upward). Under an assumption of free settling, which seems appropriate for medium-grained particles at concentrations of O(1–10) kg/m^3 (e.g. Baldock *et al.*, 2004), the deposition rate was modeled as $d = w_s C(z_a)$ (Nielsen, 1992). The pick-up rate is then given by $p = d + \Phi_z(z_a)$. Because p and d were not directly measured and are based on a modeling assumption for the deposition rate, estimations of p and d following the above approach should be interpreted with caution. For this reason they are evaluated at a wave-averaged time scale only in what follows, i.e.:

$$\overline{\Phi_z}(z_a) = \bar{p} - \bar{d} = \bar{p} - w_s \bar{C}(z_a) \qquad (3.9).$$

3.4.3.2 *Time-averaged pick-up, deposition and horizontal gradients in cross-shore transport*

At a wave-averaged time scale and for equilibrium conditions, $d\bar{C}/dt = 0$ and the vertical flux between the bedload and suspension layer $\overline{\Phi_z}(z_a)$ should equal the cross-shore gradient in suspended transport rate, i.e.

$$\overline{\Phi_z}(z_a) = \frac{dq_s}{dx} \qquad (3.10),$$

where q_s is the net total transport rate over the complete water column (Equation 3.6). **Figure 3.12a** shows both terms of Equation 3.10, with $\overline{\Phi}_z(z_a)$ obtained using Equation 3.8 time-averaged. Although the approaches for the two quantities are subjected to different

assumptions in data treatment, the validity of both approaches (Equation 3.6 and Equation 3.8) is supported by the consistent results in terms of magnitude and cross-shore behavior.

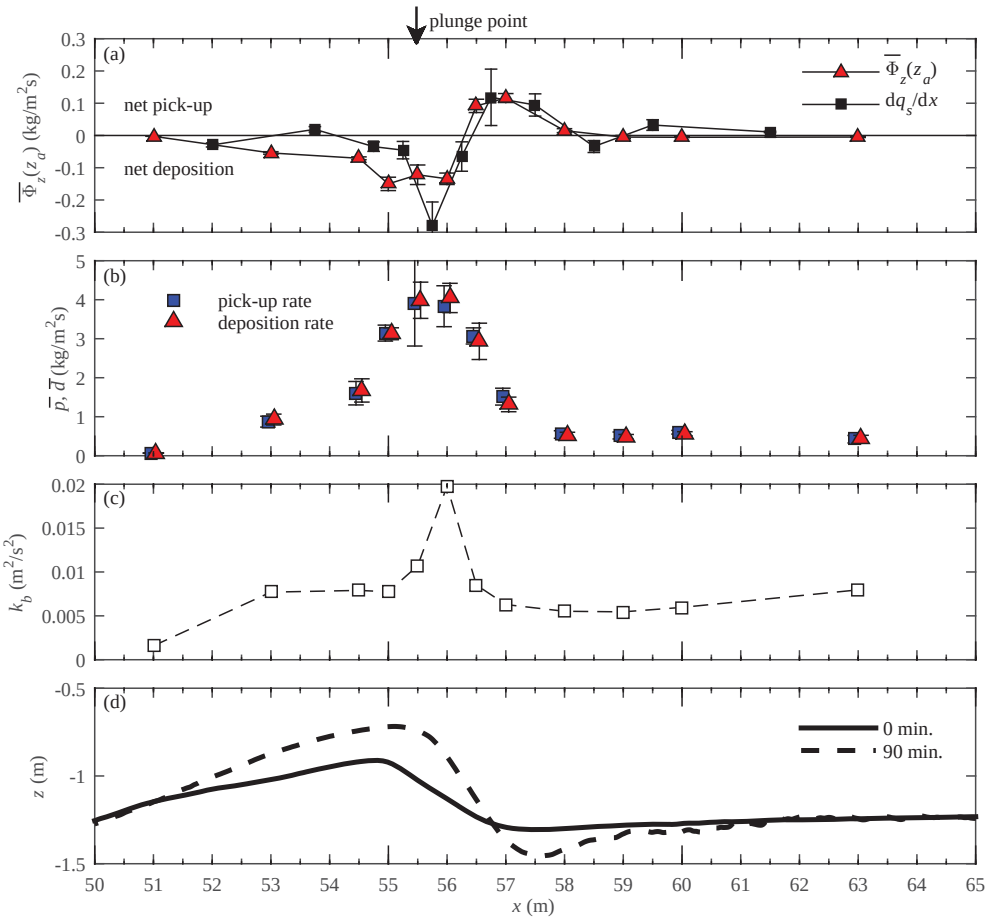

Figure 3.12. (a) Time-averaged vertical flux between bedload and suspension layer at $z=z_a$, estimated from control-volume analysis using ACVP measurements (red triangles), and cross-shore gradient of total depth-integrated (from $\zeta=z_a$ to η_{crest}) suspended load (black squares); (b) Time-averaged pick-up (blue squares) and deposition rates (red triangles); (c) maximum time-averaged TKE inside the WBL ($\zeta<\delta$); (d) Bed profile measurements at t=0 min. (solid) and t=90 min. (dashed), for reference. Values in (a- c) are means over six runs, with error bars in (a-b) marking standard deviation of mean.

$\overline{\Phi}_z(z_a)$ can be interpreted as the contribution of suspended transport to the time rate of morphological change of the bar, with $\overline{\Phi}_z(z_a)<0$ (net downward flux) corresponding to local accretion and $\overline{\Phi}_z(z_a)>0$ to erosion. If $\overline{\Phi}_z(z_a) = 0$, there is no cross-shore gradient in suspended transport and time-averaged local pick-up balances deposition. The highest magnitudes of $\overline{\Phi}_z(z_a)$ occur between x = 54.0 and 58.0 m (**Figure 3.12a**). This relates directly to the strongly non-uniform hydrodynamics in cross-shore direction due to wave breaking and due to cross-shore-varying water depths, which lead to steep cross-shore gradients in suspended sediment concentrations and suspended transport rates. Net suspended sediment pick-up ($\overline{\Phi}_z(z_a)>0$) occurs at the shoreward slope of the bar and over the bar trough (x = 56.5 to 58.0 m) while net sediment deposition ($\overline{\Phi}_z(z_a)<0$) occurs around the bar crest (x = 53.0 to 56.0 m). Between these regions, the undertow drives net offshore advection of suspended sediment from the bar

trough to the bar crest. Note that the regions of net pick-up and net deposition are roughly consistent with net erosion and accretion regions of the bed profile (**Figure 3.12d**). However, the profile evolution can only be fully explained by also considering the gradients in bedload transport.

Figure 3.12b shows the time-averaged pick-up ($\overline{p}$) and deposition ($\overline{d}$) rates, obtained through decomposition of $\overline{\Phi}_z(z_a)$ through Equation 3.9. The high pick-up rates in the vicinity of the plunge point (between bar crest and bar trough) are prominent, with values that are two to five times the pick-up rates in the shoaling zone. The cross-shore variation in pick-up (**Figure 3.12b**) does not match the cross-shore variation in maximum onshore/offshore velocities, which decrease in the breaking region (**Figure 3.3b**). The pick-up variation shows a better similarity with the cross-shore variation in near-bed TKE (**Figure 3.12c**), which is consistent with the results for reference concentrations discussed earlier (Section 3.4.1.1).

Sediment deposition and pick-up rates are of similar magnitude at all locations. The small difference between $\overline{p}$ and $\overline{d}$, i.e. the net vertical flux $\overline{\Phi}_z(z_a)$, is due to the influx of horizontally-advected sediment. The contribution by horizontal sediment influx to local $\overline{d}$ is rather weak, i.e. typically less than 10%, compared to contributions by locally entrained sediment given by $\overline{p}$. From this it follows that the time-averaged local deposition rate, and consequently the reference concentration $C_0=\overline{C}(z_a)$, is largely controlled by local pick-up.

3.4.3.3 Horizontal advection and vertical flux contributions to intra-wave concentration changes

The time-varying concentration behavior in the near-bed region, presented earlier in **Figure 3.6**, can be explained in terms of cross-shore and vertical fluxes by solving Equation 3.7 at an intra-wave time scale. For convenience, Equation 3.7 is rewritten as:

$$\frac{\partial <m_{nb}>}{\partial t} = -\frac{\partial <q_{nb}>}{\partial x} + <\Phi_z(z_a)> - <\Phi_z(D)> \qquad (3.11).$$

Here, m_{nb} is the depth-integrated suspended sediment load over the control volume (i.e. $m_{nb} = \int_{z_a}^{D} C\, d\zeta = C_{nb}\cdot(D - z_a)$; q_{nb} is the time-varying depth-averaged horizontal suspended transport rate over $\zeta = z_a$ to D; $\Phi_z(z_a)$ is the vertical flux at $\zeta = z_a$ and $\Phi_z(z_a)$ is the vertical flux at $\zeta = D$. Because of the strong decrease in concentration with distance from the bed, the magnitudes of intra-wave $<\Phi_z(z_a)>$ exceed $<\Phi_z(D)>$ with a factor 5 to 10 (i.e. $|\Phi(z_a)| >> |\Phi(D)|$). This allows Equation 3.11 to be rewritten as:

$$\frac{\partial <m_{nb}>}{\partial t} \approx -\frac{\partial <q_{nb}>}{\partial x} + <\Phi_z(z_a)> = \Delta q_{nb} + <\Phi_z(z_a)> \qquad (3.12)$$

The flux gradient Δq_{nb} is termed the horizontal influx. Note that Δq_{nb} is defined as the *negative* cross-shore gradient in near-bed suspended transport rate q_{nb}, i.e. positive Δq_{nb} corresponds to an increase in the suspended load m_{nb}. Equation 3.12 states that temporal changes in the near-bed suspended load are primarily caused by horizontal sediment advection and by vertical exchange between the bedload layer and suspension layer. The vertical influx at $\zeta = D$ has minor effect on m_{nb} at an intra-wave time scale and is not considered in the following analysis of $\partial <m_{nb}>/\partial t$.

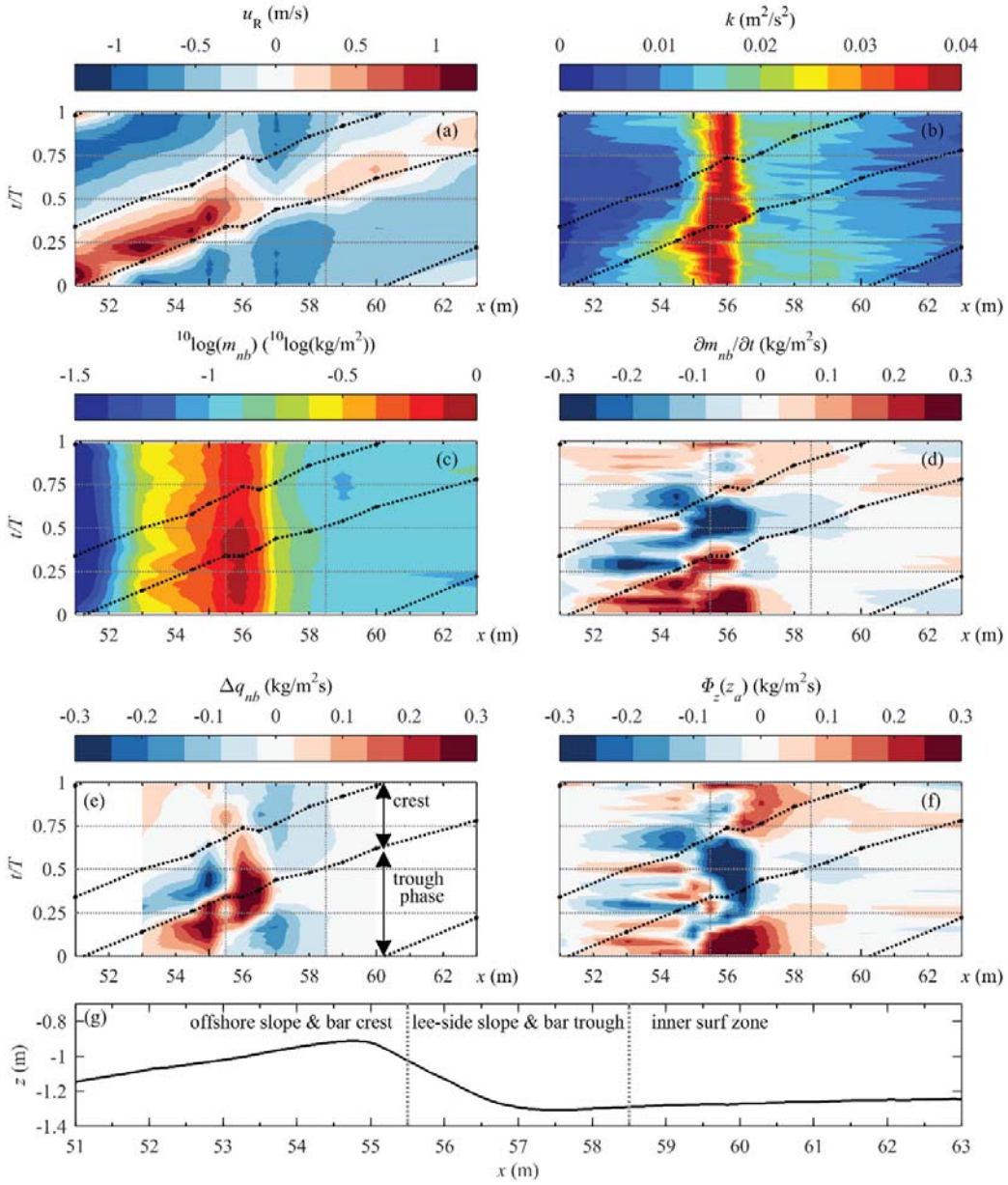

Figure 3.13. Spatio-temporal variation in phase-averaged near-bed concentrations in relation to hydrodynamics and gradients in horizontal and vertical flux, for t=0-15 min. (a) Bed-parallel velocities at ζ=δ; (b) Free-stream turbulent kinetic energy at ζ=0.11 m, measured with ADV; (c) Depth-averaged (ζ = z_a to 0.10 m) near-bed concentrations in log scale; (d) Rate of change of near-bed concentrations; (e) Sediment influx due to horizontal advection; (f) Vertical sediment influx from bedload layer; (g) Reference bed profile. Fluxes in e-f contain contributions of all transport components (current, wave, turbulent). Panels a-f include reference lines (dotted) depicting zero-up crossings of water surface level, marking reversal between wave crest and trough phase (dotted). In the analysis distinction is made between three regions, divided by vertical grey lines in all panels (see text).

Figure 3.13 shows the spatio-temporal variation in the depth-integrated mass $\langle m_{nb} \rangle$ over the near-bed layer (panel c) and its time rate of change $\partial \langle m_{nb} \rangle / \partial t$ (panel d), which relates to the

horizontal influx Δq_{nb} (panel e) and the vertical influx $\Phi_z(z_a)$ (panel f) that were quantified as described in Section 3.4.3.1. For reference, the figure includes the phase-averaged bed-parallel velocities (panel a) and the free-stream ADV-measured TKE at ζ=0.11 (corresponding roughly to the top of the control volume; panel b). Each panel includes the upward and downward zero crossings of the water surface level (dotted lines) as a phase reference. The waves propagate through the spatiotemporal domain from the lower left to the upper right corner.

Comparison of **Figure 3.13e** and **Figure 3.13f** reveals that Δq_{nb} and $\Phi_z(z_a)$ are of similar magnitude. Hence, both the horizontal sediment influx along the bed and the vertical influx between the bedload and suspension layer induce temporal changes in the suspended mass (**Figure 3.13d**).

Between x = 51.0 and 55.0 m, i.e. at the shoaling and breaking region up to the bar crest, m_{nb} increases (positive $\partial m_{nb}/\partial t$ in **Figure 3.13d**) between the middle of the wave trough phase until shortly after flow reversal and decreases during the wave crest phase (negative $\partial m_{nb}/\partial t$). **Figure 3.13f** shows that these temporal changes are partly explained by vertical influx from the bedload into the suspension layer, with $\Phi_z(z_a)>0$ around the zero-up crossing when periodic velocities are directed upward and sediment is entrained, and $\Phi_z(z_a)<0$ during the crest phase when suspended particles settle down. The phase behavior of $\partial m_{nb}/\partial t$ is further explained by the horizontal sediment influx Δq_{nb} (**Figure 3.13e**). During the wave trough phase, suspended sediment is advected offshore from the high-concentration breaking region to the low-concentration shoaling zone, leading to a positive influx of sediment ($\Delta q_{nb}>0$) and an increase in suspended mass at x = 51.0 to 55.0 m. During the wave crest phase, a reverse pattern occurs as suspended particles are advected onshore from the shoaling to the breaking zone, leading to $\Delta q_{nb}<0$ and a decrease in m_{nb}. This excursion of suspended sediment between breaking and shoaling locations explains the concentration changes above the WBL ($\zeta>\delta$) that were previously identified in **Figure 3.6** (at x = 53.0 – 55.0 m).

In the breaking region between bar crest and bar trough (x = 55.5 to 58.0 m), the temporal behavior of horizontal and vertical advection differs notably from the locations offshore from the bar crest. **Figure 3.13f** shows that at the bar trough (x = 57.0 – 58.0 m), a positive vertical influx from the bedload to the suspension layer occurs during most of the wave trough phase ($t/T \approx$ 0.75 to 0.25 in next wave cycle). This net pick-up at the bar trough is due to the combination of the large offshore-directed velocities (**Figure 3.13a**) and the presence of breaking-generated TKE that arrives at the bed during the wave trough phase (**Figure 3.13b**). Phase-averaged velocities are almost continuously directed offshore at these locations, leading to rapid offshore advection of the entrained sediment along the steep shoreward slope of the bar towards the bar crest. This explains the predominantly negative horizontal influx (i.e. removal of sediment) at the bar trough (x = 56.5 to 57.5 m; **Figure 3.13e**). This offshore-advected sediment arrives at the bar crest (x = 55.5 – 56.0 m), leading to a positive horizontal influx during most of the wave cycle (**Figure 3.13e**). This positive horizontal influx is accompanied by a negative vertical influx near the bar crest (**Figure 3.13f**) which indicates net deposition of suspended sediment. This deposition occurs particularly during the wave crest phase, when sediment concentrations are highest.

At the inner surf zone the temporal changes in suspended mass $\partial m_{nb}/\partial t$ are much smaller than at the shoaling and breaking locations; no distinct patterns in horizontal and vertical sediment influx are identified.

3.5 Discussion

Near-bed concentration changes are not only due to local pick-up and deposition processes, but are also due to horizontal influx of sediment that results from cross-shore non-uniformity in the horizontal sediment fluxes. The latter also occurs in WBLs under non-breaking waves because the velocity field changes in space and time as a wave progresses. Kranenburg *et al.* (2013) showed that horizontal sediment fluxes converge during the wave crest phase and diverge during the wave trough phase, leading to highest concentrations under the wave crest and lowest concentrations under the wave trough. Compared to these non-breaking wave observations, the phase behavior at shoaling locations in the present study is slightly shifted: maximum concentrations are reached around trough-to-crest flow reversal, i.e. before the passing of the wave crest and at an earlier stage than under non-breaking waves. This is explained by the strong cross-shore variation in suspended sediment concentrations inside and outside the WBL near the breaking point, leading to a much higher influx of sediment during the wave trough phase (arrival of high-concentration) and an earlier local maximum in suspended sediment concentrations.

The observed offshore-onshore excursion of suspended sediment between the breaking and shoaling zone is consistent with field observations under plunging breakers by Beach and Sternberg (1996), who observed a 'cloud of sediment sweeping back and forth'. Note that the suspended sediment that enters the shoaling zone during the trough phase roughly balances the sediment leaving the shoaling zone during the crest phase (**Figure 3.13e**). Hence, sediment particles seem to remain in suspension – or the settling of suspended particles balances the entrainment of particles from the bedload layer – during the complete wave cycle while following the orbital flow. This sediment excursion is consistent with the excursion of TKE highlighted in **Chapter 2**, suggesting that suspended sediment particles are trapped in turbulent vortices that are partly breaking-generated. It has been suggested that the phase-coupling of TKE and suspended sediment concentrations under plunging breakers may enhance the wave-related suspended sediment transport (Ting and Kirby, 1994; Boers, 2005; De Serio and Mossa, 2006). However, in the present study, the particles trapped in turbulent vortices are advected back and forth, resulting in local (Eulerian) concentration changes but generally not in a net wave-related transport contribution at elevations outside the WBL. This relates directly to the relatively low intra-wave variation in TKE for the present conditions: TKE does not decay fully within a wave period and significant residual turbulence persists into the next wave cycle (Van der A *et al.*, Submitted). This high residual turbulence (compared to small-scale plunging breaking wave studies with equivalent Froude-scaled wave period) may relate to the breaker bar presence, which contributes to flow non-uniformity and velocity strain rates that contribute to turbulence production in the water column (Van der A *et al.*, submitted). It is anticipated that for longer-period or random waves, which yield stronger temporal variation in TKE than the waves in the present study, the outer-flow wave-related suspension fluxes could be of higher significance. The latter may also explain why field

measurements at fine-to-medium sand beaches have shown significant wave-related fluxes at outer-flow elevations in the breaking region (Osborne and Greenwood, 1992; Ogston and Sternberg, 1995; Ruessink *et al.*, 1998).

Outer-flow concentration profiles above the breaker bar crest are approximately depth-uniform and high sediment concentrations occur in the outer flow up to wave crest level. These high concentrations are not only explained by vertical mixing by orbital velocities and (breaking-generated) turbulence, but also by vertical advective sediment fluxes due to non-zero time-averaged vertical resulting from (i) a vertical component of the undertow as it follows the bar geometry, and (ii) cross-shore gradients in the bed-parallel undertow velocities that are balanced by a velocity in bed-normal direction (i.e. because of fluid mass conservation). For the present study, time-averaged velocities follow a circulation cell with downward velocities above the bar trough and upward velocities above the bar crest (Van der A *et al.*, submitted). In morphodynamic models all three mixing mechanisms (turbulent, wave-related, time-averaged advection) should be taken into account. This also holds for the significant contribution of suspended sediment flux occurring between wave trough and wave crest level observed in the present study.

In terms of sand transport modeling, empirical formulations for enhanced wave-related suspended transport reaching elevations far outside the WBL have been proposed for the breaking region (Van Rijn, 2007b). This approach is partly supported by the present measurements. Indeed, the magnitude of the wave-related transport is enhanced in the breaking region, especially at the bar crest, compared to the shoaling zone (**Figure 3.7**; **Figure 3.10a**). However, the wave-related fluxes generally do not extend vertically into the outer flow, but remain confined to the WBL as is also the case for non-breaking waves (c.f. Schretlen, 2012). An exception is one location along the shoreward bar slope, where near-bed TKE is highest and where significant wave-related transport occurs above the WBL.

Time-averaged near-bed concentrations are largely controlled by local pick-up. Most commonly-used formulae for reference concentration C_0 are based on estimates of bed shear stress by periodic and time-averaged near-bed velocities (e.g. Nielsen, 1986; Van Rijn, 2007b) and will likely predict highest pick-up and offshore-directed suspended transport rates at the bar crest (c.f. Jacobsen and Fredsoe, 2014). In the present study, maximum pick-up rates are found shoreward from the bar crest along the shoreward-facing bar slope, where highest near-bed TKE occurs. Consistent with other surf zone observations (e.g. Voulgaris and Collins, 2000; Aagaard and Jensen, 2013), the present study shows that C_0 correlates poorly with $\bar{u}$ and $\tilde{u}_{rms}$. Hence, the cross-shore variation in sediment pick-up cannot be explained by bed shear stress purely by periodic and time-averaged velocities. Instead, C_0 correlates significantly with near-bed TKE, suggesting that breaking-generated turbulence is an important driver for sediment pick-up.

This implies that C_0 models in the breaking zone can be considerably improved through parameterizations of near-bed turbulence effects on sediment entrainment. Although such models have already been proposed (e.g. Steetzel, 1993), it should be noted that it is not trivial to quantify near-bed TKE using existing turbulence closure models (Brown *et al.*, 2016). An alternative is a C_0 model that is based on breaking-wave characteristics such as the relative wave height (Mocke and Smith, 1992) or wave energy dissipation due to breaking (Kobayashi

and Johnson, 2001). However, the present study shows that near-bed TKE is not fully determined by local 1D processes, i.e. production at the bed and water surface followed by vertical advection/diffusion; instead, TKE spreads in the cross-shore direction through advection by the undertow and orbital flow and by diffusion (van der Zanden *et al.*, 2016; van der A *et al.*, submitted). Consequently, the region at which sediment pick-up is enhanced extends to shoaling locations adjacent to the breaking zone (see **Figure 3.12bc**). The development of C_0 formulations for surf zone conditions would likely benefit from high-resolution data of near-bed concentrations, turbulence, and wave characteristics for a wider range of breaking-wave conditions and sediment characteristics than covered by the present and previous studies.

3.6 Conclusions

The effects of wave breaking on suspended sediment processes were examined through a large-scale wave flume experiment, involving regular plunging breaking waves over a barred beach of medium sand. Measurements of suspended sediment concentrations and fluxes were obtained at 12 locations from the shoaling to the inner surf zone and extend a large part of the water column, with particularly high resolution in the lowest 0.10 m that includes the wave bottom boundary layer (WBL). The measurements were related to observations of near-bed hydrodynamics including turbulent kinetic energy (TKE), as presented in **Chapter 2**, and yield new insights into sediment pick-up, deposition and horizontal advection in the breaking region. Based on the results we conclude the following:

1. Breaking-generated TKE that invades the WBL has a significant effect on near-bed sediment concentrations. Sediment pick-up rates increase by an order of magnitude between the shoaling and breaking regions. Wave-averaged reference concentrations in the breaking region correlate better with near-bed TKE than with bed-parallel periodic velocities, suggesting that breaking-generated turbulence is an important driver for sediment pick-up. At an intra-wave time scale, suspended sediment concentrations are generally phase-coherent with near-bed TKE.
2. Sediment concentration profiles are Rouse-shaped with a strong increase in concentration inside the WBL. Suspended sediment is particularly strongly mixed above the bar crest, where outer-flow concentrations are nearly depth-uniform. This vertical mixing is attributed to the combination of energetic breaking-generated vortices, the strongly asymmetric wave shape (strong upward wave-related advection), and upward-directed wave-averaged velocities resulting from a time-averaged fluid circulation cell.
3. Net (i.e. wave-averaged) suspended sediment fluxes reveal a complex pattern with alternating onshore and offshore-directed constituents. In the shoaling region and breaking locations up to the bar crest, net sediment fluxes are directed onshore inside the WBL but offshore in the outer flow. Above the breaker bar crest a substantial onshore-directed suspended transport contribution occurs above wave trough level. In the breaking region along the shoreward slope of the bar and inside the inner surf zone, net suspended sediment fluxes are offshore-directed over most of the water column.
4. Net outer-flow suspended fluxes are generally current-related and offshore-directed due to the undertow. Significant net wave-related fluxes are observed at shoaling and breaking

locations, where they are directed onshore and are generally confined to the WBL. Only at one location, i.e. the breaker location with highest near-bed TKE and near-bed concentrations, does the net wave-related flux extend vertically to outer-flow elevations.

5. Sediment flux gradients were quantified to study the advection and the pick-up and deposition of suspended sediment. At a wave-averaged time scale, sediment grains are entrained from the bed in the bar trough region, are advected offshore by the undertow, and are deposited in the region covering the shoaling zone, bar crest, and the upper part of the steep onshore bar slope. Near-bed concentrations are largely (>90%) determined by local pick-up; contributions of cross-shore advected sediment are minor.
6. Offshore from the bar crest, concentration changes are primarily due to cross-shore advection by orbital velocities. Suspended particles travel back and forth between the breaking and shoaling zone, yielding an increase in sediment concentrations at shoaling locations during the wave trough phase and a decrease in concentrations during the wave crest phase. This onshore-offshore excursion is consistent with the spatio-temporal variation in TKE, which suggests that sediment particles are trapped in breaking-generated vortices that are advected back and forth following the orbital motion.
7. Shoreward from the bar crest, concentration changes are due to cross-shore-varying and time-varying pick-up and deposition rates and due to cross-shore gradients in periodic and time-averaged velocities. Sediment is entrained in the bar trough especially during the wave trough phase, when both near-bed velocity magnitude and breaking-generated TKE arriving at the bed are highest. The entrained particles are almost instantly advected offshore and are deposited near the bar crest during the wave crest phase when velocity magnitudes reduce.

4 Bedload and suspended load contributions to the morphodynamics of a large-scale laboratory breaker bar

Highlights:

- ⇨ Sheet flow layer dynamics at breaker bar crest are not affected by breaking-generated turbulence but are affected by horizontal sediment influx from adjacent locations.
- ⇨ Onshore bedload and offshore suspended load transport are of similar magnitude but of opposite sign.
- ⇨ Bedload and suspended load transport have opposite effects on breaker bar growth and migration.

Abstract

This chapter presents measurements of sheet flow processes, grain sorting, and bedload plus suspended load transport rates around a medium-sand breaker bar in a large-scale wave flume. The results offer insights in effects of wave breaking on bedload and grain sorting processes and in the quantitative contribtions by bedload and suspended transport to breaker bar morphodynamics. The quasi-instantaneous sheet flow response to phase-averaged velocity is consistent with observations under non-breaking waves. The sheet flow layer thickness is locally somewhat higher than expected based on hydrodynamic forcing, which is attributed to a net horizontal sediment influx (i.e. due to non-uniform cross-shore advection). The cross-shore variation in bedload transport rates relates to variations in wave shape (i.e. velocity skewness and asymmetry) at locations covering the shoaling region up to the bar crest. At locations between bar crest and bar trough, bedload transport correlates positively with bed slope and turbulent kinetic energy. Bedload and suspended load transport rates are of similar magnitude but of opposite sign. Bedload transport is onshore-directed and dominates at the shoaling zone, but following wave breaking, the offshore-directed suspended sediment transport increases in magnitude and exceeds bedload transport rates at the breaking and inner surf zone. Bedload and suspended load transport contribute notably differently to bed profile evolution: bedload transfers sand grains from the offshore slope to the bar crest and additionally leads to erosion of the shoreward bar slope and deposition at the bar trough, while suspended load transport induces an opposite pattern of erosion at the bar trough and accretion at the bar crest. Suspended grain samples reveal size-selective entrainment and vertical size segregation at the inner surf zone, but suggest size-indifferent entrainment and vertical mixing by energetic vortices in the breaking region. Size-selective transport as bedload and suspended load leads to a cross-shore coarsening of the bed from shoaling to inner surf zone, with local additional sorting mechanisms around the breaker bar due to bed slope effects.

This chapter is in preparation for submission as:

Van der Zanden, J., van der A, D. A., Hurther, D., Cáceres, I., O'Donoghue, T., Hulscher, S. J. M. H. and Ribberink, J. S. *Bedload and suspended load contributions to the morphodynamics of a large-scale laboratory breaker bar.*

4.1 Introduction

Breaker bars are morphologic features that are formed naturally in wave breaking zones of dissipative and intermediate beaches (Wright and Short, 1984). Breaker bars enhance wave energy dissipation due to breaking and are one of the factors that determine the state of the beach profile (Lippmann and Holman, 1990; Wijnberg and Kroon, 2002; Price and Ruessink, 2011). Breaker bars are dynamic and tend to migrate offshore during storm conditions, when strong wave breaking occurs, and onshore during mild wave conditions (Thornton *et al.*, 1996; Ruessink *et al.*, 2007). The offshore migration is attributed to an increase in both undertow velocities and suspended sediment concentrations as the intensity of wave breaking increases, which enhances offshore-directed suspended sediment transport (Sallenger *et al.*, 1985; Thornton *et al.*, 1996). Onshore migration is explained by the vertically and horizontally asymmetric shape of the shoaled waves, leading to higher magnitudes of near-bed orbital velocities (velocity skewness) and of fluid accelerations (acceleration skewness) during the crest phase relative to the trough phase, which both favor onshore-directed wave-related sediment transport near the bed (Elgar *et al.*, 2001; Hoefel and Elgar, 2003).

By including contributions of offshore-directed current-related and onshore-directed wave-related sediment transport, numerical models can predict on- and offshore bar migration reasonably well (Henderson *et al.*, 2004; Hsu *et al.*, 2006; Dubarbier *et al.*, 2015; Fernández-Mora *et al.*, 2015). However, sediment transport predictions in these models are usually only validated on bed profile evolution and may not adequately represent the individual contributions by net bedload and suspended load transport. In addition, the effects of wave breaking on sediment transport rates are not fully understood and therefore often neglected. In order to improve understanding and numerical modeling of breaker bar evolution, it is relevant to study how wave breaking affects bedload transport processes at intra-wave and wave-averaged time scales.

Previous research has shown that large-scale wave breaking enhances turbulence levels over the entire water column including the wave bottom boundary layer (**Chapter 2**). This explains observations of enhanced instantaneous bed shear stresses (Cox and Kobayashi, 2000; Sumer *et al.*, 2013) and suspended sediment entrainment rates (Nielsen, 1984; Chapter 3) under breaking waves. The presence of additional turbulence may also increase bedload transport rates, as shown for a steady flow with artificial grid turbulence (Sumer *et al.*, 2003), but it should be noted that the latter experiment involved mild flow conditions with a bedload transport regime that differs significantly from the sheet flow conditions under full-scale breaking waves (Nielsen, 1992). Bedload in sheet flow conditions has been extensively studied in wave flumes under non-breaking waves (Dohmen-Janssen and Hanes, 2002; Schretlen, 2012) and oscillatory flow tunnels (see van der Werf *et al.*, 2009, for an overview). Observations in the swash zone revealed that bore turbulence and cross-shore sediment advection may lead to increased sheet flow layer thicknesses compared to non-breaking wave observations (van der Zanden *et al.*, 2015a; Lanckriet and Puleo, 2015). Due to a lack of high-resolution measurements, it is still unclear if and how wave breaking affects sheet flow transport rates and processes around the breaker bar. Consequently, it is also unclear whether existing engineering-type bedload transport formulae, used for morphodynamic simulations, should account for wave breaking effects (Van Rijn *et al.*, 2013). Therefore, the first motivation of the present study is to explore bedload processes across the wave breaking zone.

Research has further revealed that transport in the breaking region is size-selective, i.e. differs for each grain size class within a sediment sample. Observations of graded sediment transport under oscillatory sheet flow conditions have shown that coarser grains are transported more easily than finer grains because they are more exposed (de Meijer *et al.*, 2002; Hassan and Ribberink, 2005). The suspended load transport generally contains a relatively high fraction of fine-grained particles which are more easily entrained and mixed than coarse grains (Nielsen, 1992; Wiberg *et al.*, 1994; Davies and Thorne, 2016) and which are advected by the mean current (Sistermans, 2002). In time, the removal of fine-grained particles from the bed may lead to coarsening of the seabed's top layer. This may even lead to the formation of erosion-resistant bed surface layers of coarse grains ('armouring'), which can significantly reduce sediment pick-up and transport rates (Nielsen, 1992; Wiberg *et al.*, 1994). Finn *et al.* (2016) suggest, based on detailed simulations with a particle-based numerical model, that such armour layers for sheet flow conditions may already develop after one wave cycle. Grain size observations in field (Wang *et al.*, 1998) and laboratory (Koomans, 2000) conditions revealed a relatively large fraction of coarse sand on breaker bar crests, while bar troughs are composed of relatively fine sediment. The transport of graded particles can be modelled by calculating transport for different grain classes independently (e.g. Reniers *et al.*, 2013), with the optional inclusion of a 'hiding and exposure' factor that accounts for reduced or enhanced exposure of certain grain classes (e.g. Van Rijn, 2007c). The inclusion of size-selective transport can significantly alter numerical predictions of breaker bar position and shape compared to simulations with uniform sand (Van Rijn, 1998). This illustrates the relevance of grain sorting processes for the understanding and modeling of breaker bar morphodynamics; yet no study has examined the temporal evolution of a breaker bar's grain composition in relation to measured suspended and bedload transport rates. This forms the second motivation of the present study.

This study presents high-resolution measurements of sand transport processes under a large-scale laboratory plunging wave and along a fully mobile medium-sand breaker bar. Data from the same experiment were used before to study wave breaking effects on wave bottom boundary layer hydrodynamics (**Chapter 2**) and on suspension processes (**Chapter 3**). The present study particularly addresses four matters: (i) the potential effects of wave breaking on sheet flow dynamics, which are measured using a novel conductivity-based concentration measurement system (CCM$^+$; van der Zanden *et al.*, 2015a); (ii) the cross-shore variation in bedload transport rates in relation to the hydrodynamic forcing and to the suspended transport; (iii) the contributions of net bedload and suspended sand transport to the morphological evolution of the breaker bar; (iv) grain size sorting of suspended sediment and of the sand bed.

The paper is organized as follows. Section 4.2 explains the instrumental set-up and data treatment steps. Section 4.3 presents the measured bed evolution and the main flow parameters in the experiment. Sheet flow observations and estimated bedload transport rates are presented in Section 4.4. Section 4.5 presents and discusses the cross-shore-varying contributions of suspended and bedload transport to breaker bar morphodynamics. Section 4.6 presents measurements of grain sorting in suspended sediment and along the cross-shore bed profile. Results are discussed in Section 4.7; Section 4.8 presents the main conclusions.

4.2 Experimental description

4.2.1 Facility and test conditions

The experiments were conducted in the large-scale CIEM wave flume at the Universitat Politècnica de Catalunya (UPC) in Barcelona. The flume is 100 m long, 3 m wide and 4.5 m deep, and is equipped with a wedge-type wave paddle. **Figure 4.1** shows the experimental set-up and bed profile for the present study. Cross-shore coordinate x is defined positively towards the beach, with $x = 0$ at the toe of the wave paddle. Vertical coordinate z is defined positively upwards with $z = 0$ at the still water level (SWL). ζ is used for vertical coordinate positive upwards from the local bed level.

The bed profile consisted of medium-grained sand with sediment characteristics as detailed in Section 4.2.4. The reference bed profile consisted of a bar-trough configuration (**Figure 4.1a**, black line) that was produced by 105 minutes of wave action over an initially flat horizontal test section (**Chapter 2**). The initial profile is roughly divided into an offshore slope of the breaker bar (x = 35.0 to 54.8 m; steepness $\tan(\alpha) = 0.10$), followed by a steeper shoreward-facing bar slope (x = 54.8 to 57.5 m; $-\tan(\alpha) = 0.21$), and a mildly sloping bed shoreward from the bar trough (x = 57.5 to 68.0 m; $\tan(\alpha) = 0.01$). The profile shoreward of the mobile test section ($x >$ 68.0 m) followed a slope $\tan(\alpha) = 0.13$, was fixed with geotextile, and was covered with dissipative concrete slabs that promoted wave energy dissipation.

The experiments involved monochromatic waves with wave period T = 4 s and wave height H_0 = 0.85 m at water depth h_0 = 2.55 m near the wave paddle. These conditions correspond to a surf similarity parameter $\xi_0 = 0.54$ (where $\xi_0 = \tan(\alpha)/\sqrt{H_0/L_0}$, $\tan(\alpha)$ is the offshore bar slope and L_0 is the deep-water wave length), which, matching the classification of Battjes (1974), resulted in plunging breaking waves at the top of the breaker bar.

Following Svendsen *et al.* (1978), we define the 'break point' as the location where the wave starts to overturn (at x = 53.0 m). The 'plunge point' (x = 55.5 m) is the location where the plunging jet strikes the water surface (Peregrine, 1983). The 'splash point' (x = 58.5 m) is the location where the water mass pushed up by the plunging jet strikes the water surface a second time, and where a surf bore starts to develop (Smith and Kraus, 1991). These regions are used to define the shoaling zone (up to break point; $x \leq 53.0$ m), the breaking region (between break and splash points; $53.0 < x < 58.5$ m) and the inner surf zone (shoreward from splash point; $x >$ 58.5 m) following Svendsen *et al.* (1978). **Figure 4.1b** includes these points and regions for reference.

4.2.2 Instrumentation

Near-bed and outer-flow hydrodynamics and suspended sediment concentrations were measured with a vertical array of acoustic instruments deployed from a custom-built mobile frame (**Figure 4.2**). This frame consisted of stainless-steel tubing with 30 mm diameter and was designed such that it would have minimum flow perturbation while being sufficiently stiff to withstand wave impact. The frame was mounted to a horizontally-mobile trolley on top of the flume, and could be vertically positioned with sub-mm accuracy using a spindle. The mobile frame set-up enabled measurements at various cross-shore positions, while maintaining an

approximately equal elevation of the instrument array with respect to the bed at the start of each run.

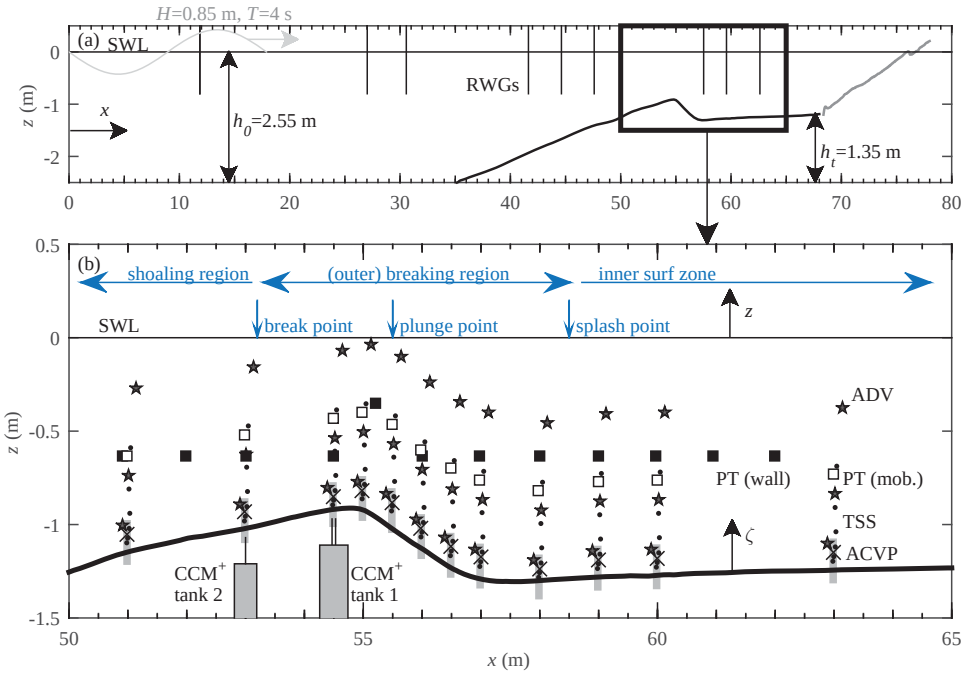

Figure 4.1. Experimental set-up and measurement locations. (a) Reference bed profile (black line) and fixed beach (grey line), plus locations of resistive wave gauges (RWGs, vertical black lines); (b) Measurement positions of ADVs (star symbols), mobile-frame Pressure Transducers (PT, white squares), wall-deployed PTs (black squares), Transverse Suction System nozzles (TSS, black dots), Optical Backscatter Sensor (black crosses), and measuring windows of mobile-frame Acoustic Concentration and Velocity Profiler (ACVP, grey boxes).

The velocity is measured at outer-flow elevations using three acoustic Doppler velocimeters (ADVs) and near the bed with an acoustic concentration and velocity profiler (ACVP), all deployed from the mobile frame. Near-bed sand concentrations are obtained by inverting the reflected ACVP-measured acoustic intensity signal to sand concentration using calibration measurements by a six-nozzle Transverse Suction System (TSS) and an optical backscatter sensor (OBS). More details on the velocity and suspended sediment concentration measurements are found in **Chapter 2** and **Chapter 3**.

Time-varying sediment concentrations in the sheet flow layer were measured using two Conductivity-based Concentration Measurement (CCM^+) tanks (**Figure 4.1b**). These tanks were located at the bar crest at x = 53.0 m (at break point where wave starts to overturn) and at x = 54.5 m (between break point and plunge point). Over the high sand concentrations (100 – 1600 kg/m^3) in the sheet flow layer, the measured conductivity of a water-sand mixture is a linear function of sand concentration, which makes the conductivity-based measuring principle highly suitable for studying sheet flow dynamics (Ribberink and Al-Salem, 1995; Dohmen-Janssen and Hanes, 2002; Lanckriet *et al.*, 2013). The CCM^+ tanks in the present study are equipped with one single conductivity probe plus a combined double probe (for tank 1), or with one single probe (tank 2), and sample with a 1000 Hz data rate. The two sensors of the

combined probe of tank 1 (**Figure 4.2** inset) are spaced 1.5 cm in cross-shore direction and can be used to estimate particle velocities in the sheet flow layer by cross-correlating both sensors' signals (see McLean *et al.*, 2001). The probes penetrate the sheet flow layer from below to minimize flow disturbance.

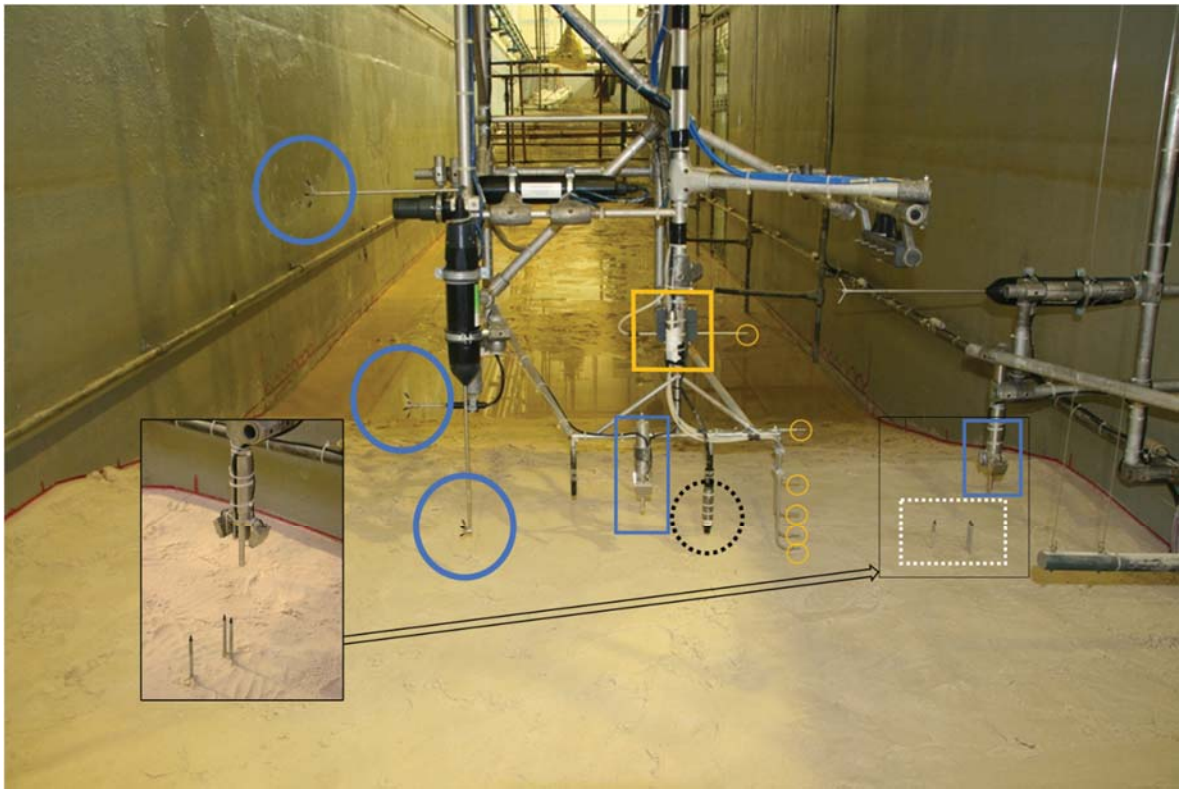

Figure 4.2.Mobile measuring frame and instrumentation. Instrumentation includes three acoustic Doppler velocimeters (ADVs, blue solid circles), one pressure transducer (PT, yellow square), a six-nozzle transverse suction system (TSS, yellow circles), an (black dashed circle) and an acoustic concentration and velocity profiler (ACVP, blue rectangle). Inset shows close-up of CCM+ tank 1 sensors and another ACVP system, deployed from the sidewall. Note that the CCM+ sensors are raised here above the bed; during the experiment the tops of the sensors are within +/- 1 cm from the bed.

The tanks are equipped with a bed level tracking system that enables automatic repositioning of the probes with sub-mm accuracy and which is fully described in van der Zanden *et al.* (2015a). In tracking mode, the probes track the continuous elevation of the bed-water interface, hence they measure the bed evolution at wave-averaged or longer time scales. Alternatively, the user can select to use the probes to measure sheet flow concentrations at a fixed absolute elevation (i.e. no tracking). In the present study, both types of measurements were alternated for fixed intervals of 60 s: sheet flow concentration measurements were obtained at elevations of -2, +0, and +4 mm with respect to the bed; after each of these intervals, the probes were repositioned to the local bed level by activating the tracking system. Through this procedure, concentrations were sampled over the complete sheet flow layer while at the same time the bed level was measured with +/– 1 mm accuracy.

A six-nozzle Transverse Suction System (TSS) was used to collect samples of suspended sediment at $\zeta \approx 0.02$, 0.04, 0.10, 0.18, 0.31 and 0.53 m (see **Chapter 3** for more details). The collected samples were dry-weighted and sealed. The grain size characteristics were determined at the University of Aberdeen using a Beckman Coulter LS 13 320 laser diffraction particle sizer (specifications found in the user manual: Beckman Coulter Inc, 2008). Previous experience using this particle sizer indicated a minimum amount of 2.5 g sand (corresponding to obscuration > 5%) to be required for a reliable estimate of the size distribution. This minimum amount was reached for all TSS samples, except for some of the samples obtained at the furthest offshore location ($x = 51.0$ m) or at elevations above wave trough level. For these combinations of locations/nozzles, samples of different runs but for the same nozzle and cross-shore location were combined to obtain the minimum amount of sand.

The water surface was measured with a combination of resistive wave gauges (RWGs) in the shoaling zone and pressure transducers (PTs) in the breaking and inner surf zone. Bed profile measurements were obtained at 2 cm cross-shore resolution along two transects, at lateral distances of 0.1 and 0.7 m with respect to the flume's centerline, using echo sounders deployed from a second mobile trolley. The echo sounders had an estimated accuracy of +/– 1 cm and the mean of both sensors is used to study the bed profile evolution and net sediment transport rates.

4.2.3 Measurement procedure

One experiment consisted of 90 minutes of waves, divided over six 15-minute runs, during which the bed profile evolved. The bed profile was measured prior to the first run and after every 2nd run, i.e. at $t = 0$, 30, 60 and 90 minutes. After the sixth run, the flume was drained. The reference bed profile, drawn as template on the flume wall, was then restored by shoveling back transported sand and flattening any bed forms that were generated. Each experiment was repeated 12 times, with the mobile measuring frame moved to a new location for each experiment. The bed profile evolution and hydrodynamics were very similar for each experiment (**Chapter 2**) and the adopted procedure resulted in a high spatial coverage of velocity and concentration measurements (**Figure 4.1b**).

Sediment samples of the bed were taken at 12 cross-shore locations at the start of the campaign (corresponding to horizontal test section), after the initial start-up stage (corresponding to reference bed level and $t = 0$ min.) and at the end of the final experimental repeat ($t = 90$ min.). Bed samples were taken at each cross-shore location by carefully scraping off the top layer (1 to 2 cm) of sediment at three positions separated in longshore direction. In the inner surf zone, in occurrence of bed forms, the samples were taken over a complete ripple. When restoring the profile, the sediment was reshuffled by bringing sediment from the shoaling to the inner surf zone and vice versa.

4.2.4 Sediment characteristics

Figure 4.3 shows the cumulative grain-size distribution measured with the laser-diffraction particle sizer for one of the bed samples at the start of the campaign. The accordingly obtained

median sediment diameter (D_{50}) is 0.29 mm. This is somewhat higher than values of 0.25 mm found for the exact same sediment by independent sieving tests at the CIEM lab and by sieving tests by the sediment supplier. This difference is explained by sand grains not being perfect spheres: the particle sizer measures an equivalent 'perfect sphere' diameter; sieving yields the diameter of the smallest cross-sectional area of a non-spherical grain (Eshel *et al.*, 2004). The degree of uniformity is quantified through the geometric method of moments σ_g (Blott and Pye, 2001). With a measured σ_g = 1.36 and following Blott and Pye (2001), the sand is classified 'well sorted'. The sand grains had a measured mean settling velocity of 0.034 m/s.

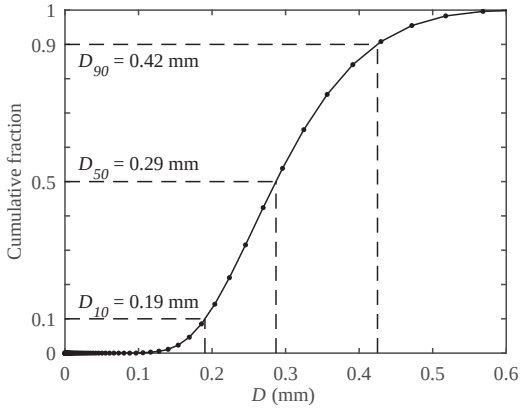

Figure 4.3: Cumulative grain-size distribution of sediment in bed at start of experiment (as obtained with laser-diffraction particle sizer).

4.2.5 Data treatment

Data treatment steps related to hydrodynamics and suspended sediment concentrations and fluxes is described extensively in **Chapter 2 and 3**. These steps are only briefly repeated here.

Visual observations and measurements revealed that a hydrodynamic equilibrium established for each run after approximately 5 minutes. Therefore, only the last 10 minutes of data from each run (corresponding to about 150 wave cycles) were used for analysis. Flume seiching induced a standing wave with an approximately 45-s period. The seiching wave could be identified in auto-spectra of water surface and horizontal velocities, but not in bed level and suspended sediment concentrations. Hence, its effect on sediment processes is considered negligible. The standing wave was removed from water surface and velocity time series by applying a high-pass filter with a cut-off frequency of 0.125 Hz (half the primary-wave frequency).

The phase-averaged value of a variable ψ are annotated with angle brackets and are calculated over N wave repetitions as

$$<\psi>(t)= \frac{1}{N}\sum_{n=1}^{N} \psi(t+(n-1)T) \qquad (4.1).$$

Reference zero-up crossings, required to phase-reference each wave cycle prior to phase-averaging, were based on water surface measurements at x = 47.6 m. Data were phase-

referenced such that t/T=0 corresponds to maximum surface elevation (wave crest) at the beginning of the test section (x = 50.0 m). Phase-averaged horizontal velocities $<u>$ consist of a time-averaged component $\bar{u}$, i.e.

$$\bar{u} = \frac{1}{T}\int_0^T <u(t)>\mathrm{d}t \qquad (4.2),$$

and a periodic component $\tilde{u} = <u> - \bar{u}$. Root-mean-squared $\tilde{u}$ is denoted $\tilde{u}_{rms}$.

The CCM$^+$ tanks were at fixed cross-shore locations during the experiment. Measurements were phase-averaged for each 15-min. stage of bar development over all 12 experimental repeats, resulting in a large number of wave repetitions (N>1000). For the time-varying sheet flow concentration measurements $C(\zeta,t)$, ζ=0 is defined as the bed level during the zero-down crossing of the wave when the bed is considered to be at rest ('immobile bed level'). Intra-wave bed level fluctuations are preserved in phase-averaged results. $C(\zeta,t)$ measurements were bin-averaged, where the bin class was based on the relative elevation ζ and the bin resolution $\Delta\zeta$ = 0.25 mm. For each wave phase and elevation bin, $<C(\zeta_i,t)>$ is calculated as the median of concentration measurements at $\zeta_i - \Delta\zeta/2 < \zeta_i < \zeta_i + \Delta\zeta/2$.

For calculating sand particle velocities in the sheet flow layer, the concentration time series of the two sensors of the combined probe were first high-pass filtered (f_{cutoff} = 1 Hz). The cross-correlation of the two sensors' signals was calculated over regular time intervals Δt = 0.1 s. Each wave cycle was assigned a concentration bin class (bin resolution ΔC = 0.1 m^3/m^3) based on wave-averaged concentration. The cross-correlation output was then averaged for each ΔC bin class and each wave phase $\Delta t/T$. The bin-averaged cross-correlation is used to quantify the time lag between both signals, which with known distance between the sensors is translated into a particle velocity (see further McLean *et al.*, 2001; van der Zanden *et al.*, 2015a).

Volumetric total sediment transport rates q_{tot}, due to contributions by both bedload and suspended load, can be obtained from measured bed profile measurements z_{bed} by solving the Exner equation:

$$q_{tot}(x) = q_{tot}(x - \Delta x) + \Delta x(1 - \varepsilon_0)\frac{\Delta z_{bed}(x)}{\Delta t} \qquad (4.3).$$

Here, ε_0 is the sand porosity (0.6 if loosely packed), Δx is the horizontal resolution of z_{bed} measurements (=0.02 m) and Δt is the time interval between two consecutive profile measurements (30 min.). Equation 4.3 can be solved if q_{tot} is known at one x location. With q_{tot} = 0 at the left-hand (i.e. x = 35 m) and right-hand boundary (x = 68 m) of the mobile test section, q_{tot} can be solved iteratively by starting from either the left- or the right-hand side of the profile. This yields two estimates of q_{tot}, annotated q_{lhs} and q_{rhs} respectively. The estimates q_{lhs} and q_{rhs} are likely different due to variations in the horizontally-integrated volume of the two profile measurements used to quantify Δz_{bed}. These variations can be attributed to sampling errors of the acoustic sensors, 3D bed forms, variations in packing density and porosity, and non-uniformity of the bed profile (e.g. Baldock *et al.*, 2011). Depending on distance to each horizontal boundary of the test section, q_{lhs} or q_{rhs} is considered more accurate. Therefore, the volumetric total transport rate q_{tot} used in the present study was calculated as the weighted average of both estimates:

$$q_{tot}(x) = \left(\frac{x_{end} - x}{x_{end} - x_0}\right) q_{lhs}(x) + \left(\frac{x - x_0}{x_{end} - x_0}\right) q_{rhs}(x) \quad (4.4),$$

with x_0 = 35 m and x_{end} = 68 m being the left- and right-hand boundary of the mobile bed profile, respectively. The transport rate $q_{tot}(x)$ was calculated for each experimental repeat and was then averaged over all repeats.

4.3 Hydrodynamics and bed profile evolution

This section presents an overview of the main hydrodynamics and the bed profile evolution. The reader is referred to **Chapter 2** for a more detailed description of the near-bed hydrodynamics (including turbulence) in the present experiment and to Van der A *et al.* (submitted) for an extensive analysis of the outer-flow hydrodynamics for an accompanying rigid-bed experiment with the same bed profile and wave conditions.

4.3.1 Hydrodynamics

Table 4.1 presents an overview of the main hydrodynamic parameters at the 12 measurement locations. **Figure 4.3a** shows the wave height H and time-averaged water level $\bar{\eta}$. The wave height reduces by 50% between the break point (around x = 53.0 m) and splash point (x = 58.5 m). Water levels $\bar{\eta}$ show a set-down at the shoaling locations and set-up at the inner surf zone. **Figure 4.3b** shows time-averaged velocity $\bar{u}$ and maximum onshore and offshore horizontal velocity $\langle u \rangle_{max}$ and $\langle u \rangle_{min}$. These values are measured at the wave bottom boundary layer (WBL) overshoot elevation δ ($\zeta \approx 0.02$ m) and are averaged over the complete experiment (t = 0 – 90 min., i.e. over six runs). Along the offshore slope up to the bar crest (x=51.0–55.0 m), $\langle u \rangle_{max}$ and $\langle u \rangle_{min}$ remain roughly constant. Time-averaged velocity magnitudes are lowest at x = 51.0 m and increase towards the bar crest. The skewness and asymmetry of $\tilde{u}$ (**Table 4.1**) show that the intra-wave shape of $\tilde{u}$ changes significantly along the offshore slope. Most notable is the large asymmetry at x = 53.0 m at the onset of breaking-wave overturning. Along the shoreward-facing bar slope (x = 55.5 to 58.0 m), the combination of decreasing H and increasing h leads to a substantial decrease in orbital velocity amplitude while at the same time the magnitudes of offshore-directed time-averaged velocity $\bar{u}$ (undertow) increases. Undertow velocity magnitudes decrease in the inner surf zone (x > 58.5 m).

Turbulent kinetic energy (TKE) is calculated through a Reynolds decomposition of the velocity time series (**Chapter 2**). **Figure 4.3c** shows the time-averaged TKE ($\bar{k}$) at outer-flow elevation and close to the bed. The latter, k_b, is defined here as the maximum $\bar{k}$ measured inside the WBL. Turbulence production by wave breaking leads to large magnitudes of outer-flow $\bar{k}$ near the plunge point at x = 55.5 m. $\bar{k}$ decreases towards the bed at most locations, which indicates that wave breaking is the primary source of turbulence. Breaking-generated turbulence is advected to offshore locations while gradually dissipating, and consequently, $\bar{k}$ decreases from the breaking zone in the offshore direction (from x = 55.5 to 51.0 m). Turbulent kinetic energy inside the WBL (k_b) follows a similar cross-shore pattern as outer-flow $\bar{k}$, i.e. it increases by an order of magnitude between the shoaling zone at x = 51.0 m to the breaking region at x = 56.0 m. This increase occurs in spite of a decrease in $\langle u \rangle_{max}$ and $\langle u \rangle_{min}$, which suggests that the increase in k_b is due to the invasion of breaking-generated turbulence into the WBL. Further

shoreward, k_b decreases above the bar trough (around x = 58.0 m) and increases gradually throughout the inner surf zone (x > 58.5 m) due to the presence of sand ripples.

Table 4.1. Hydrodynamic and bed parameters at each measurement location: water depths (h); wave heights (H); ADV-measured velocity statistics at ζ=0.11 m, with maximum onshore and offshore phase-averaged horizontal velocity, semi-excursion length ($a = \sqrt{2}T\tilde{u}_{rms}/2\pi$), velocity skewness ($Sk(u) = \overline{\tilde{u}^3}/\tilde{u}_{rms}{}^3$), velocity asymmetry ($Asy(u) = -\overline{\mathcal{H}(\tilde{u})^3}/\tilde{u}_{rms}{}^3$, where $\mathcal{H}$ marks Hilbert transform (e.g. Ruessink et al., 2011)), local bed slope $\tan(\alpha) = dz_{bed}/dx$ at start (t=0 min.) and end (t=90 min.) of experiment. Hydrodynamic parameters are measured during the first run of each experimental repeat (t = 0-15 min.).

x (m)	h (m)	H (m)	$\bar{u}$ (m/s)	$<u>_{max}$ (m/s)	$<u>_{min}$ (m/s)	a (m)	$Sk(u)$	$Asy(u)$	$\tan(\alpha)$, t=0 min.	$\tan(\alpha)$, t=90 min.
51.0	1.10	0.79	-0.13	1.04	-0.83	0.54	0.61	0.68	0.08	0.12
53.0	0.97	0.74	-0.22	0.80	-0.94	0.48	0.44	1.01	0.06	0.12
54.5	0.88	0.64	-0.19	0.84	-0.85	0.47	0.50	0.82	0.04	0.06
55.0	0.88	0.60	-0.24	0.78	-0.90	0.47	0.48	0.76	-0.10	0.03
55.5	0.97	0.51	-0.23	0.57	-0.83	0.39	0.36	0.75	-0.22	-0.12
56.0	1.10	0.50	-0.30	0.25	-0.82	0.31	0.06	0.77	-0.20	-0.45
56.5	1.19	0.53	-0.51	0.05	-0.83	0.25	0.67	0.76	-0.18	-0.51
57.0	1.24	0.48	-0.54	0.02	-0.78	0.23	0.95	0.58	-0.08	-0.35
58.0	1.28	0.47	-0.46	0.01	-0.71	0.21	0.82	0.79	0.02	0.11
59.0	1.28	0.43	-0.36	0.13	-0.71	0.23	0.39	0.88	0.02	0.16
60.0	1.26	0.42	-0.36	0.17	-0.66	0.24	0.67	0.68	0.03	0.02
63.0	1.26	0.41	-0.34	0.19	-0.58	0.23	0.79	0.45	0.01	0.01

4.3.2 Bed profile evolution and net total transport

Figure 4.4a shows the bed profile evolution. The bar crest grows and migrates slightly onshore during the experiment. This leads to an increase in the bar's offshore slope from $\tan(\alpha)$=0.10 to 0.13 and an increase in the surf similarity parameter ξ_0 from 0.54 to 0.68. At the same time the bar trough deepens, resulting in a steepening of the shoreward slope of the breaker bar from $\tan(\alpha)$ = –0.21 to –0.47. At t=90 minutes, this slope approaches the natural angle of repose ($\tan(\alpha) \approx$ 0.5 to 0.7) for sandy materials (Nielsen, 1992). Table 4.1 includes the local bed slope at the start and end of the experiment for each measurement location.

Bed forms were observed after draining the flume. The bed was flat in the shoaling region and at the bar crest (x = 48.0 to 55.5 m), indicating bedload transport in the sheet flow regime. Quasi-2D bed forms (quasi-uniform in longshore direction) were identified along the shoreward slope of the bar (x = 55.5 to 57.0 m), where they migrated progressively offshore. Shoreward-facing lunate-shaped bed forms were formed at the bar trough (x = 57.0 to 59.0 m). At the inner surf zone a gradual transition to quasi-2D bed features occurs (from x = 59.0 to 62.0 m). Further shoreward these features became increasingly irregular while their wave length reduced, resulting in 3D sand ripples (x = 62.0 m to 68.0 m). In the inner surf zone (x > 58.5 m) bed form lengths were of similar magnitude as the orbital semi-excursion length a. The bed forms in the breaking region have lengths that exceed a by a factor 2 to 5.

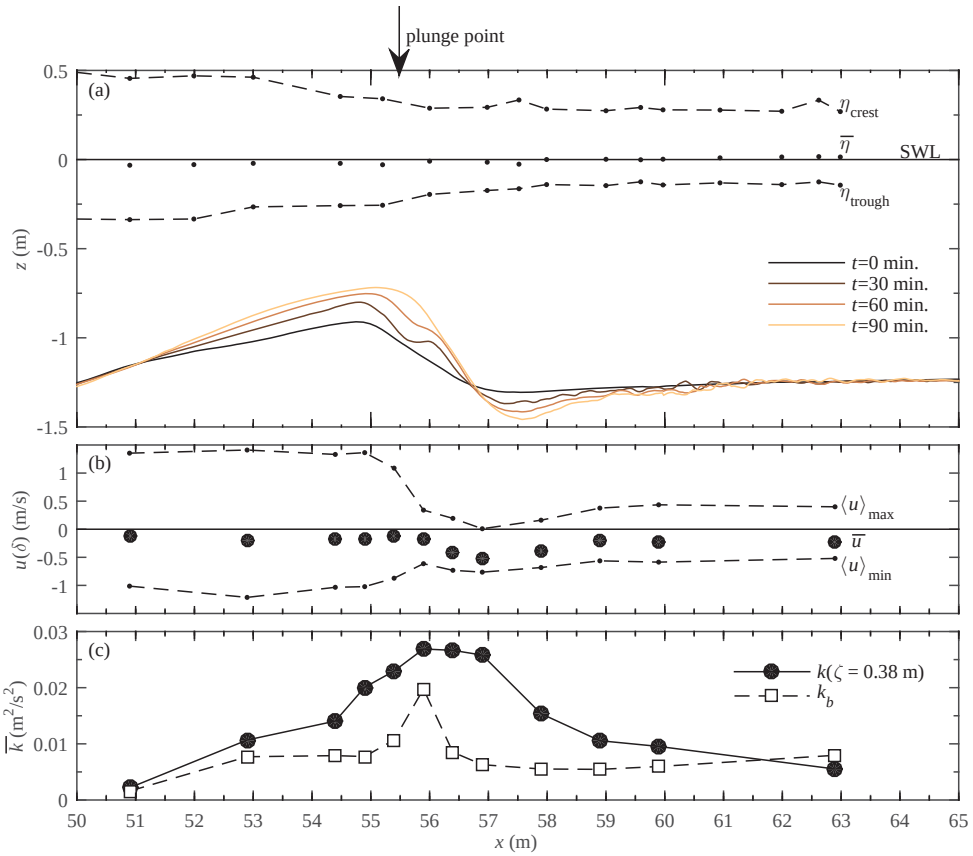

Figure 4.4. (a) Bed profile evolution (solid lines, with each line representing the mean value over all experimental days), and water levels for t=0–15 min. (dots and dashed lines depict time-averaged and envelope, respectively); (b) ACVP-measured horizontal velocity at the WBL overshoot elevation ζ=δ, for t= 0–90 min., time-averaged (circles) and maximum phase-averaged onshore and offshore velocity (dots and dashed line); (c) Turbulent kinetic energy, mean values over experiment (t=0–90 min.) at outer-flow elevation ζ = 0.38 m (measured with ADV, solid line + circles) and inside the WBL (measured with ACVP, dashed line + squares).

The bar growth can be explained by accumulation of primarily onshore-directed total transport at shoaling locations and offshore-directed transport in the breaking and inner surf zone (**Figure 4.5**). The reversal of transport direction occurs near the breaker bar crest (x = 54.5 m), about 1 m offshore from the plunge point. The sharp gradients dq_{tot}/dx at the breaking region are indicative of a strong cross-shore non-uniformity in sand transport processes. Note that q_{tot} is not constant throughout the experiment; instead, the magnitudes of onshore and offshore q_{tot} decrease as the breaker bar evolves towards a semi-equilibrium state (Van der Zanden *et al.*, 2015b). This morphologic feedback of profile evolution on time-evolving transport rates is not further considered in the present study.

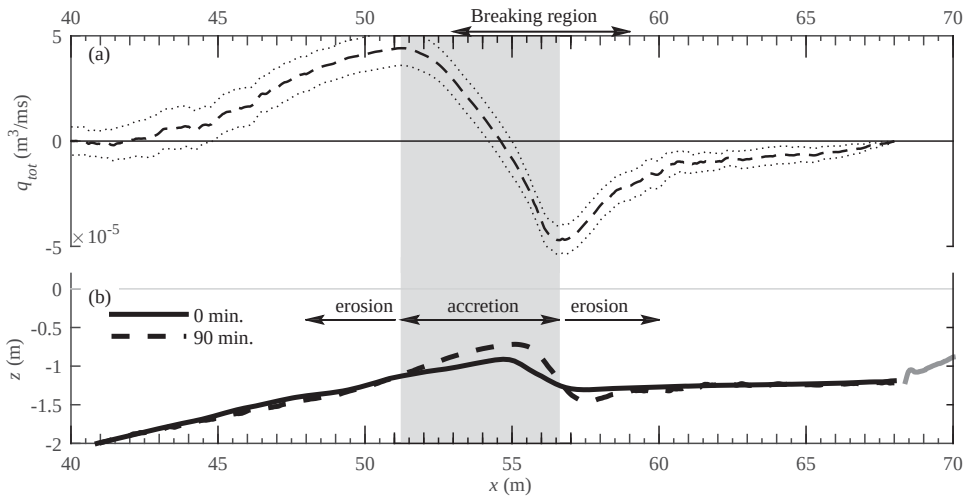

Figure 4.5. (a) Total transport during experiment (t=0–90 min.) obtained through Equation 4.4, mean values (dashed) +/- 95% confidence interval (dotted) over all experimental repeats; (b) Initial (solid) and final (dashed) bed profile. The grey shading marks the region of net accretion.

4.4 Bedload transport processes

This section first presents and discusses sheet flow measurements (Sections 4.4.1 to 4.4.3) which are compared with oscillatory sheet flow observations in tunnels and under non-breaking waves to assess the effects of wave breaking. Next, Section 4.4.4 presents the cross-shore-varying bedload transport rates and relates these to the near-bed hydrodynamics.

4.4.1 Sheet flow layer concentrations

The sheet flow layer behavior is explored using CCM$^+$ measurements at two locations near the breaker bar crest, i.e. at x = 53.0 m (below break point) and x = 54.5 m (between break point and plunge point). **Figure 4.6c,d** shows phase-averaged concentrations $\langle C(\zeta,t)\rangle$, bin-averaged for vertical elevations ζ with bin resolution $\Delta\zeta$ = 0.25 mm and based on a minimum of three wave repetitions. Due to the chosen settings for probe repositioning during acquisition, this minimum was not obtained for each ζ bin class (which explains the data gaps e.g. at $\zeta \approx 2$ mm, **Figure 4.6c**). **Figure 4.6e,f** also shows concentration time series, but for these panels C was bin-averaged based on the *wave-averaged* concentration. The latter approach preserves the temporal variation in C that occurs at intra-wave time scale and it has been adopted throughout many sheet flow studies (Ribberink and Al-Salem, 1994; O'Donoghue and Wright, 2004a; Schretlen, 2012). This approach is especially useful to study phase lags between the upper sheet flow layer (region above the 'immobile bed level', i.e. $\zeta > 0$, with typical concentrations lower than 0.3 m^3/m^3) and the erosion layer ($\zeta < 0$, C>0.3 m^3/m^3).

Despite sheet flow layers being rather thin, of O(mm), the CCM$^+$ manages to resolve the time-varying concentrations adequately. This is partly ascribed to the new automatic probe

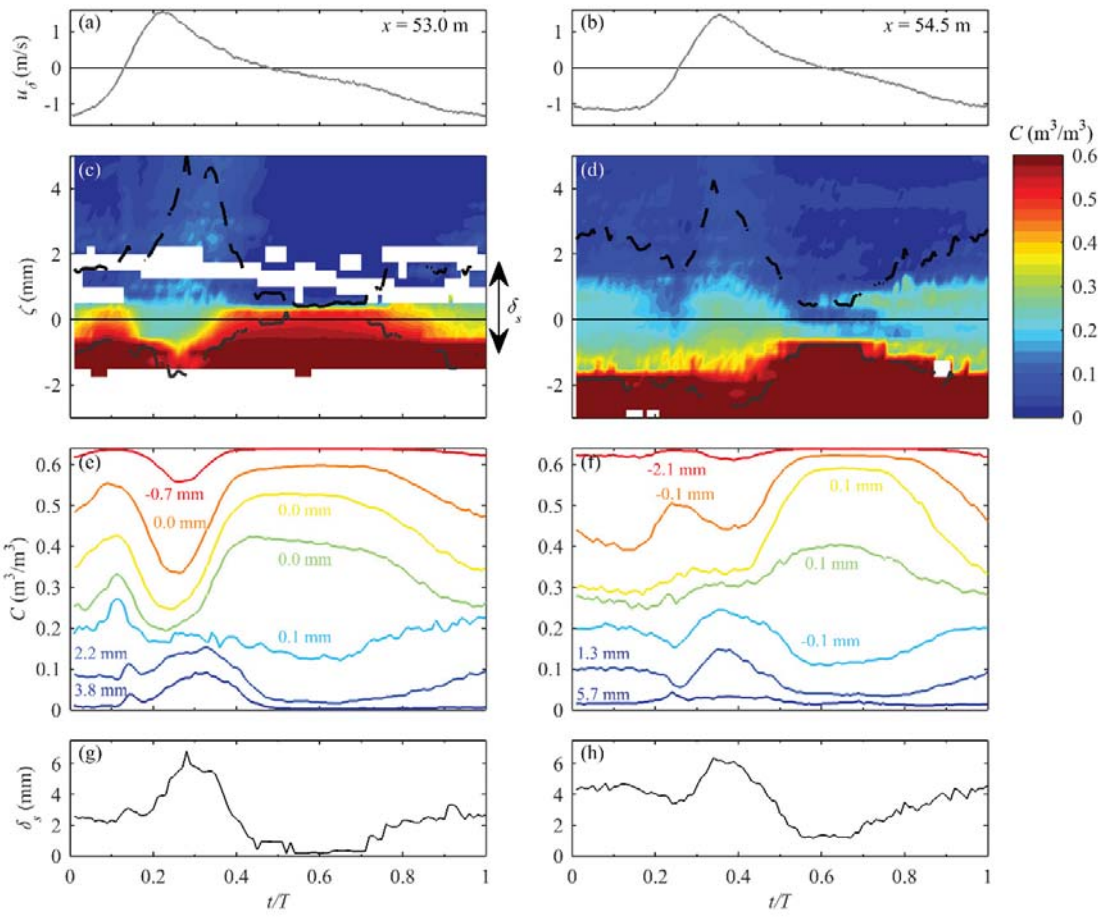

Figure 4.6. Time series of phase-averaged CCM+ measurements at x=53.0 m (left) and x=54.5 m (right), for final stage of bar development (t=75–90 min). (a,b) ACVP-measured velocities at ζ=δ. (c,d) Concentration contour, with dashed black lines marking bottom and top of sheet-flow layer (see text); (e,f) Concentration time series, obtained through bin-averaging, at 7 different relative elevations. These elevations are indicated in the panel and have a typical standard deviation of +/- 1 mm; (g,h) Sheet flow layer thickness.

repositioning system, which allows measurements of the time-varying relative bed level with higher accuracy than previous versions of the CCM system. At both CCM+ locations, instances of peak offshore and onshore velocities lead to a quasi-instantaneous concentration decrease in the erosion layer (C<0.3 m³/m³) and a simultaneous increase in the upper sheet flow layer (C<0.3 m³/m³). The erosion layer responds layer by layer to velocity forcing, i.e. concentrations at elevations deeper in the erosion layer (ζ≈-2 to -1 mm) respond slightly later than concentrations near ζ = 0. Hence, no evidence of plug flow (Sleath, 1999) is found, despite Sleath parameters estimated from flow acceleration reach magnitudes (up to 0.3) that are well above proposed critical thresholds for plug flow (Foster *et al.*, 2006). The short increase in upper sheet flow layer sediment concentration around flow reversal (t/T = 0.17) at x = 53.0 m has also been observed in oscillatory sheet flow conditions and may relate to shear instabilities around flow reversal (Ribberink and Al-Salem, 1995; O'Donoghue and Wright, 2004a).

4.4.2 Sheet flow layer thickness

The time-varying sheet flow layer δ_s is the difference between the intra-wave time-varying bottom (i.e. erosion depth, with $<C> = 0.60$ m^3/m^3) and the top of the sheet flow layer (i.e. the elevation with $<C> = 0.08$ m^3/m^3; Dohmen-Janssen and Hanes, 2002). These elevations were established by fitting the empirical function of O'Donoghue and Wright (2004a) for vertical sheet flow concentration profiles through the time-varying concentration measurements (the approach is described more extensively in Van der Zanden *et al.*, 2015a). The function fitted well through the measurements ($r^2 > 0.9$ for each profile). **Figure 4.6c,d** includes the time-varying erosion depth and top of the sheet flow layer and **Figure 4.6g,h** shows the intra-wave sheet flow thickness δ_s.

The sheet flow thickness shows similar phase behavior as the near-bed velocity magnitude, which again illustrates the quasi-instantaneous response of sheet flow pick-up to near-bed velocity. At $x = 53.0$ m, δ_s returns to near zero during the *crest-to-trough* flow reversal, which indicates that most of the sediment that was entrained from the bed to the upper sheet flow layer during the crest phase, has settled down once the flow reverses. At $x = 54.5$ m, δ_s is about 1.5 mm (i.e. non-zero) during the crest-to-trough flow reversal, possibly due to the significant deposition rate (about –0.2 kg/m^{2}s) of suspended sediment at this location during this phase of the wave cycle (**Chapter 3**).

At both locations, the non-zero δ_s around *trough-to-crest* flow reversal indicates that a major fraction of sediment particles that have been entrained during the trough phase has not fully settled as the crest phase begins. This lagging of sheet flow layer concentration is caused by the relatively short time interval between maximum offshore and maximum onshore velocities in highly acceleration-skewed flows (Watanabe and Sato, 2004; Van der A *et al.*, 2009; Ruessink *et al.*, 2011). Maximum sheet flow thicknesses at both locations are higher during the crest than during the trough phase. This can be attributed to skewness in near-bed velocities and in accelerations, both leading to higher bed shear stress during the crest phase. Surprisingly, δ_s during the trough phase reaches larger values at $x = 54.5$ m than at $x = 53.0$ m, despite trough-phase velocity magnitudes being significantly higher at $x = 53.0$ m.

To assess whether wave breaking affects the sheet flow layer thickness, δ_s is quantitatively compared with predictions by two empirical formulations for maximum δ_s that have been proposed on the basis of detailed laboratory measurements using well-sorted sand and regular oscillatory and wave conditions: firstly, the formulation by Ribberink *et al.* (2008) based on oscillatory tunnel data:

$$\delta_s/D_{50} = 10.6\,\theta \qquad (4.5),$$

and secondly, Schretlen's (2012) formulation based on uniform non-breaking waves measurements:

$$\delta_s/D_{50} = 13.1\,\theta^{0.7} \qquad (4.6).$$

The Shields parameter θ is the non-dimensional bed shear by phase-averaged velocities, i.e. $\theta = \tau_b/(\varrho_s - \varrho)gD_{50}$, with ϱ_s (=2650 kg/m^3) and ϱ (=1000 kg/m^3) being the densities of sediment particles and water, respectively, and g (=9.81 m/s^2) is the gravitational acceleration. The bed

shear stress τ_b is estimated based on the horizontal velocity at $\zeta = \delta$ through $\tau_b = 0.5 f_{wc} u(\delta)^2$. The methodology described by Ribberink (1998) is applied to calculate the wave-plus-current friction factor f_{wc} as a linear combination of the wave friction factor f_w and the current friction factor f_c. The wave friction factor f_w is calculated based on the widely used formulation by Swart (1974), modified to account for acceleration skewness (da Silva *et al.*, 2006; van der A *et al.*, 2013):

$$f_w = 0.00251 \exp\left[5.21 (2T_a)^{-0.49} \left(\frac{a}{k_{sw}}\right)^{-0.19}\right] \qquad (4.7),$$

with k_{sw} being the bed roughness, calculated iteratively as a function of the Shields parameter (see Ribberink, 1998), and T_a is the relative time duration of accelerating flow within a half-cycle. In the present study, T_a equals approximately 0.3 during the crest phase and 0.6 during the trough phase. This yields friction factors f_w that are approximately 30% higher for the crest phase and 6% lower for the trough phase compared to f_w calculated without acceleration-skewness correction (i.e. $T_a = 0.5$ in Equation 4.7). The maximum bed shear θ_{max} and sheet flow thickness δ_s are derived per half cycle and for each 15-minute stage of bar development, yielding a total of 24 data points.

Figure 4.7 shows measured δ_s versus θ_{max}. The predictions by Equations 4.5 and 4.6 describe the measured data reasonably well. This suggests that δ_s in the present breaking-wave conditions is consistent with previous observations in oscillatory flow tunnel and non-breaking wave conditions. Apparently, the effects of the sloping bed, the presence of breaking-generated turbulence in the WBL, and of horizontal sediment advection, generally have minor effects on the sheet flow layer thickness. An exception occurs at $x = 54.5$ m, where trough-phase δ_s exceeds predictions of Equation 4.5 and Equation 4.6 by 75% and 35%, respectively.

Near-bed (breaking-generated) TKE could be postulated as a factor contributing to increased δ_s (e.g. Lanckriet and Puleo, 2015). At this location, $\langle k_b \rangle$ for both half cycles is much higher than at the reference shoaling zone location (x = 51.0 m) where TKE is predominantly bed-generated (**Chapter 2**). Consequently, the presence of breaking-generated turbulence would expectedly lead to similar qualitative effects on δ_s during both half cycles. Since δ_s exceeds empirical predictions only during the trough phase, it is not likely that the increased δ_s is purely due to the presence of breaking-generated turbulence. The increase in δ_s may also be explained by non-uniform advection of sediment along the bed. It was shown for the present study that suspended sediment entrained under the plunge point is carried offshore to shoaling locations by undertow and periodic velocities during the trough phase, leading to a significant horizontal influx of sediment at $x = 54.5$ m between $t/T = 0$ and 0.3 (**Chapter 3**). It is likely that this cross-shore influx of sediment is not limited to suspended sediment, but also affects sediment concentrations in the sheet flow layer during the same time interval (see **Figure 4.6d,f**). This means that sheet flow concentrations are not fully controlled by local hydrodynamic forcing but instead, are affected by the intra-wave cross-shore sediment advection.

The empirical formulations in Equations 4.5 and 4.6 have never been validated for progressing asymmetric waves inducing strong near-bed acceleration skewness. Due to the scatter of the data and the limited range of hydrodynamic forcing covered in the present study, it cannot be

concluded whether the relation between δ_s and θ in **Figure 4.7** is linear. Although the formulation of Schretlen (2012) performs slightly better than the one of Ribberink *et al.* (2008), we remark that neither of the two original formulations were developed for acceleration-skewed flows. If the acceleration correction is dismissed (i.e. by setting T_a = 0.5 in Equation 4.7), the estimated crest-phase θ decreases while the trough-phase θ increases. In that case, as can be concluded from **Figure 4.7**, the data points approach the Ribberink *et al.* (2008) predictions more closely but move away from Schretlen's (2012) predictions.

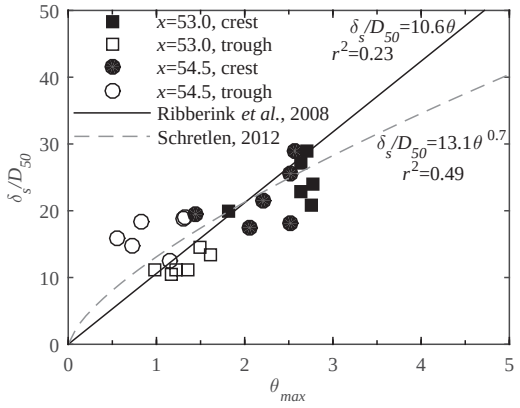

Figure 4.7. Maximum sheet flow layer thickness versus maximum Shields stress per wave half-cycle. Also included are empirical relations proposed by Ribberink et al., 2008 (solid line) and Schretlen, 2012 (dashed line).

4.4.3 Sheet flow particle velocities and fluxes

Particle velocities $u_p(\zeta)$ across the sheet flow layer were estimated for CCM+ tank 1 at x = 54.5 m through cross-correlation of concentration measurements by two probes aligned in wave direction (see Section 4.2.5). Inherent to the applied CCM cross-correlation technique is that reliable estimates of particle velocities can only be obtained when the sheet flow layer is well-developed (c.f. Dohmen-Janssen and Hanes, 2002). Because the sheet flow layer in the present study is rather thin, u_p could only be measured around instances of maximum onshore/offshore velocity. We focus here on the final run (t = 75–90 minutes) when near-bed velocities were highest and the best measurements of u_p are obtained.

Figure 4.8a shows phase-averaged particle velocities for t = 75–90 min. Reliable estimates of u_p were obtained for phases with δ_s roughly exceeding 4 mm. The particle velocities are in phase with near-bed water velocity and increase in magnitude with distance away from the bed. Magnitudes of u_p are typically about 40-70% of the near-bed flow velocity at $\zeta = \delta$. These relative magnitudes and the vertical structure are both consistent with previous observations of oscillatory sheet flows (e.g. McLean *et al.*, 2001; Dohmen-Janssen and Hanes, 2002; Dohmen-Janssen and Hanes, 2005).

The particle velocities were multiplied with corresponding concentrations to obtain horizontal sediment fluxes ϕ_x (Figure 4.8**b**). Highest sediment fluxes are found deep in the erosion layer because concentrations increase rapidly towards the bed while the vertical decay of velocities is much more gradual. Note that flux magnitudes in the sheet flow layer (100–500 kg/m²s) are

orders of magnitude higher than horizontal suspended sediment fluxes measured just above the WBL at the same location (1–10 kg/m²s) (**Chapter 3**).

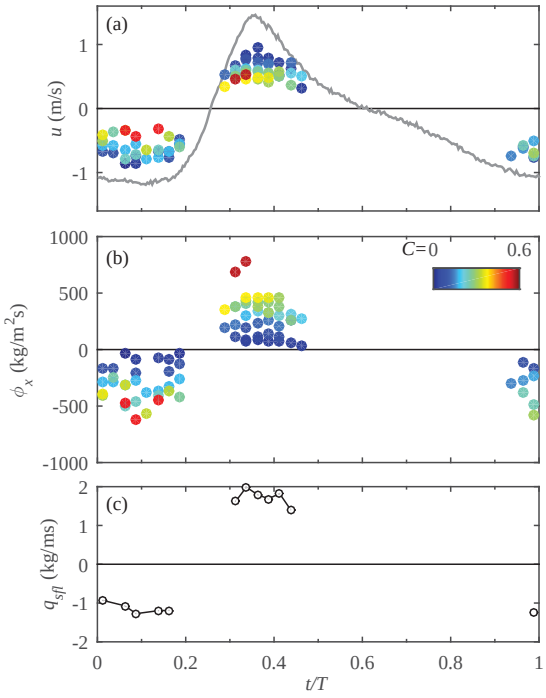

Figure 4.8. Sheet flow particle velocities and sediment fluxes measured with CCM⁺ at x=54.5 m, for t = 75-90 min. (a) ACVP-measured velocities at $\zeta=\delta$ (line) and particle velocities measured with CCM⁺ for eight concentration bin classes (circles, with color coding indicating the volumetric concentration, see color bar in panel b); (b) Flux measurements, as product of CCM⁺-measured particle velocities and concentrations; (c) Time-varying depth-integrated transport over the sheet-flow layer.

The time-varying total transport $q_{sfl}(t)$ was estimated as the depth-integrated product of measured concentrations C and estimated particle velocities u_p over the sheet flow layer, i.e. from the erosion depth z_e to the top of the upper sheet flow layer z_t:

$$q_{sfl}(t) = \int_{z_e}^{z_t} u_p(\zeta, t)C(\zeta, t)\mathrm{d}\zeta \qquad (4.8).$$

The full $u_p(\zeta,t)$ profile was obtained by fitting an empirical power-law distribution, proposed by Sumer *et al.* (1996), through the measurements:

$$u_p(\zeta) = m\cdot\zeta^n \qquad (4.9),$$

with m and n as fitting parameters. Equation 9 was log-fitted for each phase with a minimum of three $u_p(\zeta)$ measurements and accepted only if $n > 0$, yielding fitted $u_p(\zeta)$ profiles for 12 out of 40 wave instants with an average $r^2 = 0.62$. The accordingly obtained velocity distributions may not be fully correct but are considered sufficiently accurate for estimating the magnitude of $q_{sfl}(t)$.

Results of $q_{sfl}(t)$ in Figure 4.8**c** show that instantaneous transport rates during the crest phase exceed those during the trough phase with about 50%. This is consistent with δ_s being larger during the crest phase. Indeed, **Figure 4.8b** shows that sediment fluxes associated with a particular concentration are of similar magnitude during trough and crest phase. Hence, the vertical profile of horizontal fluxes is of similar shape during both crest and trough phase, and the larger sheet flow thickness during the crest phase leads to flux profiles that are vertically stretched and yield larger transport rates. It is further interesting to note that $q_{sfl}(t)$ is of O(1–2 kg/ms), which is of similar magnitude as the depth-integrated outer-flow suspended load transport $q_s(t)$ at this location (approximately 2.0 (+/- 0.2) kg/ms, **Chapter 3**).

Averaging $q_{sfl}(t)$ over the wave period yields a rough approximation of the time-averaged transport in the sheet flow layer $\overline{q_{sfl}}$, excluding transport contributions around flow reversals when u_p could not be measured. Estimated $\overline{q_{sfl}}$ = 0.03 (+/- 0.1) kg/ms, i.e. the net transport over a wave cycle is two orders of magnitude lower than the instantaneous transport rate during the half cycles.

4.4.4 Net bedload transport rates

The total net (i.e. wave-averaged) transport rate q_{tot} is formed by a depth-integrated suspended load (q_s) and a bedload (q_{bed}) contribution. Direct measurement of the bedload transport rate in oscillatory conditions is generally very difficult, because the transport is confined to layers of O(sub-mm) which cannot be accurately resolved by most measuring instruments. The CCM$^+$ is one of the few instruments capable of measuring q_{bed} in sheet flow conditions, provided that sheet flow layers are sufficiently developed (δ_s > 4 mm). Most previous laboratory studies focusing on bedload transport rates could assume negligible suspended load transport (i.e. $q_{bed} \approx q_{tot}$), allowing quantification of q_{bed} from bed profile measurements (i.e. through Equation 4.3). However, the breaking waves in the present study bring large amounts of sediment into suspension and consequently, q_s cannot be neglected. Following previous surf zone studies (Grasmeijer and Van Rijn, 1997; van der Werf *et al.*, 2015), q_{bed} is estimated at each location as the difference between the total transport (Equation 4.3) and the suspended transport rates:

$$q_{bed}(x) = q_{tot}(x) - q_s(x) = q_{tot}(x) - \int_{z_a}^{\eta_{crest}} \overline{u(x,\zeta)C(x,\zeta)}\,\mathrm{d}\zeta \qquad (4.10).$$

The net suspended transport rate q_s was estimated in **Chapter 3** as the time-averaged cross-shore sediment flux, depth-integrated from a near-bed reference elevation z_a that defines the boundary between the bedload layer (ζ<z_a) and the suspension layer (ζ<z_a) up to wave crest level η_{crest}. The reference elevation z_a = 0.005 m, which roughly equals the maximum elevation of the sheet flow layer across the test section. The possible sources of measurement errors for q_{bed} are addressed in Section 4.7 (Discussion).

Figure 4.9a presents q_{bed} across the breaker bar. The standard deviation over the six measurements of q_{bed} at each location equals 0.04 kg/ms on average, which includes the variability due to the morphologic feedback by the bed profile evolution. The figure includes the time-averaged sheet flow layer transport measured with the CCM$^+$, $\overline{q_{sfl}}$ = 0.03 kg/ms. Note

the wide error margins (+/- 0.1 kg/ms) of this measurement, which illustrate the difficulties of obtaining direct measurements of bedload transport rates. At this location, Equation 4.10 yields q_{bed} = 0.07 (+/- 0.04) kg/ms, which is close to the estimated $\overline{q_{sfl}}$ and within the latter's error margins. The bedload transport rates (**Figure 4.9a**) can be explained in terms of hydrodynamic parameters, i.e. the onshore and offshore phase-averaged velocity (**Figure 4.9b**) and the dimensional periodic velocity skewness $\overline{\langle\tilde{u}\rangle^3}$ and the dimensional acceleration skewness – $\overline{\mathcal{H}(\langle\tilde{u}\rangle)^3}$ (where $\mathcal{H}$ is the Hilbert transform, see e.g. Ruessink *et al.*, 2011) (**Figure 4.9c**).

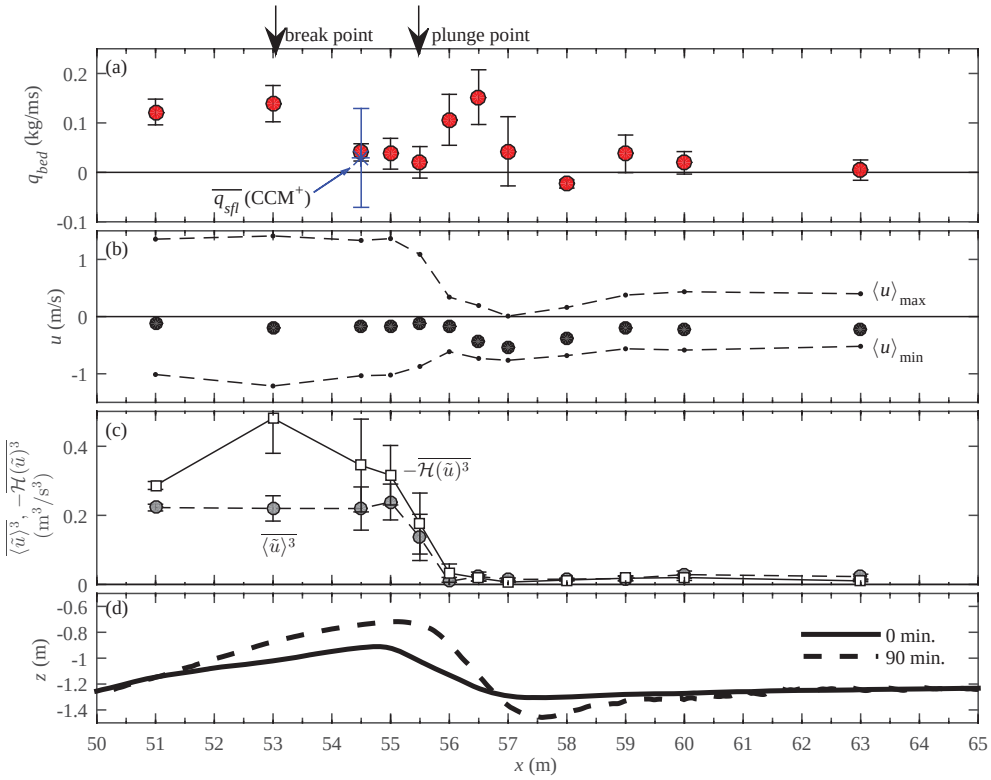

Figure 4.9. Bedload transport rates across the bed profile. (a) q_{bed}, mean (red circles) plus 95% confidence interval (error bars) over six runs per location. Also included is the time-averaged sheet flow transport measured with CCM+ at x = 54.5 m for t = 75–90 min. (blue star, with error bars indicating the estimated error = +/- 0.1 kg/ms); (b) Horizontal velocity at the WBL overshoot elevation, time-averaged (black circles) and maximum onshore and offshore phase-averaged (dots and dashed lines) for t = 0-90 min; (c) Dimensional velocity skewness (circles) and dimensional acceleration skewness (squares) at the WBL overshoot elevation, mean values over six runs plus 95% confidence interval (error bars); (d) Bed profiles at start (solid) and end (dashed) of experiment.

At x = 51.0 m, q_{bed} is positive (i.e. onshore), which is explained by the strong velocity- and acceleration-skewness of near-bed velocities and the relatively low magnitude of time-averaged undertow velocities (**Table 4.1**). Note that this location corresponds roughly to the location of maximum q_{tot} as obtained from bed profile measurements (**Figure 4.5**). Magnitudes of q_{bed} are similar at x = 53.0 m (below break point), where the dimensional acceleration skewness is maximum. Towards the bar crest (x = 54.5–55.0 m), q_{bed} decreases, which may be

caused by the horizontal influx of sediment during the wave trough phase as discussed in detail in the Discussion section (Section 4.7).

Shoreward from the plunge point and along the lee-side slope of the bar, q_{bed} increases significantly. Note that $q_{bed} > 0$ while near-bed velocities are predominantly negative. Hence, the onshore transport is likely due to the large steepness of the bar, which approaches the natural angle of repose and induces downward (onshore) bedload transport by gravity. The breaker trough (x = 58.0 m) is the only location where q_{bed} is directed offshore. This is explained by the combination of the positive bed slope dz_{bed}/dx and the strong offshore-directed undertow velocities relative to periodic velocities. Further shoreward, at the inner surf zone (x = 59.0 – 63.0 m), q_{bed} is again shoreward-directed with magnitudes gradually approaching zero.

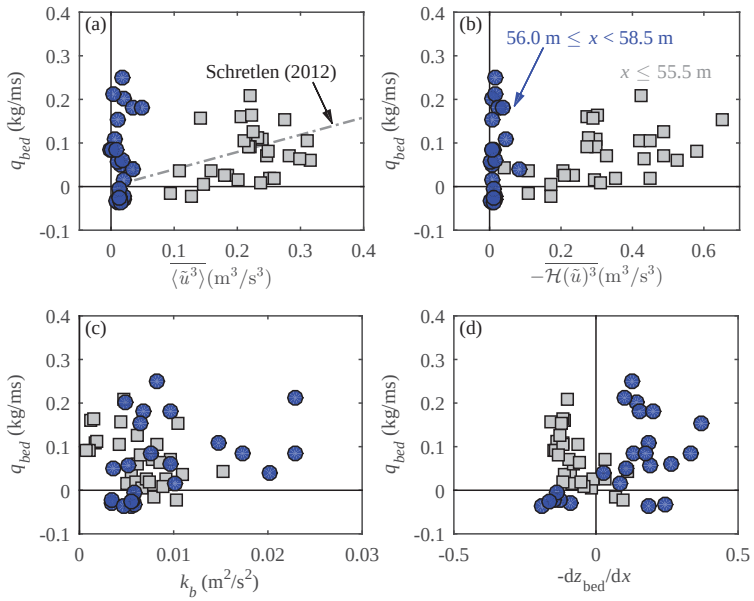

Figure 4.10. Scatter plot between bedload transport and near-bed hydrodynamic parameters for 6 runs at 12 cross-shore locations (72 data points). Explaining variables are (a) periodic velocity cubed; (b) dimensional acceleration skewness through Hilbert transform $-\overline{\mathcal{H}(\tilde{u})^3}$; (c) time-averaged TKE in WBL; (d) local bed slope. Velocity variables (a-b) are obtained at overshoot elevation ζ=δ. Distinction is made between measurements along offshore bar slope to bar crest (x≤55.5 m; grey squares) and breaking region from bar crest to bar trough (56.0≤x<58.5 m; blue circles).

In order to obtain more insight in the parameters controlling the measured bedload transport rates, **Figure 4.10** shows scatter plots of q_{bed} versus a number of hydrodynamic parameters. The chosen parameters are the dimensional orbital velocity skewness, $\overline{\langle\tilde{u}\rangle^3}$ (**Figure 4.10a**); the dimensional acceleration skewness, $-\overline{\mathcal{H}(\langle\tilde{u}\rangle)^3}$ (**Figure 4.10b**); the near-bed turbulent kinetic energy k_b (**Figure 4.10c**); and the local bed slope $-dz_{bed}/dx$ (**Figure 4.10d**). Distinction is made between two characteristic zones along the test section, i.e. the offshore slope up to the bar crest ($x \leq$ 55.5 m) and the breaking region covering the bar crest up to the bar trough (55.5 < x < 58.5 m). The bedload transport rates at the inner surf zone are not considered in this analysis because of the presence of bed forms and the associated variability in bed roughness.

For medium-sand and plane-bed conditions, q_{bed} is expected to correlate positively with the degree of orbital velocity skewness. **Figure 4.10a** shows q_{bed} versus $\overline{\langle\tilde{u}\rangle^3}$ and includes a linear trend line that was found by Schretlen (2012) for medium sand (D_{50} = 0.25 mm) under non-breaking second-order Stokes waves. Between x = 51.0 and 55.5 m, measured q_{bed} in the present study is of similar magnitude as the observations for non-breaking waves by Schretlen (2012). The scatter in measured q_{bed} is addressed to measuring uncertainties and to effects by other hydrodynamic parameters than $\overline{\langle\tilde{u}\rangle^3}$. The transport rates along the shoreward bar slope (between x = 56.0 and 58.5 m) deviate clearly from the trend line, suggesting that other forcing parameters than $\overline{\langle\tilde{u}\rangle^3}$ are significant at these cross-shore locations.

A positive correlation between q_{bed} and the dimensional acceleration skewness is expected (c.f. van der A *et al.*, 2010). **Figure 4.10b** shows that between x = 51.0 and 55.5 m, q_{bed} indeed correlates positively with $-H\overline{(\langle\tilde{u}\rangle)^3}$. However, the data points in the breaking region along the shoreward bar slope (x = 56.0 to 58.5 m) do not satisfy the overall trend.

Figure 4.10c shows the correlation between q_{bed} and the turbulent kinetic energy inside the WBL, k_b. As shown by Sumer *et al.* (2003) an increase in near-bed TKE can lead to increased q_{bed} magnitudes. **Figure 4.10c** shows indeed a weak but positive correlation (with r^2=0.13) for the observations between x = 56.0 and 58.5 m, but no significant correlation is found for the observations between x = 51.0 and 55.5 m.

Gravity favors downslope bedload transport, i.e. q_{bed} is expected to correlate positively with $-dz_{bed}/dx$. **Figure 4.10d** shows a clear positive correlation (with r^2 = 0.33) between both variables for the observations between bar crest and bar trough (x = 56.0 to 58.5 m). This region involves the locations along the shoreward-facing bar slope, where particularly steep local bed slopes with a substantial effect on bedload transport are found. It is further noted that for this region, the two forcing parameters $-dz_{bed}/dx$ and k_b are not independent (positive covariance). Because q_{bed} correlates better with $-dz_{bed}/dx$ than with k_b, it is likely that the bed slope is the primary factor affecting bedload transport along the shoreward bar slope.

4.5 Contributions of transport components to bar morphodynamics

4.5.1 Bedload and suspended load contributions to total transport

Figure 4.11a shows the cross-shore variation in the net (i.e. wave-averaged) bedload ($\zeta < z_a$ = 0.005 m) and the net depth-integrated suspended load ($\zeta > z_a$) transport rates. The net suspended load transport is further decomposed into a current-related ($q_{s,c}$) and wave-related component ($q_{s,w}$). The latter was measured with ACVP, and was generally confined to the WBL and onshore-directed (**Chapter 3**). **Figure 4.11b** shows the relative importance f_{rel} of these three components to total transport, calculated as the relative contribution to the sum of the absolute value of individual components (e.g. for bedload, $f_{rel} = |q_{bed}| / (|q_{bed}| + |q_{s,c}| + |q_{s,w}|)$.

At the most offshore shoaling location (x = 51.0 m), transport is almost fully (>90%) attributed to bedload. This location is hardly affected by breaking-generated TKE and suspended sediment pick-up rates are low. Towards the crest of the bar, between the break point (x = 53.0 m) and plunge point (x = 55.5 m), the offshore-directed suspended transport gains importance

over bedload transport, i.e. q_s increases while q_{bed} decreases. At these locations the onshore-directed wave-related suspended load contribution (f_{rel} = 10–20%) is also significant.

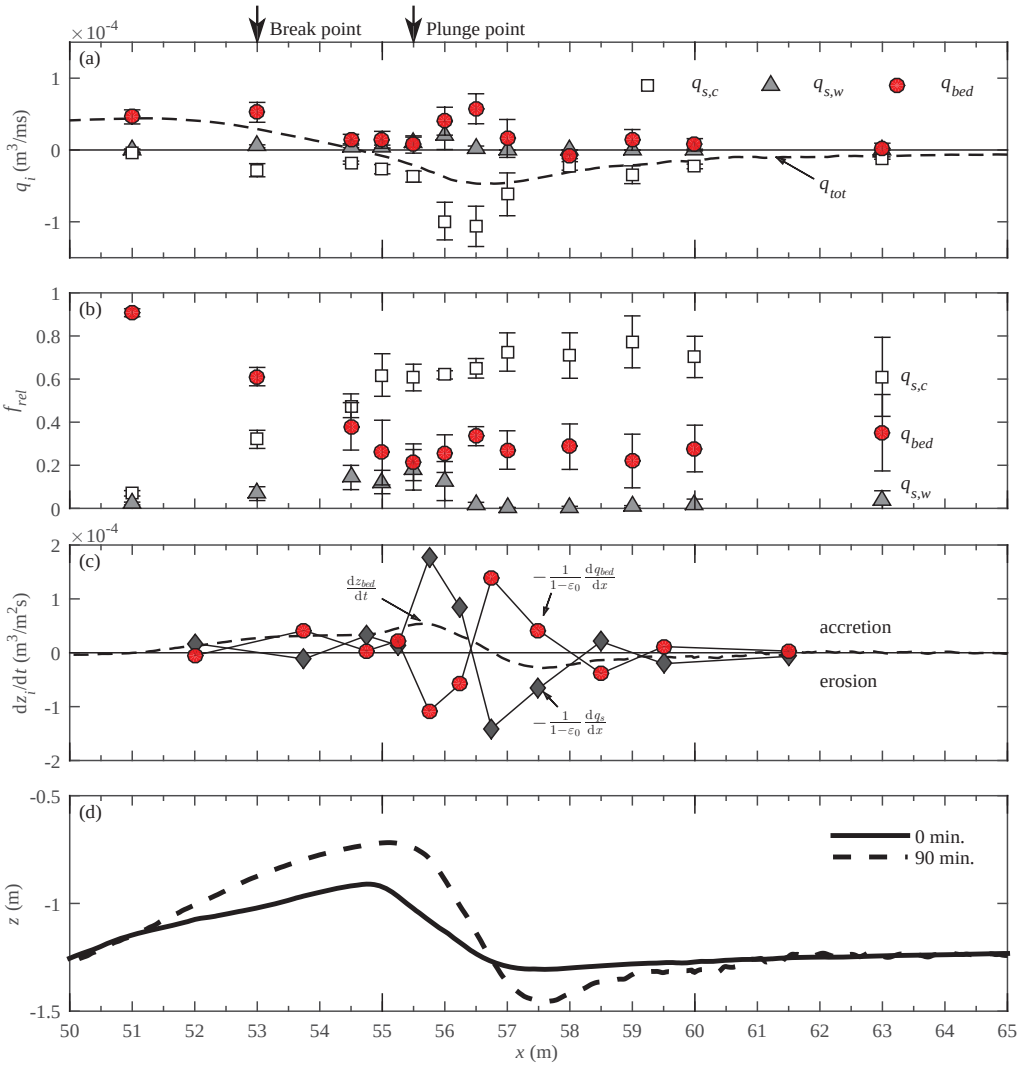

Figure 4.11. Cross-shore variation in net (wave-averaged) transport rates. (a) Transport rates along test section, split out to different components: Total net transport (dashed black line), current-related suspended transport (white squares), wave-related transport (grey triangles), and bedload (red circles); (b) Relative contribution of each component to total transport, calculated as individual contribution to the sum of absolute values of the three terms (see text in Section 4.5.1); (c) Contributions by each component to bed level change (erosion/accretion), quantified through horizontal transport gradients divided by relative sand fraction in loosely packed bed ($1 - \varepsilon_0$): contributions by suspended load (wave- plus current-related, diamonds), bedload (circles) and total transport (dashed line); (d) Bed profiles at t=0 and t=90 min. Values in (a-c) are means over six runs, with error bars in a-b marking 95% confidence interval.

Along the lee side of the bar and shoreward from the plunge point (x = 56.0 – 57.0 m), both q_s and q_{bed} increase in magnitude. Magnitudes of offshore-directed q_s exceed those of onshore-directed q_{bed} by about a factor 2 ($f_{rel} \approx 0.7$ for q_s; $f_{rel} \approx 0.3$ for q_{bed}). The physical explanations for the increase in both transport components is notably different: q_{susp} increases due to the combination of strong near-bed undertow velocities and enhanced sediment pick-up by breaking-generated turbulence, while q_{bed} increases primarily due to bed slope effects. Further shoreward at bar trough and inner surf zone locations ($x \geq 58.0$ m), both transport components decrease in magnitude and the established relative contributions by q_{susp} ($f_{rel} \approx 0.7$) and q_{bed} ($f_{rel} \approx 0.3$) remain approximately constant.

4.5.2 Bedload and suspended load transport contributions to bed profile change

Figure 4.11c shows the negative cross-shore gradients ($-\mathrm{d}/\mathrm{d}x$) of q_s and q_{bed}, divided by the sediment fraction in a loosely packed bed ($1 - \varepsilon_0$; with porosity $\varepsilon_0 = 0.4$). These terms can be interpreted as the contributions by both transport components to local bed level changes. The signs are chosen such that positive values correspond to net local accretion, and negative values to net erosion, of the bed.

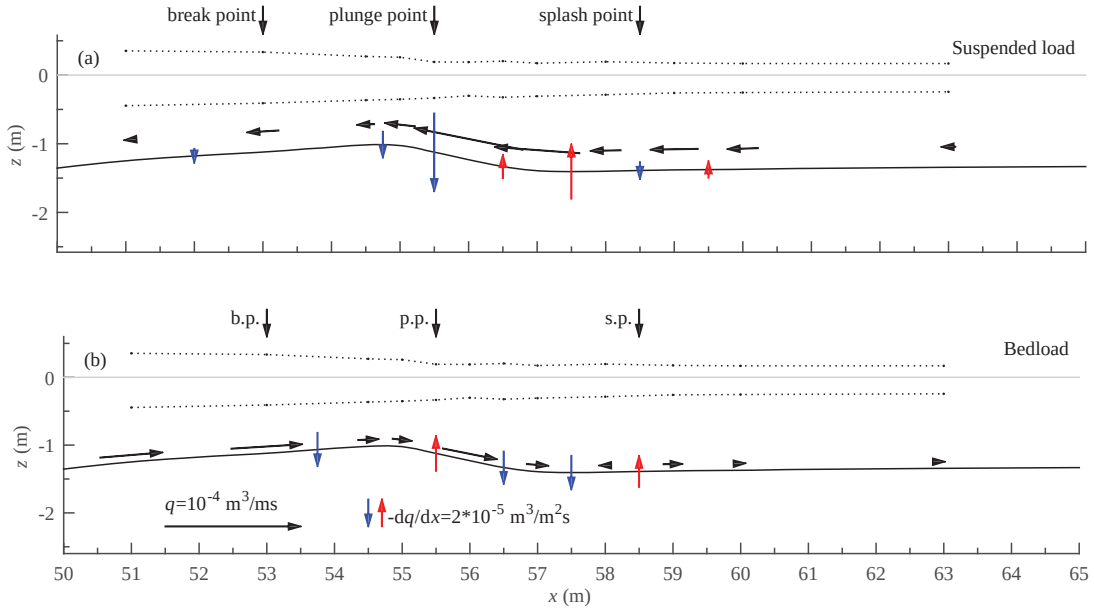

Figure 4.12. Vector plot of transport rates and transport gradients, time-averaged over t=0-90 min, of depth-integrated suspended load (panel a) and bedload (panel b) transport. Bed-parallel arrows (black) denote cross-shore transport rates, consistent with Figure 4.11a. Vertical arrows are cross-shore gradients of each transport component, with red (upward) indicating a positive gradient $\mathrm{d}q/\mathrm{d}x$ (corresponding to local erosion) and blue (downward) corresponding to negative $\mathrm{d}q/\mathrm{d}x$ (local accretion). Bed profile (solid black line) is at t=0 min. Transport gradients with magnitudes < $1.0 \cdot 10^{-5}$ $\mathrm{m}^3/\mathrm{m}^2\mathrm{s}$ were truncated for illustration purposes.

Suspended transport leads to erosion of the bar trough (x = 56.5 – 58.0 m) and accretion of the bar crest and higher ends of the shoreward bar slope (x = 54.0 – 56.5 m). Bedload transport leads to accretion of the breaker bar (x = 52.0 – 55.5 m), erosion of the shoreward bar slope (x =

55.5 – 56.5 m) and accretion of the breaker trough (x = 56.5 – 58.0 m). Hence, the net bed level change between x = 55.0 and 58.0 m (bar crest to bar trough) is explained by the net difference between opposite contributions by suspended load and bedload. Suspended load transport contributions to the bar morphodynamics exceed those by bedload, which explains the growth of the bar crest and deepening of the bar trough during the experiment.

Figure 4.12 shows the suspended load (panel a) and bedload (panel b) transport rates again, but this time as a vector plot along the bar profile and in combination with their effects on local bed level changes. The figure illustrates how sediment advection occurs as suspended and bed load in opposite directions, and how both components lead to local bed erosion or accretion. Suspended transport particularly reveals net sediment pick-up in the bar trough. Once entrained, suspended grains are advected offshore and upwards along the lee-side of the bar by the undertow. The offshore-directed suspended transport increases in offshore direction along the lee-side of the bar, due to enhanced entrainment by breaking-generated TKE (**Chapter 3**). Suspended sediment is deposited at the bar crest where both undertow magnitudes and TKE levels decrease (compared to shoreward locations).

Bedload transport rates are large at shoaling locations (x = 51.0 and 53.0 m) and reduce towards the breaker bar. This leads to net sediment deposition by bedload transport between the break point and the bar crest (x = 53.0 – 54.5 m). Bedload transport rates increase along the lee-side slope of the bar, due to bed slope and possibly because of increased near-bed TKE levels. This lee-side bedload transport leads to erosion of the bar crest and accretion of the bar trough (**Figure 4.12b**) and counterbalances a large part of the bar accretion induced by the suspended sediment transport (**Figure 4.12a**).

4.6 Grain-size sorting

This section examines the vertical grain-size sorting in suspended sediment (Section 4.6.1) and the cross-shore sorting along the bed surface of the breaker bar (Section 4.6.2). The latter is related to size-selective transport as bedload and suspended load.

4.6.1 Vertical sorting of suspended sediment

Figure 4.13 shows vertical profiles of the median diameter (D_{50}) of suspended sediment, sampled with a six-nozzle Transverse Suction System (TSS). Profiles of D_{10} and D_{90} are qualitatively similar and are not shown here for brevity. Different behavior is observed for locations relatively far offshore/shoreward from the plunge point, i.e. at the shoaling location x = 51.0 m and at inner surf-zone locations x = 59.0–63.0 m, versus the locations in the breaking region (x = 54.5–58.0 m).

At the shoaling and inner surf zone, it is firstly shown that the D_{50} of particles in suspension is substantially lower than the mean D_{50} in the flume (grey line). Secondly, vertical sorting occurs, as the suspended sediment becomes finer with distance from the bed. At inner surf zone locations (x > 58.5 m), the D_{50} at the highest TSS nozzle (ζ=0.53 m) is systematically larger than the D_{50} measured closer to the bed (at ζ=0.31 m). A possible explanation is that the sand fraction at ζ=0.53 m contains a larger fraction of sediment that is entrained in the breaking region and then advected to the inner surf zone at elevations above wave trough level (see **Chapter 3**).

Similarly, the suspended sediment at x = 51.0 m is not necessarily entrained locally, but may instead consist of the finest fractions of sediment particles that are picked up in the breaking region and then advected offshore.

In the breaking region (x = 54.5 to 58.0 m), large suspended sediment concentrations were found up to the water surface due to large pick-up rates and strong vertical mixing (**Chapter 3**). **Figure 4.13** shows little vertical segregation in D_{50} for this region, particularly for the locations +/- 1 m from the plunge point (at x = 55.5 m). The suspended sediment appears to be well-mixed and also the coarsest particles are carried to high elevations (up to water surface). Moreover, the D_{50} of suspended sediment is almost the same as the mean D_{50} of the initial bed.

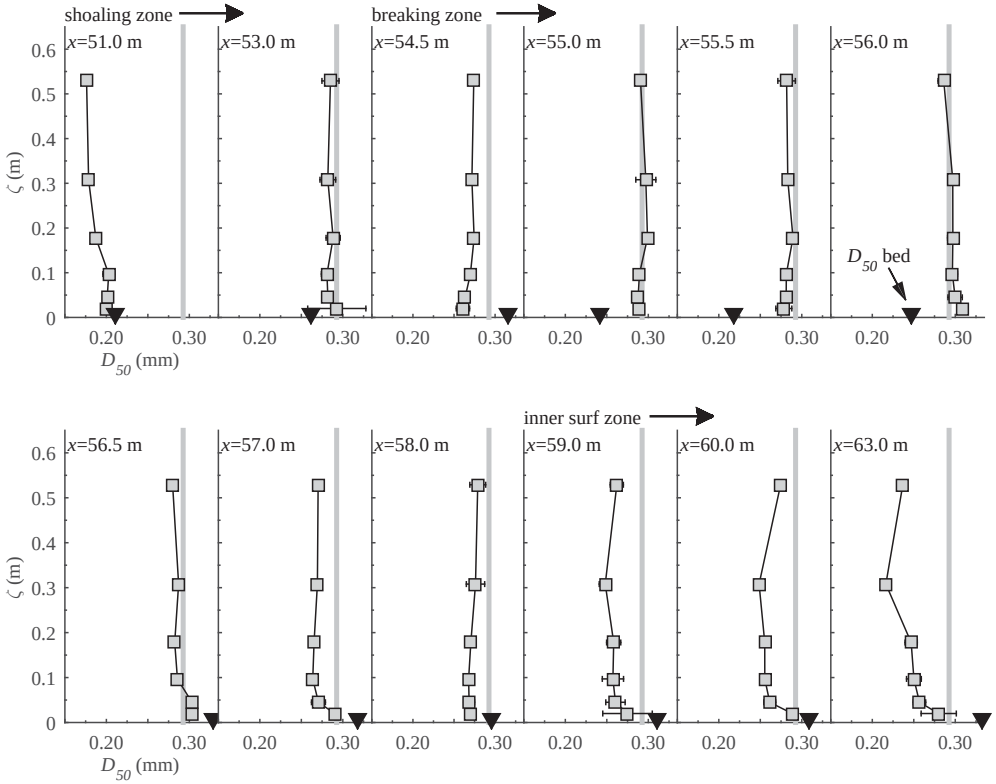

Figure 4.13. Vertical profiles of median diameter (D_{50}) of suspended sediment particles at the 12 measurement locations. Markers denote means (squares) and 95% confidence interval (horizontal error bars) over six runs (t=0-90 min.). Black triangles at ζ=0 denote the measured D_{50} of the bed at the end of the experiment (t=90 min.). Vertical grey lines denote the mean D_{50} of the original bed.

The different sorting behavior for shoaling and inner surf zone versus the breaking region can be related to the processes responsible for sediment pick-up and vertical mixing. Davies and Thorne (2016) detail how for vortex-rippled beds, vertical mixing of particles is due to combined convection (by relatively large coherent periodic vortices ejected from the bed) and diffusion (by random turbulent fluctuations). Convection becomes increasingly important in terms of sediment entrainment and mixing for the coarser fractions in a sediment mixture (Davies and Thorne, 2016). At the shoaling and inner surf zone, turbulent vortices are primarily bed-generated and have a relatively small time and length scale. These small vortices lead to size-selective pick-up and also to vertical segregation of suspended sediment due to

differences in vertical mixing and settling for each sediment size fraction, as shown for sheet flow conditions in an oscillatory flow tunnel (Hassan, 2003) and for rippled beds under uniform non-breaking waves (Sistermans, 2002; Davies and Thorne, 2016). In the wave breaking region, turbulent vortices are of larger scale and are more energetic (van der A *et al.*, Submitted), i.e. have a strong convective mixing capacity for a broad particle size range. Consequently, vertical suspended sediment particle size sorting is restricted under breaking waves (see also Wang *et al.*, 1998).

4.6.2 Cross-shore sorting in the bed

Figure 4.14a shows the cross-shore variation in D_{50} of bed samples for three stages of bar development. Starting with an almost homogeneous grain-size distribution along the test section, evident size-sorting occurs throughout the experiment, resulting in a distinct pattern of grain distribution at the end of the experiment.

At the locations along the offshore slope of the bar (x = 51.0 to 54.0 m), the D_{50} decreases in time. Considering the bedload and suspended load transport patterns (as discussed in the previous sections), the temporal evolution in D_{50} can be related to two processes: first, net removal of the coarsest grains in the mixture through selective sheet flow transport (de Meijer *et al.*, 2002; Hassan and Ribberink, 2005); second, the net deposition of fine suspended particles that are advected offshore from the inner surf and breaking zone, particularly by the undertow (c.f. Sistermans, 2002). The second process (offshore transport of fine particles) also explains the measured coarsening of the bed at inner surf zone locations (x > 58.5 m). This leads to an overall trend of increasing D_{50} from shoaling to inner surf zone that is consistent with field observations (Murray, 1967; Richmond and Sallenger, 1984).

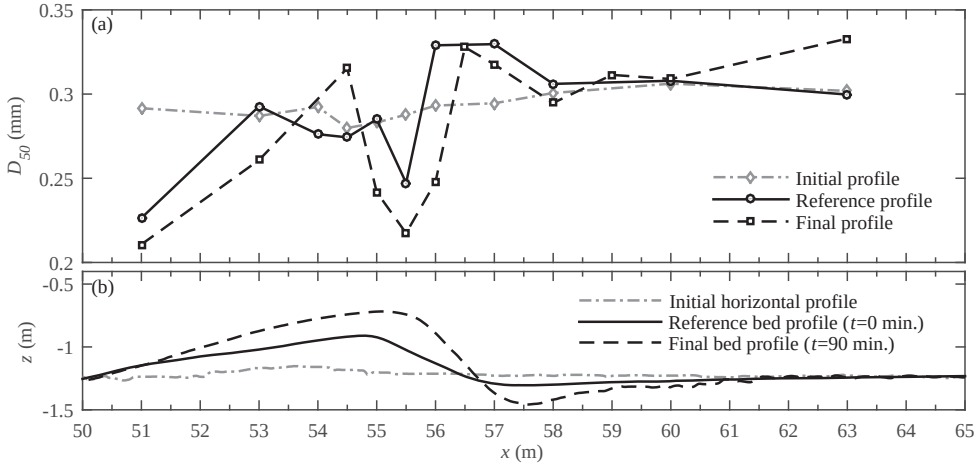

Figure 4.14. (a) D_{50} of sand bed top layer during three stages of bed profile evolution: start of the experiment with horizontal test section (dot-dashed grey line); after initial 105-min start-up stage, i.e. reference bed profile at t=0 min. (solid black line); at the end of the experiment, i.e. final bed profile at t=90 min (black dashed line). (b) Bed profiles corresponding to three bed development stages in (a).

The region around the breaker bar does not obey this overall trend; additional sorting mechanisms seem relevant. Slightly offshore from the bar crest (at x = 54.5 m) the D_{50} increases, which can be related to the transport of relatively coarse particles as sheet flow, which are deposited at the bar crest (see also **Figure 4.12**). Slightly shoreward, at the bar crest and the highest elevations along the bar lee side (x = 55.0 – 56.0 m), the diameter decreases. Net deposition of suspended grains occurs at these locations (see **Figure 4.12**). However, at these locations the grain size of suspended particles is significantly coarser than the particles forming the bed (**Figure 4.13**) and consequently, this deposition cannot explain the decreasing D_{50} in the bed. Instead, it is explained by the gravity-driven bedload transport along the steep lee-side of the breaker bar (**Figure 4.12**). Coarser grains in a sediment mixture have a larger tendency to be transported downslope than finer grains (lee-side sorting). This downslope coarsening along slopes has been shown by several studies in steady flow conditions (see Kleinhans, 2004, for an overview). The relatively coarse sediment at the breaker trough (x = 56.5 – 58.0 m) supports this explanation.

4.7 Discussion

Bedload transport rates q_{bed} are obtained indirectly by subtracting the depth-integrated suspended load q_s from the total load q_{tot} that was obtained from the bed profile evolution. Due to propagation of errors in the data treatment steps, the obtained bedload transport rates are subject to relatively large uncertainties. A quantitative indication of the random-error magnitude was obtained by calculating the standard deviation over six runs at the same cross-shore location (see **Figure 4.11a**). Unfortunately, these uncertainties in the estimated bedload transport rates cannot be easily overcome, because direct measurements of bedload transport rates in such a challenging measurement environment are extremely difficult with existing instrumentation. Two observations justify the use of the indirectly obtained bedload transport rates: first, the indirect estimates of q_{bed} are consistent with estimates of the wave-averaged sheet flow layer transport from CCM$^+$ measurements (**Figure 4.9a**); second, q_{bed} scales similarly to hydrodynamic forcing as previous transport observations of medium-sand sheet flow transport by Schretlen (2012) (see **Figure 4.10a**).

Bedload transport is defined here as the transport that occurs at ζ < 0.005 m above the undisturbed bed level. This choice affects some results, for example the absolute bedload transport rate and the ratio between bedload and suspended load transport, and it requires some reflection. If the reference elevation would be raised to the WBL overshoot elevation (at $\zeta \approx 0.02$ m), the ratio between bedload and suspended load transport would not change drastically since most (80 to 90%) of the suspended load transport occurs at outer-flow elevations above the WBL (**Chapter 3**). Results will likely be more sensitive to a decrease in reference elevation, due to the strong vertical concentration gradient inside the sheet flow layer. Nevertheless, previous medium-sand sheet flow measurements showed that the majority of sheet flow transport is due to horizontal fluxes in the pick-up layer, i.e. at ζ < 0 (Schretlen, 2012). Consequently, we do not expect the results to be very sensitive if another reference elevation had been chosen (within the range $0 < \zeta < 0.02$ m).

Total transport in the present study is formed by bedload and suspended load contributions that are of similar magnitude but of opposite direction. This is consistent with other transport

estimates around breaker bars in wave flumes (Van der Werf et al., 2015, using data of Roelvink and Reniers, 1995; Grasmeijer and Van Rijn, 1997). Note that some field studies on fine- to medium-grained beaches suggested that bedload transport under plunging breakers is minor and total transport is almost completely ascribed to suspended transport contributions (Thornton *et al.*, 1996; Gallagher *et al.*, 1998; Ruessink *et al.*, 1998; Grasmeijer, 2002). However, in these studies the bedload transport rates were not measured, but instead they were quantified using empirical sand transport models that may not be fully valid (e.g. acceleration skewness effects are neglected) and may potentially lead to large errors.

Bedload and suspended load transport contribute differently to breaker bar morphodynamics (**Figure 4.12**). Bedload contributions to bar migration have been explained in terms of cross-shore-varying acceleration skewness (Elgar *et al.*, 2001). The present study supports this, and suggests that the bed slope is an additional dominant factor that controls cross-shore-varying bedload transport rates and, consequently, breaker bar growth and migration. Suspended sediment transport leads to net sediment pick-up at the bar trough and net deposition at the bar crest. This is explained by cross-shore variation in undertow velocities and in sediment pick-up rates, the latter being partly driven by breaking-generated TKE (**Chapter 3**). Note that Dyhr-Nielsen and Sorensen (1970) highlighted the spatially varying undertow as a governing factor for breaker bar morphology. In addition, Zhang and Sunamura (1994), based on small-scale wave flume observations, qualitatively describe the effect of cross-shore-varying breaking-generated turbulence on breaker bar bed level changes. The present study supports these governing bedload and suspended load transport mechanisms for breaker bar morphodynamics by quantifying, possibly for the first time, the simultaneous contributions by both transport components to bed level changes along a large-scale breaker bar.

The hydrodynamics along the breaker bar are strongly non-uniform: parameters that affect sediment transport (e.g. periodic and time-averaged velocity, near-bed TKE, bed slope) can change substantially over a small cross-shore distance. If this distance is smaller than the distance covered by advected fluid mass during a wave cycle (i.e. twice the semi-excursion length in a situation without currents), one may expect that net sediment transport is not purely controlled by local hydrodynamic forcing but also by forcing at adjacent cross-shore locations that affect the intra-wave advection of sediment. It follows from **Table 4.1** and **Figure 4.3** that the flow is particularly non-uniform at the locations between the bar crest and bar trough. Indeed, sheet flow observations at the bar crest (x = 54.5 m) suggest that the horizontal sediment influx during the wave trough phase may lead to an increased sheet flow layer thickness. Such horizontal sediment advection effects on sheet flow concentrations have also been shown for the swash zone (van der Zanden *et al.*, 2015a), yet they mark a clear difference with uniform wave conditions where the sheet flow layer dynamics can be purely explained in terms of local hydrodynamics (e.g. Schretlen, 2012).

A crucial question is whether this influx of horizontally advected sediment has a significant effect on the local sheet flow sediment transport rate at x = 54.5 m. The sheet flow layer thickness increases by approximately 1.5 mm for a duration of about 1 s during the wave trough phase. By assuming that horizontal advection primarily affects the upper sheet flow layer, where typical concentrations are 0.1 m^3/m^3 and particle velocities are approximately 0.8 m/s, the surplus wave-averaged sediment transport rate associated with the trough-phase increase in sheet flow thickness equals approximately –0.1 kg/ms. This is of the same order of

magnitude as bedload transport rates across the test section (**Figure 4.9**). Consequently, the arrival of offshore advected sediment during the trough phase may partly explain the significantly lower bedload transport rates at x = 54.5 m compared to offshore locations (x = 51.0 and 53.0 m).

Interestingly, the estimated bedload transport rates along the shoreward bar slope are directed onshore, while near-bed velocities are directed offshore during almost the entire wave cycle. Hence, bed shear by phase-averaged velocities cannot be the only mobilizer of bedload particles and instead, bed slope and possibly breaking-generated TKE have significant effects (**Figure 4.10**). Physically, the effects of breaking-generated turbulence on bedload transport are explained as follows. Small-scale wave flume observations revealed that the intermittent arrival of breaking-generated turbulence at the bed can result in instantaneous bed shear stresses in both onshore and offshore direction with magnitudes several times the time- and phase-averaged bed shear stress (Cox and Kobayashi, 2000; Sumer *et al.*, 2013). The occurrence of such intermittent turbulence events at the bed is random, i.e. it does not correlate with a specific phase of the wave cycle (Cox and Kobayashi, 2000). The intermittent large bed shear stresses will mobilize particles which on a sloping bed will be transported downslope by gravity. Such a combined effect by TKE and bed slope may be the physical mechanism behind the observed onshore transport along the lee-side of the bar in the present study. Such transport could for instance be modeled as a separate component to bedload transport using a deterministic formulation with bed slope and breaking-generated turbulence as main input parameters (e.g. Fernández-Mora *et al.*, 2015). The present data cannot be used to unambiguously assess the individual effects by near-bed TKE and local bed slope on bedload transport, due to significant covariance between both controlling parameters in the breaking region. Additional physical or numerical experiments would be required to further understand the effects of breaking-generated turbulence on bedload transport and to account for these effects in bedload transport models.

Grain-size distributions of suspended particles reveal size-selective pick-up and vertical sorting at the rippled-bed inner surf zone, but approximately size-indifferent entrainment and mixing in the breaking region. Numerical simulations have demonstrated that selective transport in the surf zone may importantly affect breaker bar morphodynamics (Van Rijn, 1998). However, model formulations for size-selective pick-up at plane beds (e.g. Van Rijn, 2007) may need to be adapted in order to simulate the size-indifferent pick-up under plunging waves that also brings the coarser sand grains into suspension.

4.8 Conclusions

We present measurements of sand transport processes and transport rates along an evolving medium-sand breaker bar under a large-scale plunging breaking wave. Measurements of the sheet flow layer were obtained at two cross-shore locations near the crest of the breaker bar using CCM$^+$. Grain size sorting was studied through samples of suspended sediment and of the bed top layer. The total transport rate was split into a depth-integrated suspended transport rate and a bedload transport rate, which were both assessed to obtain a complete overview of the governing transport contributions to breaker bar development. From the results we conclude:

1. The sheet flow thickness at the offshore bar slope scales similarly to hydrodynamic forcing as previous observations under non-breaking waves. At the bar crest, horizontal sediment advection along the bed affects sheet flow concentrations and thicknesses during the wave trough phase due to a positive influx of sediment from the plunge point. The time-varying transport rate depth-integrated over the sheet flow layer is of similar magnitude as the time-varying suspended sediment transport rate.
2. The net (i.e. wave-averaged) total transport rate consists of a generally onshore-directed bedload and an offshore-directed suspended load component, which are of similar magnitude. Bedload transport dominates at the shoaling zone, decreases at the bar crest, and increases again at the shoreward facing bar slope. The latter is explained by bed slope effects (i.e. gravity-driven transport) and occurs in the presence of high near-bed turbulent kinetic energy, that possibly enhances the mobilization of sand grains. The suspended load increases in the breaking region, leading to a domination of suspended transport over bedload transport in the breaking and inner surf zone. Consequently, near the plunge point the net total transport reverses from onshore-directed (shoaling zone) to offshore-directed (breaking and inner surf zone).
3. During the experiment, the breaker bar crest increases in height while the bar trough deepens. Both bedload and suspended sediment transport contribute to breaker bar morphodynamics, but the effect of each component is notably different. Bedload transport leads to erosion of the offshore slope and accretion at the bar crest, and additionally leads to erosion of the steep shoreward bar slope and deposition at the bar trough. Suspended transport induces erosion of the bar trough, offshore and upward advection of sediment by the undertow along the shoreward bar slope, and net deposition at the breaker bar crest.
4. Suspended sediment samples show evidence of vertical grain sorting at the shoaling and inner surf zone, which indicates that sediment pick-up and vertical mixing is size-selective (i.e. the fraction of fine sediment increases with elevation). This contrasts with the breaking region, where sediment pick-up and vertical mixing is size-indifferent due to the large-scale energetic vortices (strong upward forcing). Bed samples reveal cross-shore sorting of sand particles by size-selective transport as bedload and suspended load. This sorting leads to a gradual increase in sediment size from shoaling to inner surf zone and reveals additional local sorting around the breaker bar due to bed slope effects (i.e. downward coarsening along the steep shoreward bar slope).

Measurements from the same experiment were used previously to study the effects of wave breaking on wave bottom boundary layer hydrodynamics (**Chapter 2**) and on suspended sediment processes (**Chapter 3**). All combined, the studies offer a detailed insight into the complex spatiotemporally-varying hydrodynamics and sediment dynamics along a breaker bar under a plunging wave.

5 Laboratory measurements of intra-swash bed level and sheet flow behavior

Highlights:

- ⇨ Bed levels respond to individual swash events and to sequences of events.
- ⇨ The bed erodes during the uprush and accretes during the backwash phase.
- ⇨ Sheet flow characteristics are not fully locally determined.

Abstract

Detailed measurements of bed level motions and sheet flow processes in the lower swash are presented. The measurements are obtained during a large-scale wave flume experiment focusing on swash zone sediment transport induced by bichromatic waves. A new instrument (CCM$^+$) provides detailed phase-averaged measurements of sheet flow concentrations, particle velocities, and bed level evolution during a complete swash cycle. The bed at the lower swash location shows a clear pattern of rapid erosion during the early uprush and progressive accretion during the middle backwash phase. Sheet flow occurs during the early uprush and mid and late backwash phases. Sheet flow sediment fluxes during these instances are highest in the pick-up layer. Sediment entrainment from the pick-up layer occurs not only during instances of high horizontal shear velocities but also in occurrence of wave-backwash interactions. As opposed to oscillatory sheet flow, the pivot point elevation of the sheet flow layer is time-varying during a swash event. Moreover, the upper sheet flow layer concentrations do not mirror the concentrations in the pick-up layer. Both differences suggest that in the lower swash zone the dynamics of the upper sheet flow layer are not only controlled by vertical sediment exchange (such as in oscillatory sheet flows) but are strongly affected by horizontal advection processes induced by the non-uniformity of the flow.

This chapter has been published as:

Van der Zanden, J., Alsina, J. M., Cáceres, I., Buijsrogge, R. H. and Ribberink, J. S. (2015). *Bed level motions and sheet flow processes in the swash zone: Observations with a new conductivity-based concentration measuring technique (CCM+)*. Coastal Engineering **105**: 47-65. doi: 10.1016/j.coastaleng.2015.08.009.

5.1 Introduction

The swash zone is the area that connects the surf zone to the emerged beach. This zone is characterized by the alternating exposed and submerged state of the bed. The swash is a highly dynamic area where water and sediment flows occur within a highly transient, aerated, and shallow water layer. The hydrodynamic forcing occurs at both short- and long-wave frequencies and as a result, also bed levels experience rapid and large changes at similar frequencies as the waves (Puleo *et al.*, 2014). Magnitudes of sediment fluxes in the swash are large and various modes of transport (sheet flow, suspended load) may coexist (Masselink and Hughes, 1998). Moreover, interactions between incident waves and bores with preceding uprush or backwash result in rapid alteration of the flow field, increased turbulence, and enhanced sediment suspension during a swash event (e.g. Hibberd and Peregrine, 1979; Hughes and Moseley, 2007; Masselink *et al*., 2009; Blenkinsopp *et al.*, 2011; Caceres and Alsina, 2012).

The small water depths and the continuous alternating state of the bed (exposed, submerged) make it extremely challenging to measure and understand the sediment dynamics and hydrodynamics in detail. Our present knowledge of the swash zone sediment dynamics is primarily based on measurements of near-bed sediment concentrations (Aagaard and Hughes, 2006; Alsina *et al.*, 2012), estimations of sediment transport from inter-wave bed level changes (Turner *et al.,* 2008; Blenkinsopp *et al.*, 2011), or sediment trap measurements (Baldock *et al.*, 2005; Alsina *et al.*, 2009). Common instruments particularly fail at obtaining high-quality measurements of (i) sheet flow dynamics and (ii) bed level evolution throughout complete swash events (for both exposed and submerged state).

Sheet flow is a sediment transport mode that occurs during highly energetic flow conditions. When near-bed velocities are sufficiently high, sand transport is confined to a high-concentration (100 to 1600 g/L) layer with a typical thickness of 10 to 100 times the grain diameter (Ribberink *et al.*, 2008). The high cross-shore sediment fluxes in this layer contribute importantly to net transport rates in the near-shore region (Ribberink and Al-Salem, 1995). Sheet flow dynamics have been studied extensively for uniform oscillatory flow conditions in laboratories, i.e. oscillatory flow tunnels (e.g. Horikawa *et al.*, 1982; O'Donoghue and Wright, 2004a; van der A *et al.*, 2010) and wave flumes (e.g. Dohmen-Janssen and Hanes, 2005; Schretlen, 2012). The sheet flow layer can be divided into a pick-up/deposition layer and an upper sheet flow layer, which are respectively found below and above the still-water bed level (Ribberink *et al.*, 2008). During a wave cycle, the vertical concentration gradient changes continuously as a result of vertical sediment exchange. More specifically, the concentration profiles pivot around a vertical reference point (pivot point) which marks the top of the pick-up layer and which is at an approximately fixed elevation throughout the wave cycle (O'Donoghue and Wright, 2004a).

Sheet flow transport has been highlighted as an important contributor to swash zone sediment transport (Yu *et al.*, 1990; Beach *et al.*, 1992; Jackson *et al.*, 2004; Masselink and Puleo, 2006). However, knowledge on swash zone sheet flow dynamics is limited since only few instruments are capable of obtaining high-quality measurements of sheet flow concentrations. Conductivity-based instruments showed the occurrence of sheet flow during early uprush and late backwash instances (Yu *et al*., 1990; Lanckriet *et al*., 2013; Lanckriet and Puleo, 2015).

Vertical concentration profiles during isolated backwash events, measured with a recently developed Conductivity Concentration Profiler (CCP), showed strong similarities to observations for oscillatory sheet flow (Lanckriet *et al.*, 2014). During the early uprush, the sheet flow thickness may be larger than for oscillatory flows with similar hydrodynamics and sediment characteristics (Lanckriet and Puleo, 2015). This increased thickness is likely attributed to additional bore turbulence (Lanckriet and Puleo, 2015). Despite these recent advances, the number of studies on sheet flow layer dynamics in the swash is still limited and does not cover the full range of swash hydrodynamics. In particular, no studies have been able to quantify sediment fluxes for swash zone sheet flow.

In terms of bed level measurements, only few instruments are able to sample the bed during both submerged and exposed state (see Puleo *et al.*, 2014, for an overview). The aforementioned CCP seems to be the only instrument with sufficient accuracy (1 mm) and temporal resolution (sampling > 1 Hz) to study the intra-wave bed evolution in detail. Field measurements of the CCP in the inner surf and lower swash zone show how mean bed levels decrease or increase almost monotonically during a swash event (Puleo *et al.*, 2014). It has been shown that swash events with relatively high onshore velocities and long onshore duration (compared to offshore velocities and duration) are more likely to induce erosion of the seaward swash region, while local accretion is predominantly caused by events with stronger offshore velocities and longer backwash duration (Puleo *et al.*, 2014). Previous experimental studies have not addressed the effects of wave-swash interactions on intra-event bed level changes. In addition, previous studies did not connect the intra-event bed level observations to sheet flow dynamics and sediment fluxes.

The limited knowledge on swash zone sediment transport processes and fluxes hampers the development of improved swash zone sediment transport formulae that can be applied in morphologic models. Energetics-based sediment transport models, which are commonly used for the near-shore region, often fail at predicting adequately the sediment transport rates in the swash zone (Masselink *et al.*, 2009). One of the main reasons is that sediment transport rates in the swash are not fully determined by local hydrodynamics as advection of pre-suspended sediment is important too (Pritchard and Hogg, 2005; Alsina *et al.*, 2009).

In this paper we present the results of recent large-scale wave flume experiments with bichromatic waves focusing on intra-event bed level variations and sheet flow dynamics. The laboratory setting allows us to generate repeatable swash events and to study sediment transport processes in great detail. The main objectives of the paper are (i) to study bed level evolution and (ii) to characterize the dynamics of the sheet flow layer in the lower swash zone.

High-quality measurements of the bed level and sheet flow concentrations and particle velocities are obtained through a new conductivity-based measuring instrument (CCM$^+$) which is presented in Section 5.2 and evaluated in Appendix 5.A. The experimental set-up and wave conditions are presented in Section 5.3, followed by the beach profile evolution (Section 5.4). Section 5.5 presents bed level measurements at different time scales. Section 5.6 presents measurements of the sheet flow dynamics in the lower swash zone. Finally, we reflect on the obtained new insights and their connection to existing knowledge on swash zone and sheet flow dynamics and to sediment transport modeling (Section 5.7).

5.2 Description of CCM+

The CCM+ system is based on existing CCM technology (c.f. Ribberink and Al-Salem, 1995; McLean *et al.*, 2001; Dohmen-Janssen and Hanes, 2005). Previous CCM versions required constant repositioning of the measuring sensors in order to cope with the time-varying bed level. Moreover, they relied on another instrument for a measurement of the reference bed level. In the new CCM+ technology, these problems are overcome with a new tracking system that allows automatic repositioning of the sensors. Sheet flow concentrations are measured by one pair of sensors, while an independently operating third sensor is used to measure the bed level.

5.2.1 Hardware

The exterior of the CCM+ tank is formed by a closed stainless-steel cylinder with a 0.48 m diameter and height of 0.63 m (**Figure 5.1**). The tank is welded to a steel base plate that can be mounted to the flume bottom or a palette, which in combination with the heavy weight (70 kg) of the tank ensures the stability for compensating buoyancy and other destabilizing mechanisms. The probes containing the measuring sensors are mounted to two slim stainless-steel rods that emerge from the tank. Both rods operate independently and can move vertically over a range of 28 cm. Their positions are controlled with sub-mm accuracy by electromagnetic servomotors within the tank. O-rings prevent water and sand intrusion. The tank is equipped with a total of three probes (**Figure 5.2**, top left). Probes 1 and 2 are mounted to the same rod, while a third probe is mounted to the second rod. Reference to the former, combined probe is made as 'probe 1/2'.

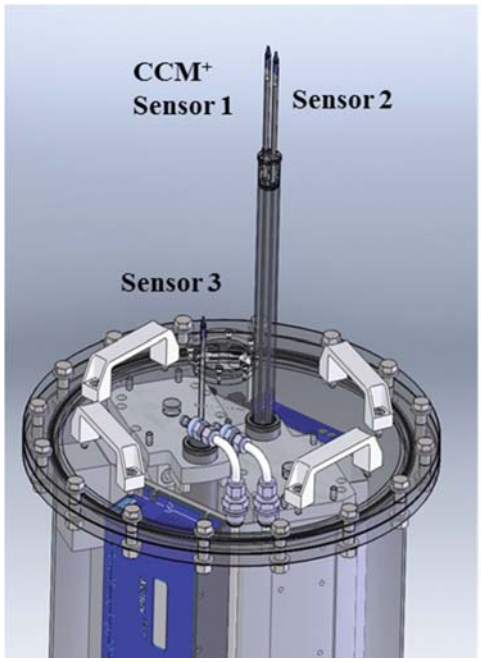

Figure 5.1. SolidWorks image of CCM+ tank with three sensors.

The sensors in the top of each probe are formed by four platinum electrodes with a thickness of 0.3 mm and spacing of 0.6 mm, covered by an epoxy topping such that the exposed part of the electrodes is 0.8 mm high (**Figure 5.2**, top right). The two sensors on probe 1/2 are aligned in cross-shore flow direction with 1.5 cm spacing, and can be used to determine sediment velocities through cross-correlation of the high-pass measured signal (McLean *et al.*, 2001). Sensors 1/2 and sensor 3 are co-located in terms of cross-shore position and separated 9 cm in longitudinal direction.

Figure 5.2. Photos of CCM+ system. Top: probes in lowest position (left) and probe sensors (right). Bottom: installation of tanks during an experiment (left) and zoom of probes after installation (right; note that during an experiment, the probes are lowered such that only the probe sensors emerge from the bed).

The measuring principle of the sensors is conductivity-based. An alternating current is generated over the outer two electrodes while the inner two electrodes measure the electrical resistance of the water which is translated to a voltage U_m. This voltage can be translated to a sediment volume concentration C (m^3 sand/m^3 mixture):

$$C = (1 - \frac{U_0}{U_m}) \cdot f_{cal} \qquad (5.1)$$

where U_0 is the reference voltage for clear water (V) and f_{cal} is a dimensionless calibration factor that usually approaches unity. Both U_0 and f_{cal} depend on probe characteristics and in-situ

water conditions. Before the start of an experiment, the voltages in clear water and in a loosely packed sand bed are measured in order to calibrate the measurements.

During an experiment, the tank and rods are fitted into the sand bed and only the probe sensors reach into the sheet flow layer (**Figure 5.2**, bottom). In the lowest position, the sensors in the tips of the probes are at 14 cm above the tank. Hence, the tank itself is always far from the bed and is not expected to affect sediment transport.

The sampling volume of the probe was assessed by moving the probe up and down a sand bed (grain diameter D_{50} = 0.24 mm). The calibration graphs showed a concentration change from 0.10 to 0.90 times the volumetric concentration in the bed over a vertical range of 1.5 mm. This indicates that the sampling volume of the sensor extends vertically up to 1-2 mm. During initial pilot tests, the sensors were vertically positioned in the upper half of a water column that was frequently aerated by wave collapsing. The conductivity measurements did not reveal a noticeable change in signal as a result of bubble presence.

5.2.2 Signal processing and bed level tracking system

Within the CCM+ system, two types of signals are sampled: (i) the conductivity-measurements of the sensors; (ii) their vertical positions ($z_{1,2}$ and z_3). The sampling frequency is a set 1000 Hz, which is required for determining the particle velocities.

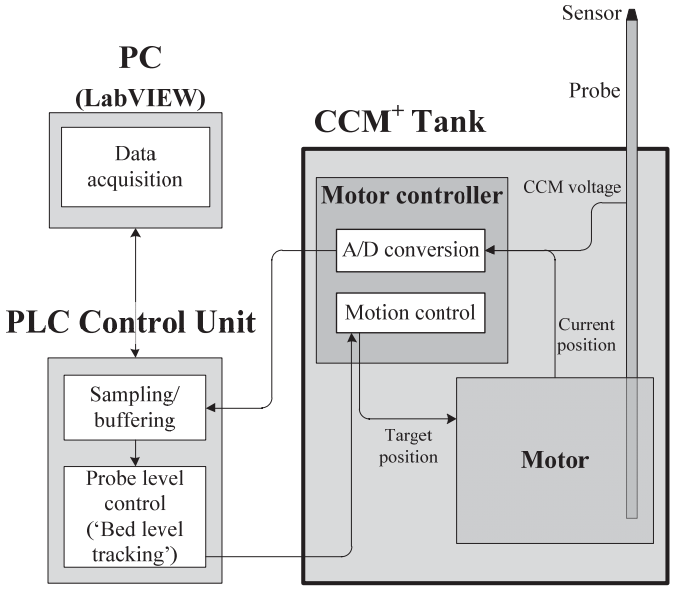

Figure 5.3. Flow chart of signals in CCM+ system.

Figure 5.3 shows a simplified flow chart of the various subsystems, their main tasks, and the signals between the subsystems. The system is controlled through LabVIEW. An Ethernet cable connects the PC to a Beckhoff PLC control unit inside the control box. The new feedback loop for automatic concentration or bed level tracking is programmed in this unit. The computation step simply translates the difference between the measured voltage U_m and a set target voltage U_t, that represents a specific target concentration, to a velocity for vertical probe movement:

$$v = (U_m - U_t) \cdot k_p \tag{5.2}$$

where v is the velocity of probe movement (m/s; defined positively upward); U_t (V) is the target voltage that corresponds to a target concentration through Equation 5.1; and the 'gain factor' k_p (m/s/V) is an input factor that controls the sensitivity of the probe's response. A measured voltage (concentration) that exceeds the target value results in a positive vertical velocity through Equation 5.2, so the probe will move upward. where voltages (hence concentrations) are lower. The speed of movement is proportional to the offset of the measured voltage with respect to the target value. A typical target value used when tracking the bed is the voltage corresponding to half the concentration in the loosely packed bed. This ensures that the probe moves continuously towards the interface between bed and water.

The PLC control unit is equipped with a correction for probe exposure to air when measuring in the swash zone, preventing the probes to move upwards when above water. After the computation step, the PLC control unit transfers the velocity to two Copley Controls Xenus Plus motor controllers inside the tank, which each contain a motion controller that translates the velocity to a desired position.

The CCM+ electrodes are connected to a sensor interface, which contains a chip that treats the measured voltage signal (e.g. demodulating and analogue filtering). The analogue position and voltage (concentration) signals are translated into digital signals by the motor controller. By digitizing the signal near the source, signal distortions are minimized. The bed level tracking loop is repeated every 0.02 s and the U_m value used in Equation 5.2 represents the moving average with a lag of 20 samples (buffering step to reduce effect of signal variations).

The performance of the bed level tracking system greatly depends on the system's ability to respond rapidly and adequately to a concentration offset. Therefore, the signal processing scheme is developed such that a stable vertical probe motion is realized with minimum delay between input (measured concentration) and response (probe movement) of the tracking system. The probes are able to move with velocities over 0.1 m/s, but the users risk unstable probe behavior and overshooting of the target concentration level when the applied gain factor value is too high.

Section 5.3.3 provides more details about the applied tracking system settings of the 3 CCM+ probes throughout the experiment.

5.3 Description of the experiments

5.3.1 Experimental set-up

The CCM+ system was applied during the 'CoSSedM' experimental campaign that was done in the Canal de Investigacion y Experimentacion Maritima (CIEM) at the Universitat Politècnica de Catalunya (UPC), Barcelona. This is a large-scale wave flume of 100 m length, 3 m width and 4.5 m depth. The aim of the experimental campaign was to study cross-shore morphology and swash-zone sediment transport processes under various bichromatic wave conditions of equal wave energy but different modulation periods. In this paper we consider the measurements for one erosive condition, labeled 'BE1_2'. For this condition, the experiment consisted of 8 runs of approximately 30 min.

The beach consisted of commercial well-sorted medium sand with a characteristic diameter (D_{50}) of 0.25 mm, a narrow grain size distribution (D_{10} = 0.15 mm and D_{90} = 0.37 mm), a measured settling velocity of 0.034 m/s, and a porosity of 0.36 when loosely packed. The beach was shaped to a 1:15 constant slope prior to the experiment (**Figure 5.4**).

The vertical coordinate z is defined positively upwards from the still water level (SWL). The shoreline (intersect between SWL and initial profile) at the start of the experiment is used as horizontal datum. Cross-shore coordinates x are defined positive towards the beach (onshore) and negative (offshore) towards the wave paddle (**Figure 5.4**). The toe of the bed profile is located at x = -42.5 m. waves are generated by the wave paddle at a water depth of 2.48 m and an x-position of -75.2 m. Between the wave paddle and the toe of the profile, the waves travel over the concrete bottom of the wave flume.

Figure 5.4 includes the instrumentation applied during the campaign. Outside and at the surf zone, water surface elevations were measured through a sequence of Resistive Wave Gauges (RWGs). Most instrumentation was located at the targeted research area (around shoreline), corresponding to the inner-surf and swash zones. Here, instruments at various cross-shore positions measured velocities (Acoustic Doppler Velocimeters, ADVs), suspended sediment concentrations (Optical Backscatter Sensors, OBSs) and water surface elevation (Acoustic Wave Gauges, AWGs; Pore Pressure Transducers, PPTs). Two CCM+ tanks were installed close to the shoreline (**Figure 5.4**). This paper focuses on the lower swash zone, so results of CCM+ tank 2 are not considered.

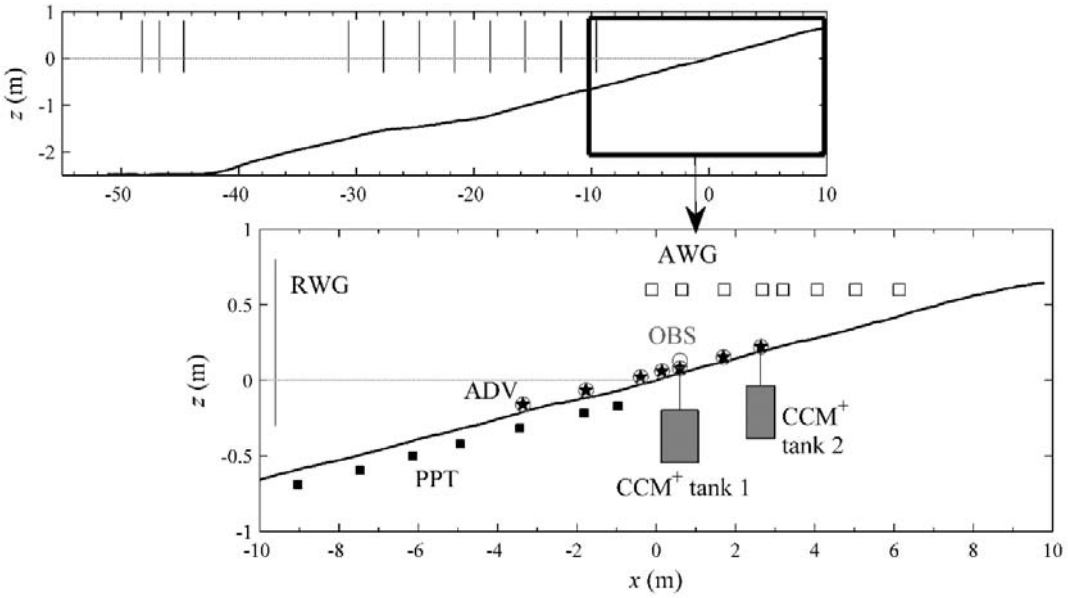

Figure 5.4. Wave flume configuration with measured bathymetry averaged over all initial profiles obtained during the experimental campaign. Upper panel: general view with Resistive Wave Gauge (RWG) positions (vertical black lines); Lower panel: amplification of the beach-face area with instrument locations. Solid squares are Pore Pressure Transducers (PPTs), open squares are Acoustic Wave Gauges (AWGs), open circles correspond to Optical Backscatter Sensors (OBSs) and stars symbols refer to Acoustic Doppler Velocimeters (ADVs).

CCM+ tank 1 was located at an x-position of 0.60 m shoreward of the SWL intersect. As is shown and discussed later (Section 5.4), this position is within the lower swash zone (following the submergence criterion of Aagaard and Hughes, 2006). An AWG and ADV were installed at the same cross-shore position. Above the tank, the downward-looking AWG measured water surface and exposed bed levels with a practical accuracy of about 1 mm and sampling frequency f_s of 40 Hz. The ADV, a Nortek side-looking laboratory Vectrino, measured all three velocity components (f_s = 100 Hz). Prior to each experimental run, the ADV was vertically re-positioned in order to maintain a constant elevation of 0.03 m with respect to the bed.

A mechanical bed profiler, consisting of a pivoting arm and a wheel that are deployed from a mobile trolley, was used to measure the beach profile along the centerline of the wave flume. The profiler is able to measure both the sub-aerial and the sub-aqueous beach and is described in detail by Baldock *et al.* (2011). Given the wheel-diameter of 0.2 m, the profiler is unable to follow individual ripples and it has an estimated accuracy of +/- 10 mm (Baldock *et al.*, 2011). Profile measurements were obtained prior to the experiment and after each 30-minute run.

5.3.2 Wave conditions

Throughout the CoSSedM experimental campaign, various types of bichromatic wave conditions were run. Wave condition BE1_2, considered in this paper, is an erosive condition which was expected to lead to highly energetic flow conditions in the swash. The bichromatic wave consists of a frequency component f_1 of 0.303 Hz with wave height H_1 of 0.30 m and a frequency component f_2 of 0.237 Hz with wave height H_2 = 0.25 m (**Table 5.1**). Together they form a bichromatic wave group with a frequency $f_{gr} = f_1 - f_2$ = 0.067 Hz (T_{gr} = 15.0 s).

Table 5.1. Overview of wave components bichromatic wave condition BE1_2.

Wave component	Subscript	f (Hz)	T (s)	H (m)
Short wave 1	*1*	0.303	3.3	0.30
Short wave 2	*2*	0.237	4.2	0.25
Wave group	*gr*	0.067	15.0	-
Repeat frequency	*R*	0.005	195	-

For this particular condition it is important to note that not all wave groups repeat exactly at the group frequency. Instead, there is a gradual transition of the short-wave phase within the group. This type of modulation at the so-called 'repeat frequency' (f_R) has been reported earlier by Baldock *et al.* (2000). It is emphasized that the modulations at the repeat frequency change the short-wave phase and overall shape of the wave groups, but they have minor effect on the wave energy of the individual groups.

For this experiment, f_R equals 0.0051 Hz (repeat period T_R = 195 s). As a result of the modulations at f_R, the short-wave phase within the group repeats exactly after 13 wave groups but it repeats approximately every second wave group. As will be shown later, the groups that are similar in terms of short-wave phasing are also comparable in terms of hydrodynamics and sediment dynamics at the CCM+ measuring location (bed level changes; Sections 5.5.2 and 5.5.3). This allows us to phase-average sheet flow measurements for two different 'characteristic swash events' that are induced by comparable wave groups.

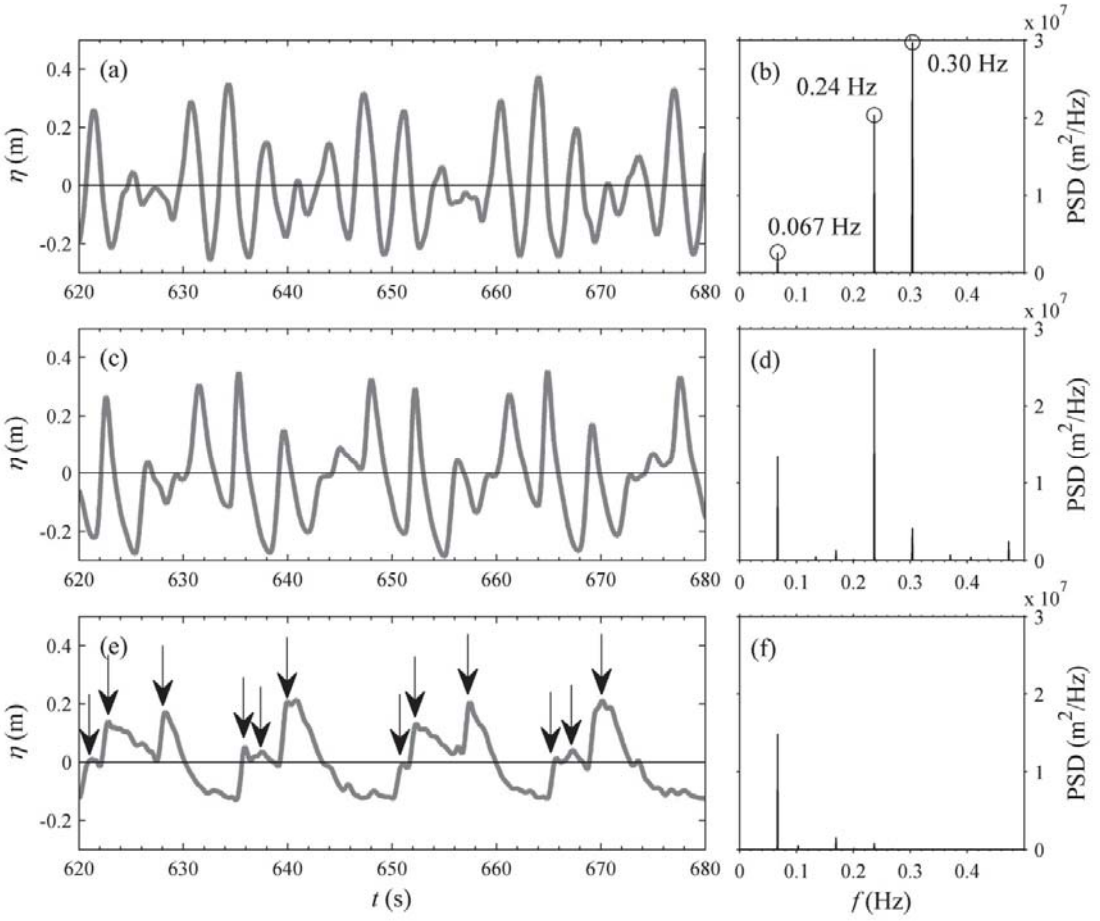

Figure 5.5. Time series for a 60 s time slot (four swash cycles) and power spectral densities of water levels for one of the semi-equilibrium runs, at three x locations: (a,b) resistive wave gauge at x = -67.6 m (close to wave paddle); (c,d) resistive wave gauge at x = -9.7 m (around breaker bar); (e,f) acoustic wave gauge at x = 0.60 m (lower swash zone). Arrows in panel (e) mark the incident surf bores.

Some characteristics of the measured water levels are presented in **Figure 5.5** at three cross-shore positions. Close to the wave paddle, the spectrum (**Figure 5.5b**) clearly shows the two wave components (f_1 and f_2) forming the bichromatic wave group, plus a sub-harmonic at the group frequency related to the wave group envelope. While the waves propagate towards the shoreline, the energy of the higher frequencies dissipates and is transferred to other harmonics and to the wave group frequency (**Figure 5.5d**). This process is well-described in literature (Longuet-Higgins and Stewart, 1964; Baldock *et al.*, 2000; Janssen *et al.*, 2003). As a result, the shape of the wave group changes. At the CCM⁺ location in the lower swash, the energy content is predominant at the wave group frequency f_{gr} (**Figure 5.5f**).

Each swash event at the CCM⁺ location is characterized by three major surf bores followed by the backwash (**Figure 5.5e**). Note that during the final backwash phases, just before the arrival of the first bore of an event, a thin swash lens of *O*(mm) may still exist.

The results in **Figure 5.5** also illustrate how modulations at the repeat frequency f_R affect the short-wave phase but not the wave energy of the 15-second groups. The time series reveal different shapes of the four swash events, as a result of the short-wave phase modulations at

f_R (**Figure 5.5e**). Evidently, the relative timing of the arrival of the bores differs for each event. The relative phase of the bores within the swash event is found to repeat approximately every second event. At the same time, the spectral energy at f_R is negligible (**Figure 5.5b,d,f**). In addition, low-pass filtering of the AWG measurements showed that water level fluctuations at the repeat frequency f_R were of O(mm) in the inner-surf and swash zone (results not shown). These observations on the effects of the f_R modulations are in line with the work of Baldock *et al.* (2000).

5.3.3 CCM+ settings

Each of the two probes of the CCM+ tank serves a different purpose. Hence, different control settings of the bed level tracking system are applied for each probe. As detailed below, probe 1/2 is used to measure instantaneous concentration at fixed vertical levels ($C(z,t)$), while probe 3 measures the continuous instantaneous bed level ($z_{bed}(t)$).

Probe 1/2 (sensors 1 and 2) is set to a slow tracking mode (k_p = 0.5 m/s/V), which means that in terms of vertical repositioning, the probe responds only to gradual bed motions. On an intra-group time scale, the probe can be considered to be on a fixed vertical position. Note that at this fixed level, sediment concentrations are time-varying due to vertical and horizontal advection processes that occur on time scales shorter than the wave group period. The concentration changes at this level are captured by the sensors. In order to capture the complete profile of time-varying concentrations in the sheet flow layer, concentration measurements are required at different (fixed) vertical levels. This is achieved by varying the target concentration (target C values between 0.15 and 0.45 m^3/m^3). Consequently, probe 1/2 slowly traverses through the sheet flow layer providing (intra-wave-group) concentration information at varying vertical levels under the repeating swash events.

Probe 3 is set to a quick tracking mode (k_p = 5 m/s/V). The target voltage of the probe corresponds to a concentration of 0.30 m^3/m^3, which roughly equals half the sediment concentration in the bed and which is close to the middle (or 'pivot point') of the sheet flow layer (see O'Donoghue and Wright, 2004a). In this way probe 3 is able to follow the evolution of the interface between sediment bed and water on a wave-group-averaged time scale (time scales ≥ 15 s). This result is used as reference bed level z_{ref} for the concentrations measured with probe 1/2. It should be noted that the control system is not fast enough to allow perfect tracking of the bed at time scales of seconds and shorter. Instead, probe 3 shows a reduced amplitude and phase-delays of about 2 s with the actual intra-wave bed level (see Appendix A). In the CCM+ tank set-up this high-frequency bed level information can still be obtained from the concentration behavior as measured with probe 1/2 (see Section 5.5.3.3).

The results of the CCM+ bed level and concentration measurements are discussed further in the framework of the swash measurements (see Sections 5.5 and 5.6). Reference is made to Appendix A for more details about the CCM+ performance in terms of bed level measurements.

5.4 Morphological evolution of the swash zone

Figure 5.6a shows the bottom profile evolution during the complete experiment (240 minutes), measured by the wheeled bottom profiler. The mean net transport rates for each run (**Figure**

5.6b) were obtained through solving the mass balance by means of integrating the volume change, starting from the toe of the profile where net transport was known to be 0 (see e.g. Baldock *et al*., 2011). **Figure 5.6** shows a rapid erosion at the shoreline during the first two runs (0 to 60 min.), leading to a semi-equilibrium state that is reached after the second run. During the next six runs, net transport at the shoreline is still offshore although the magnitude is minor compared to the first two runs.

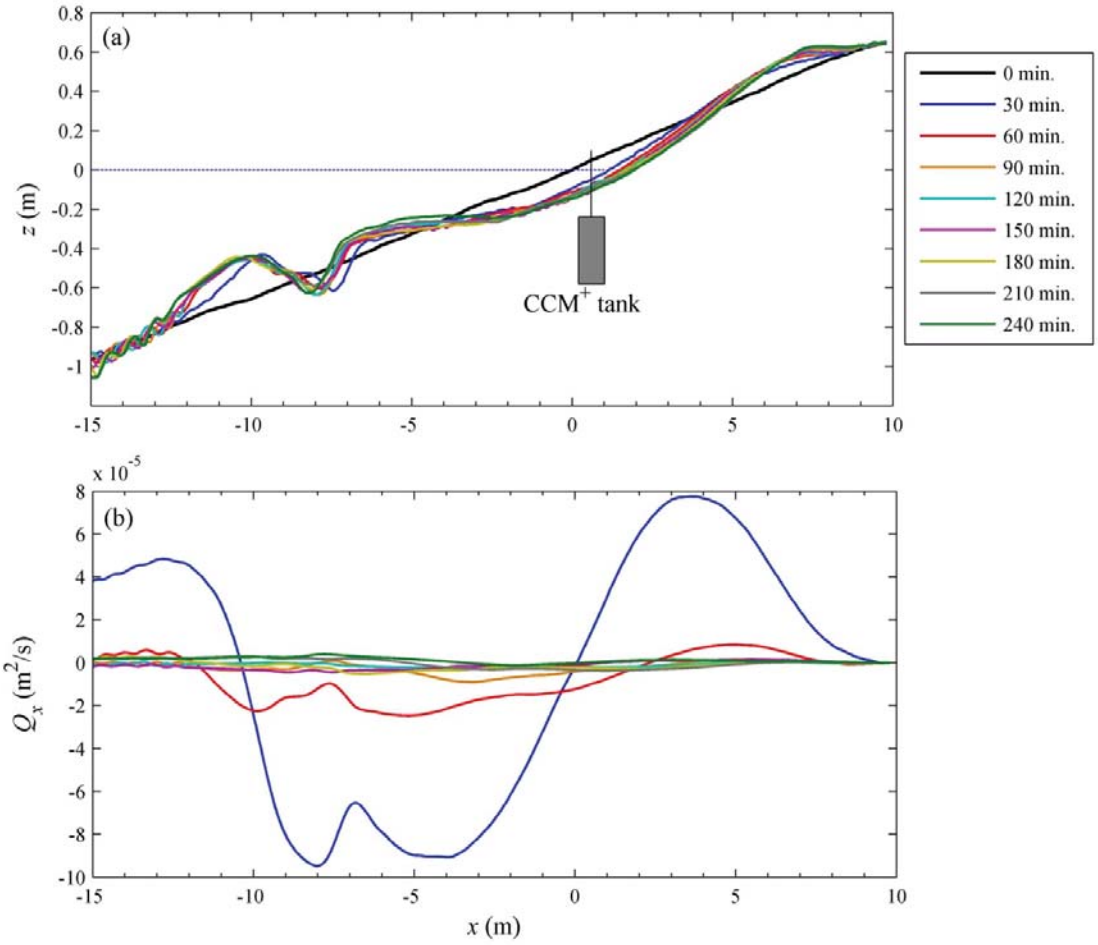

Figure 5.6. (a) Beach profile evolution; (b) net sediment transport rates (Q_x) for each profile measurement.

A bar forms initially at around x = -9.7 m, migrates slightly offshore, and stabilizes around x = -10.0 m. Over the eight runs, the shoreline retreats with 1.95 m. The erosion of the shoreline includes erosion of the inner-surf and mid-low swash area (where the CCM+ tank is located), from x = -3.6 m to x = 4.6 m approximately. Furthermore, berm formation and accretion of the upper/mid-swash can be observed from x = 4 m to x = 9 m.

The shoreline retreat induces a shift in minimum run-down location. The swash zone length was visually measured and inspected by linear interpolation of the AWG and PPT signals, and was found to cover a wave flume extension of 10.4 m (from x = -1.4 to +9.0 m) during the initial run and of around 9.0 m (x = 0.25 to 9.3 m) during the final run. Positions in the swash zone

can be characterized depending on the relative exposure duration of the bed. Following the definitions of Aagaard and Hughes (2006), the lower swash zone runs from x = 0.25 to 1.6 m (up to 25% of time exposed), the mid swash from x = 1.6 to 4.7 m (25 to 60% exposed) and the upper swash for x > 4.7 m (over 60% exposure time). Hence, the CCM$^+$ tank was situated in the lower swash zone, 0.35 m shoreward from the inner surf zone. This location also corresponds to the outer swash zone following the definition of Hughes and Moseley (2007), being the sub-region where wave swash interactions occur – as opposed to the inner swash zone where the swash events are free of interactions.

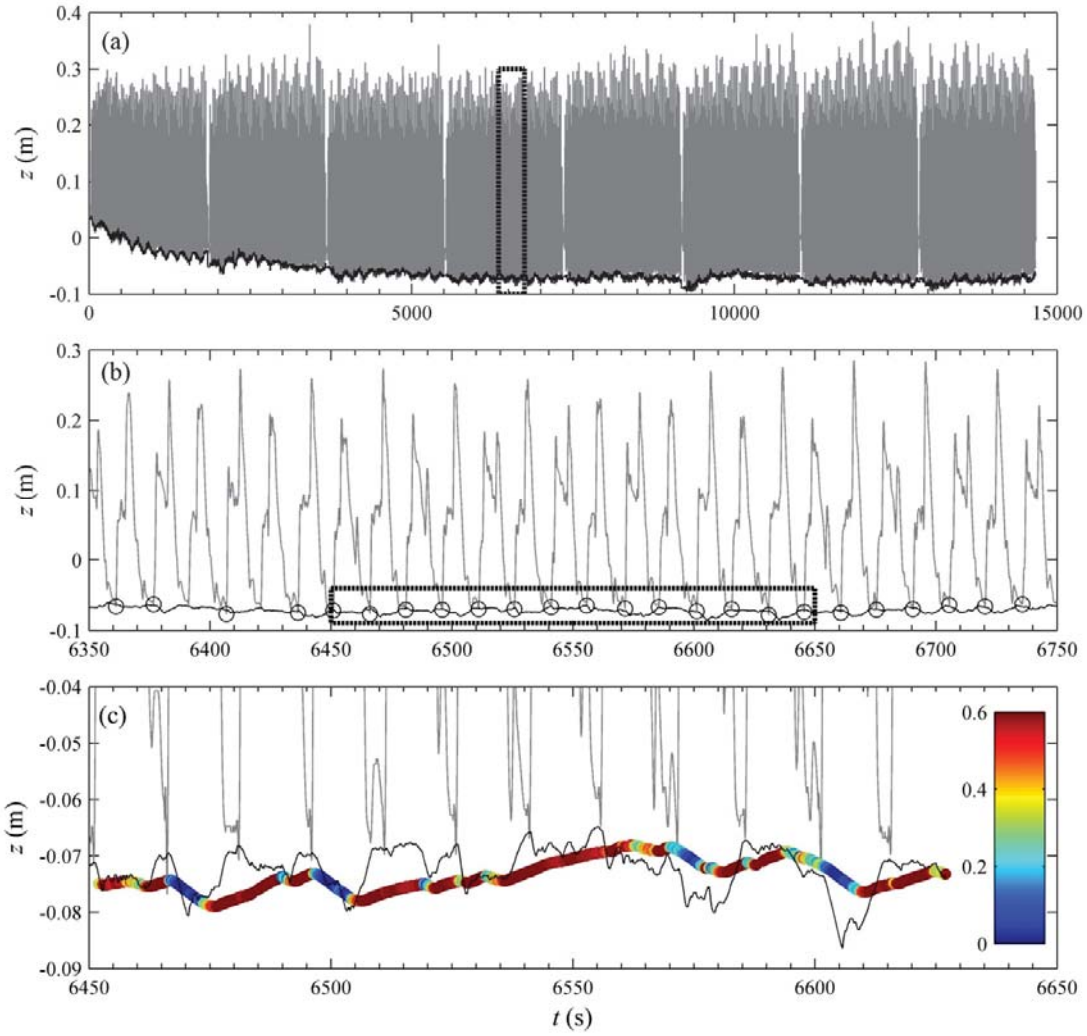

Figure 5.7. Time series of acoustic wave gauge (grey lines) and bed level measurements by CCM$^+$ probe 3 (black lines), for three time frames: (a) continuous time series for complete experiment (8 runs of 30 minutes); (b) close-up of one of the semi-equilibrium runs; (c) close-up of bed level and concentration measurements. Open circles in panel (b) mark identified instances of bed exposure; filled circles in panel (c) mark position of sensor 1/2, with colors referring to the instantaneous concentration measurement. The target concentration of sensor 1/2 for the period in panel (c) equaled 0.45 m^3/m^3.

5.5 Bed level motions in the lower swash

5.5.1 Spectral analysis

In this section the CCM+ bed level measurements (probe 3) are analyzed in both time and frequency domain, in order to identify and characterize dominant time scales of bed level changes.

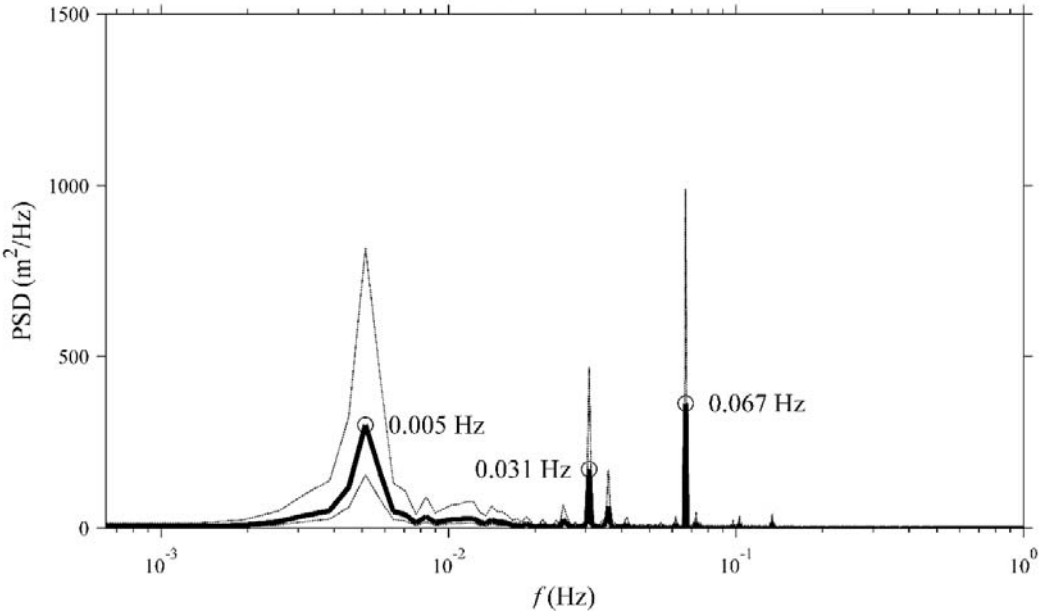

Figure 5.8. Mean spectral density function of the bed level measurements (CCM+ probe 3). Average spectrum of 6 semi-equilibrium runs (thick solid line) and 95% confidence interval based on a chi-square distribution with 12 (twice number of runs used) degrees of freedom (dashed lines).

Figure 5.7 presents time series of the CCM+ probe 3 position, for three selected time frames with increasing level of detail. AWG data is included as a reference. **Figure 5.7a** shows the gradual erosion during the complete experiment (8 runs of 30 min = 14,400 s). During instances of bed exposure, the CCM+ levels match well (order: millimeters) with the lower boundary of the AWG levels (**Figure 5.7a,b**). The measured local erosion of the bed over the experiment (magnitude of 0.1 m), agrees with erosion observed in the beach profile measurements (**Figure 5.6a**). While the AWG data can be used to study gradual bed level changes, the CCM+ provides additional information about the existence of regular bed oscillations at smaller time scales. The bed clearly responds to the passing of the 15-second wave groups (**Figure 5.7c**).

Figure 5.7c also shows the vertical motion of the 'slow' concentration-measuring probe CCM+ probe 1/2 (colored circles), lagging behind the actual bed level as measured by the 'quick' bed level probe 3. Probe 1/2 traverses the near-bed layer while measuring concentrations at varying elevations (see colors). When probe 1/2 is positioned below the bed interface, clearly higher concentrations are found than when it is positioned above the bed interface. Offsets between

concentration measurements of probe 1/2 and the depicted bed level by probe 3 are the result of small local wave flume asymmetries.

The spectrum of the CCM+ bed level measurements is shown in **Figure 5.8**. To derive this figure, power spectral densities (PSDs) were calculated for the measured bed levels by CCM+ probe 3 (after subtracting the gradual erosion trend) with a Fast Fourier Transform. This was done for each of the last six runs, when the bed reached a semi-equilibrium state (experimental time $t > 60$ min), and the obtained PSDs were subsequently averaged. As discussed earlier (see also Appendix A) it is expected that bed level spectral energy at frequencies equal to or larger than the wave group frequency f_{gr} is underestimated.

The spectrum contains dominant peaks at three frequencies, all of which can be related to the hydrodynamics. The highest peak is at a frequency of 0.067 Hz, which corresponds to the frequency of the bichromatic wave groups f_{gr} (T_{gr} = 15 s). At this cross-shore location, also the water-surface level spectra were shown to be dominated by this group frequency (**Figure 5.5f**). The other two bed level spectral peaks are not visible in the water-surface level spectrum, but can both be related to the modulation of the short-wave phase at the repeat frequency as discussed in Section 5.3.2. The peak at 0.005 Hz corresponds to the repeat frequency f_R of the wave groups (T_R = 195 s), i.e. the frequency at which the sequence of 13 wave groups repeats exactly. The peaks at 0.031 Hz and a smaller peak at a slightly higher frequency are close to half the frequency of the wave group ($0.5 \cdot f_{gr}$ =0.033 Hz) and can be related to the short-wave phase repeating approximately every second wave group. Apparently, there is a clear response of the bed level to the systematically varying short-wave phase within the groups – even though the water level spectra show negligible energy at these frequencies. These bed level oscillations with a period of T_R = 195 s can also be identified from the time series of the experiment (**Figure 5.7a**) and are studied in the next section (5.5.2).

5.5.2 Bed level motions at time scale of the wave group sequence (T_R = 195 s)

In order to study the bed level motions in more detail, the measurements are phase-averaged at different time scales. Due to the observed variability between successive swash events, phase-averaging of the CCM+ probe 3 bed level measurements is firstly done for the occurring sequences of 13 swash events (i.e. over the repeat period T_R = 195 s). For this analysis, the first sequence of 13 wave groups and the last incomplete sequence of groups within each run were not considered. This leaves seven sequences per run, adding up to 42 repetitions of the sequence during semi-equilibrium conditions. The ensembles are normalized using the start of the uprush of the first wave group in the time series.

Phase-averaged results of the hydrodynamic measurements (water levels η and cross-shore near-bed velocities u) at the CCM+ cross-shore position are found in **Figure 5.9**. Due to emergence of the ADV probe, the velocity measurements are discontinuous. The relatively small standard deviations (**Figure 5.9a,b**) indicate that the sequences of 13 wave groups repeat themselves rather well. The individual wave-group-induced swash events within the ensemble (marked by the alternating grey/white backgrounds in **Figure 5.9**) are also to a large extent comparable. Each event consists of two or three major broken waves that can be identified from the water surface levels. Cross-shore velocities reveal a strong onshore

maximum at the start of each uprush with magnitudes up to about 1 m/s. Maximum velocity magnitudes are measured in the backwash, where offshore velocities reach 1.5 m/s.

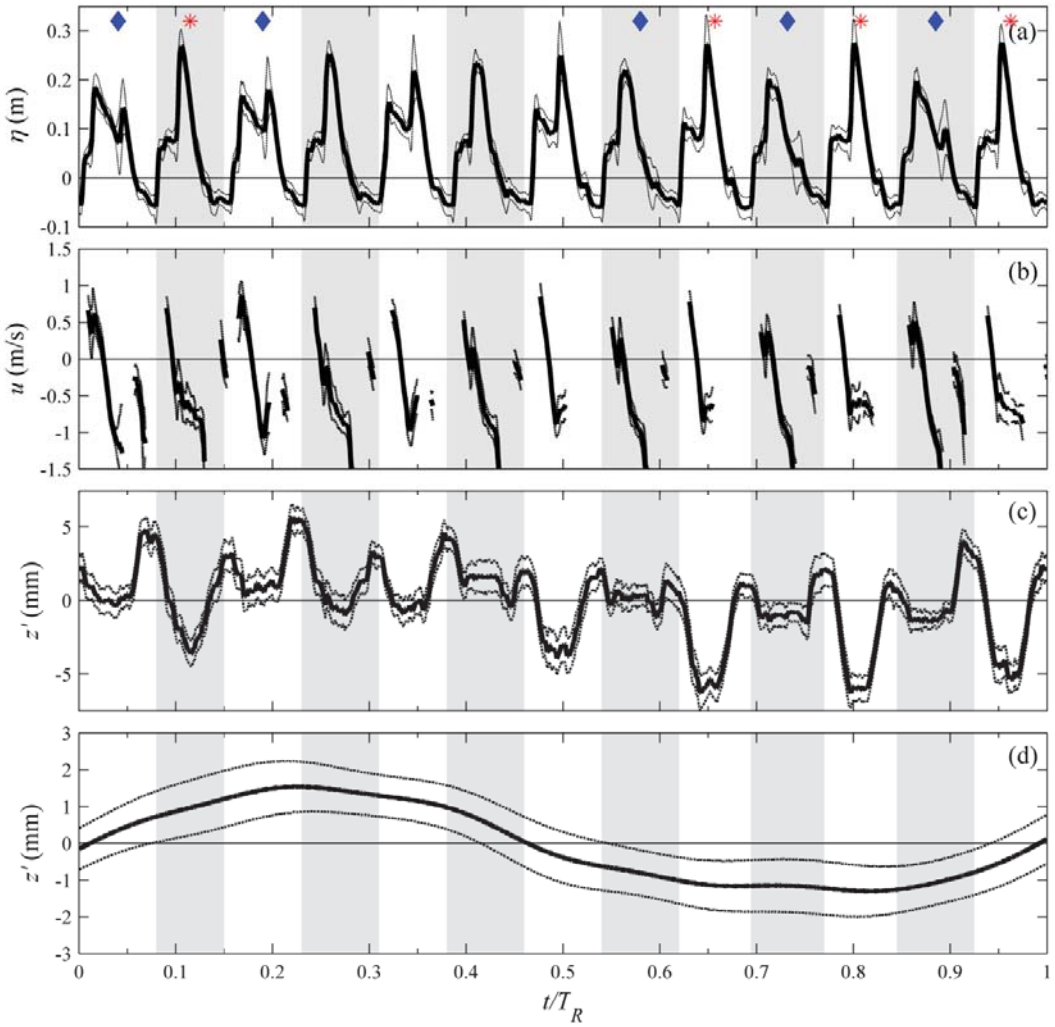

Figure 5.9. Phase-averaged hydrodynamics and bed level measurements at the CCM+ location for the repeat period T_R = 195 s: (a) water level (w.r.t. SWL) measured by AWG, ensemble mean +/- standard deviation; (b) cross-shore velocities measured by ADV, ensemble mean +/- standard deviation; (c) high-pass filtered bed level measurements (cutoff frequency 0.004 Hz) by CCM+ probe 3, ensemble mean and 95% confidence interval; (d) bed level measurements, band-pass filtered (high pass cutoff frequency 0.004 Hz and low-pass cutoff 0.020 Hz). Grey-white background pattern highlights the various 15.0 s wave groups within the ensemble. Symbols in panel (a) mark the selected events for in-depth analysis: swash event of type "A" (blue diamond) and type "B" (red star).

Despite hydrodynamic patterns being largely similar for all groups, subtle differences exist in timing and magnitude of the individual waves composing the swash events. As shown before (**Figure 5.5e**), the wave groups show better repeatability with every second preceding group than with each directly preceding group. This leads to slightly different velocities and wave-

swash interactions for each swash event. These interactions are for some events described in more detail in the next section.

The bed level measurements required additional processing data processing prior to phase-averaging. The gradual erosion trend was removed by applying a high-pass Fourier filter, with a chosen cutoff frequency (0.004 Hz) that was slightly lower than the frequency of interest (being $f_R = 1/T_R = 0.0051$ Hz). In addition, in order to characterize the pattern and magnitude of the bed level fluctuations that are exclusively the result of the short-wave modulations at f_R, a band-pass filter was applied (with lower and upper cutoff frequencies of 0.004 Hz and 0.020 Hz, respectively). The applied upper cutoff frequency is slightly lower than the lowest spectral peak associated with the individual wave groups (0.031 Hz, see **Figure 5.8**). The band-pass filter removes both gradual erosion and the bed level oscillations induced by the individual wave-group-induced swash events. The accordingly obtained phase-averaged bed levels are shown in **Figure 5.9c,d**.

The bed measurements show that for each 15 s event the uprush induces local erosion, that for some waves continues during the first part of the backwash and which alters to sedimentation during the later backwash stage (**Figure 5.9c**). It also becomes evident that, although the group-to-group differences seem small in terms of hydrodynamics, the magnitudes of intra-group bed level oscillations vary substantially (see Section 5.5.3.2 for further discussion). An additional larger-scale sedimentation/erosion pattern can also be seen: during the first 6 groups the bed slowly accretes, while during the following 7 groups a slow erosion process occurs (**Figure 5.9cd**). Apparently, the sequence of net erosion/accretion events of each swash event drives an overall bed level fluctuation at the repeat frequency. The oscillation approaches a sine form with a period equal to the repeat period (T_R = 195 s) and with an amplitude of about 1.5 mm, and it explains the bed level spectrum peak at f_R (**Figure 5.8**).

5.5.3 Bed level motions during individual swash events

5.5.3.1 Selection of characteristic swash events

A more detailed analysis of sediment transport process measurements by the CCM+ at the wave group time scale requires a substantial amount of repeating wave cycles. This holds in particular for sheet flow concentration profiles and particle velocities. Phase-averaged results for the 42 repetitions of the 195 s sequence (Section 5.5.2) proved to contain too much scatter to draw solid conclusions. Therefore, for this section and Section 5.6, measurements are phase-averaged at the group period T_{gr} (= 15 s). Since hydrodynamics and sediment transport processes are not exactly the same for each swash event, two selections are made of characteristic swash events within the sequence of 13 groups.

For each selection, wave-group-induced swash events that induce similar behavior in terms of horizontal velocities and bed level changes are chosen. In order to arrive at two ensembles that are to a large extent complementary, succeeding events were selected. In the following we refer to events of type "A" (marked by blue diamond symbol in Figure 5.9a) and type "B" (red star symbol). The obtained ensembles (**Figure 5.10**) consist of 210 repetitions for event A and 168 repetitions for event B. For each ensemble, $t/T_{gr} = 0$ refers to the arrival of the first bore of the swash event.

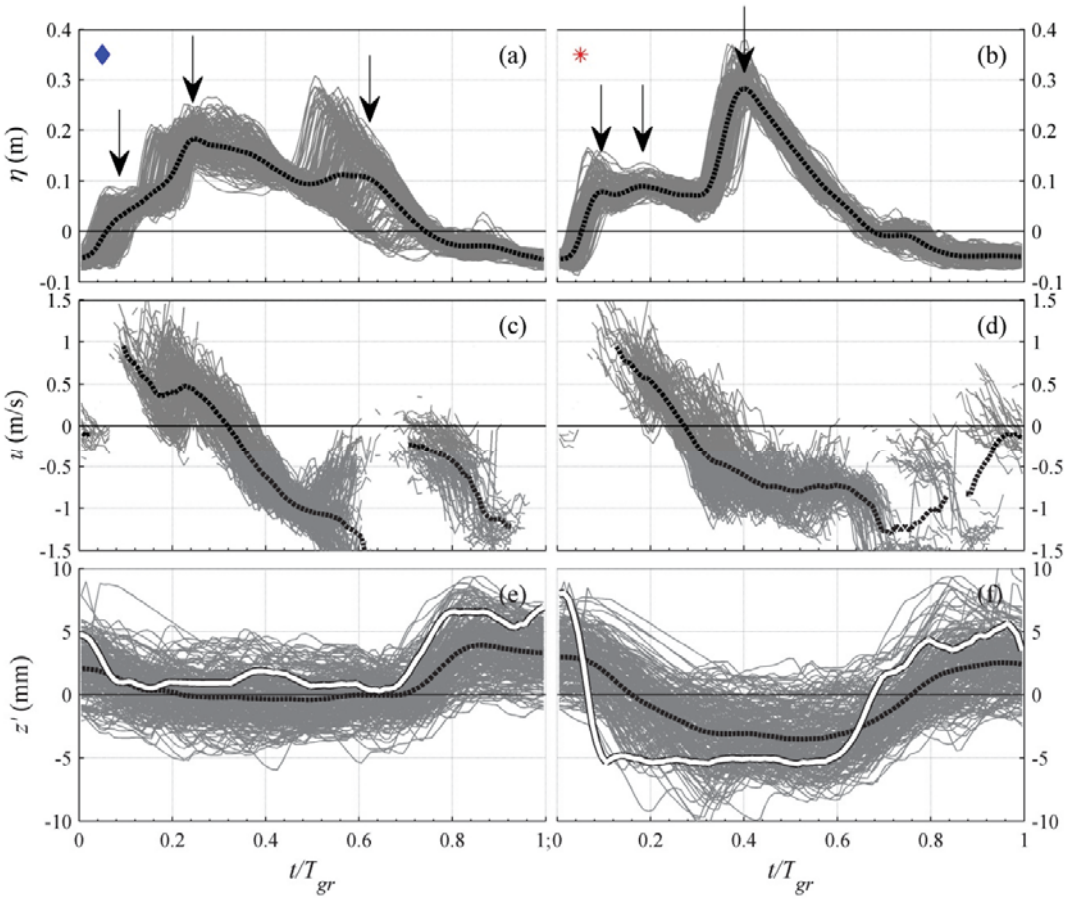

Figure 5.10. Phase-averaged intra-wave bed level measurements of CCM+ system for characteristic swash events "A" (left) and "B" (right). (a,b) water level measurements by AWG; (c,d) horizontal velocity measurements by ADV; (e,f) high-pass filtered (cutoff frequency 0.02 Hz) bed level measurements CCM+ probe 3. All panels contain ensembles (solid grey lines) and ensemble-means (dashed black lines). Also depicted in panels e,f is the elevation of the pivot point (solid white line), derived from the concentration measurements of probe 1/2. Arrows in panels a,b mark the arrival of surf bores that form the swash event.

The selection of the events forming the two ensembles may appear somewhat arbitrary, since the selected wave groups do not repeat exactly within the sequence. Consequently, differences between the individual swash events within each ensemble can be observed, for instance in terms of timing of the incoming bore during the backwash of event A (t/T_{gr} = 0.5 to 0.7, **Figure 5.10a** – grey lines). However, the bed level ensemble does not show any enhanced variation at this instance (**Figure 5.10e**). Overall there is good qualitative and quantitative agreement between the various swash events that form the ensemble. In terms of water levels, it is pointed out that the differences within the two ensembles A and B are small compared to the differences between the two ensembles. The latter statement cannot be repeated for the velocity measurements, which show substantial variation caused partly by turbulent velocity fluctuations that were not removed (**Figure 5.10c,d**).

5.5.3.2 Hydrodynamics

Both events are formed by three major incident waves, and are similar in terms of maximum onshore and offshore velocities (**Figure 5.10a-d**). Also the relative duration of uprush and backwash is similar for both types of swash events. Differences between the events are found mainly in terms of timing of incident-bore arrival. These bores induce differences in terms of timing and magnitude of wave-swash interactions, which are described in the following. The characterization of interactions is supported by visual (video) observations and additional AWG measurements. Reference is made to existing literature that describes these interactions in more detail (e.g. Hughes and Moseley, 2007; Caceres and Alsina, 2012).

For swash event A, the early uprush is generated by a single bore. A second bore arrives during the uprush, lagging the first bore with about 2 s (wave capture; Peregrine, 1974; Hughes and Moseley, 2007). The backwash formed by these waves reaches offshore-directed velocities of high magnitude (up to 1.5 m/s), but gets interrupted by the arrival of a third bore (around t/T_{gr} = 0.62). The incident bore is halted by the preceding backwash, and the momentum exchange results in a stationary bore at/close to the CCM+ location. This stationary bore is the result of strong wave-backwash interactions and has been compared to a hydraulic jump (Hughes and Moseley, 2007). The injection of air bubbles into the water column and the entrainment of sediment by this bore (Caceres and Alsina, 2012) may explain the loss of ADV signal despite water depths being sufficiently large. During the final stage of the swash event (t/T_{gr} = 0.7 to 1), the remainder of the bore is washed seawards by the backwash.

Swash events of type B (**Figure 5.10b,d**) are characterized by a strong single uprush that results from the combination of two incident bores (t/T_{gr} = 0.1 to 0.2). The second bore captures the front of the uprush, that was generated by the first bore, close to the CCM+ location (wave-uprush interactions; Hughes and Moseley, 2007). A third bore arrives at the start of the backwash (around t/T_{gr} = 0.32), i.e. at an earlier stage within the swash event cycle than for event A. In contrast to event A, the incident bore in event B is not completely halted at the CCM+ location but continues to propagate shoreward (weak wave-backwash interactions at the CCM+ location). Subsequently, it results in a stationary bore (strong wave-backwash interactions) about a meter shoreward from the CCM+ location. This bore dissipates and is washed seaward during the final backwash stage.

Evidently, near-bed velocities are not in phase with water levels. Of particular notice are the backwash velocities for event B, which remain negative while the incident bore passes the measuring location (t/T_{gr} = 0.32 to 0.50). The observed (video/AWG measurements) onshore propagation of the bore suggests that velocities in the top of the water column are directed onshore, while measured near-bed velocities are offshore-directed. This suggests a strong velocity shear in the water column, which has been shown to occur for incident bores before (Butt *et al.*, 2004; Cowen *et al.*, 2003).

5.5.3.3 Bed level motions

Bed level motions throughout the swash event are quantified in two ways. Firstly, the direct intra-wave measurements of CCM+ probe 3 are analyzed. Secondly, the bed can be estimated from the time-variant vertical concentration profile as measured by probe 1/2. For both approaches, intra-wave bed level fluctuations are presented with respect to a reference wave-averaged bed level (z_{ref}). This wave-averaged bed level should include the mean bed evolution

trend plus the fluctuations occurring at the repeat frequency as displayed in **Figure 5.9d**. Therefore, z_{ref} is given by the low-pass filtered (0.020 Hz cutoff) bed level measurement by the 'quick' CCM+ sensor 3 (z_3). The direct intra-wave bed level measurements by probe 3 (z'_3) are obtained by subtracting z_{ref} from z_3.

Before extracting the bed from the concentration profiles (probe 1/2), we need to define which concentration value adequately represents the bed level. We try to differentiate between local intra-group erosion/accretion of the bed as a result of incoming/outgoing sediment advection (this section), and time-varying bed level fluctuations as a result of sheet flow dynamics (Section 5.6). Note that for uniform sheet flow conditions, the maximum level of the immobile bed varies in time due to vertical sediment exchange (pick-up and deposition). As a result, this level seems inappropriate to study net horizontal advection. Instead, we suggest that for a situation with simultaneous sheet flow occurrence and net bed level changes, the intra-group bed level is best represented by the sheet flow pivot point elevation. At the pivot point elevation, which marks the middle of the sheet flow layer, concentrations in uniform conditions are nearly constant throughout a wave cycle (O'Donoghue and Wright, 2004a). Consequently, changes in the elevation of the pivot point for non-uniform conditions are likely driven by horizontal advection processes and not by vertical exchange of sediment in the sheet flow layer. Section 5.6.1 explains how the pivot elevation was extracted from the mesaurements.

For both swash event types, all bed level measurements within the z'_3 ensemble show a consistent pattern of local bed erosion during the uprush and accretion during the backwash (**Figure 5.10e-f**). This confirms previous observations (**Figure 5.9**). However, as stated repeatedly, the CCM+ sensors are unable to perfectly track the bed on time scales smaller than the swash event (see Appendix A). The pivot point elevation (white lines in **Figure 5.10e,f**) provides therefore a more accurate estimate of the bed. Evidently, the bed measurements by probe 3 show a reduced amplitude and a phase lag compared to the pivot elevation.

The time-varying pivot point elevation shows a similar pattern as z'_3. Rapid local erosion occurs during the early uprush (t/T_{gr} = 0 to 0.1) and starts upon arrival of the first incident bore. During the mid backwash phase (t/T_{gr} = 0.6 to 0.8), the bed accretes to a level close to the state at the start of the event. This accretion is more gradual than the erosion during the uprush. Although patterns are similar, the magnitudes of the bed level fluctuations differ substantially between the two groups: about 6 mm for swash event A and about 13 mm for swash event B.

The net bed level change induced by a single swash event results from the sum of erosion during the uprush and accretion during the backwash. The net effect is small compared to the bed level fluctuations during the event. Also in terms of net bed level change, both events are different. Swash event A leads to net accretion (about 2 mm), while event B induces net erosion (about 3 mm) at the lower swash zone. Recall that bed level changes that occur at the repeat frequency f_R were removed before this analysis.

5.6 Sheet flow dynamics

The measured sediment concentrations and grain velocities, as obtained from the CCM+ sensors 1 and 2, are studied at the time scale of the individual wave groups. Existing

knowledge about oscillatory sheet flow dynamics (Ribberink and Al-Salem, 1995; O'Donoghue and Wright, 2004a) is used as a comparison to obtain insights in sheet flow characteristics in the swash. The concentrations shown in this section were measured with sensor 2, which proved to be slightly more stable in terms of calibration values than sensor 1. Overall, phase-averaged results by sensors 1 and 2 were highly comparable. Hence, perturbations caused by one sensor being in the lee of the other seem to be negligible.

5.6.1 Vertical concentration profiles

Each of the instantaneous concentration measurements C by sensors 1 and 2 was taken at a certain known absolute elevation of the probe ($z_{1/2}$). To proceed, these concentration measurements are related to the wave-group-averaged bed through $z'_{1/2} = z_{1/2} - z_{ref}$. As the bed is dynamic, the height $z'_{1/2}$ of a concentration point measurement at a relative instance t/T_{gr} is different for each swash cycle (see also Figure 5.7c). Through phase-averaging, the $C(z',t)$ values that were obtained at different elevations z' but at the same relative phase t/T_{gr} of repeating swash events can be combined into time-varying vertical concentration profile ensembles for each phase. These concentration profiles consist of 210 $C(z',t)$ points for event A and 168 for event B (amounts equal total number of repetitive swash events). Next, these profiles are for each phase smoothened by taking the median C measurement for vertical bin classes with 0.5 mm step size.

Figure 5.11 shows these vertical concentration profiles for 10 phases of event A. The errors bars are occasionally high when the number of concentration measurements within an elevation class is small. Even after averaging, some scatter can still be seen. Nevertheless, the profiles consistently follow concave shapes with concentrations decreasing with height, much alike observations for oscillatory sheet flow (e.g. O'Donoghue and Wright, 2004a).

As a result of the chosen control settings of the CCM+, the sheet flow layer was not captured completely at all wave phases (**Figure 5.11**). Therefore, in order to make a quantitative comparison between sheet flow observations in this experiment and previous observations for oscillatory flow conditions, the empirical model of O'Donoghue and Wright (2004a, from here on: ODW04) for sheet flow layer concentrations profiles was fitted through the $C(z',t)$ measurements. Although this model was originally derived for uniform conditions, Lanckriet *et al*. (2014) and Lanckriet and Puleo (2015) illustrated the applicability of the equation to sheet flow concentration profiles during uprush and backwash in the swash zone. The approach is also supported by the apparent similarity between the measured concentration profiles in **Figure 5.11** and the profiles of O'Donoghue and Wright (2004a). The adopted ODW04 function reads:

$$C(z',t) = C_b \cdot \frac{\beta(t)^{\alpha}}{\beta(t)^{\alpha} + [z'+z_e]^{\alpha}} \qquad (5.3)$$

Where $C(z',t)$ is the volumetric concentration at height z' (mm) relative to the original bed at instance t; C_b is the concentration in the bed (=0.64 m³/m³ in this experiment); $\beta(t)$ and α are shape factors; and $z_e(t)$ is the so-called erosion depth of the sheet flow layer at time t which marks the bottom of the sheet flow layer.

We used a least-square method to fit Equation 5.3 through the data. A fixed value of 1.5 was used for α (O'Donoghue & Wright, 2004), while leaving the variables β and z_e as two free fitting

parameters. Values for the shape factor β are directly connected to the sheet flow thickness (Section 5.6.4). The agreement between fit and measurements is reasonably good, with an average coefficient of determination $r^2 = 0.85$.

The curve fitting results include quantitative estimates of the time-dependent bed/water interface or pivot point level (where $C = 0.3$) and the time-dependent lower boundary of the sheet flow layer ($C = C_b = 0.64$). These elevations were used in Section 5.5.3.3 to study the intra-wave bed level behavior (**Figure 5.10e,f**).

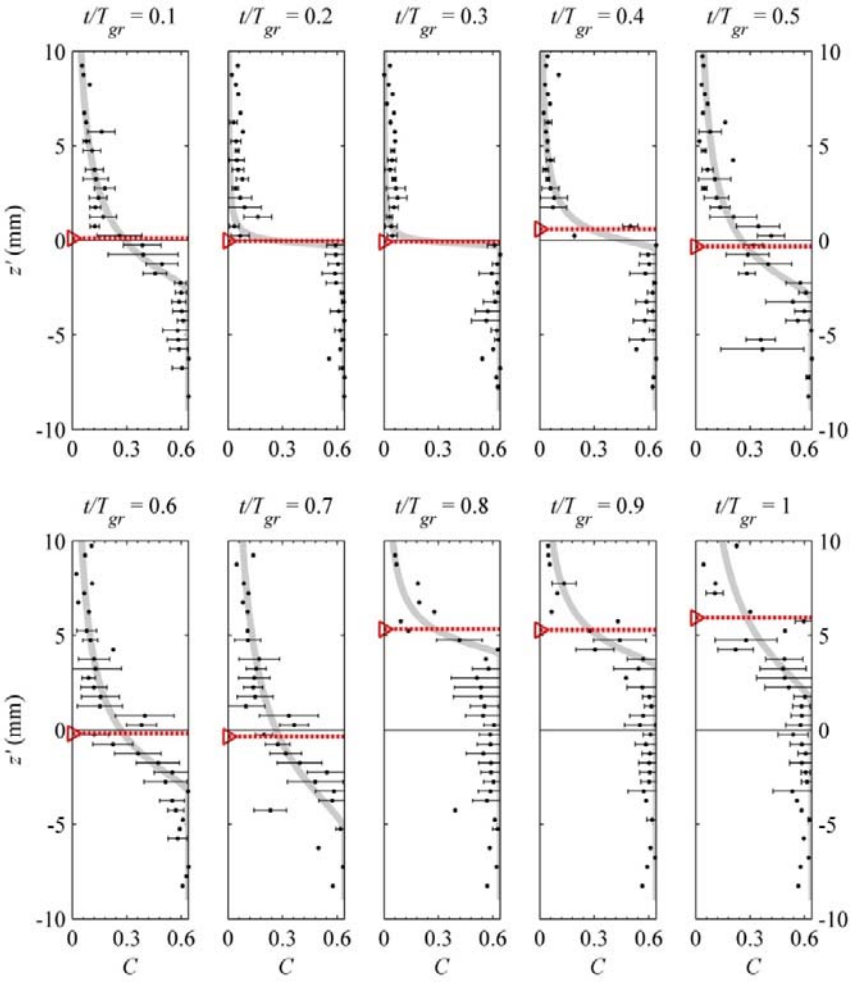

Figure 5.11. Vertical concentration profiles for various t/T_{gr} instances of wave group A. Panels include mean $C(z',t)$ values (black dots), standard deviations of mean (vertical error bands), fitted ODW04 curve (thick grey line), and position of the pivot point (triangle + dotted red line).

The time-varying nature of sheet flow concentration profiles becomes evident from **Figure 5.11**. For $t/T_{gr} = 0.2$ and 0.3, the profiles show a sharp interface between the immobile bed and the water. This suggests that the bed is at rest (no sheet flow). Note that these instances correspond to low near-bed velocity magnitudes (c.f. **Figure 5.10c**). Towards $t/T_{gr} = 0.6$ and 0.7, the concentration gradient becomes less steep as the sheet flow layer develops. From $t/T_{gr} = 0.1$ to 0.7, the pivot elevation is at a more or less fixed level and the temporal variation in vertical

concentration gradients is attributed to vertical exchange of sediment. At t/T_{gr} = 0.8, the bed starts to rise which agrees with bed level measurements of probe 3 (**Figure 5.10e**).

5.6.2 Time series of sheet flow concentrations

Concentration time series are noisy, and more insights are obtained when focusing at phase-averaged concentrations obtained at different vertical elevations. Phase-averaging is done for six concentration bin classes, ranging from C = 0 to 0.6 m^3/m^3 with steps of 0.1 m^3/m^3. These bin classes are based on wave-group-averaged concentrations per swash cycle and consequently, intra-wave-group concentration fluctuations are still captured (**Figure 5.12e,f**). For each concentration class, the mean vertical elevation z' with respect to the wave-averaged bed was calculated. In the present experiments the six classes contain about 30 swash repetitions and it is estimated that the mean elevations have an accuracy of about ±1 mm. This small variation explains why occasionally concentrations are found to increase with height. This way of presenting the CCM concentration data was developed for oscillatory sheet flow measurements (Ribberink and Al-Salem, 1995; McLean *et al*., 2001) and is especially useful when studying the sheet flow response at various elevations of the sheet flow layer (e.g. pick-up layer and upper sheet flow layer).

Another way of presenting the same data is through color contours of the time-varying concentration profiles (**Figure 5.12i,j**). Note that for wave A, the concentration profiles in **Figure 5.12i** corresponds to the profiles in **Figure 5.11**. Also included in **Figure 5.12i,j** are the pivot elevation (corresponding to **Figure 5.10e,f**) and the time-varying bottom of the sheet flow layer derived from the ODW04 curve fit.

Typical sheet flow layer pick-up behavior, as known from oscillatory sheet flows, can be observed in the concentration time series (**Figure 5.12e,f**) at the lowest elevations where the concentrations are close to 0.6 (packed-bed). The concentrations show temporary dips at instances of sediment pick-up from the bed. Deeper dips suggest stronger sediment pick-up. This pick-up happens once during the uprush (shortly after bore arrival; around t/T_{gr} = 0.10 for both swash events) and one or two times during the backwash phase (around t/T_{gr} = 0.5 and 0.65). For swash event A the strongest pick-up occurs during the backwash (around t/T_{gr} = 0.65), while for event type B this happens during the uprush. Similar to oscillatory sheet flows, this pick-up behavior is observed at low elevations in the bed where the concentrations exceed the bed-water interface value (C > 0.3) and it occurs generally when velocity magnitudes are high.

At higher elevations, in the so-called upper sheet flow layer (C < 0.3), the concentration behavior differs strongly from oscillatory sheet flows. For oscillatory sheet flows in wave tunnels (O'Donoghue and Wright, 2004a) as well as under non-breaking surface waves (Schretlen, 2012), sediment exchange occurs between pick-up and upper sheet flow layer. The consequence of this predominantly vertical exchange is that a concentration dip in the pick-up layer is accompanied by a similar concentration peak in the upper sheet flow layer (mirroring behavior). Moreover, this sediment exchange occurs around a steady interface elevation where C = 0.3 (pivot point). In the present swash experiments this type of behavior is not clearly visible. Firstly, the pivot level is not steady but fluctuates over a vertical distance of several millimeters during the wave cycle (**Figure 5.12i,**j). Secondly, the present swash experiment

does not show the mirroring behavior in concentrations during each instance of sheet flow. During the early uprush, the sediment pick-up around t/T_{gr} = 0.1 is not accompanied by an increase in upper sheet flow layer concentrations. Instead, concentrations drop at all elevations as a result of the strong bed level decrease (**Figure 5.12i,j**). During the pick-up event in the backwash (around t/T_{gr} = 0.65 for both events), concentrations in the upper sheet flow layer are indeed increasing. Although this may point towards vertical sediment exchange (pick-up), during the remainder of the backwash the upper sheet flow layer concentrations continue to increase even though no pick-up is observed (t/T_{gr} = 0.65 to 0.90). These observations are discussed in more detail in Section 5.7.2.

5.6.3 Particle velocities and fluxes in the sheet flow layer

Particle velocities in the sheet flow layer were calculated following the approach of McLean *et al.* (2001). This method assumes that (clouds of) particles travel past the co-located sensors 1 and 2, and the travel time can be found by estimating the phase lag through cross-correlating the high-pass filtered (1 Hz cutoff) signals of the two sensors. This cross-correlation is done for each individual wave and for a selected number of phases of the wave cycle (in this case 100). For each phase, the cross-correlation output for all wave cycles is averaged. This averaging is done per wave-averaged concentration bin class, using the same six classes as in Section 5.6.2. For each bin class and phase, the time lag corresponding to the maximum averaged cross-correlation output is used to estimate the mean travel time of particles between both sensors. Data for which the maximum cross-correlation value did not exceed the background noise are emitted. Particle velocities are defined as the distance between both sensors (1.5 cm) divided by the derived travel time. **Figure 5.12c,d** shows that particle velocity estimations are only obtained when instantaneous ADV velocity magnitudes approach or exceed a threshold of roughly 1.0 m/s.

Although the measurements show considerable scatter, it is clear that for both swash events the measured particle velocities in the sheet flow layer (**Figure 5.12c,d**) follow a similar intra-wave pattern as the flow velocities measured by the ADV at an elevation of about 3 cm above the bed. During both uprush and backwash the particle velocities in the sheet flow layer can reach large magnitudes (1 m/s and higher). Particle velocities in the upper sheet flow layer approach the near-bed water velocity magnitudes, which is not uncommon for sheet flow observations (e.g. McLean *et al.*, 2001). Vertical structure of the particle velocities is only evident for the long backwash of swash event B, with particle velocities decreasing towards the bed (in line with observations of McLean *et al.*, 2001; Dohmen-Janssen and Hanes, 2005; Schretlen, 2012).

The combination of concentration and particle velocity measurements by the CCM+ sensors allows us to directly estimate the intra-wave horizontal sediment fluxes, as the product of the measured particle velocities (**Figure 5.12c,d**) and concentrations (**Figure 5.12e,f**) per bin class. The horizontal sediment fluxes (**Figure 5.12g,h**) show a similar oscillating pattern as the particle velocities. Both swash events A and B show large fluxes during the relatively short uprush, followed by a longer period with smaller fluxes during the backwash. The magnitudes of the fluxes during swash event B are clearly larger than during event A. Despite the scatter

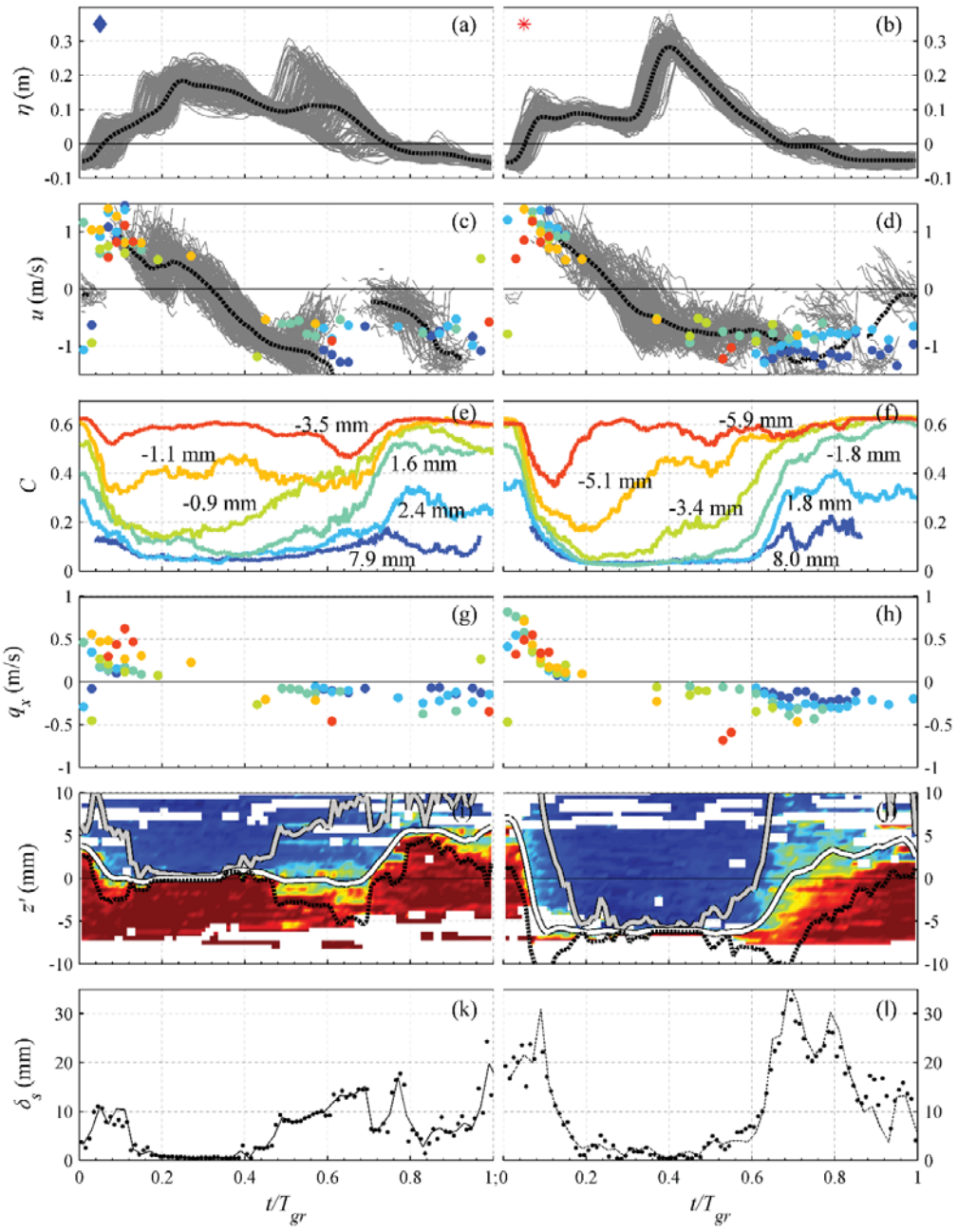

Figure 5.12. Phase-averaged hydrodynamics and intra-wave sheet flow behavior at group period T_{gr} = 15 s for characteristic swash events "A" (left) and "B" (right). (a,b) water level measurements by AWG, ensemble (grey lines) and mean (dashed black line); (c,d) horizontal velocity measurements by ADV, ensemble (grey) and mean (dashed black line), plus CCM+ particle velocities for six concentration bin classes (colors corresponding to panels e,f); (e,f) concentration measurements C for six wave-group-averaged concentration bin classes, including corresponding mean relative elevations z' per bin class; (g,h) sediment fluxes derived from CCM+ measurements for six concentration bin classes; (i,j) contour of concentrations $C(z',t)$ measured by probe 1/2, including elevations of sheet flow layer top (solid grey line), pivot point (solid white line), and bottom (dashed black line); (k,l) sheet flow layer thickness, estimations from ODW04 fit (dots) and spline-smoothened estimations (dashed line).

of the data a general tendency can be seen: the fluxes increase with decreasing elevations in the sheet flow layer (see e.g. the backwash of wave B). The reduction of velocities towards the bed is more than compensated by the larger volumetric sediment concentrations at these levels. Note that also for oscillatory sheet flows, highest fluxes were found in the pick-up layer (McLean *et al.*, 2001; Dohmen-Janssen and Hanes, 2005; Schretlen, 2012).

5.6.4 Sheet flow layer thickness

The thickness was estimated from the interpolated profiles derived from the ODW04 fit (Section 5.6.1). The sheet flow layer thickness (δ_s) is defined as the distance between the bottom of the sheet flow layer and the level where the volume concentration reaches 0.08 m^3/m^3 (Dohmen-Janssen and Hanes, 2002; O'Donoghue and Wright, 2004a). Hence, the thickness relates to the vertical concentration gradients (**Figure 5.12i,j** and **Figure 5.11**).

Temporal behavior of δ_s (**Figure 5.12k,l**) agrees with results in previous sections. The thickness increases at the previously identified instances of sediment pick-up (during early uprush and mid backwash phase; **Figure 5.12e,f**). There is also a clear correspondence between thick, well-developed sheet flow layers, and the derived fluxes (**Figure 5.12g,h**).

The measured maximum δ_s values are substantially higher than observations of oscillatory sheet flow with similar grain-size and velocity magnitudes. Tunnel measurements of O'Donoghue and Wright (2004a) with narrow-distributed medium-grained sand (D_{50} = 0.28 mm) and peak velocities of 1.5 m/s, yielded maximum sheet flow thicknesses of 8 mm (case MA5010). Measurements under progressive surface waves in a wave flume (Schretlen, 2012; case RE1575m) yielded sheet flow thicknesses of 10.3 mm for medium-grained sand (D_{50} = 0.245 mm) and crest velocities of 1.63 m/s. Compared to aforementioned experiments, peak flow velocities are lower but sheet flow thicknesses during both uprush and backwash are over twice as high. This holds in particular for swash event B.

5.7 Discussion

The new experiments with the CCM+ instrumentation have resulted in new detailed results in the bed level and sediment (sheet flow) dynamics during swash events in the lower swash zone. In this section, the bed level (Section 5.7.1) and sheet flow (results) are connected to existing knowledge on sediment dynamics in the swash and to previous observations of oscillatory sheet flows.

5.7.1 Bed level motions at various time scales

The measured intra-group bed levels in the lower swash show a consistent pattern of rapid erosion during the uprush and gradual accretion during the backwash phase. Steep horizontal sediment transport gradients, induced by the strong non-uniformity of the waves and flow in the swash as pointed out for instance by Hughes *et al.* (2007), may directly lead to these types of erosion/accretion events. The measurements suggest that the sediment mobilized at the start of the event is transported onshore during the uprush and brought back during the backwash (i.e. cross-shore advection). The importance of cross-shore sediment advection on swash

morphology has been addressed before and has been associated to suspended sediment settling lags due to enhanced turbulence and hindered settling (Pritchard and Hogg, 2005; Hughes *et al.*, 2007; Alsina *et al.*, 2009). The results further show that the net bed level change after a single swash cycle results from a difference between uprush erosion and backwash accretion, and support the idea that the swash zone bed level change results from a small difference of two opposing sediment movements with similar high magnitudes (Masselink and Hughes, 1998). Our observations for one wave condition do not object reported cases for random wave conditions, where a few "large" swash events were responsible for the measured beach face elevation changes (e.g. Puleo *et al.*, 2014).

Swash events A and B are similar in terms of wave energy, peak onshore and offshore velocities, and relative durations of uprush and backwash. The modulation of the short-wave phase at the repeat frequency triggers different types of specific wave-swash interactions, that are characteristic for the lower swash zone (Hughes and Moseley, 2007). This leads to local differences in terms of hydrodynamics (e.g. velocities, turbulence, pressure gradients) which in return affect sediment transport patterns. Little is known about the effects of wave-swash interactions on bed level changes. Here, effort is made to relate the observations in bed level changes to the wave-swash interactions observed for both events in a qualitative sense.

The bed level drop during the early uprush for event B is larger than for event A, suggesting steeper horizontal sediment transport gradients for event B at this instance. The higher sheet flow thickness and fluxes for the event B uprush suggest that this uprush is more energetic, in terms of bed shear, horizontal pressure gradients, and/or turbulence (Lanckriet and Puleo, 2015). These same factors affect local sediment entrainment by bores (Puleo *et al.*, 2000; Butt *et al.*, 2004; Jackson *et al.*, 2004). The interaction between the two incident bores which form the uprush of event B and which are close in phase at the CCM^+ measuring location may partly explain why uprush B is more energetic than uprush A. Note that the bed level change is a result of instantaneous sediment transport gradients, which means that pre-suspended sediment that is advected from the inner surf towards the lower swash zone may also be an important factor (Jackson *et al.*, 2004; Pritchard and Hogg, 2005).

For event A, strong wave-backwash interactions result in a stationary bore at the CCM^+ location which seems to promote sediment pick-up (**Figure 5.12i**, t/T_{gr} = 0.5 to 0.7). Sediment suspension events under stationary bores have been observed before (Caceres and Alsina, 2012) and relate to strong vertical (turbulent) velocity fluctuations (Aagaard and Hughes, 2006). Accretion of the bed starts a couple of seconds after the incident bore arrives at the measuring location, and is possibly explained by a decrease in velocities and sediment settling as a result of the backwash interruption (Puleo *et al.*, 2014). For event B, the combination of strong accretion and high near-bed sediment concentrations during the mid-final backwash stage suggests a large amount of advected sediment arriving from the shoreward direction (i.e. a larger amount than for event A). This large amount of sediment is possibly mobilized by the stationary bore that was observed about 1 m shoreward from the CCM^+ location for event B.

The sequence of the various erosion and accretion events induced by the individual wave groups forms an overall bed level fluctuation at the repeat period T_R (= 195 s). This slow bed level fluctuation is of similar magnitude (1-2 mm amplitude) as the net bed level change

induced by each swash event (2-3 mm), which suggests that both are potentially relevant for swash zone morphology. To the authors' knowledge, only one study discusses the effects of this repeat frequency on near-shore processes. Baldock *et al.* (2000) report the potential relevance of wave phase modulations at the repeat frequency on the generation of wave breakpoints and on water surface levels and run-up in the swash. Similar to Baldock *et al.* (2000), the low-frequency regions in our experiment show negligible energy in the water level spectrum (**Figure 5.5f**) and the wave groups are approximately equal in terms of wave energy. This suggests that the bed level changes occurring at f_R are the result of sediment transport processes repeating at this repeat frequency, e.g. processes driven by wave-swash interactions during uprush and backwash, rather than the result of water surface oscillations associated to this frequency. A spectral coherence analysis between bed levels (CCM$^+$) and water surface levels (AWG) for these data supports this explanation, showing minor energy at f_R compared to the values at f_{gr} (Alsina et al., 2014). This marks a clear difference from previous studies that highlighted the importance of low-frequency (infra-gravity) waves on swash zone sediment transport processes (Beach and Sternberg, 1991) and bed level changes (Puleo et al., 2014), as these studies found substantial energy in the low-frequency bands of the water level spectrum.

The present results highlight the importance of wave-swash interactions on bed level changes and swash morphology. However, a more thorough explanation of the observed local bed level changes requires a characterization of bed level changes and sediment transport rates along the complete swash zone. Moreover, bed level measurements for a wider range of swash conditions (e.g. including uprushes and backwashes that are free of interactions) are required for a more generic assessment of the importance of these interactions.

5.7.2 Sheet flow dynamics and implications for modeling sheet flow transport in the swash zone

Sheet flow transport is observed at instances with sufficiently high instantaneous velocities (> 1 m/s), which agrees with observations of oscillatory sheet flows (O'Donoghue *et al.*, 2006). These instances occur mainly during the uprush and during the middle/final stage of the backwash phase, which agrees with earlier observations for natural swash zones (Yu *et al.*, 1990; Lanckriet *et al.*, 2013; Lanckriet *et al.*, 2014). The dynamics of the sheet flow layer for the lower swash in this experiment exhibit both similarities and differences with oscillatory sheet flow. Differences are attributed to (i) effects of bore-induced turbulence and (ii) the importance of flow non-uniformity and horizontal advective transport.

At the lowest vertical elevations, the pick-up of sediment during the wave group shows a strong similarity with the pick-up occurring in oscillatory flows (also surface waves). Pick-up events occur predominantly at instances of large horizontal velocities and accelerations (during uprush and backwash) and can probably largely be explained by horizontal shear-induced turbulence (see e.g. Kranenburg *et al*. 2013). However, in line with Lanckriet and Puleo (2015), our results indicate that not only horizontal shear but also bore turbulence can promote sediment pick-up and sheet flow layer growth. This is observed firstly for the early uprush (t/T_{gr} = 0 to 0.1) of both events, where pick up is major and sheet flow thicknesses are higher than for oscillatory sheet flow studies with similar sediment and peak velocities, and secondly for the backwash, where the stationary bore at the CCM$^+$ location for swash event A (from t/T_{gr}

= 0.6 to 0.8) promotes vertical sediment exchange even though water and particle velocities are low.

During the backwash, the local bed slope may promote the mobilization of sediment. However, the absence of sediment pick-up during the final backwash stage suggests that the high near-bed sediment mass is not locally entrained (vertical exchange) and must therefore be arriving from the middle/higher swash (horizontal advection). The accretion of the bed during the backwash supports this idea of a large amount of advected sediment arriving from the onshore direction. This large transport is confined to a small water layer, so sediment concentrations are likely of similar magnitude as concentrations restricted to upper sheet flow layers for oscillatory flow conditions. As a result, the sheet flow layer thickness during the backwash of both events is larger than expected based on local hydrodynamics and previous observations for oscillatory sheet flows. This is in particular true for event B, where backwash sediment advection is likely higher (see Section 5.7.1), resulting in a large sheet flow thickness.

The new measurements show that cross-shore sediment advection in the swash is not only relevant for suspended sediment transport, but it also affects the characteristics of the sheet flow layer. Consequently and unlike previous observations for oscillatory sheet flow, the sheet flow dynamics and fluxes during uprush and backwash are not purely controlled by local hydrodynamics. This implies firstly that vertical profiles of particle velocities and fluxes do not necessarily scale to sheet flow thicknesses: sediment fluxes may be low even when sheet flow thicknesses are high (e.g. below stationary bore during event A backwash). A second implication is that 'local' formulations for sheet flow sediment transport of the type of Meyer-Peter & Mueller (e.g. Nielsen, 2006) may not be valid for the swash zone. Instead, sheet flow transport models for the swash may require a coupling with an intra-wave advection-diffusion model that calculates time-dependent near-bed suspended sediment transport (such as Alsina *et al.*, 2009; Zhu and Dodd, 2015). On the other hand the measurements showed that (i) especially the upper sheet flow layer is influenced by advection effects – the pick-up layer still shows a strong resemblance with oscillatory sheet flows; (ii) the largest sheet flow fluxes seem to occur in the lower parts of the sheet flow layer. Therefore, characteristics of the sheet flow pick-up layer may still be locally controlled, and sand transport in this layer could be modeled as such.

5.8 Conclusions

Measurements of bed level fluctuations and detailed sheet flow characteristics throughout a complete swash cycle are presented. These measurements were obtained in the lower swash during a wave flume experiment involving bichromatic wave groups. A new instrument (CCM^+), capable of measuring continuous gradual bed level evolution as well as concentrations and particle velocities in the sheet flow layer, was applied for the first time.

At the lower-swash location studied here, observations of the CCM^+ system show a consistent pattern of rapid net bed erosion during the early uprush and gradual accretion during the middle backwash phase. Subtle differences in hydrodynamics between the various wave groups lead to substantial differences in both the magnitude of the intra-group bed level fluctuations (6-13 mm) and in the net bed level change (2-3 mm erosion or accretion) induced

by each group. This causes the bed to respond not only at the group frequency of the bichromatic waves, but also at the repeat frequency of the wave group sequence.

Sheet flow transport was observed at the early uprush and during the middle and late backwash phase. At the early uprush, the growth of the sheet flow layer and the drop in bed level occur almost simultaneously. The sheet flow layer exhibits some features similar to oscillatory sheet flow, such as sediment entrainment from the pick-up layer. This pick-up is observed not only when horizontal shear velocities are high, but also in occurrence of wave-swash interactions during the backwash. Direct cross-shore sediment flux measurements in the sheet flow layer from the CCM$^+$ show similarities with oscillatory sheet flow conditions, with highest flux rates found in the pick-up layer.

Notable differences from observations of oscillatory sheet flow are (i) a time-varying elevation of the concentration pivot-point within a wave group cycle; (ii) an absence of mirroring concentration behavior in pick-up layer and upper sheet flow layer. These differences can be explained from the highly non-uniform flow conditions. Sediment advection dominates the upper sheet flow layer concentration behavior and the properties of the sheet flow layer are not fully locally determined. This implies that existing 'local' formulations for sediment transport may not be valid for the swash zone.

5.A. Evaluation of CCM$^+$ bed level measurements

The new concentration tracking system is in essence a feedback loop between concentrations and sensor movement, ensuring that the sensor will always move in the direction of a certain target concentration. If the tracking system would perform ideally, the system would be able to keep the measured concentrations at all times at a target value through continuous adjustment of the sensor elevation. In practice, the probe fluctuates around the elevation of the target concentration. This is due to (i) the limitations of control system (e.g. system lags and probe risks overshooting); (ii) the spiky nature of the measured concentration signal; (iii) the time-varying vertical concentration gradients. As a result of the latter, there is not a single perfect setting for the tracking system's gain factor for an experiment, as the response sensitivity (in terms of vertical distance to be covered for a certain measured concentration offset) should be constantly varying.

This section evaluates the performance of the new concentration tracking system. This is done in two ways: (i) by studying the probe's tracking ability in the spectral domain (Section 5.A.1); (ii) by comparing the phase-averaged intra-group bed level measurements of the 'quick' CCM$^+$ probe 3 with bed level estimations obtained from the CCM$^+$ probe 2 concentration measurements (Section 5.A.2). The results are evaluated in Section 5.A.3.

5.A.1 Evaluation of CCM$^+$ in the spectral domain

As a start, the probe's response at various time scales is analyzed. Rather than examining the time series of the probe, the power spectra of concentrations and positions of the various CCM$^+$ probes are studied. In order to explain this, consider a first case of a fixed probe at a constant level near the bed interface (so no bed level tracking). This probe measures concentration

fluctuations as a result of sheet flow behavior or bed level motions. The various types of fluctuations will appear as energy peaks in a power spectrum of the measured concentrations. Now consider a second case of an ideally tracking probe, i.e. the probe is able to keep up with all elevation changes necessary to keep the measured concentration constantly at its target value. In this situation the power spectrum of the (constant) concentration signal will not show any energy, while on the other hand the power spectrum of the probe elevation will show energy peaks at the dominant physical frequencies. In practice, the probe control system is not ideal, and it can be expected that especially the high-frequency fluctuations of the bed cannot be followed by the probe. Consequently, these frequencies will not appear in the power spectrum of the probe elevation but will appear in the power spectrum of the concentration signal instead.

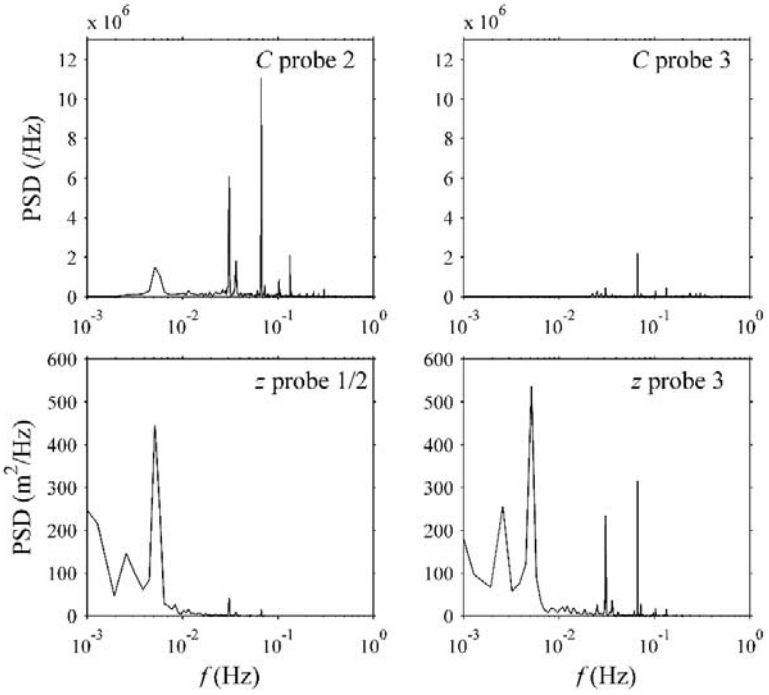

Figure 5.A.1. Power spectral densities of concentrations (upper) and positions (lower) for 'slow' probe 2 (left) and 'quick' probe 3 (right). Data of one run in semi-equilibrium conditions.

Power spectra of concentrations and positions for both probes are found in **Figure 5.A.1**. Concentration measurements of probe 2 show distinct peaks at f_{gr} (0.067 Hz) and $0.5f_{gr}$, and a smaller peak at f_R (0.005 Hz). Physical explanations of these peaks are given in Section 5.1. Spectral energy of this probe's position is restricted to the lower-frequency bands, with a clear peak at f_R. This suggests that probe 2 moves with the lower-frequency bed level motions, but it is at an approximately fixed level at frequencies higher than 0.01 Hz. At these higher frequencies, the probe measures concentrations while being at a close-to-fixed position – so its movements do not distort the measurement.

Probe 3 shows a reverse pattern. As expected, the total energy in the concentration spectrum is less than for probe 2, while there is more energy in the position spectrum. The concentration spectrum shows negligible energy at frequencies lower than f_{gr}. Apparently, in this lower

frequency range, the probe is able to keep concentrations constantly at its target value, i.e. the probe is well able to follow bed level evolution. The peak in the concentration spectrum of probe 3 at f_{gr} indicates that the probe is not able to respond perfectly to bed level changes driven by the wave groups. The spectral energy of this peak in C is much smaller for probe 3 than for probe 2, which suggests that the probe approaches but not perfectly tracks the intra-group bed level.

Based on these results in the present swash experiments, CCM$^+$ probe 3 is only used to provide bed level (reference) information at time scales larger than the wave group time scale (frequencies < 0.067 Hz). CCM$^+$ probe 2 is used to provide concentration information at time-scales equal to or smaller than the scale of individual wave groups (f > 0.067 Hz).

5.A.2 Evaluation of the CCM$^+$ bed level tracking system in the time domain at short (intra-wave group) time scales

Figure 5.10e,f can be used to compare the phase-averaged intra-group bed level measurements (CCM$^+$ sensor 3) and the pivot elevation extracted from the concentration measurements (sensor 2). The latter approaches closely the real bed, as it should not be experiencing any phase delay.

Qualitatively, the intra-wave bed measurement (probe 3) resembles the actual pattern of pivot level fluctuations. It is obvious that the magnitudes of the intra-group bed level measurements by probe 3 (4 and 6 mm for events A and B, respectively) are smaller than the observed pivot point fluctuations (event A: 6 mm; event B: 13 mm). In addition, the bed level measurements of probe 3 lag the pattern of the "real" bed with a delay up to about 2 s. This is most evident during the uprush phase where erosion is severe. Apparently, the probe is not able to follow the bed when it evolves rapidly on a time scale of 1 to 2 s.

5.A.3 Discussion of CCM$^+$ capabilities

The CCM$^+$ in quick tracking mode is well able to track the bed at frequencies lower than f_{gr} (0.067 Hz) in the present swash experiment. At frequencies similar to or higher than f_{gr}, the quality of the CCM$^+$ measurement decreases. On an intra-group time scale the CCM$^+$ bed level measurement shows a smoothened and lagged representation of the actual bed. This smoothening and lagging depends on the magnitudes and time scales of the erosion and accretion events that induce the bed level fluctuations. E.g. for swash event A, characterized by a less severe erosion/accretion pattern than event B, the direct bed level measurement of CCM$^+$ is of better quality.

The CCM$^+$ probes are physically able to move substantially faster than during the current experiment. The gain factor that controls the probe's movement sensitivity can be increased. However, this soon results in probe overshooting and unstable behavior, in particular when sheet flow layers are small or absent (i.e. when there is a direct vertical transition from the immobile bed to 'clear' water). The CCM$^+$ tracking capabilities can possibly be improved by including more sophisticated proportional-integral-derivative (PID) control loops. However, for experiments with repeating wave conditions as reported herein, the main purpose of the

CCM+ bed level tracking system would be to measure the gradual erosion patterns only; something the measuring system is well capable of.

As discussed in the introduction, most of the 'classic' instrumentation (e.g. echo sounders) fails to measure the bed during both exposed stages and submerged stages of the bed. In terms of concentration measurements, most instruments (e.g. OBSs) fail at measuring the high concentrations during the early uprush and late backwash phase when water depths are shallow. The recently developed Conductivity Concentration Profiler (CCP; Lanckriet *et al.*, 2013) is the only instrument capable of measuring sheet flow concentration profiles and bed level changes with high temporal ($f > 1$ Hz) resolution. The CCP measures a complete sheet flow concentration profile at once, which is a major advantage in many conditions. However, it also has limitations, e.g. (i) sheet flow thicknesses smaller than 3.5 mm cannot be resolved (Lanckriet *et al.*, 2013); (ii) the measuring window (30 mm) is limited, which may lead to a substantial loss of data when the bed is evolving (Puleo *et al.*, 2014); (iii) the system is unable to measure particle velocities. Regarding the latter, it is stressed that to the authors' knowledge none of the existing instrumentation but the CCM+ is capable of direct particle velocity measurements. Yet, these measurements are of crucial importance for estimation of sediment fluxes and understanding of swash morphology.

Obvious limitations of the CCM+ system are (i) it cannot directly measure rapid instantaneous bed level changes; (ii) it provides a point measurement of concentrations (and not a complete profile). As a result, phase-averaging is required to sample the complete sheet flow layer including time-varying bed levels during a wave (group). More of practical nature is the fact that the dimensions and weight of the tank make it an instrument more suitable for laboratory than field conditions.

6 Discussion

This Discussion chapter first reflects on the research methodology as followed in this thesis (6.1) and then on the possible implications of the new results for improving engineering-type sand transport models (6.2).

6.1 Methodology

This section addresses the choices made in the experimental design and the extent to which these choices affect the results. Specifically, the section addresses general uncertainties related to the wave flume experiments (6.1.1), scale effects (6.1.2), the choice of wave conditions (6.1.3) and instrumental limitations and uncertainties (6.1.4).

6.1.1 Experimental constraints

The main advantages of wave flume experiments are that processes can be isolated and that wave conditions can be controlled and repeated. This for example enables ensemble-averaging over many wave cycles to improve confidence in the results (see also **Section 1.5**). In addition, the experiments are fully reproducible. However, there are also drawbacks of such experiments. These drawbacks are extensively discussed by Hughes (1993); the most important ones for the present study are shortly addressed in this section.

Flume seiching generated a standing long wave with period of about 45 s and amplitude of *O*(cm), which was identified from the spectra and was filtered out prior to the analysis of velocities (**Chapter 2**). Waves in the CIEM flume were generated based on first-order theory, which leads to the generation of 'spurious' free long waves that interact with the short waves (Barthel *et al.*, 1983). In addition, short waves were reflected by the bar slope and bar and by the not fully dissipative fixed beach. Both effects (spurious waves and reflection) induce cross-shore modulations in wave statistics (wave height, skewness, asymmetry), particularly along the offshore slope of the bar (c.f. Van der A *et al.*, Submitted). The modulations in wave height were of *O*(cm) and were considered negligible relative to changes induced by wave shoaling and breaking. Higher-order wave statistics (skewness, asymmetry) may be more significantly affected by spurious and reflected waves, and this in return affects cross-shore-varying sediment transport rates (c.f. **Chapter 4**). Unfortunately, the dynamic pressure measurements did not enable detailed examination of the wave shape deformation. Note that the cross-shore variation in near-bed velocity and acceleration skewness is qualitatively consistent with observations of water surface levels (Flick *et al.*, 1981; Beji and Battjes, 1993). Therefore, it is concluded that wave deformation is largely explained by shoaling, breaking and de-shoaling, and that effects of spurious and reflective waves are inferior.

The flow in the wave flume is two-dimensional (x, z) by approximation: transverse asymmetries in flow and in sediment transport did appear. Circulations in the x-y plane were confirmed by accompanying experiments (Van der A *et al.*, Submitted) and are possibly

explained by an imbalance in flow perturbation by the measuring instrumentation at either side of the flume's centerline. This circulation is not expected to importantly affect the near-bed measurements, since the ACVP was deployed close to the center of the flume, but it may lead to a slight offset (<0.05 m/s) in ADV-measured time-averaged velocities at outer-flow elevations. In addition, the bed profile was not fully symmetric; instead, the bed was consistently lower at the flume's side-walls and higher along the flume's centerline. This was particularly true at inner surf zone locations during the breaking-wave experiments. The bed asymmetry may be caused by circulations in the y-z plane or by scouring at the flume's side-walls. For the swash experiments (**Chapter 5**), bed asymmetries were levelled out after every 2 hours of experimental duration. For the breaking-wave experiments (**Chapters 2 to 4**), a 3-D scan of the bed profile was obtained using a sand ripple profiler after finishing one of the experimental repeats. The scan showed that although transverse asymmetries were evident, the transverse-averaged bed profile was close to bed profile measurements obtained from one of the acoustic bed level sensors (the sensor deployed about halfway between the flume's centerline and flume side-walls). Therefore, bed levels used for further analysis were at inner surf zone locations based only on this sensor, while the bed at other locations was taken as the mean of both sensors.

Most instruments were deployed in-situ. The mobile frame and wall frames holding the instrumentation were designed to be sufficiently stiff to withstand the impact of wave forcing. The natural frequency of the mobile frame was checked through accelerometer testing prior to the breaking-wave experiments. During the experiment, auto-spectra of velocities did reveal small peaks at the frame's natural frequency (around 10 Hz), but the associated energy was orders of magnitude smaller than the energy contained in the physical turbulence. The in-situ deployment of the instruments plus frames further led to flow interference and possible wake turbulence. The effects of wake turbulence were assessed using the most offshore location as a reference, as physical turbulence due to waves and currents is small at this location. No clear effects of wake turbulence on the ACVP data were found (**Chapter 2**). Accompanying experiments by Van der A *et al.* (Submitted) revealed, through inter-comparing turbulence intensities by two separate instruments, a local increase in outer-flow turbulence intensity by ADVs due to wake turbulence induced by the measuring frame. However, the turbulent velocity fluctuations associated with such wake turbulence are of O(0.01 m/s) and are only significant far from the breaking region where other sources of turbulence are minor.

The research in **Chapters 2 to 4** involves complex interactions between various hydrodynamic and sediment transport processes. Due to these interactions it is not always trivial to explain the physical processes based on the experimental observations alone. This is for example true for combined bed slope and breaking-generated TKE effects on wave bottom boundary layer thickness (**Chapter 2**) and on bedload transport rates (**Chapter 4**). Further experiments that isolate such processes, or simulations with process-based numerical models, can help to further advance the understanding of sediment transport physics in the surf and swash zones (Section 7.2**)**.

6.1.2 Scale of experiments

The scale of the breaking and swash zone experiments does not differ much from field scale. The median sediment diameter (D_{50}) of 0.24 mm in the experiments is close to the typical size (D_{50} = 0.25 mm) found on Dutch shorefaces (Van der Spek and Lodder, 2015). Results for the breaking zone (**Chapters 2 to 4**) are based on regular waves with period T = 4.0 s and 'offshore' wave height H_0 = 0.85 m. These waves are of slightly smaller period/height than reported average wave conditions near the Dutch coast (c.f. Wijnberg and Terwindt, 1995; Grasmeijer, 2002) (yet still considerably smaller and shorter than reported swell waves, c.f. Ruessink, 2010). Offshore wave heights for the swash zone experiments (**Chapter 5**) are substantially smaller than waves at Dutch coasts, but the wave conditions result in cross-shore velocity magnitudes in the swash zone that are similar to field observations (c.f. Chardón-Maldonado *et al.*, 2015).

As the experiments are near-full-scale, the sediment properties were not scaled. The large-scale waves led to Reynolds numbers and turbulence properties that are similar to field scales over the complete water column including the wave bottom boundary layer. The importance of such large scale conditions is best illustrated by comparing the temporal turbulence behavior. In small-scale laboratory studies with plunging waves, breaking-generated TKE rapidly saturates the water column and dissipates almost completely before the end of the wave cycle, leading to a strong temporal variation in TKE (e.g. Ting and Kirby, 1995; De Serio and Mossa, 2006). However, in the present experiments, the temporal variation in TKE is much smaller; TKE builds up over multiple wave cycles since a large fraction of breaking-generated turbulence persists into the subsequent wave cycle (c.f. **Chapter 2**; Van der A *et al.*, Submitted). Van der A *et al.* (Submitted) argue that this difference is purely due to the scale of the experiments: the ratio between the largest and the smallest turbulence length scale increases with Reynolds number (e.g. Pope, 2000) and this ratio is therefore much higher in a full-scale experiment. Consequently, in a larger scale experiment, the largest turbulent vortices require a longer duration to fully dissipate.

Drawbacks of such large-scale experiments are that instruments have to be deployed in-situ (see also previous section). This differs from small-scale wave flume experiments, where hydrodynamics can be measured more easily with ex-situ optical instruments that do not disturb the flow (e.g. LDA, PIV). Another advantage of small-scale experiments is that instruments such as PIV can instantly measure the two-dimensional velocity field with high spatial resolution; in large-scale conditions, the existing instrumentation requires many experimental repeats to obtain a high spatial coverage of measurements. The in-situ deployment further requires a very carefully designed experimental set-up, in order to obtain such high-resolution (mm scale) measurements without flow blocking or instrumental vibrations. Especially the measuring frame requires a careful design and often needs to be custom-built for the experimental purpose. Other constraints of large-scale experiments are more of practical nature: (i) the restoration of bed profile is a laborious exercise; (ii) a significant portion of the experimental time gets lost in the draining and filling of the flume; (iii) a team of 4-5 persons is required to conduct the experiments. These practical constraints explain possibly why such few datasets of sand transport process measurements under large-scale wave conditions are available.

6.1.3 Wave conditions

An important limitation in the present thesis is the limited number of experimental conditions. The experiments were designed primarily for obtaining new insights in sediment transport processes. However, different wave conditions would have resulted in differences in terms of hydrodynamics which in return would alter sediment transport processes. For instance, two important wave parameters controlling turbulence and sediment dynamics in the breaking region are the breaker index (H/h) and the breaker type (plunging, spilling). The breaker index importantly controls time-averaged turbulent kinetic energy in the water column (Ruessink, 2010) and, in return, sediment entrainment (Steetzel, 1993). The breaker index also correlates positively with wave asymmetry, and consequently, with near-bed velocity and acceleration skewness (Grasso *et al.*, 2012). The breaker type affects the vertical distribution of TKE, with stronger mixing and a larger penetration depth of breaking-generated turbulence under plunging than under spilling breakers (e.g. Ting and Kirby, 1994). This leads to significant differentiation in terms of sediment entrainment and mixing between both breaker types (Aagaard and Jensen, 2013). Both breaker types differ notably in terms of TKE transport and production/dissipation, resulting in stronger temporal variability in TKE for plunging than for spilling breakers (Ting and Kirby, 1994). In return, the spatiotemporally-varying TKE affects suspended sediment transport (e.g. **Chapter 3**). Section 3.5 discusses how other wave conditions may lead to different behavior in spatiotemporally-varying TKE and in suspended sediment transport.

These studies show that the results in the present experiments will not be valid for the full spectrum of wave conditions at natural beaches. At the same time, the present study (with a large spatial coverage of measurements for a limited number of wave conditions) allows a more in-depth analysis of the cross-shore variation in sand transport processes than most of the previous studies (that involved varying wave conditions but limited spatial coverage). Both approaches yield different insights in cross-shore sand transport processes in the surf and swash zones.

Non-breaking wave studies have shown how sediment processes and transport rates greatly depend on sediment diameter, with finer sediment leading to suspension at higher elevations and exhibiting phase lags that may alter the direction of time-averaged sediment fluxes (Dohmen-Janssen *et al.*, 2002; O'Donoghue and Wright, 2004b). Compared to the present medium-sand experiments, where near-bed vertical concentration gradients are steep and wave-related suspension remains largely confined to the wave bottom boundary layer, experiments with finer sand or larger waves could lead to substantial differences in terms of sediment entrainment and vertical distributions of sediment fluxes. Specifically, higher contributions of (current-related and wave-related) suspended transport relative to bedload transport may be expected for finer sediment/larger waves.

The choice for regular (monochromatic) waves leads to higher time-averaged velocities (undertow magnitudes) than for equivalent irregular waves (Ting, 2001). The undertow in the breaking region dominates net transport of TKE (Van der A *et al.*, Submitted) and of suspended sediment (**Chapter 3**). In field conditions, where waves are irregular, one would find less strong undertow magnitudes (c.f. Garcez-Faria *et al.*, 2000) and a lower relative importance of current-related suspended fluxes to total suspended load (c.f. Ogston and Sternberg, 1995;

Ruessink *et al.*, 1998). The monochromatic waves further lead to strong cross-shore gradients in transport rates as energetic waves continuously break at the same location. Consequently, the evolving breaker bar is much sharper-crested and has steeper bed slopes than bars on natural medium-sand beaches (c.f. Gallagher *et al.*, 1998). Hence, bed-slope-related processes (e.g. bedload transport) are likely more important in the present study (**Chapters 2 to 4**) than in a natural situation.

Altogether, it is recommended to validate the breaking-wave results in the present study (**Chapter 2 to 4**) for a wider range of (combinations of) wave conditions, bed profiles, and sediment sizes (see also Section 7.2).

The *swash zone* experiment (**Chapter 5**) was, analogous to the breaking-wave experiment, designed primarily to extend insights in *sediment transport processes* for a specific wave condition rather than in transport rates or morphology for a wider range of conditions. The wave condition was designed to result in energetic flow (high onshore/offshore velocities) and strong wave-backwash interactions in the lower swash zone. Such interactions are common for natural beaches and have been described by many studies (see **Chapter 5**, or Chardón-Maldonado *et al.*, 2015, for an overview). **Chapter 5** illustrates that wave-swash interactions affect local pick-up and can alter sediment transport gradients, inducing local accretion of the bed. The magnitudes of pick-up, bed changes, and horizontal advection processes depends highly on the wave conditions: even very subtle differences in offshore wave conditions may lead to large quantitative differences in sheet flow thickness and bed level changes in the swash zone (**Chapter 5**). Note further that sediment transport in the swash zone is not determined fully locally, but also by the time-varying sediment exchange with the inner surf zone (c.f. Alsina *et al.*, 2012). Moreover, transport in the swash is not only due to a (quasi-)instantaneous response to local hydrodynamic forcing: instead, particles that are mobilized as bedload during the backwash phase may be entrained as suspended load upon the start of the subsequent swash event (Sou and Yeh, 2011; Pujara *et al.*, 2015b). Due to these three factors (sensitivity to hydrodynamic forcing, not only locally determined, response not fully instantaneous), *quantitative* results in **Chapter 5** depend greatly on the chosen bed geometry and (combination of) wave conditions. However, it is expected that sediment processes identified in **Chapter 5** are *qualitatively* representative for a wider range of swash conditions (i.e. energetic swash events with strong wave-backwash interactions at a medium-grained intermediate-state beach).

6.1.4 Instrumentation

For the *breaking-wave* experiments (**Chapters 2 to 4**) the spatial coverage and temporal resolution of the velocity and concentration measurements in the present experiments were large compared to previous studies. This is particularly true for the lowest 0.10 m of the water column, a region including the wave bottom boundary layer (WBL) and the sheet flow layer. A higher spatial coverage at outer-flow elevations would have been useful in terms of understanding the full extent of spatiotemporally varying hydrodynamics (including turbulence) and in order to arrive at more reliable estimates of depth-integrated suspended transport (**Chapter 3**), which in return would also improve the indirect estimates of bedload transport (**Chapter 4**). However, a higher coverage could not be achieved during the present

study as (i) adding more instruments to the frame was no option due to the potential risk of flow blocking; (ii) the labor-intensive experimental procedure (draining flume, restoring profile, filling flume) did not allow coverage of more cross-shore positions. Instead, the outer- and inner-flow velocity and turbulence field were sampled with higher spatial (vertical + horizontal + temporal) resolution during a separate campaign, for which the bed was fixed by covering it with a concrete layer (Van der A *et al.*, Submitted).

Highest near-bed TKE, and consequently the most prominent effects of breaking-generated turbulence on sediment transport, is found along the steep shoreward-facing bar slope. Unfortunately, no detailed measurements of the bedload layer were obtained at this location. Consequently, the experiment does not provide full insights in how the bedload transport layer is affected by breaking-generated turbulence and by the dynamic vertical sediment exchange with the suspension layer. This knowledge gap may be filled through additional experiments whilst measuring the sheet flow layer with the CCM^{+}, although one should be aware that the rapid local bed level evolution at this location will make it extremely challenging to obtain high-quality measurements of the sheet flow layer.

In addition to the Transverse Suction System (TSS) measurements of time-averaged concentrations, outer-flow time-varying sediment concentrations were also measured with higher spatial resolution using an Aquascat Acoustic Backscatter System (ABS) deployed from the mobile frame. However, these ABS data had to be discarded due to substantial signal attenuation by air bubbles. Data of two OBSs at the middle and top of the water column were discarded for the same reason. This shows that one should be cautious with optical and acoustic sand concentration measurements acquired in the bubbly breaking region; the data may be invalid and should ideally be validated with reference measurements that are insensitive to air bubble presence (e.g. TSS).

A prototype Acoustic Concentration and Velocity Profiler (ACVP) was applied to measure near-bed hydrodynamics (**Chapter 2**) and sediment dynamics (**Chapter 3**). The data of the ACVP formed an important basis for the present study, but some concerns are raised here. Firstly, the combination of instrumental limitations and necessary data treatment steps leads to an underestimation of physical (vertical) turbulent fluctuations, particularly at elevations very close (<1 cm) from the bed. This drawback is extensively discussed in the Appendix to **Chapter 2**. Secondly, it should be noted that the acoustic inversion (from acoustic backscatter intensity to sediment concentration) based purely on theoretical considerations (following routines of Thorne and Hurther, 2014) did not yield physically meaningful concentration distributions (see **Chapter 3**). Despite ongoing work on acoustic scattering theory (see Thorne and Hurther, 2014, for an overview), one should be cautious when interpreting acoustically measured concentrations that have not been compared against reference measurements (e.g. TSS). Thirdly, the vertical bin size of the ACVP measurements (1.5 mm) was, given the rather thin sheet flow layers and small intra-wave bed level fluctuations (O(mm), see **Chapter 4**), too coarse for studying the bedload/sheet flow layer. The bin size is limiting here, as the ACVP seems physically capable of sampling the (upper) sheet flow layer when this layer is thicker (e.g. when using light-weight particles, see Revil-Baudard *et al.*, 2015). The performance of the ACVP is yet to be assessed for well-developed sheet flow conditions with real sediment.

Sheet flow layers that are very thin or that occur in very shallow water (i.e. in the swash zone) cannot be studied using present acoustic instrumentation. For such conditions, novel conductivity-based instruments such as the CCM+ (**Chapter 5**) and the CCP (Lanckriet *et al.*, 2013) can measure the high sediment concentrations over the region where acoustic instruments are unsuccessful. However, the quantification of bedload transport rates using these instruments remains extremely difficult. The CCP cannot provide velocities in the sheet flow layer and relies on semi-empirical models for velocity distributions inside the sheet flow layer to quantify fluxes (Puleo *et al.*, 2016). The CCM+ can measure particle velocities, but only during a fraction of the wave cycle with sufficiently developed sheet flow thickness and for a significant amount of wave repetitions (**Chapter 5**). In the present study, these measuring constraints hampers not only the estimates of bedload transport, but also the understanding of processes such as sheet flow pick-up behavior, the effects of external turbulence, and the coupling between suspended and bedload transport. Additional experiments or simulations with detailed process-based numerical models may elucidate on these research topics (see also **Section 7.2**).

The swash zone experiments showed continuous erosion and accretion at various time scales, which could for the first time be quantified using the new CCM+ system (**Chapter 5**). Although the observation itself is interesting and sheds new light on beach response to grouped waves, the measurements do not address whether the bed level changes are induced primarily by bedload or by suspended load transport gradients, and whether the bed changes in the lower swash zone at the 'repeat period' are due to sediment exchange between the lower swash with the inner surf zone or by an exchange with the upper swash zone. The understanding of swash morphology would benefit greatly from combined detailed measurements of bed level changes and time-varying transport rates at adjacent locations (see **Section 7.2**). For understanding the importance of sheet flow transport for swash morphology, these transport rates should ideally be separated into a bedload (sheet flow) and suspended load contribution. However, as stated in the above, the quantification of bedload transport rates using present instrumentation is very challenging.

6.2 Implications for morphodynamic modeling

This section addresses how the insights obtained from the experiments can lead to improved formulations in engineering-type morphodynamic models. Some possible improvements are also suggested in the discussions sections in **Chapters 2 to 5**; the present section focuses on topics that have not been covered in these chapters.

6.2.1 Wave-averaged approach in morphodynamic models

Engineering-type morphodynamic models operate at a wave-averaged time scale to reduce calculation times. Total sediment transport is commonly calculated through a combination of a wave-averaged advection/diffusion model for suspended sediment transport and parameterizations of intra-wave sediment transport processes (i.e. wave-related mixing, wave-related suspended transport, bedload transport). The present study generally supports

such a wave-averaged approach for modeling morphology in the surf and swash zones, although some adaptations may be required (see next sections).

One concern raised here is the parameterization of intra-wave velocities, which provides the hydrodynamic input for bedload transport models. Intra-wave velocity parameters (e.g. peak onshore and offshore velocity, velocity and acceleration skewness) are predicted through empirical parameterizations (e.g. Ruessink *et al.*, 2012). **Figure 6.1** shows a comparison between measurements and predictions of the near-bed velocity and acceleration skewness. Measured skewness and asymmetry vary strongly across the breaker bar. These cross-shore changes in wave shape are likely due to complex behavior of higher-order wave harmonics as waves break and de-shoal along the shoreward slope of the breaker bar (c.f. Flick *et al.*, 1983; Beji and Battjes, 1993). Furthermore, as the wave breaks, it splits into a newly reformed surf bore and a secondary crest (**Chapter 2**). The parameterization by Ruessink *et al.* (2012) does not properly capture these cross-shore variations (**Figure 6.1**). A likely explanation is that the parameterization is calibrated for a wide range of shoaling to inner surf zone conditions but it does not account for complex local wave deformation in the breaking region.

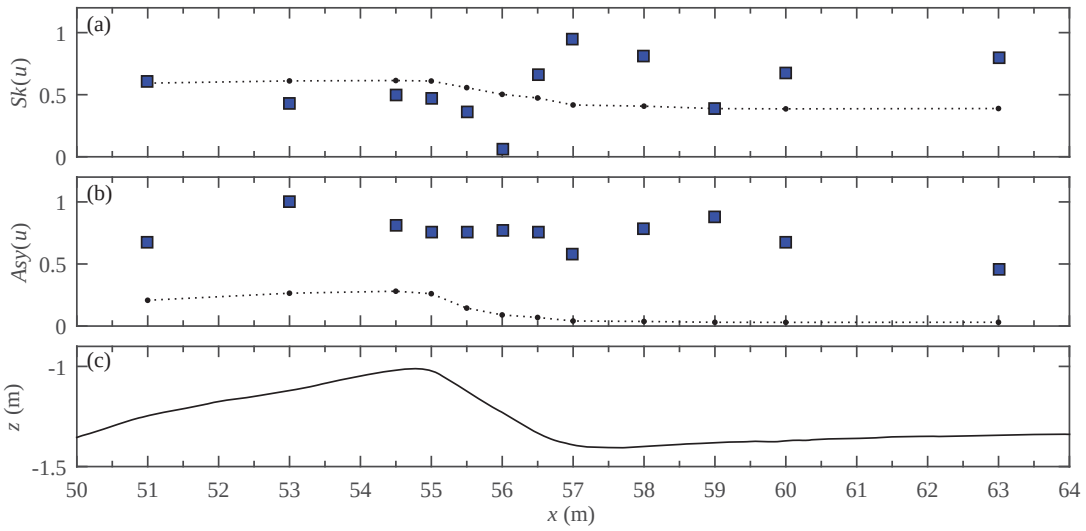

Figure 6.1. Velocity skewness (a) and asymmetry (b) around breaker bar: measurements by ADV at $\zeta \approx 0.11$ m (squares) and predictions based on local Ursell number following Ruessink et al. (2011) (dotted line) for t = 0-15 min. Definitions for skewness and asymmetry are found in Chapter 2 and 4. Panel c shows the bed profile at t = 0 min.

It is further seen that the parameterization predicts the magnitudes of skewness reasonably well (**Figure 6.1a**), but it significantly underestimates the magnitude of the velocity asymmetry (**Figure 6.1b**). A possible explanation for the underestimated velocity asymmetry is that the present study involves monochromatic waves. Field conditions are different in that (i) interaction between irregular short waves (and interaction with long waves) will likely promote breaking of the steepest wave in a sequence, hence resulting in a lower wave asymmetry; (ii) the parameterization is based on data that were time-averaged (over 15 min. sampling intervals) and bin-averaged (over Ursell number classes) and these averaging steps likely result in smoothening of local maximum values. The uncertainties in predicted

skewness/asymmetry values hamper predictions of bedload transport rates in the breaking region, as shown by Schnitzler (2015) using the present study's measurements in combination with Delft3D as a research tool.

To what extent time-averaged velocities near the bed are affected by the large penetration depth of breaking-generated turbulence (**Chapter 2**) cannot be concluded from the data. More detailed analyses with process-based numerical models are required to verify whether the applied formulations for time-averaged velocities are appropriate. Specifically, the data presented here can be used to verify whether near-bed time-averaged velocities can be adequately modeled using morphodynamic models. Schnitzler (2015) showed that Delft3D can qualitatively predict the cross-shore variation in undertow velocity for the present experiment, but the model underestimates undertow magnitudes by up to a factor 2 and it cannot always capture the vertical structure in the undertow profiles.

6.2.2 Turbulence in breaking zone

Turbulence is important in morphodynamic models as it (i) induces a spatial exchange of momentum that affects wave-averaged velocities; (ii) it affects the vertical and horizontal mixing of suspended sediment. The present study further shows that breaking-induced turbulence enhances suspended sediment entrainment (**Chapter 3**) and may also affect bedload transport (**Chapter 4**) in the surf zone. However, the modelling of TKE in the breaking zone is not trivial as many turbulence closure models seem to systematically overestimate TKE under both spilling and plunging waves. This has been shown with process-based numerical simulations at high spatial and temporal resolution (i.e. intra-wave time scale) and for a range of turbulence models, i.e. k-ε (Lin and Liu, 1998; Brown *et al.*, 2016), k-ω (Brown *et al.*, 2016), or, more advanced, large-eddy simulation (Christensen, 2006). Further improvement of turbulence closure models seems essential if near-bed TKE is used as input for sediment entrainment or bedload transport. Alternatively, near-bed TKE could be predicted through parameterizations based on wave and bed characteristics. However, near-bed TKE is firstly not fully locally determined as turbulence spreads horizontally and vertically, and secondly it may not respond instantaneously to forcing at the water surface but is built up over several wave cycles. For these reasons, a quantitative approach through a more detailed TKE model seems to be preferred. The further development of such models may benefit from detailed model-data comparison of the individual terms forming the TKE budget (production, dissipation, transport) under large-scale breaking waves.

6.2.3 Suspended sediment transport in breaking zone

Reference concentrations (C_0) are predominantly determined by local pick-up from the bed and are hardly affected by horizontally advected sediment (**Chapter 3**). In contrast to non-breaking waves, C_0 seems to be determined by near-bed TKE instead of horizontal near-bed velocities. This means that traditional reference concentration/pick-up formulae (e.g. Nielsen, 1992; Van Rijn, 2007a) may not be appropriate for breaking-wave conditions.

A reference concentration formulation based on near-bed TKE was proposed by Steetzel (1991) in the form of $C_0 = K_c \cdot k_b^{3/2}$, in which K_c is a semi-empirical function that depends on sediment diameter and which yields values of $O(500\ \mathrm{kg \cdot s^3/m^6})$ for medium sand; and k_b is the turbulent kinetic energy at the bed. The present experiment supports a direct relation between C_0 and k_b, although C_0 seems to correlate better with k_b^2 than with $k_b^{3/2}$ (**Chapter 3**). Steetzel's (1991) C_0 formulation is straightforward to implement, but it has not been thoroughly validated because hardly any datasets contain simultaneous measurements of k_b and C_0. Other studies have suggested a direct relationship between C_0 and (breaking) wave characteristics (Mocke and Smith, 1992) or between sediment pick-up and wave energy dissipation by wave breaking (Kobayashi and Johnson, 2001). Such models assume that wave breaking leads to a local and instantaneous increase in C_0. This is not supported by the present measurements since breaking-generated turbulence, responsible for the enhanced pick-up, spreads horizontally and vertically and does not arrive instantaneously at the bed at all locations (**Chapter 2**).

As an alternative to 3D morphodynamic models, depth-integrated 1D/2DH models have been developed for research (e.g. Reniers *et al.*, 2004) or engineering purposes (e.g. XBeach: Deltares, 2015b). The aforementioned models use an equilibrium concentration approach to calculate the depth-integrated suspended sediment load and transport rates. Effects of breaking-induced turbulent 'stirring' to depth-integrated suspended load are accounted for by raising the *rms* horizontal velocities through $u_{rms,n}^2 = u_{rms}^2 + K_s \cdot k_b$. The empirical factor K_s is set equal to unity (Reniers *et al.*, 2004) or to 1.45 (Deltares, 2015, Van Thiel de Vries, 2009) and k_b is computed through an empirical model based on turbulence at the water surface and assuming a vertical decrease that depends on breaker index (Roelvink and Stive, 1989). The newly calculated velocity, $u_{rms,n}$ is then used to calculate equilibrium concentrations. Using measured data from the present study, it becomes readily apparent that the addition of k_b ($=O(0.05\ \mathrm{m^2/s^2})$) to u_{rms}^2 ($=O(0.5\ \mathrm{m^2/s^2})$) does not yield a substantial increase in $u_{rms,n}^2$. This suggests that the effect of wave breaking on suspended sediment load, with a K_s of $O(1)$, can only be substantial if k_b is significantly overestimated by the model.

Suspended sediment transport at outer-flow elevations is predominantly current-related (**Chapter 3**) and can therefore be properly modeled at wave-averaged time scale. However, the wave-related transport inside the WBL should be accounted for using a separate formulation as part of suspended (e.g. Van Rijn, 2007b) or of near-bed transport (e.g. van der A *et al.*, 2013). Note that Van Rijn (2007b) assumes that wave breaking induces a vertical extension of the wave-related transport to the outer flow, and therefore the transport is enhanced with an empirical breaking-wave parameter. This vertical extension is supported by previous measurements that found significant wave-related transport at outer-flow elevations under breaking waves (Houwman and Ruessink, 1996; Grasmeijer, 2002; van Thiel de Vries *et al.*, 2008; Yoon, 2011). However, these observations lack detailed measurements of time-varying (turbulent) velocities near the bed and consequently, it is unclear whether the wave-related suspension is due to the arrival of breaking-generated turbulence or due to the vertical advection by strong upward-directed periodic velocities at the wave front of a strongly asymmetric wave. The present study provides such high-resolution measurements but it finds little support for a vertical extension of wave-related transport to the outer flow. Instead, the wave-related transport is confined to the WBL (except at one location along the shoreward bar slope), similar to previous observations under non-breaking waves. This negligible outer-flow

wave-related transport may be attributed to the short wave period and the limited temporal variation in TKE (see **Chapter 3**). The significance of wave-related transport in the breaking region, and the understanding of the underlying physical processes, requires further assessment for a wider range of wave conditions in order to develop a wave-related suspended transport formulation with a better scientific basis and predictive capability.

6.2.4 Bedload transport in breaking zone

Two topics that can be addressed with the present data are (i) the possible enhancing effects of breaking-generated turbulence on bedload transport; (ii) to what extent bedload transport is still locally determined for the strongly non-uniform flow around the breaker bar.

Along the offshore slope up to the breaker bar crest the cross-shore variation in bedload transport rates is predominantly explained by variations in (dimensional) velocity skewness and asymmetry (**Chapter 4**). This is consistent with non-breaking waves and the results do therefore not indicate that an adaptation of existing bedload transport formulations is required for this region. On the other hand, one should be aware that the common application of a bedload transport formulation based purely on local forcing is not fully consistent with the underlying physics. In situations where hydrodynamic conditions vary strongly within the cross-shore length of the orbital excursion (e.g. for the present breaking-wave setting), bedload dynamics can be affected by the influx of sediment or of turbulence from adjacent locations. This is illustrated by the sheet flow layer thickness at the bar crest, which is during the trough-phase higher than expected based on oscillatory sheet flow observations under non-breaking waves because of a positive cross-shore sediment influx. Due to water-particle and particle-particle interactions, such non-zero sediment influx may affect local bedload transport rates. For such situations the application of bedload transport formulations based only on local forcing may not be fully appropriate, although it is arguably the most straightforward and pragmatic approach for engineering-type morphodynamic models.

At the locations between bar crest up to bar trough, i.e. along the steep shoreward-facing bar slope, bedload transport rates correlate significantly with bed slope and with near-bed TKE. Note that due to significant covariation between both parameters, it could not be assessed whether this correlation is physically induced by either one of the two parameters, or whether it is the combined effect of both parameters that affects bedload transport rates. Model formulations have been proposed that account separately for effects by bed slope (Van Rijn, 1993) and by near-bed TKE (Butt *et al.*, 2004; Reniers *et al.*, 2013) on bedload transport, but alternative formulations based on a combined bed slope/TKE effect have also been proposed (Fernández-Mora *et al.*, 2015). Additional experiments that systematically examine the individual effects by both parameters in the breaking region seem necessary to properly include bed slope and turbulence effects in bedload transport models.

6.2.5 Sediment transport in the swash zone

Many studies (see Chárdon-Maldonado *et al.*, 2015, for an overview) have tried to make existing bedload transport formulations applicable to swash zone conditions, for instance through adapting wave friction factors. Such (adapted) sediment transport formulations have a limited to moderate predictive capability in the swash zone, although this is partly due to

the large uncertainties in the data used for validation (Chárdon-Maldonado *et al.*, 2015). Results in **Chapter 5** raise three issues regarding the engineering-type modeling of net (swash-event-averaged) transport in the swash zone:

1. The sheet flow layer does not only respond to hydrodynamic forcing by phase-averaged velocities, but also to turbulence produced by wave-swash interactions. Such interactions will likely affect transport rates and should therefore be taken into account in bedload transport models.
2. Apparently small deviations in offshore hydrodynamic conditions may induce significant differences in terms of wave-swash interactions. This in return leads to considerable variability in bed level changes between swash events at an intra-swash and at an event-averaged time scale. This high sensitivity of transport rates to hydrodynamic forcing makes it extremely challenging to develop proper parameterizations of wave-swash interactions effects on bedload transport.
3. The results reveal a complex intra-swash cross-shore exchange of sediment between the lower and upper swash zone, which affects the sheet flow layer thickness and, consequently, transport rates. Such a time-varying horizontal exchange differs essentially from transport in uniform oscillatory sheet flows, and can only be modeled using detailed intra-wave sediment advection/diffusion solvers. At present, such an approach cannot be easily implemented in morphodynamic models that operate at a wave-averaged time scale.

Due to these difficulties, and due to additional complex swash zone processes that were identified by others (see e.g. **Chapter 1**), morphodynamic models may achieve better results through morphological schemes that directly predict bed level changes without resolving sediment transport rates throughout the swash zone. Such schematizations have already been proposed (e.g. Walstra and Steetzel, 2003; Van Rijn, 2009) and they typically estimate erosion/accretion in the swash zone by combining the calculated transport rates at the shoreline with an empirical prediction of the wave run-up length. However, these schemes do not always yield satisfactory results because they omit much of the relevant physics (Van Rijn *et al.*, 2011). Section 7.2 lists a number of additional swash-zone processes that could be included to improve such swash-zone morphodynamic schemes.

Further development of such model schemes would benefit from high-resolution measurements of spatiotemporally-varying morphology of the complete swash zone for a wide range of wave conditions. Measuring bed level changes in the swash zone has been challenging, but novel instrumentation that measures the swash morphology at high spatial and temporal resolution, for instance through stereoscopic imaging (Astruc *et al.*, 2012; Vousdoukas *et al.*, 2014), is becoming increasingly available.

7 Conclusions and recommendations

7.1 Conclusions

The research questions posed in Chapter 1 were answered through large-scale wave flume experiments focusing on cross-shore sediment transport processes in the surf zone along an evolving breaker bar and in the swash zone. The novelty in these experiments is found in the large scale, the application of novel high-resolution measurement techniques, and the high spatial temporal coverage of measurements.

A proto-type acoustic concentration and velocity profiler (ACVP) was applied to measure, for the first time under a large-scale breaking wave, the hydrodynamics of the wave bottom boundary layer and the spatiotemporal behavior of near-bed turbulence. The ACVP also measured near-bed sediment fluxes, which offer insights in the complex spatiotemporal advection of suspended sediment in the surf zone at both an intra-wave and a wave-averaged time scale. The measurements further quantify the contributions of bedload and suspended sediment transport to the onshore migration and growth of the breaker bar. A novel conductivity-based measurement system (CCM$^+$) was applied to examine sheet flow dynamics and bed level changes in the surf and swash zones.

> RQ1 (Chapter 2): *How does wave breaking affect near-bed (wave bottom boundary layer) flow and turbulence?*

Near-bed hydrodynamics, including turbulent velocities, were measured with the ACVP at 12 cross-shore locations around an evolving medium-sand breaker bar under a regular large-scale plunging breaking wave.

Phase-averaged wave bottom boundary layer (WBL) velocities show similar behavior to non-breaking and oscillatory WBL studies, including distinct velocity overshooting. Time-averaged velocities in the WBL are largely dominated by the strong undertow and show consistent behavior with previous observations for wave-current interactions. Effects of wave (shape) streaming mechanisms are only evident in the shoaling region where the undertow is relatively weak. Near the plunge point and along the shoreward slope of the bar, the dimensionless WBL thickness is about 3 times higher than predictions based on uniform oscillatory flows. This can be attributed to the combined effects of breaking-induced turbulent kinetic energy (TKE) and flow divergence induced by the bed geometry.

Outer-flow TKE matches with previous breaking-wave studies, showing highest values in the breaking region at the breaker bar crest, followed by a decrease in the bar trough. In close vicinity of the plunge point (+/- 0.5 m), TKE is almost depth-uniform over the complete water column (including the WBL), indicating large turbulence production at the water surface and a strong penetration into the water column down to the bed. Near the plunge point, TKE enters the boundary layer during two instances of the wave cycle: a first occurrence rapidly (about 0.5 s) after wave plunging, when breaking-induced TKE rapidly saturates the complete water column including the WBL; a second occurrence during the wave trough phase, when

undertow and periodic velocities transport TKE towards the breaker bar. This invasion results in an increase in maximum TKE inside the WBL with a factor of almost three and in an increase in near-bed Reynolds stress magnitudes with about a factor two between shoaling and breaking region, despite decreasing near-bed periodic velocity magnitudes.

Breaking-generated turbulence travels horizontally offshore (during trough phase) and back onshore (during crest phase) between breaking and shoaling zone. Due to advection by periodic and offshore-directed time-averaged velocities, the area affected by breaking-generated turbulence extends from the breaking region to shoaling locations about 3 m (i.e. 6 times the semi-excursion amplitude) offshore from the plunge point. Advection of TKE from plunge point in onshore direction is restricted by the combination of a decreased orbital velocity amplitude and strong offshore-directed undertow velocities.

RQ2 (Chapter 3): *How are suspended sediment transport processes affected by wave breaking?*

Suspended sediment concentrations and fluxes were measured with the ACVP at the same 12 cross-shore locations covering the shoaling to inner surf zone, with particular high resolution in the lowest 0.10 m that includes the WBL.

Sediment pick-up rates increase with up to an order of magnitude from shoaling to breaking region. Wave-averaged reference concentrations in the breaking region correlate better with near-bed TKE than with bed-parallel periodic velocities, suggesting that breaking-generated turbulence is an important driver for sediment pick-up. At an intra-wave time scale, suspended sediment concentrations are phase-coherent with near-bed TKE. Suspended sediment is particularly well-mixed above the bar crest, where outer-flow concentrations are nearly depth-uniform. This vertical mixing is attributed to the combination of energetic breaking-generated vortices, the strongly asymmetric wave shape (strong upward wave-related advection), and upward-directed wave-averaged velocities resulting from a time-averaged fluid circulation cell.

Net (i.e. wave-averaged) suspended sediment fluxes reveal a complex pattern with vertically alternating onshore and offshore-directed constituents. Net outer-flow fluxes are generally current-related and are directed offshore due to the undertow. Above the breaker bar, net onshore fluxes between wave trough and wave crest level contribute significantly to the depth-integrated suspended transport. Net fluxes inside the WBL are directed onshore at shoaling locations and at breaking locations up to the bar crest due to significant wave-related flux contributions. The net wave-related suspended transport is generally confined to the WBL, except at the breaking location with highest near-bed TKE where net wave-related fluxes extend vertically to outer-flow elevations.

Sediment flux gradients were quantified to study the advection and the pick-up/deposition of suspended sediment. At a wave-averaged time scale, sediment grains are entrained from the bed in the bar trough region, are advected offshore by the undertow, and are deposited in the region covering the shoaling zone, bar crest, and the upper part of the steep onshore bar slope. Wave-averaged near-bed concentrations are largely (>90%) determined by local pick-up; contributions of cross-shore advected sediment are minor.

The flux gradients at intra-wave time scale reveal that the entrainment of sediment in the bar trough occurs primarily during the wave trough phase, when both near-bed velocity

magnitude and near-bed (breaking-generated) TKE are highest. The entrained particles are almost instantly advected offshore during the wave trough phase. Net deposition near the bar crest occurs during the wave crest phase when velocity magnitudes reduce. The suspended particles further follow an onshore-offshore excursion between shoaling and breaking region at an intra-wave time scale. This excursion is consistent with spatiotemporal patterns in TKE, which suggests that sediment particles are trapped in breaking-generated vortices that are advected back and forth following the orbital motion.

> RQ 3 (Chapter 4): *How are bedload processes affected by wave breaking and how do suspended and bedload transport contribute to breaker bar morphodynamics?*

During the same experiment with regular plunging waves, sheet flow layer dynamics were measured just offshore from the breaker bar crest using the CCM$^+$. The sheet flow thickness at the offshore bar slope scales similarly to hydrodynamic forcing as previous observations under non-breaking waves. At the bar crest, horizontal sediment advection along the bed affects sheet flow concentrations and thicknesses during the wave trough phase due to a positive influx of sediment.

The net total transport rate along the breaker bar is decomposed into measured suspended load and bedload contributions. Bedload and suspended load transport are of similar magnitude but of opposite direction. Onshore-directed bedload transport dominates at the shoaling zone, decreases at the bar crest, and increases again at the shoreward facing bar slope. The latter is explained by bed slope effects (i.e. gravity-driven transport) and occurs in presence of high near-bed TKE, that possibly enhances the mobilization of sand grains. The offshore-directed suspended transport rate increases in the breaking region, leading to a domination of suspended transport over bedload transport in the breaking and inner surf zone. Consequently, near the plunge point the net total transport rate reverses from onshore-directed (shoaling zone) to offshore-directed (breaking and inner surf zone).

During the experiment, the breaker bar crest increases in height while the bar trough deepens. Both bedload and suspended sediment transport contribute to breaker bar morphodynamics, but the effect of each component is notably different. Bedload transport leads to erosion of the offshore bar slope and accretion at the bar crest, and additionally leads to erosion of the steep shoreward bar slope and deposition at the bar trough. Suspended transport induces erosion of the bar trough and net deposition at the breaker bar crest.

Suspended sediment samples reveal evident vertical grain sorting at the shoaling and inner surf zone, which indicates that sediment pick-up and vertical mixing is size-selective (i.e. the fraction of fine sediment increases with elevation). This contrasts the breaking region, where sediment pick-up and vertical mixing is size-indifferent due to the strong upward forcing by large-scale energetic vortices and upward time-averaged velocities. Bed samples reveal cross-shore sorting of sand particles by size-selective bedload and suspended load transport. This sorting leads to a gradual increase in sediment diameter from shoaling to inner surf zone and reveals additional local sorting around the breaker bar due to bed slope effects (i.e. downward coarsening along the steep shoreward bar slope).

RQ 4 (Chapter 5): *How do swash processes such as wave-swash interactions and cross-shore intra-swash advection of sediment affect bed level changes and sheet flow layer dynamics?*

During another experiment, the CCM+ was deployed for the first time to measure bed level changes and sheet flow dynamics at the lower swash zone during a complete swash cycle.

Intra-swash bed level changes follow a consistent pattern of rapid bed erosion during the early uprush and gradual accretion during the middle backwash phase. Subtle differences in hydrodynamics between the various wave groups lead to substantial differences in both the magnitude of the intra-group bed level fluctuations (6-13 mm) and in the net bed level change (2-3 mm erosion or accretion) induced by each wave group. This causes the bed to respond not only at the group frequency of the bichromatic waves, but also at the repeat frequency of the wave group sequence.

Sheet flow transport was observed at the early uprush and during the middle and late backwash phase. At the early uprush, the growth of the sheet flow layer and the drop in bed level occur almost simultaneously. The sheet flow layer exhibits some features similar to oscillatory sheet flow, such as sediment entrainment from the pick-up layer. This pick-up is observed not only when horizontal shear velocities are high, but also in occurrence of wave-swash interactions during the backwash. Direct cross-shore sediment flux measurements in the sheet flow layer show similarities with oscillatory sheet flow conditions, with highest flux rates found in the pick-up layer.

Notable differences from observations of oscillatory sheet flow are (i) a time-varying elevation of the concentration pivot-point within a wave group cycle; (ii) an absence of mirroring concentration behavior in pick-up layer and upper sheet flow layer. These differences relate to the highly non-uniform flow: horizontal sediment advection affects the upper sheet flow layer concentrations, i.e. the properties of the sheet flow layer are not fully locally determined.

7.2 Recommendations

This section presents recommendations for further research steps towards improving morphodynamic modeling of the surf and swash zones on the basis of the new experimental results in this thesis. Distinction is made between three research topics (surf zone suspended load, surf zone bedload, and swash zone sediment transport). For each topic, suggestions are made for improving sand transport model formulations, i.e. through model-data comparisons and through additional numerical/experimental research that can help to improve process insights.

Suspended transport in the surf zone

An important step is the inclusion of breaking-generated turbulence effects on suspended sediment pick-up/reference concentrations. Formulations are available (e.g. Mocke and Smith, 1992; Steetzel, 1993; Kobayashi and Johnson, 2001; Reniers *et al.*, 2004) but require more thorough validation against suspension measurements for a wide range of large-scale breaking wave conditions (including the present dataset). The further development of such formulations would benefit from a better understanding of the physical mechanism of sediment pick-up by breaking-generated vortices. Measurements of pore pressure in the bed

under a large-scale breaking wave may contribute to explain the pick-up behavior (c.f. Sumer *et al.*, 2013).

Pick-up formulations based on near-bed turbulence can only be implemented if near-bed TKE is properly predicted. Given the poor performance of present turbulence closure models in predicting near-bed TKE (Brown *et al.*, 2016), simplified approaches (e.g. Roelvink and Stive, 1989) or empirical predictions for near-bed TKE could be considered. However, such formulations would also require a thorough validation against measurements for a wide range of breaking-wave and sediment bed conditions. The performance of turbulence closure models may benefit from surf zone studies that present not only the spatiotemporal variation in TKE but also quantify various terms of the TKE budget (c.f. Van der A *et al.*, Submitted).

The modelling of wave-related suspended transport inside and/or above the WBL requires additional experimental research. In the present study, the wave-related transport is generally confined to the WBL (as is the case for non-breaking waves) although it can locally extend to outer-flow elevations. This apparent inconsistency with previous surf zone observations at outer-flow elevations may be due to the short wave period compared to typical turbulence decay times for this particular wave condition (Section 6.2.3) . Additional high-resolution measurements of near-bed sediment fluxes for a wider range of wave conditions – particularly longer-period or irregular waves with an expectedly stronger intra-wave variation in near-bed TKE – may benefit the further development of wave-related suspended transport formulations.

The data in this thesis allow validation and improvement of formulations for size-selective suspended sediment pick-up and vertical mixing (e.g. Van Rijn, 2007c).

Bedload transport in the surf zone

Bedload transport formulations in the surf zone may need to account for effects of intermittent high bed shear stresses that are expected based on the invasion of TKE into the WBL. Such effects could in combination with local sloping bed lead to an additional net transport contribution. The present measurements could be used to validate existing bedload transport models used in combination with parameterizations for bed slope effects and TKE.

The insights in wave breaking effects on bedload transport remain still somewhat restricted after this study. Sheet flow layer observations at the breaker bar crest did not reveal a significant effect of breaking-generated turbulence. However, such effects may still occur along the shoreward-facing bar slope where the invasion of breaking-generated turbulence into the WBL is much stronger. Additional sheet flow measurements at this particular location would improve process insights, but such measurements are challenging due to the evolving and steep bed. Therefore, one may instead consider experiments in an oscillatory flow tunnel using grid turbulence to study the effects of external TKE on oscillatory bedload transport processes and transport rates. Such an experiment could be more easily done for a wide range of wave and sediment bed conditions and would also isolate TKE effects from bed slope effects. Grid turbulence has been used before to study effects of external turbulence on WBL dynamics for a rigid-bed (Fredsoe *et al.*, 2003) and on bedload transport in steady flows (Sumer *et al.*, 2003). Effects of time-varying turbulence could be examined by running asymmetric flows that would result in different grid-induced TKE for each half cycle.

Simulations of sheet flow layer dynamics with detailed process-based models (e.g. Kranenburg *et al.*, 2014; Finn *et al.*, 2016) can offer another approach in understanding the effects of external (breaking-generated) turbulence on bedload transport rates. Such local process-based models, or process-based morphodynamic models that operate at an intra-wave time scale, may also be used to assess the effects of cross-shore sediment influx on local bedload transport rates, i.e. to assess whether bedload transport in such a non-uniform breaking-wave setting is still locally controlled.

Bedload transport models also rely on an appropriate hydrodynamic input of local near-bed velocities, including the velocity and acceleration skewness. Although existing skewness parameterizations may capture the overall trend of wave deformation from shoaling to inner surf zone (e.g. Ruessink *et al.*, 2012), they do not include the local wave deformation around the breaker bar where the wave breaks. Given the significance of this deformation in affecting breaker bar morphodynamics (through cross-shore-varying bedload transport rates), the numerical reproduction of bar morphodynamics would benefit from further improvement of velocity skewness and asymmetry parameterizations for the breaking region. Existing parameterizations may be improved on the basis of numerical data created with process-based numerical models, as existing process-based RANS models seem to properly predict velocity skewness and asymmetry patterns (e.g. Torres-Freyermuth *et al.*, 2010; Jacobsen *et al.*, 2014).

Sediment transport in the swash zone

For the swash zone, it is recommended to further develop modeling schemes for bed evolution in the swash zone, based on existing formulations (e.g. Walstra and Steetzel, 2003; Van Rijn, 2009). Results in the present study particularly illustrate the significance of wave-swash interactions and of intra-swash cross-shore sediment advection. The degree of wave-swash interactions can be parameterized based on the relative swash event duration (Alsina *et al.*, 2009), which in turn can be estimated based on bed slope and wave breaking parameters (Pujara *et al.*, 2015b). The cross-shore variation in transport rates may be parameterized based on the combination of breaker type and cross-shore velocities at the shoreline, which was found to control the bed shear along the swash zone (Pujara et al., 2015a).

Such numerical morphodynamic schemes require proper datasets that ideally include (i) high-resolution (spatially and temporally) measurements of swash zone bed evolution at event-by-event time scale, which can be used to quantify transport rates along the swash and the total sediment load entering/leaving the swash zone (by solving the Exner equation); (ii) measurements of offshore hydrodynamic forcing parameters. Although such datasets are currently scarce – if not non-existent – such measurements could be acquired through novel techniques for measuring the complete swash zone morphology (e.g. stereoscopic imaging).

Swash zone sediment transport processes have predominantly been examined in the field where typically only a few cross-shore locations were covered. Most laboratory studies focused on hydrodynamic processes of (bore-driven) swash on rigid beds. Experiments that systematically cover the complete swash zone with high spatial and temporal resolution are presently lacking, but may greatly improve insights on effects of intra-swash sediment advection on spatiotemporally varying bed levels.

References

Aagaard, T. and M. G. Hughes (2006). *Sediment suspension and turbulence in the swash zone of dissipative beaches.* Marine Geology **228**(1-4): 117-135. *doi: 10.1016/j.margeo.2006.01.003*.

Aagaard, T. and M. G. Hughes (2010). *Breaker turbulence and sediment suspension in the surf zone.* Marine Geology **271**(3-4): 250-259. *doi: 10.1016/j.margeo.2010.02.019*.

Aagaard, T. and S. G. Jensen (2013). *Sediment concentration and vertical mixing under breaking waves.* Marine Geology **336**: 146-159. *doi: 10.1016/j.margeo.2012.11.015*.

Alsina, J. M., S. Falchetti and T. E. Baldock (2009). *Measurements and modelling of the advection of suspended sediment in the swash zone by solitary waves.* Coastal Engineering **56**(5-6): 621-631. *doi: 10.1016/j.coastaleng.2009.01.007*.

Alsina, J. M., I. Caceres, M. Brocchini and T. E. Baldock (2012). *An experimental study on sediment transport and bed evolution under different swash zone morphological conditions.* Coastal Engineering **68**: 31-43. *doi: 10.1016/j.coastaleng.2012.04.008*.

Alsina, J., I. Caceres, J. van der Zanden, J. S. Ribberink and T. E. Baldock (2014). *Large scale experiments on beach evolution induced by bichromatic wave groups with varying group period*. Proceedings of the 34th International Conference on Coastal Engineering, Seoul, Korea**:** 10 pp

Astruc, D., S. Cazin, E. Cid, O. Eiff, L. Lacaze, P. Robin, F. Toublanc and I. Cáceres (2012). *A stereoscopic method for rapid monitoring of the spatio-temporal evolution of the sand-bed elevation in the swash zone.* Coastal Engineering **60**: 11-20. *doi: 10.1016/j.coastaleng.2011.08.007*.

Bagnold, R. A. (1956). *The Flow of Cohesionless Grains in Fluids.* Philosophical Transactions of the Royal Society A: Mathematical, Physical and Engineering Sciences **249**(964): 235-297. *doi: 10.1098/rsta.1956.0020*.

Bailard, J. A. and D. L. Inman (1981). *An energetics bedload model for a plane sloping beach: local transport.* Journal of Geophysical Research **86**(C3): 2035-2043. *doi*.

Baldock, T. E., D. A. Huntley, P. A. D. Bird, T. O'Hare and G. N. Bullock (2000). *Breakpoint generated surf beat induced by bichromatic wave groups.* Coastal Engineering **39**(2-4): 213-242. *doi: 10.1016/S0378-3839(99)00061-7*.

Baldock, T. E., M. R. Tomkins, P. Nielsen and M. G. Hughes (2004). *Settling velocity of sediments at high concentrations.* Coastal Engineering **51**(1): 91-100. *doi: 10.1016/j.coastaleng.2003.12.004*.

Baldock, T. E., M. G. Hughes, K. Day and J. Louys (2005). *Swash overtopping and sediment overwash on a truncated beach*. Coastal Engineering **52**(7): 633-645. *doi: 10.1016/j.coastaleng.2005.04.002*.

Baldock, T. E., J. M. Alsina, I. Caceres, D. Vicinanza, P. Contestabile, H. Power and A. Sanchez-Arcilla (2011). *Large-scale experiments on beach profile evolution and surf and swash zone sediment transport induced by long waves, wave groups and random waves.* Coastal Engineering **58**(2): 214-227. *doi: 10.1016/j.coastaleng.2010.10.006*.

Barthel, V., E. P. D. Mansard, S. E. Sand and F. C. Vis (1983). *Group bounded long waves in physical models.* Ocean Engineering **10**(4): 261-294. *doi*.

Battjes, J. A. (1974). Surf Similarity. Proceedings of the 14th International Conference on Coastal Engineering. Copenhagen, Denmark, American Society of Civil Engineers**:** 466-480

Beach, R. A. and R. W. Sternberg (1991). *Infragravity-driven suspended sediment transport in the swash, inner and outer-surf zone*. Proc. Coastal Sediments, ASCE: 114-128

Beach, R. A., R. W. Sternberg and R. Johnson (1992). *A fiber optic sensor for monitoring suspended sediment.* Marine Geology **103**(1-3): 513-520. *doi: 10.1016/0025-3227(92)90036-h*.

Beach, R. A. and R. W. Sternberg (1996). *Suspended-sediment transport in the surf zone: Response to breaking waves.* Continental Shelf Research **16**(15): 1989-2003. *doi*.

Beckman Coulter Inc (2008). Manual LS 13 320 Particle Size Analyzer**:** 235

Beji, S. and J. A. Battjes (1993). *Experimental Investigation of Wave-Propagation over a Bar.* Coastal Engineering **19**(1-2): 151-162. *doi: 10.1016/0378-3839(93)90022-Z*.

Blenkinsopp, C. E., I. L. Turner, G. Masselink and P. E. Russell (2011). *Swash zone sediment fluxes: Field observations.* Coastal Engineering **58**(1): 28-44. *doi: 10.1016/j.coastaleng.2010.08.002*.

Blott, S. J. and K. Pye (2001). *GRADISTAT: a grain size distribution and statistics package for the analysis of unconsolidated sediments.* Earth Surface Processes and Landforms **26**(11): 1237-1248. *doi: 10.1002/esp.261*.

Berni, C., E. Barthélemy and H. Michallet (2013). *Surf zone cross-shore boundary layer velocity asymmetry and skewness: An experimental study on a mobile bed*. Journal of Geophysical Research: Oceans **118**(4): 2188-2200. doi: 10.1002/jgrc.20125

Boers, M. (2005). Surf zone turbulence. PhD Thesis, TU Delft, The Netherlands.

Bosman, J. J., E. T. J. M. van der Velden and C. H. Hulsbergen (1987). *Sediment concentration measurement by transverse suction.* Coastal Engineering **11**(4): 353-370. *doi: 10.1016/0378-3839(87)90033-0*.

Brinkkemper, J. A., T. Lanckriet, F. Grasso, J. A. Puleo and B. G. Ruessink (2015). *Observations of turbulence within the surf and swash zone of a field-scale sandy laboratory beach*. Coastal Engineering 113: 62-72, doi: 10.1016/j.coastaleng.2015.07.006.

Brown, S. A., D. M. Greaves, V. Magar and D. C. Conley (2016). *Evaluation of turbulence closure models under spilling and plunging breakers in the surf zone.* Coastal Engineering **114**: 177-193. *doi: 10.1016/j.coastaleng.2016.04.002*.

Butt, T., P. Russell, J. Puleo, J. Miles and G. Masselink (2004). *The influence of bore turbulence on sediment transport in the swash and inner surf zones.* Continental Shelf Research **24**(7-8): 757-771. *doi: 10.1016/j.csr.2004.02.002*.

Caceres, I. and J. M. Alsina (2012). *A detailed, event-by-event analysis of suspended sediment concentration in the swash zone.* Continental Shelf Research **41**: 61-76. *doi: 10.1016/j.csr.2012.04.004*.

Campbell, L. J., T. O'Donoghue and J. S. Ribberink (2007). *Wave Boundary Layer Velocities in Oscillatory Sheet Flow*. Proceedings ICCE 2006: 2207-2219. doi: 10.1142/9789812709554_0186.

Chardón-Maldonado, P., J. C. Pintado-Patiño and J. A. Puleo (2015). *Advances in swash-zone research: Small-scale hydrodynamic and sediment transport processes.* Coastal Engineering. *doi: 10.1016/j.coastaleng.2015.10.008*.

Chassagneux, F. X. and D. Hurther (2014). *Wave bottom boundary layer processes below irregular surfzone breaking waves with light-weight sheet flow particle transport.* Journal of Geophysical Research-Oceans **119**(3): 1668-1690. *doi: 10.1002/2013jc009338*.

Chen, B.-T., G. A. Kikkert, D. Pokrajac and H.-J. Dai (2016). *Experimental study of bore-driven swash–swash interactions on an impermeable rough slope.* Coastal Engineering **108**: 10-24. *doi: 10.1016/j.coastaleng.2015.10.010*.

Christensen, E. D. and R. Deigaard (2001). *Large eddy simulation of breaking waves.* Coastal Engineering **42**(1): 53-86. *doi: 10.1016/S0378-3839(00)00049-1*.

Christensen, E. D. (2006). *Large eddy simulation of spilling and plunging breakers.* Coastal Engineering **53**(5-6): 463-485. *doi: 10.1016/j.coastaleng.2005.11.001*.

Conley, D. C. and D. L. Inman (1992). *Field Observations of the Fluid-Granular Boundary-Layer under near-Breaking Waves.* Journal of Geophysical Research-Oceans **97**(C6): 9631-9643. *doi*.

Cowen, E. A., I. M. Sou, P. L. F. Liu and B. Raubenheimer (2003). *Particle image velocimetry measurements within a laboratory-generated swash zone.* Journal of Engineering Mechanics-Asce **129**(10): 1119-1129. doi: 10.1061/(Asce)0733-9399(2003)129:10(1119)

Cox, D. T., N. Kobayashi and A. Okayasu (1996). *Bottom shear stress in the surf zone.* Journal of Geophysical Research-Oceans **101**(C6): 14337-14348. *doi: 10.1029/96JC00942*.

Cox, D. T. and N. Kobayashi (2000). *Identification of intense, intermittent coherent motions under shoaling and breaking waves.* Journal of Geophysical Research-Oceans **105**(C6): 14223-14236. *doi: 10.1029/2000JC900048*.

da Silva, P. A., A. Temperville and F. Seabra Santos (2006). *Sand transport under combined current and wave conditions: A semi-unsteady, practical model.* Coastal Engineering **53**(11): 897-913. *doi: 10.1016/j.coastaleng.2006.06.010*.

Davies, A. G., R. L. Soulsby and H. L. King (1988). *A Numerical-Model of the Combined Wave and Current Bottom Boundary-Layer.* Journal of Geophysical Research-Oceans **93**(C1): 491-508. *doi: 10.1029/Jc093ic01p00491*.

Davies, A. G., J. S. Ribberink, A. Temperville and J. A. Zyserman (1997). *Comparisons between sediment transport models and observations made in wave and current flows above plane beds.* Coastal Engineering **31**(1-4): 163-198. *doi*.

Davies, A. G., L. C. Van Rijn, J. S. Damgaard, J. van de Graaff and J. S. Ribberink (2002). *Intercomparison of research and practical sand transport models.* Coastal Engineering **46**(1): 1-23. *doi: 10.1016/s0378-3839(02)00042-x*.

Davies, A. G. and P. D. Thorne (2016). *On the suspension of graded sediment by waves above ripples: Inferences of convective and diffusive processes.* Continental Shelf Research **112**: 46-67. *doi: 10.1016/j.csr.2015.10.006*.

de Meijer, R. J., J. Bosboom, B. Cloin, I. Katopodi, N. Kitou, R. L. Koomans and F. Manso (2002). *Gradation effects in sediment transport.* Coastal Engineering **47**(2): 179-210. *doi: 10.1016/s0378-3839(02)00125-4*.

De Serio, F. and M. Mossa (2006). *Experimental study on the hydrodynamics of regular breaking waves.* Coastal Engineering **53**(1): 99-113. *doi: 10.1016/j.coastaleng.2005.09.021*.

Deigaard, R., J. Fredsøe and M. B. Mikkelsen (1991). *Measurements of the bed shear stress in a surf zone.* Progress Report Institute of Hydodynamics and Hydraulic Engineering. **73:** 21-30

Deigaard, R., J. B. Jakobsen and J. Fredsøe (1999). *Net sediment transport under wave groups and bound long waves.* Journal of Geophysical Research **104**(C6): 13559. *doi: 10.1029/1999jc900072*.

Deltares (2015a). Delft3D-FLOW User Manual. Version: 3.15.34158, Deltares, Delft**:** 710

Deltares (2015b). XBeach manual, Deltares, the Netherlands**:** 145

Dibajnia, M. and A. Watanabe (1992). Sheet Flow under Nonlinear waves and currents. Proceedings of the 23rd International Conference on Coastal Engineering, Venice, Italy. B. L. Edge**:** 2015-2028

Dohmen-Janssen, C. M., W. N. Hassan and J. S. Ribberink (2001). *Mobile-bed effects in oscillatory sheet flow.* Journal of Geophysical Research-Oceans **106**(C11): 27103-27115. *doi: 10.1029/2000jc000513*

Dohmen-Janssen, C. M. and D. M. Hanes (2002). *Sheet flow dynamics under monochromatic nonbreaking waves.* Journal of Geophysical Research **107**(C10). *doi: 10.1029/2001jc001045*.

Dohmen-Janssen, C. M., D. F. Kroekenstoel, W. N. Hassan and J. S. Ribberink (2002). *Phase lags in oscillatory sheet flow: experiments and bed load modelling.* Coastal Engineering **46**(1): 61-87. *doi: 10.1016/s0378-3839(02)00056-x*.

Dohmen-Janssen, C. M. and D. M. Hanes (2005). *Sheet flow and suspended sediment due to wave groups in a large wave flume.* Continental Shelf Research **25**(3): 333-347. *doi: 10.1016/j.csr.2004.10.009*.

Downing, J. P. and R. A. Beach (1989). Laboratory apparatus for calibrating optical suspended solids sensors. Marine Geology 86(2-3): 243-249. doi: 10.1016/0025-3227(89)90053-4

Dubarbier, B., B. Castelle, V. Marieu and G. Ruessink (2015). *Process-based modeling of cross-shore sandbar behavior.* Coastal Engineering **95**: 35-50. *doi: 10.1016/j.coastaleng.2014.09.004*.

Dyhr-Nielsen, M. and T. Sorensen (1970). Some sand transport phenomena on coasts with bars. Proceedings of the 12th International Conference on Coastal Engineering. Washington, D.C. **54:** 855-865

Elgar, S. and R. T. Guza (1985). *Observations of bispectra of shoaling surface gravity waves.* Journal of Fluid Mechanics **161**(-1): 425. *doi: 10.1017/s0022112085003007*.

Elgar, S., E. L. Gallagher and R. T. Guza (2001). *Nearshore sandbar migration.* Journal of Geophysical Research **106**(C6): 11623. *doi: 10.1029/2000jc000389*.

Eshel, G., G. J. Levy, U. Mingelgrin and M. J. Singer (2004). *Critical Evaluation of the Use of Laser Diffraction for Particle-Size Distribution Analysis.* Soil Science Society of America Journal **68**(3): 736. *doi: 10.2136/sssaj2004.7360*.

Feddersen, F. and J.H. Trowbridge (2005). *The effect of wave breaking on surf-zone turbulence and alongshore currents: A modeling study*. Journal of Physical Oceanography **35**(11): 2187-2203

Feddersen, F. and A. J. Williams (2007). *Direct Estimation of the Reynolds Stress Vertical Structure in the Nearshore.* Journal of Atmospheric and Oceanic Technology **24**(1): 102-116. *doi: 10.1175/jtech1953.1*.Feddersen, F. (2012). *Observations of the Surf-Zone Turbulent Dissipation Rate.* Journal of Physical Oceanography **42**(3): 386-399. *doi: 10.1175/Jpo-D-11-082.1*.

Feddersen, F., J. H. Trowbridge and A. J. Williams (2007). *Vertical Structure of Dissipation in the Nearshore.* Journal of Physical Oceanography **37**(7): 1764-1777. *doi: 10.1175/jpo3098.1*.

Fernández-Mora, A., D. Calvete, A. Falqués and H. E. de Swart (2015). *Onshore sandbar migration in the surf zone: New insights into the wave-induced sediment transport mechanisms.* Geophysical Research Letters **42**(8): 2869-2877. *doi: 10.1002/2014gl063004*.

Finn, J. R., M. Li and S. V. Apte (2016). *Particle based modelling and simulation of natural sand dynamics in the wave bottom boundary layer.* Journal of Fluid Mechanics **796**: 340-385. *doi: 10.1017/jfm.2016.246*.

Flick, R. E., R. T. Guza and D. L. Inman (1981). *Elevation and Velocity-Measurements of Laboratory Shoaling Waves.* Journal of Geophysical Research-Oceans and Atmospheres **86**(Nc5): 4149-4160. *doi: 10.1029/Jc086ic05p04149*.

Foster, D. L., R. A. Beach and R. A. Holman (2000). *Field observations of the wave bottom boundary layer.* Journal of Geophysical Research-Oceans **105**(C8): 19631-19647. *doi: 10.1029/1999jc900018*.

Foster, D. L., R. A. Beach and R. A. Holman (2006a). *Turbulence observations of the nearshore wave bottom boundary layer.* Journal of Geophysical Research-Oceans **111**(C4). *doi: 10.1029/2004jc002838*.

Foster, D. L., A. J. Bowen, R. A. Holman and P. Natoo (2006b). *Field evidence of pressure gradient induced incipient motion.* Journal of Geophysical Research **111**(C5). *doi: 10.1029/2004jc002863*.

Fredsøe, J. (1984). *Turbulent Boundary Layer in Wave-current Motion*. Journal of Hydraulic Engineering **110**(8): 1103-1120. doi: 10.1061/(asce)0733-9429(1984)110:8(1103).F

Fredsøe, J. and R. Deigaard (1992). Mechanics of Coastal Sediment Transport, World Scientific.

Fredsoe, J., B. M. Sumer, A. Kozakiewicz, L. H. C. Chua and R. Deigaard (2003). *Effect of externally generated turbulence on wave boundary layer.* Coastal Engineering **49**(3): 155-183. *doi: 10.1016/S0378-3839(03)00032-2*.

Fuhrman, D. R., J. Fredsøe and B. M. Sumer (2009a). *Bed slope effects on turbulent wave boundary layers: 1. Model validation and quantification of rough-turbulent results*. Journal of Geophysical Research **114**(C3). doi: 10.1029/2008jc005045.

Fuhrman, D. R., J. Fredsøe and B. M. Sumer (2009b). *Bed slope effects on turbulent wave boundary layers: 2. Comparison with skewness, asymmetry, and other effects*. Journal of Geophysical Research **114**(C3). doi: 10.1029/2008jc005053.

Gallagher, E. L., S. Elgar and R. T. Guza (1998). *Observations of sand bar evolution on a natural beach.* Journal of Geophysical Research-Oceans **103**(C2): 3203-3215. *doi: 10.1029/97jc02765*.

Garbini, J. L., F. K. Forster and J. E. Jorgensen (1982). *Measurement of Fluid Turbulence Based on Pulsed Ultrasound Techniques .1. Analysis.* Journal of Fluid Mechanics **118**(May): 445-470. Doi 10.1017/S0022112082001153.

Garcez-Faria, A. F., E. B. Thornton, T. C. Lippmann and T. P. Stanton (2000). *Undertow over a barred beach.* Journal of Geophysical Research **105**(C7): 16999. *doi: 10.1029/2000jc900084*.

Giardino, A., J. Mulder, J. de Ronde and J. Stronkhorst (2011). *Sustainable Development of the Dutch Coast: Present and Future.* Journal of Coastal Research **SI**(61): 166-172. *doi*.

Govender, K., G. P. Mocke and M. J. Alport (2002). *Video-imaged surf zone wave and roller structures and flow fields.* Journal of Geophysical Research **107**(C7). *doi: 10.1029/2000jc000755*.

Grasmeijer, B. T. and L. C. Van Rijn (1997). Sand transport over a breaker bar in the surf zone. Coastal Dynamics. Plymouth, UK**:** 88-98

Grasmeijer, B. T. (2002). Process-based cross-shore modelling of barred beaches. PhD Thesis, Universiteit Utrecht.

Grasso, F., B. Castelle and B. G. Ruessink (2012). *Turbulence dissipation under breaking waves and bores in a natural surf zone.* Continental Shelf Research **43**: 133-141. *doi: 10.1016/j.csr.2012.05.014*.

Guza, R. T. and E. B. Thornton (1980). *Local and shoaled comparisons of sea surface elevations, pressures, and velocities.* Journal of Geophysical Research **85**(C3): 1524. *doi: 10.1029/JC085iC03p01524*.

Hanes, D. M. and D. A. Huntley (1986). *Continuous Measurements of Suspended Sand Concentration in a Wave Dominated Nearshore Environment.* Continental Shelf Research **6**(4): 585-596. *doi*.

Hassan, W. N. M. (2003). Transport of size-graded and uniform sediment under oscillatory sheet-flow conditions. PhD Thesis, University of Twente.

Hassan, W. N. and J. S. Ribberink (2005). *Transport processes of uniform and mixed sands in oscillatory sheet flow.* Coastal Engineering **52**(9): 745-770. *doi: 10.1016/j.coastaleng.2005.06.002*.

Henderson, S. M., J. S. Allen and P. A. Newberger (2004). *Nearshore sandbar migration predicted by an eddy-diffusive boundary layer model.* Journal of Geophysical Research **109**(C6). *doi: 10.1029/2003jc002137*.

Hibberd, S. and D. H. Peregrine (1979). *Surf and Run-up on a Beach - Uniform Bore*. Journal of Fluid Mechanics **95**(Nov): 323-345. doi: 10.1017/S002211207900149x.

Hoefel, F. and S. Elgar (2003). *Wave-induced sediment transport and sandbar migration.* Science **299**(5614): 1885-1887. *doi: 10.1126/science.1081448*.

Horikawa, K., A. Watanabe and S. Katori (1982). Sediment Transport Under Sheet Flow Condition. Proceedings of the 18th International Conference on Coastal Engineering, Cape Town, South Africa**:** 1335-1352

Houwman, K. T. and G. Ruessink (1996). *CROSS-SHORE SEDIMENT TRANSPORT MECHANISMS IN THE SURFZONE ON A TIMESCALE OF MONTHS TO YEARS.* Coastal Engineering Proceedings(25). *doi: 10.9753/icce.v25.*

Hsu, T. J., J. T. Jenkins and P. L. F. Liu (2004). *On two-phase sediment transport: sheet flow of massive particles.* Proceedings of the Royal Society A: Mathematical, Physical and Engineering Sciences **460**(2048): 2223-2250. *doi: 10.1098/rspa.2003.1273*.

Hsu, T.-J., S. Elgar and R. T. Guza (2006). *Wave-induced sediment transport and onshore sandbar migration.* Coastal Engineering **53**(10): 817-824. *doi: 10.1016/j.coastaleng.2006.04.003*.

Huang, Z. C., H. H. Hwung, S. C. Hsiao and K. A. Chang (2010). *Laboratory observation of boundary layer flow under spilling breakers in surf zone using particle image velocimetry*. Coastal Engineering **57**(3): 343-357. doi: 10.1016/j.coastaleng.2009.11.004.

Hughes, S. A. (1993). Physical models and laboratory techniques in coastal engineering. Singapore, Wrod Scientific Publishing Co. Pte. Ltd.

Hughes, M. G., T. Aagaard and T. E. Baldock (2007). *Suspended Sediment in the Swash Zone: Heuristic Analysis of Spatial and Temporal Variations in Concentration.* Journal of Coastal Research **236**: 1345-1354. *doi: 10.2112/05-0531.1*.

Hughes, M. G. and A. S. Moseley (2007). *Hydrokinematic regions within the swash zone.* Continental Shelf Research **27**(15): 2000-2013. *doi: 10.1016/j.csr.2007.04.005*.

Hurther, D. and U. Lemmin (2001). *A correction method for turbulence measurements with a 3D acoustic Doppler velocity profiler*. Journal of Atmospheric and Oceanic Technology **18**(3): 446-458. doi: 10.1175/1520-0426(2001)018<0446:Acmftm>2.0.Co;2.

Hurther, D. and U. Lemmin (2008). *Improved Turbulence Profiling with Field-Adapted Acoustic Doppler Velocimeters Using a Bifrequency Doppler Noise Suppression Method.* Journal of Atmospheric and Oceanic Technology **25**(3): 452-463. doi: 10.1175/2007jtecho512.1.

Hurther, D. and P. D. Thorne (2011). *Suspension and near-bed load sediment transport processes above a migrating, sand-rippled bed under shoaling waves.* Journal of Geophysical Research **116**(C7). *doi: 10.1029/2010jc006774*.

Hurther, D., P. D. Thorne, M. Bricault, U. Lemmin and J. M. Barnoud (2011). *A multi-frequency Acoustic Concentration and Velocity Profiler (ACVP) for boundary layer measurements of fine-scale flow and sediment transport processes.* Coastal Engineering **58**(7): 594-605. *doi: 10.1016/j.coastaleng.2011.01.006*.

Isobe, M. and K. Horikawa (1982). *Study on water particle velocities of shoaling and breaking waves.* Coastal Engineering Journal **25**: 109-123. *doi*.

Jackson, N. L., G. Masselink and K. F. Nordstrom (2004). *The role of bore collapse and local shear stresses on the spatial distribution of sediment load in the uprush of an intermediate-state beach.* Marine Geology **203**(1-2): 109-118. *doi: 10.1016/S0025-3227(03)00328-1*.

Jacobsen, N. G. and J. Fredsoe (2014). *Formation and development of a breaker bar under regular waves. Part 2: Sediment transport and morphology.* Coastal Engineering **88**: 55-68. *doi: 10.1016/j.coastaleng.2014.01.015*.

Jacobsen, N. G., J. Fredsoe and J. H. Jensen (2014). *Formation and development of a breaker bar under regular waves. Part 1: Model description and hydrodynamics.* Coastal Engineering **88**: 182-193. *doi: 10.1016/j.coastaleng.2013.12.008*.

Janssen, T. T., J. A. Battjes, and A. R. van Dongeren (2003). *Long waves induced by short-wave groups over a sloping bottom*. Journal of Geophysical Research, **108**(C8): 3252, 1-14. *doi:10.1029/2002JC001515*,

Jensen, B. L., B. M. Sumer and J. Fredsoe (1989). *Turbulent Oscillatory Boundary-Layers at High Reynolds-Numbers.* Journal of Fluid Mechanics **206**: 265-297. *doi: 10.1017/S0022112089002302*.

Jonsson, I. G. and N. A. Carlsen (1976). *Experimental and Theoretical Investigations in an Oscillatory Turbulent Boundary Layer.* Journal of Hydraulic Research **14**(1): 45-60. *doi: 10.1080/00221687609499687*.

Kemp, P. H. and R. R. Simons (1983). *The interaction of waves and a turbulent current: waves propagating against the current.* Journal of Fluid Mechanics **130**: 73-89. doi: 10.1017/s0022112083000981.

Kimmoun, O. and H. Branger (2007). *A particle image velocimetry investigation on laboratory surf-zone breaking waves over a sloping beach.* Journal of Fluid Mechanics **588**: 353-397 doi: 10.1017/s0022112007007641.

Kleinhans, M. G. (2004). *Sorting in grain flows at the lee side of dunes.* Earth-Science Reviews **65**(1-2): 75-102. *doi: 10.1016/s0012-8252(03)00081-3*.

Kobayashi, N. and B. D. Johnson (2001). *Sand suspension, storage, advection, and settling in surf and swash zones.* Journal of Geophysical Research **106**(C5): 9363. *doi: 10.1029/2000jc000557*.

Kobayashi, N., H. Zhao and Y. Tega (2005). *Suspended sand transport in surf zones.* Journal of Geophysical Research **110**(C12). *doi: 10.1029/2004jc002853*.

Koomans, R. L. (2000). Sand in motion: effects of density and grain size, Rijksuniversiteit Groningen, the Netherlands.

Kranenburg, W. M., J. S. Ribberink, R. E. Uittenbogaard and S. J. M. H. Hulscher (2012). *Net currents in the wave bottom boundary layer: On waveshape streaming and progressive wave streaming.* Journal of Geophysical Research F: Earth Surface **117**(3). *doi: 10.1029/2011jf002070*.

Kranenburg, W. M. (2013). Modeling sheet-flow sand transport under progressive surface waves, University of Twente.

Kranenburg, W. M., J. S. Ribberink, J. J. L. M. Schretlen and R. E. Uittenbogaard (2013). *Sand transport beneath waves: The role of progressive wave streaming and other free surface effects.* Journal of Geophysical Research: Earth Surface **118**(1): 122-139. *doi: 10.1029/2012jf002427*.

Kranenburg, W. M., T.-J. Hsu and J. S. Ribberink (2014). *Two-phase modeling of sheet-flow beneath waves and its dependence on grain size and streaming.* Advances in Water Resources **72**: 57-70. *doi: 10.1016/j.advwatres.2014.05.008*.

Lanckriet, T., J. A. Puleo and N. Waite (2013). *A Conductivity Concentration Profiler for Sheet Flow Sediment Transport.* Ieee Journal of Oceanic Engineering **38**(1): 55-70. *doi: 10.1109/joe.2012.2222791*.

Lanckriet, T. (2014). Near-bed hydrodynamics and sediment transport in the swash zone, University of Delaware.

Lanckriet, T., J. A. Puleo, G. Masselink, I. L. Turner, D. Conley, C. Blenkinsopp and P. Russell (2014). *Comprehensive Field Study of Swash-Zone Processes. II: Sheet Flow Sediment Concentrations during Quasi-Steady Backwash.* Journal of Waterway, Port, Coastal, and Ocean Engineering **140**(1): 29-42. *doi: 10.1061/(asce)ww.1943-5460.0000209*.

Lanckriet, T. and J. A. Puleo (2015). *A semianalytical model for sheet flow layer thickness with application to the swash zone.* Journal of Geophysical Research-Oceans **120**(2): 1333-1352. *doi: 10.1002/2014jc010378*.

Lin, P. and P. L. F. Liu (1998). *A numerical study of breaking waves in the surf zone.* Journal of Fluid Mechanics **359**: 239-264. *doi: 10.1017/s002211209700846x*.

Lippmann, T. C. and R. A. Holman (1990). *The spatial and temporal variability of sand bar morphology.* Journal of Geophysical Research **95**(C7): 11575. *doi: 10.1029/JC095iC07p11575*.

Longuet-Higgins, M. S. and R. W. Stewart (1964). *Radiation Stresses in Water Waves - a Physical Discussion, with Applications.* Deep-Sea Research **11**(4): 529-562. *doi: 10.1016/0011-7471(64)90001-4*.

Masselink, G. and M. Hughes (1998). *Field investigation of sediment transport in the swash zone.* Continental Shelf Research **18**(10): 1179-1199. *doi: 10.1016/S0278-4343(98)00027-2*.

Masselink, G. and J. A. Puleo (2006). *Swash-zone morphodynamics.* Continental Shelf Research **26**(5): 661-680. *doi: 10.1016/j.csr.2006.01.015*.

Masselink, G., P. Russell, I. Turner and C. Blenkinsopp (2009). *Net sediment transport and morphological change in the swash zone of a high-energy sandy beach from swash event to tidal cycle time scales.* Marine Geology **267**(1-2): 18-35. *doi: 10.1016/j.margeo.2009.09.003*.

McLean, S. R., J. S. Ribberink, C. M. Dohmen-Janssen and W. N. Hassan (2001). *Sand Transport in Oscillatory Sheet Flow with Mean Current.* Journal of Waterway, Port, Coastal, and Ocean Engineering **127**(3): 141-151. *doi: 10.1061/(asce)0733-950x(2001)127:3(141)*.

Melville, W. K., F. Veron and C. J. White (2002). The velocity field under breaking waves: coherent structures and turbulence. Journal of Fluid Mechanics **454**: 203-233. doi: 10.1017/s0022112001007078.

Meyer-Peter, A. and R. Muller (1948). Formulas for bed-load transport. Proceedings of the 2nd Meeting of the International Association for Hydraulic Structures Research. Delft, The Netherlands**:** 39-64

Mocke, G. P. and G. G. Smith (1992). Wave breaker turbulence as a mechanism for sediment suspension. Proc. 23rd International Conference on Coastal Engineering. Venice, Italy**:** 2279-2292

Murray, S. P. (1967). *Control of Grain Dispersion by Particle Size and Wave State.* The Journal of Geology **27**(5): 612-634. *doi*.

Nadaoka, K., S. Ueno and T. Igarashi (1988). *Sediment suspension due to large scale eddies in the surf zone.* Proceedings of the 21st International Conference on Coastal Engineering, Torremolimos, Spain: 1646-1660. *doi*.

Naqshband, S., J. S. Ribberink, D. Hurther and S. J. M. H. Hulscher (2014). *Bed load and suspended load contributions to migrating sand dunes in equilibrium.* Journal of Geophysical Research-Earth Surface **119**(5): 1043-1063. *doi: 10.1002/2013jf003043*.

Nielsen, P. (1984). *Field-Measurements of Time-Averaged Suspended Sediment Concentrations under Waves.* Coastal Engineering **8**(1): 51-72. *doi: 10.1016/0378-3839(84)90022-X*.

Nielsen, P. (1986). *Suspended Sediment Concentrations under Waves.* Coastal Engineering **10**(1): 23-31. *doi: 10.1016/0378-3839(86)90037-2*.

Nielsen, P. (1992). Coastal Bottom Boundary Layers and Sediment Transport. Singapore, World Scientific.

Nielsen, P. (2006). *Sheet flow sediment transport under waves with acceleration skewness and boundary layer streaming.* Coastal Engineering **53**(9): 749-758. *doi: 10.1016/j.coastaleng.2006.03.006*.

O'Donoghue, T. and S. Wright (2004a). *Concentrations in oscillatory sheet flow for well sorted and graded sands.* Coastal Engineering **50**(3): 117-138. *doi: 10.1016/j.coastaleng.2003.09.004*.

O'Donoghue, T. and S. Wright (2004b). *Flow tunnel measurements of velocities and sand flux in oscillatory sheet flow for well-sorted and graded sands.* Coastal Engineering **51**(11-12): 1163-1184. *doi: 10.1016/j.coastaleng.2004.08.001*.

O'Donoghue, T., Doucette, J.S., Werf, J.J. Van der, Ribberink, J.S. (2006). *The dimensions of sand ripples in full-scale oscillatory flows*. Coastal Engineering, 53, 997-1012

O'Donoghue, T., G. A. Kikkert, D. Pokrajac, N. Dodd and R. Briganti (2016). *Intra-swash hydrodynamics and sediment flux for dambreak swash on coarse-grained beaches.* Coastal Engineering **112**: 113-130. *doi: 10.1016/j.coastaleng.2016.03.004*.

Ogston, A. S. and R. W. Sternberg (1995). *On the importance of nearbed sediment flux measurements for estimating sediment transport in the surf zone.* Continental Shelf Research **15**(13): 1515-1524. *doi: 10.1016/0278-4343(95)00036-z*.

Ogston, A. S. and R. W. Sternberg (2002). *Effect of wave breaking on sediment eddy diffusivity, suspended-sediment and longshore sediment flux profiles in the surf zone.* Continental Shelf Research **22**(4): 633-655. *doi: 10.1016/s0278-4343(01)00033-4*.

Osborne, P. D. and B. Greenwood (1992). *Frequency-Dependent Cross-Shore Suspended Sediment Transport .1. A Non-Barred Shoreface.* Marine Geology **106**(1-2): 1-24. *doi*.

Peregrine, D. H. (1974). *Water-wave interactions in the surf zone*. Proceedings of 14th Conference on Coastal Engineering, Copenhagen Denmark, (28):500-517

Peregrine, D. H. (1983). *Breaking Waves on Beaches.* Annual Review of Fluid Mechanics **15**(1): 149-178. *doi: 10.1146/annurev.fl.15.010183.001053*.

Phillips, O. M. (1960). *On the dynamics of unsteady gravity waves of finite amplitude Part 1. The elementary interactions.* Journal of Fluid Mechanics **9**(02): 193. *doi: 10.1017/s0022112060001043*.

Pope, S. B. (2000). Turbulent Flows, Cambridge University Press.

Price, T. D. and B. G. Ruessink (2011). *State dynamics of a double sandbar system.* Continental Shelf Research **31**(6): 659-674. *doi: 10.1016/j.csr.2010.12.018*.

Pritchard, D. and A. J. Hogg (2005). *On the transport of suspended sediment by a swash event on a plane beach.* Coastal Engineering **52**(1): 1-23. *doi: 10.1016/j.coastaleng.2004.08.002*.

Pujara, N., P. L. F. Liu and H. Yeh (2015a). *The swash of solitary waves on a plane beach: flow evolution, bed shear stress and run-up.* Journal of Fluid Mechanics **779**: 556-597. *doi: 10.1017/jfm.2015.435*.

Pujara, N., P. L. F. Liu and H. H. Yeh (2015b). *An experimental study of the interaction of two successive solitary waves in the swash: A strongly interacting case and a weakly interacting case.* Coastal Engineering **105**: 66-74. *doi: 10.1016/j.coastaleng.2015.07.011*.

Puleo, J. A., R. A. Beach, R. A. Holman and J. S. Allen (2000). *Swash zone sediment suspension and transport and the importance of bore-generated turbulence.* Journal of Geophysical Research **105**(C7): 17021. *doi: 10.1029/2000jc900024*.

Puleo, J. A., T. Lanckriet and C. Blenkinsopp (2014). *Bed level fluctuations in the inner surf and swash zone of a dissipative beach.* Marine Geology **349**: 99-112. *doi: 10.1016/j.margeo.2014.01.006*.

Puleo, J. A., T. Lanckriet, D. Conley and D. Foster (2016). *Sediment transport partitioning in the swash zone of a large-scale laboratory beach.* Coastal Engineering **113**: 73-87. *doi: 10.1016/j.coastaleng.2015.11.001*.

Reniers, A. J. H. M., J. A. Roelvink and E. B. Thornton (2004). *Morphodynamic modeling of an embayed beach under wave group forcing.* Journal of Geophysical Research-Oceans **109**(C1). *doi: 10.1029/2002jc001586*.

Reniers, A. J. H. M., E. L. Gallagher, J. H. MacMahan, J. A. Brown, A. A. van Rooijen, J. S. M. V. de Vries and B. C. van Prooijen (2013). *Observations and modeling of steep-beach grain-size variability.* Journal of Geophysical Research-Oceans **118**(2): 577-591. *doi: 10.1029/2012jc008073*.

Revil-Baudard, T. and J. Chauchat (2013). *A two-phase model for sheet flow regime based on dense granular flow rheology.* Journal of Geophysical Research: Oceans **118**(2): 619-634. *doi: 10.1029/2012jc008306*.

Revil-Baudard, T., J. Chauchat, D. Hurther and P.-A. Barraud (2015). *Investigation of sheet-flow processes based on novel acoustic high-resolution velocity and concentration measurements.* Journal of Fluid Mechanics **767**: 1-30. *doi: 10.1017/jfm.2015.23*.

Ribberink, J. S. and A. A. Al-Salem (1994). *Sediment transport in oscillatory boundary layers in cases of rippled beds and sheet flow.* Journal of Geophysical Research **99**(C6): 12707 - 12727. *doi: 10.1029/94jc00380*.

Ribberink, J. S. and A. A. Al-Salem (1995). *Sheet Flow and Suspension of Sand in Oscillatory Boundary-Layers.* Coastal Engineering **25**(3-4): 205-225. *doi: 10.1016/0378-3839(95)00003-T*.

Ribberink, J. S. (1998). *Bed-load transport for steady flows and unsteady oscillatory flows.* Coastal Engineering **34**: 59-82. *doi*.

Ribberink, J. S., J. J. van der Werf, T. O'Donoghue and W. N. M. Hassan (2008). *Sand motion induced by oscillatory flows: Sheet flow and vortex ripples.* Journal of Turbulence **9**(20): 1-32. *doi: 10.1080/14685240802220009*.

Ribberink, J. S., D. A. Van der A, J. Van der Zanden, T. O'Donoghue, D. Hurther, I. Cáceres and P. D. Thorne (2014). SandT-Pro: Sediment transport measurements under irregular and breaking waves. Proceedings of the 34th International Conference on Coastal Engineering, Seoul, Korea. P. Lynett. Seoul, Korea, Coastal Engineering Research Council**:** 14

Richmond, B. M. and A. H. Sallenger (1984). Cross-shore transport of bimodal sands. ICCE**:** 1997-2008

Roelvink, J. A. and M. J. F. Stive (1989). *Bar-Generating Cross-Shore Flow Mechanisms on a Beach.* Journal of Geophysical Research-Oceans **94**(C4): 4785-4800. *doi: 10.1029/Jc094ic04p04785*.

Roelvink, J. A. and A. Reniers (1995). LIP 11D Delta Flume Experiments - Data report. W. D. Hydraulics. Delft, The Netherlands**:** 124

Ruessink, B. G., K. T. Houwman and P. Hoekstra (1998). *The systematic contribution of transporting mechanisms to the cross-shore sediment transport in water depths of 3 to 9 m.* Marine Geology **152**(4): 295-324. *doi: 10.1016/S0025-3227(98)00133-9*.

Ruessink, B. G., Y. Kuriyama, A. J. H. M. Reniers, J. A. Roelvink and D. J. R. Walstra (2007). *Modeling cross-shore sandbar behavior on the timescale of weeks.* Journal of Geophysical Research **112**(F3). *doi: 10.1029/2006jf000730*.

Ruessink, B. G. (2010). *Observations of Turbulence within a Natural Surf Zone.* Journal of Physical Oceanography **40**(12): 2696-2712. *doi: 10.1175/2010jpo4466.1*.

Ruessink, B. G., H. Michallet, T. Abreu, F. Sancho, D. A. Van der A, J. J. Van der Werf and P. A. Silva (2011). *Observations of velocities, sand concentrations, and fluxes under velocity-asymmetric oscillatory flows.* Journal of Geophysical Research **116**(C3). *doi: 10.1029/2010jc006443*.

Ruessink, B. G., G. Ramaekers and L. C. Van Rijn (2012). *On the parameterization of the free-stream non-linear wave orbital motion in nearshore morphodynamic models.* Coastal Engineering **65**: 56-63. *doi: 10.1016/j.coastaleng.2012.03.006*.

Sallenger, A. H., R. A. Holman and W. A. Birkemeier (1985). *Storm-induced response of a nearshore-bar system.* Marine Geology **64**: 237-257. *doi*.

Schnitzler, B. (2015). Modeling sand transport under breaking waves. MSc thesis, University of Twente.

Schretlen, J. L. M. (2012). Sand transport under full-scale progressive surface waves. PhD Thesis, University of Twente, The Netherlands.

Scott, C. P., D. T. Cox, T. B. Maddux and J. W. Long (2005). *Large-scale laboratory observations of turbulence on a fixed barred beach.* Measurement Science and Technology **16**(10): 1903-1912. *doi: 10.1088/0957-0233/19/10/004*.

Scott, N. V., T. J. Hsu and D. Cox (2009). *Steep wave, turbulence, and sediment concentration statistics beneath a breaking wave field and their implications for sediment transport.* Continental Shelf Research **29**(20): 2303-2317. *doi: 10.1016/j.csr.2009.09.008*.

Sistermans, P. G. J. (2002). Graded sediment transport by non-breaking waves and currents. PhD thesis, TU Delft, the Netherlands.

Sleath, J. F. A. (1987). *Turbulent oscillatory flow over rough beds.* Journal of Fluid Mechanics **182**(-1): 369. *doi: 10.1017/s0022112087002374*.

Sleath, J. F. A. (1991). *Velocities and shear stresses in wave-current flows.* Journal of Geophysical Research **96**(C8): 15237. *doi: 10.1029/91jc01458*.

Sleath, J. F. A. (1999). *Conditions for plug formation in oscillatory flow*. Continental Shelf Research 19(13): 1643-1664. *doi: 10.1016/s0278-4343(98)00096-x*.

Smith, E. R. and N. C. Kraus (1991). *Laboratory Study of Wave-Breaking over Bars and Artificial Reefs.* Journal of Waterway, Port, Coastal, and Ocean Engineering **117**(4): 307-325. *doi: 10.1061/(asce)0733-950x(1991)117:4(307)*.

Sou, I. M. and H. Yeh (2011). *Laboratory study of the cross-shore flow structure in the surf and swash zones.* Journal of Geophysical Research **116**(C3). *doi: 10.1029/2010jc006700*.

Soulsby, R. L. (1980). Selecting Record Length and Digitization Rate for Near-Bed Turbulence Measurements. Journal of Physical Oceanography 10(2): 208-219. doi: 10.1175/1520-0485(1980)010<0208:srladr>2.0.co;2.

Steetzel, H. (1993). Cross-shore transport during storm surges. PhD thesis, Delft University of Technology.

Stive, M. J. F. and H. G. Wind (1986). *Cross-Shore Mean Flow in the Surf Zone.* Coastal Engineering **10**(4): 325-340. *doi: 10.1016/0378-3839(86)90019-0*.

Sumer, B. M. and B. Oguz (1978). *Particle Motions near Bottom in Turbulent-Flow in an Open Channel.* Journal of Fluid Mechanics **86**(May): 109-127. *doi: 10.1017/S0022112078001020*.

Sumer, B. M., T. S. Laursen and J. Fredsøe (1993). *Wave boundary layers in a convergent tunnel.* Coastal Engineering **20**(3-4): 317-342. *doi: 10.1016/0378-3839(93)90006-t*.

Sumer, B. M., A. Kozakiewicz, J. Fredsøe and R. Deigaard (1996). *Velocity and Concentration Profiles in Sheet-Flow Layer of Movable Bed.* Journal of Hydraulic Engineering **122**(10): 549-558. *doi: 10.1061/(asce)0733-9429(1996)122:10(549)*.

Sumer, B. M., L. H. C. Chua, N. S. Cheng and J. Fredsoe (2003). *Influence of turbulence on bed load sediment transport.* Journal of Hydraulic Engineering-Asce **129**(8): 585-596. *doi: 10.1061/(Asce)0733-9429(2003)129:8(585)*.

Sumer, B. M., H. A. A. Guner, N. M. Hansen, D. R. Fuhrman and J. Fredsøe (2013). *Laboratory observations of flow and sediment transport induced by plunging regular waves.* Journal of Geophysical Research: Oceans **118**(11): 6161-6182. *doi: 10.1002/2013jc009324*.

Svendsen, I. A., P. A. Madsen and J. Buhr Hansen (1978). Wave characteristics in the surf zone. Proc. 16th Conf. Coastal Eng. Hamburg, Germany, American Society of Civil Engineers**:** 520-539

Svendsen, I. A. (1984). *Mass flux and undertow in a surf zone.* Coastal Engineering **8**: 347-365. *doi*.

Svendsen, I. A. (1987). *Analysis of Surf Zone Turbulence.* Journal of Geophysical Research-Oceans **92**(C5): 5115-5124. *doi: 10.1029/JC092iC05p05115*.

Swart, D. H. (1974). Offshore sediment transport and equilibrium beach profiles. PhD Thesis, TU Delft.

Thornton, E. B. and R. T. Guza (1983). *Transformation of wave height distribution.* Journal of Geophysical Research **88**(C10): 5925. *doi: 10.1029/JC088iC10p05925*.

Thornton, E. B., R. T. Humiston and W. Birkemeier (1996). *Bar/trough generation on a natural beach.* Journal of Geophysical Research-Oceans **101**(C5): 12097-12110. *doi: 10.1029/96jc00209*.

Ting, F. C. K. and J. T. Kirby (1994). *Observation of Undertow and Turbulence in a Laboratory Surf Zone.* Coastal Engineering **24**(1-2): 51-80. *doi: 10.1016/0378-3839(94)90026-4*.

Ting, F. C. K. and J. T. Kirby (1995). *Dynamics of Surf-Zone Turbulence in a Strong Plunging Breaker.* Coastal Engineering **24**(3-4): 177-204. *doi: 10.1016/0378-3839(94)00036-W*.

Ting, F. C. K. (2001). *Laboratory study of wave and turbulence velocities in a broad-banded irregular wave surf zone.* Coastal Engineering **43**(3-4): 183-208. *doi*.

Ting, F. C. K. and J. R. Nelson (2011). *Laboratory measurements of large-scale near-bed turbulent flow structures under spilling regular waves*. Coastal Engineering **58**(2): 151-172. doi: 10.1016/j.coastaleng.2010.09.004.

Torres-Freyermuth, A., J. L. Lara and I. J. Losada (2010). *Numerical modelling of short- and long-wave transformation on a barred beach.* Coastal Engineering **57**(3): 317-330. *doi: 10.1016/j.coastaleng.2009.10.013*.

Trowbridge, J. and O. S. Madsen (1984). *Turbulent Wave Boundary-Layers .2. 2nd-Order Theory and Mass-Transport.* Journal of Geophysical Research-Oceans **89**(Nc5): 7999-8007. *doi*.

Turner, I. L., P. E. Russell and T. Butt (2008). *Measurement of wave-by-wave bed levels in the swash zone.* Coastal Engineering **55**(12): 1237-1242. *doi: 10.1016/j.coastaleng.2008.09.009*.

van der A, D. A., T. O'Donoghue and J. S. Ribberink (2009). *Sheet flow sand transport processes in oscillatory flow with acceleration skewness*. Proc. Coastal Sediments 2009, Singapore, World Scientific.

van der A, D. A., T. O'Donoghue and J. S. Ribberink (2010). *Measurements of sheet flow transport in acceleration-skewed oscillatory flow and comparison with practical formulations.* Coastal Engineering **57**(3): 331-342. *doi: 10.1016/j.coastaleng.2009.11.006*.

van der A, D. A., T. O'Donoghue, A. G. Davies and J. S. Ribberink (2011). *Experimental study of the turbulent boundary layer in acceleration-skewed oscillatory flow.* Journal of Fluid Mechanics **684**: 251-283. *doi: 10.1017/jfm.2011.300*.

van der A, D. A., J. S. Ribberink, J. J. van der Werf, T. O'Donoghue, R. H. Buijsrogge and W. M. Kranenburg (2013). *Practical sand transport formula for non-breaking waves and currents.* Coastal Engineering **76**: 26-42. *doi: 10.1016/j.coastaleng.2013.01.007*.

van der A, D. A., J. Van der Zanden, T. O'Donoghue, I. Cáceres, S. J. McLelland and J. S. Ribberink (Submitted). *Hydrodynamics and turbulence under a large-scale plunging wave over a fixed bar.* Journal of Geophysical Research: Oceans. *doi*.

van der Spek, A. and Q. Lodder (2015). A new sediment budget for the Netherlands: the effect of 15 years of nourishing (1991-2005). Proceedings of the Coastal Sediments 2015. San Diego, USA**:** 14

van der Werf, J. J., J. S. Doucette, T. O'Donoghue and J. S. Ribberink (2007). *Detailed measurements of velocities and suspended sand concentrations over full-scale ripples in regular oscillatory flow.* Journal of Geophysical Research **112**(F2). *doi: 10.1029/2006jf000614*.

van der Werf, J. J., V. Magar, J. Malarkey, K. Guizien and T. O'Donoghue (2008). *2DV modelling of sediment transport processes over full-scale ripples in regular asymmetric oscillatory flow.* Continental Shelf Research **28**(8): 1040-1056. *doi: 10.1016/j.csr.2008.02.007*.

van der Werf, J. J., J. J. L. M. Schretlen, J. S. Ribberink and T. O'Donoghue (2009). *Database of full-scale laboratory experiments on wave-driven sand transport processes.* Coastal Engineering **56**(7): 726-732. *doi: 10.1016/j.coastaleng.2009.01.008*.

van der Werf, J. J., R. Veen, J. S. Ribberink and J. van der Zanden (2015). Testing of the new SANTOSS transport formula in the Delft3D morphological modeling system. Proceedings of Coastal Sediments. San Diego, USA**:** 14

van der Zanden, J., J. M. Alsina, I. Cáceres, R. H. Buijsrogge and J. S. Ribberink (2015a). *Bed level motions and sheet flow processes in the swash zone: Observations with a new conductivity-based concentration measuring technique (CCM+).* Coastal Engineering **105**: 47-65. *doi: 10.1016/j.coastaleng.2015.08.009*.

van der Zanden, J., D. A. Van der A, J. S. Ribberink, T. O'Donoghue, D. Hurther, I. Caceres and P. D. Thorne (2015b). *Sand transport process measurements under large-scale breaking waves*. Coastal Sediments. San Diego, USA**:** 14 pp.

van der Zanden, J., D. A. van der A, D. Hurther, I. Cáceres, T. O'Donoghue and J. S. Ribberink (2016). *Near-bed hydrodynamics and turbulence below a large-scale plunging breaking wave over a mobile barred bed profile.* Journal of Geophysical Research: Oceans **121**(8): 6482-6506. *doi: 10.1002/2016jc011909*.

van Doorn, T. (1981). *Experimental investigation of near-bottom velocities in water waves without and with a current*, Delft Hydraulics Laboratory. TOW Report M 1423 part 1

van Duin, M. J. P., N. R. Wiersma, D. J. R. Walstra, L. C. Van Rijn and M. J. F. Stive (2004). *Nourishing the shoreface: observations and hindcasting of the Egmond case, The Netherlands.* Coastal Engineering **51**(8-9): 813-837. *doi: 10.1016/j.coastaleng.2004.07.011*.

van Rijn, L. C. (1993). Principles of Sediment Transport in Rivers, Estuaries and Coastal Seas. the Netherlands, Aqua Publications, the Netherlands.

van Rijn, L. C. (1998). The effect of sediment composition on cross-shore bed profiles. Proc. 26th Int. Conf. on Coastal Engineering**:** 2495-2508

van Rijn, L. C., D. J. R. Walstra, B. Grasmeijer, J. Sutherland, S. Pan and J. P. Sierra (2003). *The predictability of cross-shore bed evolution of sandy beaches at the time scale of storms and seasons using process-based Profile models.* Coastal Engineering **47**(3): 295-327. *doi: 10.1016/s0378-3839(02)00120-5*.

van Rijn, L. C. (2007a). *Unified view of sediment transport by currents and waves. I: Initiation of motion, bed roughness, and bed-load transport.* Journal of Hydraulic Engineering-Asce **133**(6): 649-667. *doi: 10.1061/(Asce)0733-9429(2007)133:6(649)*.

van Rijn, L. C. (2007b). *Unified View of Sediment Transport by Currents and Waves. II: Suspended Transport.* Journal of Hydraulic Engineering **133**(6): 668-689. *doi: 10.1061/(asce)0733-9429(2007)133:6(668)*.

van Rijn, L. C. (2007c). *Unified view of sediment transport by currents and waves. III: Graded beds.* Journal of Hydraulic Engineering-Asce **133**(7): 761-775. *doi: 10.1061/(Asce)0733-9429(2007)133:7(761)*.

van Rijn, L. C., D. J. R. Walstra and M. van Ormondt (2007d). *Unified view of sediment transport by currents and waves. IV: Application of morphodynamic model.* Journal of Hydraulic Engineering-Asce **133**(7): 776-793. *doi: 10.1061/(Asce)0733-9429(2007)133:7(776)*.

van Rijn, L. C. (2009). *Prediction of dune erosion due to storms.* Coastal Engineering **56**(4): 441-457. *doi: 10.1016/j.coastaleng.2008.10.006*.

van Rijn, L. C., P. K. Tonnon and D. J. R. Walstra (2011). *Numerical modelling of erosion and accretion of plane sloping beaches at different scales.* Coastal Engineering **58**(7): 637-655. *doi: 10.1016/j.coastaleng.2011.01.009*.

van Rijn, L. C., J. S. Ribberink, J. V. D. Werf and D. J. R. Walstra (2013). *Coastal sediment dynamics: recent advances and future research needs.* Journal of Hydraulic Research **51**(5): 475-493. *doi: 10.1080/00221686.2013.849297*.

van Thiel de Vries, J. S. M., M. R. A. van Gent, D. J. R. Walstra and A. J. H. M. Reniers (2008). *Analysis of dune erosion processes in large-scale flume experiments.* Coastal Engineering **55**(12): 1028-1040. *doi: 10.1016/j.coastaleng.2008.04.004*.

van Thiel de Vries, J. S. M. (2009). Dune erosion during storm surges. PhD Thesis, TU Delft.

Vousdoukas, M. I., T. Kirupakaramoorthy, H. Oumeraci, M. de la Torre, F. Wübbold, B. Wagner and S. Schimmels (2014). *The role of combined laser scanning and video techniques in monitoring wave-by-wave swash zone processes.* Coastal Engineering **83**: 150-165. *doi: 10.1016/j.coastaleng.2013.10.013*.

Walstra, D. J. R. and H. Steetzel (2003). Description of improvements in the UNIBEST-TC model, WL | Delft Hydraulics**:** 88

Wang, P., R. A. Davis and N. C. Kraus (1998). *Cross-shore distribution of sediment texture under breaking waves along low-wave-energy coasts.* Journal of Sedimentary Research **68**(3): 467-506. *doi*.

Watanabe, A. and S. Sato (2004). A sheet-flow transport rate for asymmetric, forward-leaning waves and currents. Proceedings 29th International Conference on Coastal Engineering, World Scientific. **2:** 1703-1714

Wiberg, P. L., D. E. Drake and D. A. Cacchione (1994). *Sediment resuspension and bed armoring during high bottom stress events on the northern California inner continental shelf: measurements and predictions.* Continental Shelf Research **14**(10-11): 1191-1219. *doi: 10.1016/0278-4343(94)90034-5*.

Wijnberg, K. M. and J. H. J. Terwindt (1995). *Extracting decadal morphological behaviour from high-resolution, long-term bathymetric surveys along the Holland coast using eigenfunction analysis.* Marine Geology **126**(1-4): 301-330. *doi: 10.1016/0025-3227(95)00084-c*.

Wijnberg, K. M. and A. Kroon (2002). *Barred beaches.* Geomorphology **48**(1-3): 103-120. *doi: 10.1016/S0169-555x(02)00177-0*.

Wright, L. D. and A. D. Short (1984). *Morphodynamic Variability of Surf Zones and Beaches - a Synthesis.* Marine Geology **56**(1-4): 93-118. *doi: 10.1016/0025-3227(84)90008-2*.

Yoon, H. D. and D. T. Cox (2010). *Large-scale laboratory observations of wave breaking turbulence over an evolving beach.* Journal of Geophysical Research-Oceans **115**. *doi: 10.1029/2009jc005748*.

Yoon, H. D. (2011). Observations and Prediction of Intermittent Sediment Suspension in the Surf Zone. PhD Thesis, Oregon State University.

Yoon, H. D. and D. T. Cox (2012). *Cross-shore variation of intermittent sediment suspension and turbulence induced by depth-limited wave breaking.* Continental Shelf Research **47**: 93-106. *doi: 10.1016/j.csr.2012.07.001*.

Yoon, H.-D., D. Cox and N. Mori (2015). *Parameterization of Time-Averaged Suspended Sediment Concentration in the Nearshore.* Water **7**(11): 6228-6243. *doi: 10.3390/w7116228*.

Yu, Z., H. D. Niemeijer and W. T. Bakker (1990). *Site investigation on sand transport in the sheet flow layer*. Proceedings of the 22nd International Conference on Coastal Engineering, ASCE.

Yu, Y., R. W. Sternberg and R. A. Beach (1993). *Kinematics of breaking waves and associated suspended sediment in the nearshore zone.* Continental Shelf Research **13**(11): 1219-1242. *doi: 10.1016/0278-4343(93)90050-8*.

Zhang, D. P. and T. Sunamura (1994). Multiple bar formation by breaker-induced vortices: a laboratory approach. Proc. Intern. Conf. Coastal Eng.**:** 2856-2870

Zhu, F. F. and N. Dodd (2015). *The morphodynamics of a swash event on an erodible beach.* Journal of Fluid Mechanics **762**: 110-140. *doi: 10.1017/Jfm.2014.610*.

About the author

Joep van der Zanden was born in Roermond, the Netherlands, on the 11th October 1987 and grew up in Someren in the province of Noord-Brabant. After finishing his pre-university secondary education at Het Varendonck College in Asten in 2005, he enrolled in the BSc study 'Soil, Water and Atmosphere' at Wageningen University which he completed in 2008 with a graduation project focusing on morphodynamic processes in a river flume with a cohesive bed.

After a full-time board year as secretary of students sports foundation Thymos, Joep started his MSc 'Hydrology and Water Management' at Wageningen University. He obtained his MSc degree in 2012 after a six-month graduation project on numerical modeling of groundwater–vegetation interactions, conducted at the University of Sydney, and a five-month internship at Hydrologic (Netherlands). During his studies, Joep participated in extracurricular activities by his study association and several sports organizations in Wageningen.

Joep moved to Enschede in 2012 to start his PhD research at the Water Engineering and Management department of the University of Twente. During his PhD research he spent over six months in Barcelona to participate in four experimental campaigns in the CIEM wave flume. He further tutored seminars during courses at BSc and MSc level and (co-)supervised four BSc and three MSc graduation projects. In 2016, he froze his PhD research for a six-month research assistant position at the University of Aberdeen, UK. He presented his research results at international conferences in Lisbon, San Diego, Schoorl and Edinburgh.

In his free time Joep enjoys outdoor sports activities (running, cycling). He further enjoys listening music and guitar playing. His holidays are best spent by exploring new grounds through trekking in nature.

Publications

Peer-reviewed journal papers

van der Zanden, J., J. M. Alsina, I. Cáceres, R. H. Buijsrogge and J. S. Ribberink (2015). *Bed level motions and sheet flow processes in the swash zone: Observations with a new conductivity-based concentration measuring technique (CCM+).* Coastal Engineering 105: 47-65. *doi: 10.1016/j.coastaleng.2015.08.009*.

van der Zanden, J., D. A. van der A, D. Hurther, I. Cáceres, T. O'Donoghue and J. S. Ribberink (2016). *Near-bed hydrodynamics and turbulence below a large-scale plunging breaking wave over a mobile barred bed profile.* Journal of Geophysical Research: Oceans 121(8): 6482-6506. *doi: 10.1002/2016jc011909*.

van der Zanden, J., D. A. van der A, D. Hurther, I. Caceres, T. O'Donoghue and J. S. Ribberink (submitted). *Suspended sediment transport around a large-scale laboratory breaker bar.* Coastal Engineering

van der A, D. A., **J. van der Zanden**, T. O'Donoghue, I. Cáceres, S. J. McLelland and J. S. Ribberink (submitted). *Hydrodynamics and turbulence under a large-scale plunging wave over a fixed bar.* Journal of Geophysical Research: Oceans.

van der Zanden, J., D. A. van der A, D. Hurther, I. Caceres, T. O'Donoghue, S. J. M. H. Hulscher and J. S. Ribberink (in preparation). *Bedload and suspended load contributions to the morphodynamics of a large-scale laboratory breaker bar.*

Non-reviewed papers

van der Zanden, J., J.S. Ribberink, S.J.M.H. Hulscher and D.A. van der A (2016). *Betere modellen nodig voor zandtransport onder brekende golven*. Land en Water 2016(12)

Ribberink, J.S., T. O'Donoghue, D.A. van der A, **J. van der Zanden**, D. Hurther, I. Cáceres and P.D. Thorne (2014). *Measurements of sand transport processes under breaking and irregular waves*. IAHR newsletter 2014(3), 86-87.

van der Zanden, J. (2014). *Het effect van golfbreking op zandtransport*. ConcepTueel, 23(2), 24-27.

Conference papers

van der Werf, J. J., R. Veen, J. S. Ribberink and **J. van der Zanden** (2015). *Testing of the new SANTOSS transport formula in the Delft3D morphological modeling system.* Proc. of Coastal Sediments. San Diego, USA: 14 pp.

van der Zanden, J., D. A. van der A, J. S. Ribberink, T. O'Donoghue, D. Hurther, I. Caceres and P. D. Thorne (2015). *Sand transport process measurements under large-scale breaking waves*. Proc. of Coastal Sediments. San Diego, USA: 14 pp.

Alsina, J., I. Caceres, **J. van der Zanden**, J. S. Ribberink and T. E. Baldock (2014). *Large scale experiments on beach evolution induced by bichromatic wave groups with varying group period.* Proc. of the 34th ICCE, Seoul, Korea: 10 pp.

Alsina, J. M., **J. van der Zanden**, J. S. Ribberink, R. H. Buijsrogge, T. E. Baldock, M. Brocchini, E. Peña, F. Sanchez-Tembleque and I. Caceres (2014). *Sediment transport and beach profile evolution induced by bichromatic waves with different grouping periods*. Proc. of the HYDRALAB IV Joint User Meeting, Lisbon

Ribberink, J. S., D. A. van der A, **J. van der Zanden**, T. O'Donoghue, D. Hurther, I. Cáceres and P. D. Thorne (2014). *SandT-Pro: Sediment transport measurements under irregular and breaking waves*. Proc. of the 34th ICCE, Seoul, Korea. P. Lynett. 14 pp.

van der Zanden, J., J. M. Alsina, I. Cáceres, R. H. Buijsrogge and J. S. Ribberink (2013). *New CCM technique for sheet-flow measurements and its first application in swash-zone experiments*. Proc. of Short Course/Conference on Applied Coastal Research, Lisbon, Portugal, 10 pp.

Presentations at national and international conferences:

Oral presentations at *SCACR* (Lisbon, Portugal, 2013), *NCK Days* (Schoorl, Netherlands, 2015), *Coastal Sediments* (San Diego, USA, 2015), *Scottish Fluid Mechanics meeting* (Edinburgh, UK, 2016).

Poster presentations at *NCK Days* (2013, 2014, 2016).

Teaching experience

BSc Civil Engineering courses at University of Twente:

Fluid Mechanics (seminar tutoring)

MSc Civil Engineering and Management courses at University of Twente:

Mathematical Physics in Water Systems (seminar tutoring)

Data Analysis in Water Engineering and Management (Matlab/ArcGIS seminars)

Marine Dynamics (seminar tutoring)

Academic Research Skills, pre-master (supervising practical assignment)

Seminar morphology (supervising practical assignment)

(co-)Supervision of three MSc graduation projects and four BSc graduation projects.

Awards

Nominated for Twente Water Centre 'PhD paper of the year', 2016.